

Liquid Metal MHD Studies at High Magnetic Fields

Relevant to Fusion Test Blankets

By

Pravat Kumar Swain

Enrolment No: PHYS01201404021

Bhabha Atomic Research Centre, Mumbai

A thesis submitted to the

Board of Studies in Physical Sciences

In partial fulfillment of requirements

for the Degree of

DOCTOR OF PHILOSOPHY

HOMI BHABHA NATIONAL INSTITUTE

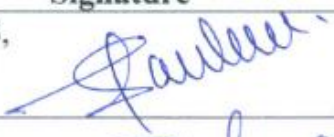
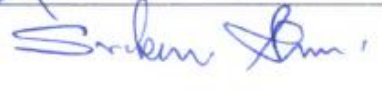
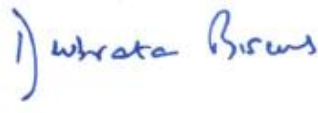
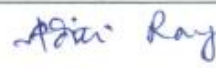


December, 2019

Homi Bhabha National Institute¹

Recommendations of the Viva Voce Committee

As members of the Viva Voce Committee, we certify that we have read the dissertation prepared by Shri Pravat Kumar Swain entitled "Liquid metal MHD studies at high magnetic fields relevant to fusion Test Blankets" and recommend that it may be accepted as fulfilling the thesis requirement for the award of Degree of Doctor of Philosophy.

Designation	Name	Signature	Date
Chairman	Dr. Ravi Kumar, OS, Head, SIRD, BARC		10/11/2020
Guide/ Convener	Dr S.Ghorui, SO(H), L&PTD, BARC		10/11/2020
Co-guide	-		
Examiner	Prof. Vinayak Eswaran, Dept. Mech. Engg, IIT Hyderabad		16/11/20
Member 1	Dr. Raghwendra Kumar, SO(G), AM&TPS, BARC		14/11/2020
Member 2	Dr. D. Biswas, SO(H), Head, AM&TPS, BARC		10.11.2020
Member 3	Dr. Aditi Ray, SO(H), Head, ThPS, BARC		10/11/2020

Final approval and acceptance of this thesis is contingent upon the candidate's submission of the final copies of the thesis to HBNI.

I/We hereby certify that I/we have read this thesis prepared under my/our direction and recommend that it may be accepted as fulfilling the thesis requirement.

Date: 10/11/2020

Place: Trombay

Signature

Co-guide (if any)



Signature

Guide

¹ This page is to be included only for final submission after successful completion of viva voce.

STATEMENT BY AUTHOR

This dissertation has been submitted in partial fulfillment of requirements for an advanced degree at Homi Bhabha National Institute (HBNI) and is deposited in the Library to be made available to borrowers under rules of the HBNI.

Brief quotations from this dissertation are allowable without special permission, provided that accurate acknowledgement of source is made. Requests for permission for extended quotation from or reproduction of this manuscript in whole or in part may be granted by the Competent Authority of HBNI when in his or her judgment the proposed use of the material is in the interests of scholarship. In all other instances, however, permission must be obtained from the author.

Signature:

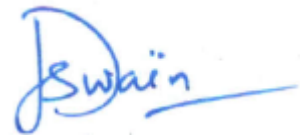


(Pravat Kumar Swain)

DECLARATION

I, hereby declare that the investigation presented in the thesis has been carried out by me. The work is original and has not been submitted earlier as a whole or in part for a degree / diploma at this or any other Institution / University.

Signature:



(Pravat Kumar Swain)

List of Publications arising from the thesis

Journal

1. P.K. Swain, P. Satyamurthy, R. Bhattacharyay, A. Patel, A. Shishko, E. Platacis, et al., 3D MHD lead–lithium liquid metal flow analysis and experiments in a test section of multiple rectangular bends at moderate to high Hartmann numbers, *Fusion Eng. Des.* 88 (2013) 2848–2859
2. S. Subramanian, P.K. Swain, A V. Deshpande, P. Satyamurthy, Effect of Hartmann layer resolution for MHD flow in a straight conducting duct at high Hartmann numbers; *Sadhana*,40 (2015), 851–861
3. P. Satyamurthy, P.K. Swain, V. Tiwari, I.R. Kirillov, D.M. Obukhov, D.A. Pertsev, Experiments and numerical MHD analysis of LLCB TBM test-section with NaK at 1T magnetic field, *Fusion Eng. Des.* 91 (2015) 44–51
4. P.K. Swain, A. Shishko, P. Mukherjee, V. Tiwari, S. Ghorui, R. Bhattacharyay, A.Patel, P. Satyamurthy, S. Ivanov, E. Platacis, A. Ziks., Numerical and experimental MHD studies of Lead-Lithium liquid metal flows in multichannel test-section at high magnetic fields, *Fusion Eng. Des.* 132 (2018) 73–85
5. P.K. Swain, Pratik Koli, S. Ghorui, P. Mukherjee, A.V. Deshpande, Thermofluid MHD studies in a model of Indian LLCB TBM at high magnetic field relevant to ITER, *Fusion Eng. Des.* 150 (2020) 111374
6. P.K. Swain, R. S. Rawat, K. Mukherjee, S. Kumar, P. K. Rai, V. Tiwari, S. Rajan, S. Malhotra, S. Ghorui, MHD effects of partition plates on thermofluid performance of Indian variant LLCB TBM for ITER, *Fusion Eng. Des.* (2020) 112193

Conference

1. Pravat Swain, Sanket Tole, P. Satyamurthy, Arvind Deshpande, R.P. Bhattacharyay, 3D computational analysis of Lead-lithium MHD flows at high magnetic field in an electrically coupled multichannel Test Blanket Module, National Conference on Fluid Mechanics and Fluid Power, NIT Hamirpur (HP), December 2013
2. Sharanya Subramanian, Pravat Swain, Satyamurthy and Arvind Deshpande, Resolving Hartmann layer and its effect on MHD flow parameters for a straight, conducting duct at moderate to high Hartmann number, National Conference on Fluid Mechanics and Fluid Power, NIT Hamirpur(HP), December 2013

Signature:



(Pravat Kumar Swain)

Acknowledgements

I express sincere gratitude to my guide, Professor Srikumar Ghorui, for his valuable guidance, timely suggestions and constant encouragement. His confidence in my abilities has been a source of great inspiration. My special thanks to Dr. P. Satyamurthy for his constant guidance in understanding the basic concepts and giving me the exposure to take up this project. I would like to extend my sincere thanks to Professor Andrey Shishko for his continuous support and suggestive technical discussions.

I express my deep sense of gratitude to the doctoral committee for their valuable suggestions to timely complete this dissertation. I am thankful to Sushil Kumar, Ravindra Singh Rawat, Kallol Mukherjee, Vikas Tiwari and Pravin Rai for their generous help and maintaining friendly ambiance in the office. I extend my sincere thanks to Dr. Rajendra Bhattacharaya, Mrs Anita patel and IPUL colleagues for conducting joint experiments and technical support for the thesis work. I am also thankful to Professor A. V. Deshpande for providing CFD facility at VJTI, Mumbai to carry out computation studies of this thesis work.

I take this opportunity to thank Head ATDS, Sanjay Malhotra and Sundar Rajan for their unstinted cooperation. I also wish to thank all my friends and my wife Monalisa Parida without whose contribution, this project would not have been completed on time.

CONTENTS

List of figures 1

List of tables 9

Synopsis 11

1	CHAPTER.....	23
	<u>Magnetohydrodynamic Phenomena in Test Blanket Module of ITER.....</u>	23
1.1	<u>Introduction.....</u>	23
1.2	<u>Test blanket program of ITER.....</u>	24
1.3	<u>Fusion blanket concepts of ITER and worldwide program.....</u>	26
1.4	<u>Magnetohydrodynamics (MHD) issues in TBM.....</u>	29
1.5	<u>Q2D MHD turbulence.....</u>	32
1.6	<u>Boundary layer stability in MHD duct flow.....</u>	34
1.7	<u>Aim and work plan of the present study.....</u>	40
1.8	<u>References.....</u>	43
2	CHAPTER.....	46
	<u>Benchmarking Studies with Linear Analytical Solutions.....</u>	46
2.1	<u>Introduction.....</u>	46
2.2	<u>Benchmarking with Hunt's Exact Analytical solution.....</u>	48
2.3	<u>Numerical simulation for benchmarking with Hunt's analytical solution.....</u>	53
2.3.1	<u>Governing Equation.....</u>	54
2.3.2	<u>Boundary conditions.....</u>	55
2.3.3	<u>Solving methodology.....</u>	55
2.3.4	<u>Mesh.....</u>	56
2.3.5	<u>Physical properties.....</u>	58
2.3.6	<u>Results of numerical simulation.....</u>	58
2.4	<u>Benchmarking problems recommended by International team for verification and validation of MHD codes.....</u>	63
2.4.1	<u>Results of numerical study.....</u>	64
2.5	<u>Summary of the key results of benchmarking studies with Hunt problem.....</u>	68
2.6	<u>Benchmarking studies with analytical model based on variational approach.....</u>	69
2.6.1	<u>Description of analytical model.....</u>	69
2.7	<u>Numerical simulation of 3D MHD flow in electrically conducting square duct.....</u>	72
2.7.1	<u>Results of numerical simulation and comparison with analytical model.....</u>	73
2.8	<u>Comparison of variational model with Hunt's exact analytical solution.....</u>	78
2.9	<u>Summary of the benchmarking studies with analytical model.....</u>	79

2.10	<u>References</u>	80
3	<u>CHAPTER</u>	82
	<u>Numerical Model Validation with Experiment at High Magnetic Field</u>	82
3.1	<u>Introduction</u>	82
3.2	<u>Experiment set up</u>	84
3.2.1	<u>Liquid metal (Lead-lithium) experiment loop</u>	84
3.2.2	<u>Experiment test section</u>	85
3.3	<u>Diagnostics and Instrumentation</u>	89
3.3.1	<u>Potential measurement</u>	89
3.3.2	<u>Pressure measurement</u>	91
3.3.3	<u>Methodology for the measurement of pressure drop</u>	92
3.4	<u>Analysis of Experimental Data</u>	94
3.4.1	<u>Mean velocity estimation from side wall potential distribution</u>	94
3.4.2	<u>Estimation of Core Velocity from Hartmann Wall Potential Distribution</u>	100
3.5	<u>Pressure drop</u>	104
3.5.1	<u>Pressure drop in bend where flow turns from parallel to perpendicular direction</u>	104
3.5.2	<u>Pressure drop in bend where flow turns from perpendicular to parallel direction of the applied magnetic field</u>	106
3.5.3	<u>Pressure drop at the bend where flow is normal to the magnetic field in both the legs</u>	108
3.6	<u>Brief summary of experimental data analysis in the test section of multiple bends</u>	110
3.7	<u>3D numerical study of MHD flow in test section of multiple bends</u>	111
3.7.1	<u>Model Geometry and Mesh</u>	111
3.8	<u>Comparison of numerical simulation results with experiment</u>	113
3.8.1	<u>Side wall electric potential distribution</u>	113
3.8.2	<u>Hartmann wall potential distribution</u>	116
3.9	<u>Flow distribution in the bends based on numerical simulation</u>	119
3.9.1	<u>Velocity distribution in the inlet duct ($0 < x < 0.031\text{m}$, $0 < y < 0.031\text{m}$ and $0 < z < 0.104$)</u>	119
3.9.2	<u>Velocity distribution in the vertical duct ($0 < x < 0.031\text{m}$, $0.028\text{m} < y < 0.169\text{m}$ and $0.104\text{m} < z < 0.16$)</u>	121
3.9.3	<u>Velocity distribution in the horizontal duct ($0.031\text{m} < x < 0.149\text{m}$, $0.169\text{m} < y < 0.2\text{m}$ and $0.104\text{m} < z < 0.16\text{m}$)</u>	124
3.10	<u>Pressure distribution</u>	127
3.11	<u>Brief qualitative comparison of the present results with the simulation using other MHD codes</u>	129

3.12	<u>Summary of numerical simulation in test section of multiple bends</u>	130
3.13	<u>References</u>	131
4	<u>CHAPTER</u>	133
	<u>Effects of Magnetic Properties of the Structural Material and Non-resolved Hartmann Layer on Liquid Metal MHD Flow</u>	133
4.1	<u>Effects of magnetic properties of the structural material on PbLi MHD flow</u>	133
4.2	<u>Test section and diagnostics</u>	134
4.3	<u>Analysis of Experiment result</u>	136
4.3.1	<u>Comparison of side wall voltage</u>	136
4.3.2	<u>Comparison of pressure drop</u>	140
4.4	<u>Summary of the effects of magnetic properties of the material on MHD flow</u>	143
4.5	<u>Numerical study for quantifying effects of non resolved Hartmann layer on MHD flow in electrically conducting channel</u>	143
4.6	<u>Description of geometry and grid</u>	145
4.7	<u>Governing equations</u>	147
4.7.1	<u>Boundary Conditions</u>	148
4.8	<u>Results and discussion</u>	148
4.8.1	<u>Comparison for induced electrical current density</u>	149
4.8.2	<u>Comparison for core velocity</u>	152
4.8.3	<u>Comparison for side layer jet velocity</u>	154
4.8.4	<u>Pressure drop comparison</u>	155
4.9	<u>Summary of the numerical studies for non-resolved Hartmann layer</u>	156
4.10	<u>References</u>	157
5	<u>CHAPTER</u>	159
	<u>Mock-up Experiments and Numerical Studies for LLCB TBM Variants</u>	159
5.1	<u>Introduction</u>	159
5.2	<u>Numerical and experimental MHD studies in a multichannel test section</u>	161
5.3	<u>Experiments in multichannel test section</u>	163
5.3.1	<u>Details of test section</u>	165
5.3.2	<u>Diagnostics in multichannel test section</u>	166
5.4	<u>Flow modelling</u>	167
5.4.1	<u>Governing Equations</u>	167
5.4.2	<u>Boundary conditions</u>	169
5.5	<u>Numerical model geometry and mesh</u>	169
5.5.1	<u>Grid details and Physical properties</u>	169
5.6	<u>Numerical results in multi-channel test model and comparison with experiment</u> .	170

5.6.1	<u>Numerical wall electric potential distribution and comparison with experiment</u>	170
5.6.2	<u>Estimation of flow rate using numerical profile of wall electric potential distribution</u>	175
5.7	<u>Discussion on of flow distribution in two parallel channels</u>	180
5.8	<u>Evaluation of actual flow rate in the test section based on measured side wall potential</u>	183
5.9	<u>Pressure in multichannel test section</u>	184
5.10	<u>Summary of MHD studies in multichannel test section</u>	188
5.11	<u>Numerical analysis of MHD flow in RF-test section for mock-up of LLCB variant with liquid metal NaK</u>	190
5.12	<u>RF-test section and experiment set up</u>	192
5.13	<u>Numerical simulation</u>	195
5.13.1	<u>Grid details and Physical properties</u>	196
5.14	<u>Applied magnetic field profile</u>	196
5.15	<u>Numerical electric potential distribution and comparison with experiment in RF-test section</u>	197
5.16	<u>Flow Rate distribution in RF-test section</u>	200
5.17	<u>Velocity distribution in RF-test section</u>	202
5.18	<u>Velocity Vector and current stream lines</u>	206
5.19	<u>Pressure distribution in RF-test section</u>	208
5.20	<u>Summary of the numerical simulation in RF-test section</u>	209
5.21	<u>References</u>	209
6	<u>CHAPTER</u>	212
	<u>Thermofluid MHD Studies in a Model of Indian LLCB TBM at High Magnetic Field Relevant to ITER</u>	212
6.1	<u>Introduction</u>	212
6.2	<u>Description of model geometry</u>	216
6.3	<u>Numerical Flow Modeling</u>	217
6.3.1	<u>Governing Equations</u>	218
6.3.2	<u>Boundary conditions</u>	221
6.3.3	<u>Mesh</u>	222
6.4	<u>Results of MHD flow analysis</u>	224
6.4.1	<u>Velocity profile</u>	224
6.4.2	<u>Current and Velocity Streamlines</u>	230
6.5	<u>Flow rate distribution in LLCB TBM model</u>	237
6.6	<u>Pressure distribution</u>	239

6.7	<u>Thermofluid MHD analysis of LLCB TBM</u>	242
6.7.1	<u>Results of thermofluid analysis</u>	244
6.7.2	<u>Modification in flow properties due to buoyancy effects</u>	247
6.7.3	<u>Comparison with classical Boussinesq model</u>	249
6.8	<u>Summary of thermofluid analysis in LLCB TBM</u>	250
6.9	<u>References</u>	251
7	<u>CHAPTER</u>	254
	<u>Thermofluid MHD Effects of Partition Plates in the Indian Variant LLCB TBM for ITER</u>	254
7.1	<u>Introduction</u>	254
7.2	<u>Problem definition and governing equations</u>	258
7.2.1	<u>Model geometry</u>	260
7.2.2	<u>Governing equations</u>	263
7.2.3	<u>Boundary conditions</u>	265
7.3	<u>Numerical simulation</u>	266
7.3.1	<u>Details of Grid</u>	267
7.4	<u>Results and discussions</u>	268
7.4.1	<u>Effects of partition plate on velocity profile</u>	268
7.4.2	<u>Electric potential distribution and current streamlines</u>	275
7.4.3	<u>Flow rate distribution</u>	278
7.5	<u>Thermofluid analysis</u>	279
7.5.1	<u>Steady state heat distribution</u>	280
7.5.2	<u>Temperature distribution</u>	281
7.5.3	<u>Comparison of breeder wall temperature with a case without partition wall</u>	287
7.5.4	<u>Effects of buoyancy with partition wall</u>	290
7.6	<u>Pressure</u>	294
7.7	<u>Summary of thermofluid MHD effects of partition plates in LLCB TBM</u>	296
7.8	<u>References</u>	297
8	<u>Conclusion and Future work</u>	299

List of figures

<u>Figure 1.1: Schematic layout of blanket assembly with Port Plug in a typical blanket system of ITER.....</u>	<u>27</u>
<u>Figure 1.2: Different flow regime of MHD duct flow and expected regime for LLCB variants</u>	<u>39</u>
<u>Figure 1.3: Model of representative LLCB TBM variant with helium cooled First wall.....</u>	<u>42</u>
<u>Figure 1.4: PbLi flow path in a poloidal-radial plane of LLCB TBM.....</u>	<u>43</u>
<u>Figure 2.1: Characteristic flow regions in a cross section of typical MHD flow.....</u>	<u>47</u>
<u>Figure 2.2: Non dimensional co-ordinates in a 2D flow plane of Hunt's problem.....</u>	<u>49</u>
<u>Figure 2.3: Non dimensional velocity profile in the side layer at different height.....</u>	<u>52</u>
<u>Figure 2.4: Schematics of geometry for 3D numerical computation of Hunt's problem.....</u>	<u>54</u>
<u>Figure 2.5:View of grid structure in a flow cross section, for square geometry ($\epsilon=1$) in Fig. 2.5(a) and for rectangular geometry($\epsilon=1/2$) in Fig. 2.5(b)cross section.....</u>	<u>57</u>
<u>Figure 2.6: Comparison of velocity profile across the side walls at the centre of flow cross section for $Ha = 519$ and $\epsilon=1$.....</u>	<u>60</u>
<u>Figure 2.7: Comparison of velocity profile across the Hartmann walls at the centre of flow cross section for $Ha = 519$ and $\epsilon=1$. Hartmann layer profile is zoomed in the embedded picture.....</u>	<u>60</u>
<u>Figure 2.8: Comparison of electric potential distribution across the side walls and at the centre of the duct cross section for $Ha=519$ and $\epsilon=1$.....</u>	<u>61</u>
<u>Figure 2.9: Comparison of velocity profile across the side walls at the centre of flow cross section for $Ha = 1038$ and $\epsilon=1$.....</u>	<u>61</u>
<u>Figure 2.10: Comparison of velocity profile across the Hartmann walls at the center of flow cross section for $Ha = 1038$and $\epsilon=1$. Hartmann profile is zoomed in the embedded picture. .</u>	<u>62</u>
<u>Figure 2.11: Comparison of electric potential distribution across the side walls and at the center of the duct cross section for $Ha=1038$ and $\epsilon=1$.....</u>	<u>62</u>
<u>Figure 2.12: Computation geometry for Hunt's benchmarking problem.....</u>	<u>64</u>
<u>Figure 2.13: Non dimensional velocity distribution across the centre of side walls for case A2 with $C_w = 0.01$, at $Ha=500$ in Fig. 2.13 (a) and at $Ha=5000$ in Fig. 2.13(b).....</u>	<u>67</u>
<u>Figure 2.14: Non dimensional velocity distribution across the center of side walls for case A1 (Insulating walls, $C_w = 0$) and $Ha=500$.....</u>	<u>67</u>
<u>Figure 2.15: Analytical problem geometry(2D) considered by variational model.....</u>	<u>70</u>
<u>Figure 2.16: Computation geometry for benchmarking study with variational model. All the dimensions are in mm unit.....</u>	<u>74</u>
<u>Figure 2.17: 3D axial velocity profile for a conducting square duct at $Ha = 1000$ and mean velocity 0.01 m/s.....</u>	<u>74</u>

<u>Figure 2.18: Pathlines of electric current in a flow cross section of conducting square duct.</u>	<u>.75</u>
<u>Figure 2.19: Pressure gradient along the flow length of a conducting square duct for $Ha = 1000$ and mean velocity 0.01 m/s.</u>	<u>75</u>
<u>Figure 2.20: Comparison of numerical velocity distribution across the center of side walls in a conducting square duct for $Ha = 1000$ and mean velocity 0.01 m/s with the corresponding analytical profile.</u>	<u>76</u>
<u>Figure 2.21: Comparison of numerical electric potential distribution across the center of side walls in a conducting square duct for $Ha = 1000$ and mean velocity 0.01 m/s with the corresponding analytical profile.</u>	<u>77</u>
<u>Figure 2.22: Distribution of side wall electric potential difference along the applied field for a conducting square duct at $Ha=1000$ and mean velocity of 0.01 m/s.</u>	<u>77</u>
<u>Figure 2.23: Comparison of side wall velocity profile predicted by Hunt and Variational analytical solution in a channel of LLCB at $Ha=18000$.</u>	<u>79</u>
<u>Figure 3.1: Photograph of Experimental loop with various components.</u>	<u>85</u>
<u>Figure 3.2: Photograph of the multiple bend test section, Orientation of different 90^0 bends with respect to applied B_0 in Fig. 3.2(a), connection of test section inlet/outlet to loop pipes though transition pieces in Fig. 3.2(b), arrangement of heaters in Fig. 3.2(c).</u>	<u>87</u>
<u>Figure 3.3: Detail dimension of the experiment test section of multiple 90^0 bends.</u>	<u>88</u>
<u>Figure 3.4: Labelling of potential sensors in the multiple bend test section, locations in Fig. 3.4(a), arrangement of pins for an array ‘A’ in Fig. 3.4(b).</u>	<u>89</u>
<u>Figure 3.5: Experimental test section with attached potential pins at various locations before integration into the MHD loop.</u>	<u>90</u>
<u>Figure 3.6: Locations of the pressure transmitters in test section of multiple bends.</u>	<u>92</u>
<u>Figure 3.7: Schematic of the integrated MHD loop with arrangement of expansion tanks for pressure measurement in test section of multiple bends.</u>	<u>93</u>
<u>Figure 3.8: Liquid metal and gas column level (mm unit) schematic in expansion tanks for measurement.</u>	<u>94</u>
<u>Figure 3.9: Assumed location of fully develop flow in the test section of multiple bends.</u>	<u>97</u>
<u>Figure 3.10: Measured side wall potential difference along the applied magnetic field direction for various mean velocity at $B_0= 4.0$ T.</u>	<u>98</u>
<u>Figure 3.11: Calibration curve of the MHD flow meter.</u>	<u>100</u>
<u>Figure 3.12: Measured Hartmann wall potential distribution at location ‘E’ for various flow rates; for applied magnetic field of $4T$ in Fig. 3.12(a) and for applied magnetic field of $2T$ in Fig. 3.12(b).</u>	<u>103</u>
<u>Figure 3.13: Measured pressure drop verses flow rate in the bend of parallel to perpendicular flow at different magnetic field strength.</u>	<u>104</u>
<u>Figure 3.14: ΔP_1^{3-D} as a function of interaction parameter (N) for different Hartmann number (Ha) at the bend where the flow is turning from parallel to perpendicular direction of the applied field with sudden expansion.</u>	<u>106</u>

<u>Figure 3.15: Measured pressure drop verses flow rate for different magnetic field at the bend where flow turns from perpendicular to parallel direction of the applied magnetic field.....</u>	<u>107</u>
<u>Figure 3.16: Non dimensional pressure drop as a function of N at the bend where flow turns from perpendicular to parallel direction of the applied magnetic field.....</u>	<u>107</u>
<u>Figure 3.17: Measured pressure drop variation with flow rate at the bend where flow is normal to the applied magnetic field in both legs.....</u>	<u>109</u>
<u>Figure 3.18: ΔP_2^{3-D} as a function of interaction parameter (N) for different Hartmann number (Ha) at the bend where the flow is normal to the applied magnetic field in both the legs of bend.....</u>	<u>109</u>
<u>Figure 3.19: Computation geometry for simulation of multiple bend test section.....</u>	<u>112</u>
<u>Figure 3.20: Grid structure in computation geometry for test section of multiple bends.....</u>	<u>113</u>
<u>Figure 3.21: Comparison of measured side wall potential difference with numerical profile (continuous line) at location ‘A’ for different N.....</u>	<u>114</u>
<u>Figure 3.22: Comparison of measured side wall potential difference with numerical profile (continuous line) at location ‘C’ for different N.....</u>	<u>115</u>
<u>Figure 3.23: Comparison of measured side wall potential difference with numerical profile (continuous line) at location ‘D’ for different N.....</u>	<u>115</u>
<u>Figure 3.24: Comparison of measured side wall potential difference with numerical profile (continuous line) at location ‘E’ for different N.....</u>	<u>116</u>
<u>Figure 3.25: Comparison of measured Hartmann wall potential distribution with numerical results (continuous line) at Location ‘A’ for different N.....</u>	<u>117</u>
<u>Figure 3.26: Comparison of measured Hartmann wall potential distribution with numerical results (continuous line) at Location ‘C’ for different N.....</u>	<u>118</u>
<u>Figure 3.27: Comparison of measured Hartmann wall potential distribution with numerical results (continuous line) at Location ‘D’ for different N.....</u>	<u>118</u>
<u>Figure 3.28: Comparison of measured Hartmann wall potential distribution with numerical results (continuous line) at Location ‘E’ for different N.....</u>	<u>119</u>
<u>Figure 3.29: Velocity profile in the square duct with flow axis parallel to the magnetic field at z = 0.08 m for Ha =2060 and mean velocity 0.244 m/s.....</u>	<u>120</u>
<u>Figure 3.30: Current density vector at z = 0.08 m for Ha=2060 and mean velocity 0.1221 m/s</u>	<u>120</u>
<u>Figure 3.31: Normalized U_y velocity profile across the center of Hartmann walls (along z) at y=0.039 m for various N.....</u>	<u>122</u>
<u>Figure 3.32: Contours of axial current component (J_x) in a plane at y = 0.032 m for Ha=2060 and mean velocity (U_{av}) of 0.322m/s.....</u>	<u>122</u>
<u>Figure 3.33: Normalized U_y velocity profile across the side walls (along x, centre of the duct) at y=0.039 m for various N.....</u>	<u>123</u>
<u>Figure 3.34: Normalized U_y velocity profile across the side walls (along x, centre of the duct) at y=0.161 m for various N.....</u>	<u>123</u>

<u>Figure 3.35: Velocity profile across the side walls in a plane just after the bend ($x=0.032$ m) for different N.....</u>	124
<u>Figure 3.36: Velocity distribution across the side walls in a plane just after the bend ($x=0.032$ m) for different N.....</u>	125
<u>Figure 3.37: Analytical estimation of normalised velocity distribution in a flow cross section of the test section. A contour plot is shown beneath the mesh.....</u>	126
<u>Figure 3.38: Comparison of U_x velocity distribution across the side walls (centre of the duct) with fully developed profile for $B_0=4$ T and mean velocity 0.122 m/s.....</u>	126
<u>Figure 3.39: Comparison of numerical pressure profile with experiments in the test section of multiple bends for various flow rate and $B_0=4$ T. The dotted lines are the corresponding theoretical prediction based on fully developed flow.....</u>	128
<u>Figure 4.1: Schematic lay out of the square loop test section with locations of diagnostics.</u>	134
<u>Figure 4.2: Photograph of the test section of square loop with diagnostic instrumentation. .</u>	136
<u>Figure 4.3: Comparison of observed voltage with flow rate for SS430 and SS316 test section at location LB and $B_0=4$ T.....</u>	138
<u>Figure 4.4: Comparison of observed voltage with flow rate for SS430 and SS316 test section at location LB and $B_0=1$ T.....</u>	138
<u>Figure 4.5: Comparison of observed voltage with flow rate for SS430 and SS316 test section at location LB and $B_0=4$ T for reverse flow condition.....</u>	139
<u>Figure 4.6: Comparison of observed voltage with flow rate for SS430 and SS316 test section at location LB and $B_0=1$ T for reverse flow condition.....</u>	140
<u>Figure 4.7: Comparison of total pressure drop with flow rate for SS430 and SS316 test section at applied magnetic field strength of $B_0=4$ T.....</u>	141
<u>Figure 4.8: Comparison of total pressure drop with flow rate for SS430 and SS316 test section at applied magnetic field strength of 1 T.....</u>	142
<u>Figure 4.9: Comparison of total pressure drop with flow rate for SS430 and SS316 test section at different magnetic field for reverse flow condition.....</u>	142
<u>Figure 4.10: Rectangular model geometry for numerical experiment of effects of Hartmann layer resolution.....</u>	146
<u>Figure 4.11: Mesh structure in the cross section of model geometry for numerical experiment of effects of Hartmann layer resolution.....</u>	147
<u>Figure 4.12: Comparison for side layer peak velocity in different grid system; for square channel in Fig. 4.12(a) and for rectangular channel in Fig. 4.12(b).....</u>	155
<u>Figure 4.13: Variation of pressure drop with applied magnetic field for various grid system.....</u>	156
<u>Figure 5.1: Schematic PbLi flow path in multichannel experiment test section.....</u>	163
<u>Figure 5.2: Photograph of the Pb-Li liquid metal experiment loop integrated with multichannel test section at IPUL, Latvia.....</u>	164
<u>Figure 5.3: Dimensional details of various flow channels in multichannel test geometry....</u>	166

<u>Figure 5.4: Photograph of multi-channel test section and diagnostic locations labelled with B, M, T at different channel of the test section.....</u>	167
<u>Figure 5.5: Comparison of measured side wall electric potential difference data with the corresponding numerical counterpart (represented by continuous lines) in each channel for different flow rates and applied magnetic field strength; at location ‘M’ in Fig. 5.5(a) and at location ‘T’ in Fig. 5.5(b).....</u>	172
<u>Figure 5.6: Normalized side wall electric potential difference distribution and comparison with corresponding theoretical profile (dotted line) in all the channels at location ‘M’ for different flow rates; for $B_0=2$ T in Fig. 5.6(a) and for $B_0=3$ T in Fig. 5.6(b).....</u>	176
<u>Figure 5.7: Contours of electric potential and iso-surfaces in various walls of the multi-channel test section. Level-1, 2, 3, 4, 5, 6 and 7 corresponds to potential value (mV) of -6, -5, -4, -2, 0, 3 and 4 mV respectively.....</u>	182
<u>Figure 5.8: Axial current (J_y) profile along the centre of the channel-1 including the bottom inlet header region.....</u>	182
<u>Figure 5.9: Variation of normalized measured pressure drop (ΔP^i) with Ha/Re in multi-channel test section including inlet/outlet pipe (up to A1 & A2); for all experiment range in Fig. 5.9(a) and for lower range in Fig. 5.9(b).....</u>	186
<u>Figure 5.10: Variation of normalized pressure drop with Interaction parameter (N) in multichannel test section.....</u>	186
<u>Figure 5.11: Photograph of inlet/outlet pipe and their extension towards pressure transmitters A1 and A2.....</u>	188
<u>Figure 5.12: Region of MHD flow simulation (shaded ellipse) for Indian LLCB variant....</u>	191
<u>Figure 5.13: Photograph of the RF-test section in Experimental NaK loop at Efremov Institute, Russian Federation.....</u>	193
<u>Figure 5.14: Detail dimension of the RF-test section and computation model. The cross section view of various sub-ducts is shown in embedded picture (SD: Sub-Duct).....</u>	194
<u>Figure 5.15: Contours and profile of B_z field in a plane perpendicular to the applied field. .</u>	197
<u>Figure 5.16: Side wall electric potential difference distribution along the applied magnetic field in ducts of CHA-1 and CHA-2 of RF-test section; for mass flow rate of 1.91kg/s (8.0m³/h) in Fig. 5.16(a) and for mass flow rate of 0.55kg/s (2.3 m³/h) in Fig. 5.16(b).....</u>	198
<u>Figure 5.17: Side wall electric potential difference distribution at different cross sections for total mass flow rate of 0.55 kg/s (2.3 m³/h); for CHA-1 in Fig. 5.17(a) and for CHA-2 in Fig. 5.17(b).....</u>	200
<u>Figure 5.18: Fraction of flow in CHA-1 and CHA-2 for different flow rates and comparison with experiment.....</u>	202
<u>Figure 5.19: U_x (X-velocity) contour and profile at the centre of inlet pipe exit ($X=0.07$ m, near to the entry of mock up Test section) for flow rate of 8.0m³/h.....</u>	203
<u>Figure 5.20: Numerical velocity profile across the side walls at cross section $Y=0.092$ and $Y=0.383$ m for various flow rates; at the centre of the sub-duct 1-1 in Fig. 5.20 (a) and at the centre of the sub-duct 2-3 in Fig. 5.20(b).....</u>	204

<u>Figure 5.21: Non dimensional measured and numerical velocity profiles across the side walls of sub-duct 1-1 at Y=0.128 m and Z=0.075m for total flow rate of 2.3 m³/h and for 6.3 m³/h</u>	206
<u>Figure 5.22: Velocity vectors and stream lines at different cross sections (Y=0.024 m (plane passing through the centre of the inlet pipe), Y=0.046 m (near exit of the inlet collector), Y=0.092 m) for flow rate of 8.0 m³/h</u>	207
<u>Figure 5.23: Current streamlines in the plane Y=0.383 m for flow rate 8.0 m³/h</u>	207
<u>Figure 5.24: Pressure profile along the flow path at the centre of various sub-ducts for different flow rates (Q=8.0m³/h and Q=2.3 m³/h)</u>	208
<u>Figure 6.1: Exploded view of PbLi flow configuration in LLCB TBM variant</u>	215
<u>Figure 6.2: Dimensional details (in mm) of numerical model geometry integrated with FW</u>	217
<u>Figure 6.3: Mesh structure in a vertical cross section of LLCB. Close view of FW interface at top corner (zoomed label-1) and entrance region of channel-1(zoomed label-2)</u>	223
<u>Figure 6.4: View of mesh in a flow cross section of bottom inlet outlet header. Close view at Hartmann wall (zoomed label-1) and elements in Hartmann layer (zoomed label-2)</u>	223
<u>Figure 6.5: Axial velocity profile across the center of side walls at different poloidal heights; for return channel and channel-1 in Fig. 6.5(a) and for channel-2 to channel-5 in Fig. 6.5(b)</u>	225
<u>Figure 6.6: 3D axial velocity profile in a flow cross section at Y=0.75m and B₀=4T; for channel-1 and return path in Fig. 6.6(a) and for channel-2 to channel-5 in Fig. 6.6(b)</u>	227
<u>Figure 6.7: Axial velocity profile across the side walls of bottom inlet/outlet header at the center of header cross section and B₀=4T</u>	227
<u>Figure 6.8: Schematic for cut view of FW radial poloidal cross section</u>	229
<u>Figure 6.9: Poloidal variation of jet velocity and transverse electric field(Ex) in the side layer of return channel adjacent to helium cooled FW</u>	229
<u>Figure 6.10: Electric potential distribution and current path in a vertical plane near the common partition wall of channel-1 and return path</u>	231
<u>Figure 6.11: The electric potential (left) and transverse electric field (right) profile across the side walls of channel-1 and return channel separated by common partition wall</u>	231
<u>Figure 6.12: Current streamline and potential distribution in a cross section of all the flow channels at Y=0.7m</u>	232
<u>Figure 6.13: Contour of electric potential and current streamlines in the central plane at z=0.214m</u>	234
<u>Figure 6.14: Electric potential contour with converging/diverging current lines in right side wall of channel-1 and channel-5</u>	234
<u>Figure 6.15: Comparison of pressure and electromagnetic force at the centerline of channel-1 and channel-5 for B₀=4T</u>	236
<u>Figure 6.16: Y-velocity contour and velocity streamlines in the central plane at z=0.214m</u>	236

<u>Figure 6.17: Hydrodynamic velocity profile across the radial width of all channels.....</u>	<u>238</u>
<u>Figure 6.18: Axial pressure variation along the flow path ABCDEF as illustrated in the embedded picture at the central plane ($Z=0.214\text{m}$).....</u>	<u>239</u>
<u>Figure 6.19: Variation of normalized pressure ($p/\sigma_a U_m B_0^2$) against the normalized poloidal flow length of channel-1 to channel-5.....</u>	<u>240</u>
<u>Figure 6.20: Schematic of cross sectional cut view of FW with surface and volumetric heat data.....</u>	<u>244</u>
<u>Figure 6.21: Contour of temperature in the central plane in Fig. 6.21(a), breeder-1 wall in contact with PbLi in Fig. 6.21(b), common partition wall plasma facing side in Fig. 6.21(C), Inner side of the first wall in contact with PbLi in Fig. 6.21(d).....</u>	<u>246</u>
<u>Figure 6.22: Comparison of radial velocity profile for case of isothermal MHD and thermal-MHD flow in the central plane ($Z=0.214\text{m}$) and poloidal height of $Y=0.85\text{ m}$ at $B_0=4\text{T}$....</u>	<u>248</u>
<u>Figure 6.23: Temperature contour and velocity streamlines in the central plane ($Z=0.214\text{ m}$) for thermal MHD flow at $B_0=4\text{T}$.....</u>	<u>248</u>
<u>Figure 6.24: Comparison of radial temperature profile for case of density variation with temperature with that of classical Boussinesq approximation at $Y=0.85\text{m}$.....</u>	<u>250</u>
<u>Figure 7.1: Schematic of PbLi flow configuration in variants of Indian LLCB TBM.....</u>	<u>257</u>
<u>Figure 7.2: Schematic of helium flow in actual FW and model configuration.....</u>	<u>260</u>
<u>Figure 7.3: Isometric cut-view of the model with partition plate in poloidal flow channels.</u>	<u>261</u>
<u>Figure 7.4: Detail dimension (mm) of various elements of the numerical model; Front view in Fig. 4(a) and Top view in Fig. 4(b).....</u>	<u>262</u>
<u>Figure 7.5: Mesh structure and zoomed view of Hartmann and side layer resolution in a flow cross section of channel-1 and return channel.....</u>	<u>268</u>
<u>Figure 7.6: Velocity profile across the Hartmann walls including partition plate for different channels.....</u>	<u>270</u>
<u>Figure 7.7: 3-D velocity profile in a flow cross section of LLCB; for channel-1 and return path in Fig. 7.7 (a) and for channel-1 to channel-5 in Fig. 7.7 (b).....</u>	<u>271</u>
<u>Figure 7.8: Velocity profile across the center of side walls at different poloidal heights and $B_0=4\text{T}$; for sub-channel-1 and return flow sub-channel in Fig. 7.8(a) and for sub-channel-2 to sub channel-5 in Fig. 7.8(b).....</u>	<u>273</u>
<u>Figure 7.9: Comparison of axial velocity profile across the center of side walls at $Y=0.85\text{m}$; for channel-1 and return path in Fig. 7.9(a) and for channel-2 to channel-5 in Fig. 7.9(b)....</u>	<u>275</u>
<u>Figure 7.10: Contour of electric potential and current stream line in a flow cross section at $Y=0.875\text{m}$.....</u>	<u>276</u>
<u>Figure 7.11: Zoomed view of current stream lines; near the partition wall of return channel and channel-1 in Fig. 7.11(a), for channel-2, 3, 4 and channel-5 in Fig. 7.11(b).....</u>	<u>277</u>
<u>Figure 7.12: Radial variation of heat density profile in various zones of LLCB model.....</u>	<u>280</u>
<u>Figure 7.13: Temperature contour in the internal partition walls.....</u>	<u>282</u>

<u>Figure 7.14: Temperature contour in the vertical/horizontal barrier wall.....</u>	<u>283</u>
<u>Figure 7.15: Temperature contour for the walls of breeder-1 in Fig. 7.15 (a) and for breeder-2 in Fig. 7.15 (b).....</u>	<u>283</u>
<u>Figure 7.16: Temperature profile along radial direction at different heights.....</u>	<u>284</u>
<u>Figure 7.17: Nusselt number variation along the poloidal direction for side walls cooled by high axial velocity jet in Fig. 17(a) and for internal partition wall cooled by low axial velocity in Fig. 17(b).....</u>	<u>286</u>
<u>Figure 7.18: Temperature distribution in breeder-1 surface contact with PbLi flow channel-2 in Fig. 7.18(a) and breeder-2 associated with channel-3 in Fig. 7.18(b) for the simulation case without any partition wall.....</u>	<u>288</u>
<u>Figure 7.19: Comparison of centerline temperature of breeder walls for the case with and without partition wall in LLCB flow channel.....</u>	<u>289</u>
<u>Figure 7.20: Contour of density in the vertical central plane of channel-1 and return flow path</u>	<u>291</u>
<u>Figure 7.21: Comparison of axial velocity profile across the side walls for magneto-hydraulic (without buoyancy) and thermofluid MHD case studies at the central plane ($Z=0.106\text{m}$) and poloidal height $Y=0.85\text{m}$, (a) for return path and sub-channel-1 and (b) for sub-channel-2 to channel-5.....</u>	<u>293</u>
<u>Figure 7.22: Velocity path lines in the central plane of sub-channel-1, sub-channel-2 and return flow sub-channel obtained from thermofluid MHD simulation.....</u>	<u>294</u>
<u>Figure 7.23: Contour of static pressure in the central poloidal plane ($Z=0.106\text{m}$).....</u>	<u>295</u>

List of tables

<u>Table 2-1: Details of grid structure used for numerical computation of Hunt’s case.....</u>	<u>57</u>
<u>Table 2-2: Comparison of numerical results with Hunt’s analytical estimation.....</u>	<u>59</u>
<u>Table 2-3: Boundary layer thickness and number of elements in each boundary layer used in computation for different Hartmann number.....</u>	<u>64</u>
<u>Table 2-4: Comparison of pressure gradient and non-dimensional flow rate for different Ha.....</u>	<u>65</u>
<u>Table 2-5: comparison of parameters estimated from numerical and analytical solution for a conducting square duct at Ha=1000 and mean velocity of 0.01 m/s.....</u>	<u>78</u>
<u>Table 3-1: Estimation of mean velocity at location ‘E’ from the measured potential.....</u>	<u>99</u>
<u>Table 3-2: Estimation of core velocity from measured Hartmann wall potential at location ‘E’.....</u>	<u>102</u>
<u>Table 3-3: Non Dimensional parameters for the Numerical simulation.....</u>	<u>111</u>
<u>Table 3-4: Comparison of total pressure drop in the model test section obtained by numerical simulation and experiment.....</u>	<u>128</u>
<u>Table 4-1: Meshing details of various grid systems in the model geometry for numerical experiment of Hartmann layer resolution.....</u>	<u>147</u>
<u>Table 4-2: Comparison of the induced currents in different grid system for square geometry.....</u>	<u>150</u>
<u>Table 4-3: Comparison of the induced currents in different grid system for rectangular geometry.....</u>	<u>151</u>
<u>Table 4-4: Deviation of Hartmann layer current in different grid system w. r. t Grid-1.....</u>	<u>151</u>
<u>Table 4-5: Comparison of numerical and analytical fully developed core current density.....</u>	<u>152</u>
<u>Table 4-6: comparison of core velocity in different Grid system.....</u>	<u>153</u>
<u>Table 4-7: Comparison of numerical and analytical core velocity.....</u>	<u>153</u>
<u>Table 5-1: Characteristics parameters of numerical model geometry of multi-channel test section.....</u>	<u>170</u>
<u>Table 5-2: Similarity coefficients of numerical and experimental data for case of $B_0=3T$ and $Q=240.2\text{ cm}^3/\text{s}$ in multi-channel test section.....</u>	<u>173</u>
<u>Table 5-3: Root mean square deviation of similarity coefficients in multichannel experiment.....</u>	<u>175</u>
<u>Table 5-4: Local average velocity at Location ‘M’ of channel-1 estimated from measured side wall potential for various case studies.....</u>	<u>179</u>
<u>Table 5-5: Estimated flow rate distribution based on the measured side wall potential data and comparison with numerical prediction for different case studies.....</u>	<u>180</u>
<u>Table 5-6: Actual flow rate for various case studies and its comparison with estimated flow rate based on measured side wall potential data and numerical profile.....</u>	<u>184</u>

<u>Table 5-7: Comparison of total pressure drop obtained by numerical solution and corresponding values of the experiments for various case studies in multi-channel test section</u>	188
<u>Table 5-8: Hartman number (Ha) and MHD interaction parameter (N) for various sub-ducts and inlet pipe in RF-test section</u>	195
<u>Table 5-9: Flow rate distribution in various sub-ducts of RF-test section from numerical solution and comparison with experiment</u>	201
<u>Table 5-10: Total pressure drop in the RF-test section for different flow conditions</u>	209
<u>Table 6-1: Physical properties of materials used in numerical simulation (non-thermal)</u>	221
<u>Table 6-2: Number of nodes along radial (X), toroidal(Y) and poloidal direction(Z) for various element of LLCB TBM</u>	224
<u>Table 6-3: flow rate distribution in parallel channels for case of Ha= 17845 and its comparison with the case without any magnetic field</u>	238
<u>Table 6-4: Comparison of theoretical and numerical values of pressure gradient in LLCB flow channels</u>	241
<u>Table 6-5: Heat density in various zones of LLCB TBM based on neutronic estimation</u>	243
<u>Table 7-1: Physical properties of materials used in numerical simulation</u>	267
<u>Table 7-2: Comparison of flow rate distribution for the case of with and without partition plate</u>	279
<u>Table 7-3: The average temperature of structural wall and PbLi temperature rise in different channels of LLCB</u>	285
<u>Table 7-4: Comparison of normalized pressure drop for case with and without partition wall</u>	295

SYNOPSIS

Blanket Module (BM) of International Thermonuclear Experimental Reactor (ITER) is a key section in the fusion system located in a region adjacent to the plasma. These blankets form the first physical boundary, surrounding the fusion plasma, to efficiently extract the energy from fusion neutrons for power generation and breed tritium fuel. Since tritium is not available naturally, it has to be bred in the fusion reactor itself for sustaining D-T cycle and fusion power generation. The design of different BM is being conceptualized by many international partners. ITER will provide a unique platform as an integrated reactor system to verify and assess the performance of the proposed tritium breeding concepts through their respective Test Blanket Module (TBM) program at the well designated ITER ports [1]. With the demonstration of primary objectives at ITER, successful TBMs will lay the guiding path for future advanced variants to harness commercial fusion power. In general, the blanket modules which are currently pursued worldwide can be classified as two types: 1) Liquid metal concepts, 2) Solid breeder concepts. Each concept has its own advantages with respect to thermal efficiency, design simplicity and also have specific feasibility issues [2]. In the liquid breeder concept, pure lithium or alloys of lithium is either used as an exclusive breeder or as a self-cool breeder that serves the dual purpose of breeder and coolant to the structure. In most of the advanced liquid metal based TBM concepts like Helium Cooled Lithium Lead (HCLL) TBM as proposed by European Union [3] or Dual Coolant Lead Lithium (DCLL) concept of USA [4], Liquid metal Lead-Lithium (PbLi) eutectic alloy is considered as either an exclusive breeder or preferred coolant with dual functionality. The reason for its attractiveness includes higher operating temperature of liquid metal, good breeding ratio, less susceptibility to radiation damage and potential to achieve high thermal efficiency. India as well as Russian Federation (RF) has proposed Lead Lithium cooled Ceramic Breeder (LLCB) TBM which is a hybrid

concept having features of both solid and liquid breeders [5]. Lithium of PbLi (83Pb17Li) will be used for breeding tritium from interaction with neutrons and lead acts as a neutron multiplier and thus enhancing the breeding of tritium. Due to continuous circulation of PbLi liquid in the reactor, continuous extraction of heat and tritium can be achieved [6].

Liquid metal flow in the channels of TBM experience high transverse toroidal magnetic field induction ($\sim 4\text{T}$) which is meant for confinement of the fusion fuel. As per Faraday's law of induction the interaction of the external magnetic field with the moving electrically conducting fluid induces an e.m.f which leads to circulation of electric current in the flow domain either closed through confining conducting walls or associated stagnant boundary layers. The induced current then interacts with the external magnetic field giving rise to electromagnetic body force (often called Lorentz force) which has substantial consequence in governing the flow physics determined by magnetohydrodynamics (MHD) rather classical hydrodynamics. The governing equations are then hydrodynamic equations coupled with Maxwell's electrodynamics equations that increase complexity of the problem [7]. The dominating electromagnetic force term in the Navier-Stokes equation results in large pressure drop, significant modification in the velocity profile, suppression of the turbulence and modification in the heat transfer characteristics. The strength of the electromagnetic force over viscous and inertial force is measured by the square of a dimensionless parameter known as Hartmann Number ($Ha = B_0 a \sqrt{\sigma/\mu}$) and an interaction parameter ($N = \sigma a B_0^2 / \rho u$) respectively. Numerical values of these characteristic parameters are very large at ITER condition with typical values for Ha in the order of $10^3 - 10^4$ and N in the range of $10 - 10^3$. So the flow is subject to intense MHD effects that causes inhomogeneity in the flow domain in comparison to hydrodynamic counterparts. A typical flow cross section of MHD flow exhibit slow moving core of flat profile, fast moving fluid accompanied with high velocity jets near the side walls (wall parallel to the applied magnetic field), stiff velocity gradient with

exponential profile near the Hartmann walls (Wall perpendicular to the applied magnetic field) [8]. In addition, the flow distribution is also governed by the channel aspect ratio ($\varepsilon=a/b$) which is the ratio of channel width along the applied magnetic field to the transverse width and relative wall electrical conductance ($C = \sigma_{wtw}/\sigma a$) [9]. The high velocity gradient in the base profile can cause instabilities and eventually leads to strong turbulence [10, 11]. As the magnetic field of TBM condition is strong, special type of Q2D turbulence is also expected [12, 13]. Successful design of the blanket module requires accurate prediction of the flow field variables and addressing key MHD phenomena expected at high Hartmann number. The present studies aim at understanding and analyzing various MHD phenomena of a generic liquid metal blanket. The analysis is further extended to address thermo-fluid MHD issues in context to the design of Indian LLCB TBM.

Indian Lead-Lithium cooled Ceramic Breeder (LLCB) blanket module for ITER is conceptualized with the philosophy of self-cooling and tritium breeding from both the solid ceramics (LiTiO_3) and circulating Lead-Lithium (PbLi) liquid metal eutectic in a single variant [14]. Inside the LLCB TBM, liquid metal Lead-Lithium alloy (PbLi) flows in long slotted parallel poloidal channels formed by solid ceramic breeder blocks to extract the self-heat and nuclear heat of the breeder blocks deposited by neutrons generated in D-T reaction. The structural material of the blanket module including plasma facing First wall (FW) that encloses internal Pb-Li channels and encapsulated Li_2TiO_3 breeder blocks is primarily envisaged as low activation India specific ferritic martensitic steel (IN-RAFMS) [15]. Strong MHD effects due to high toroidal magnetic field (4T), complex liquid metal flow paths in electrically coupled parallel channels, multiple L/U bends with sudden expansion or contraction, radial variation of volumetric heat density, presence of toroidal-poloidal components of magnetic field etc, lead to complex thermo-fluid MHD phenomena. The design and optimization of various

components of blanket module relies on accurate prediction of the flow field variables through 3-D numerical simulation.

The present studies aim at understanding and analyzing various MHD phenomena in context to the design of Indian LLCB TBM. A systematic approach is followed to arrive at reliable numerical modeling of the MHD flow in a full scale LLCB variant. First, the CFD code used for numerical computation is benchmarked with analytical solutions for various test cases. Experiments are carried out in various test sections at high magnetic fields with working fluid PbLi. Based on the analysis of the experimental data, the numerical model and its applicability to blanket scenarios is validated. Then mock up experiments were carried out with PbLi /NaK in scaled test sections to simulate different elements of a typical blanket. 3D Numerical simulation is carried out in the same experiment test sections for comparison of the results. With the experience in numerous test experiments and corresponding numerical analysis, suitable grid structure and number of elements in the characteristic boundary layers are identified for simulating MHD flow in complex geometries. Thermofluid simulation is then performed in a full scale variant of LLCB TBM integrated with helium cooled First wall. Subsequently, numerical simulation is performed in other variants that include partition plates in poloidal channels to analyze MHD effects and its consequence on thermofluid performance. Research works of this dissertation are organised in various chapters as described in the following.

In Chapter-1, literature survey is carried out to understand different concepts of blanket modules and the key magnetohydrodynamic issues in a generic blanket module of ITER including India proposed LLCB TBM. The gap areas pertaining to the design of LLCB TBM, expected flow regimes, computation challenges in resolving the boundary layers etc. are identified. The necessity of benchmarking of the CFD code and procedure to qualify the CFD code suitable for blanket application is highlighted [16]. Existing analytical solutions and

models based on fully developed flow are identified for the purpose of benchmarking commercial CFD code. MHD experiments with PbLi and NaK are planned with various scaled down mock up test sections typically representing the elements of TBM at either uniform or varying applied magnetic fields. The comparison of numerical results with experiment data is envisaged to quantify the predictive capability of the numerical code and reliability of the numerical models.

In Chapter-2, Numerical simulation of 3D MHD flow in a straight rectangular channel is performed using CFD code FLUENT [17] for steady state, and laminar flow driven by constant pressure gradient. The main objective is to benchmark the code result with existing analytical solutions derived by J. C.R Hunt for two classes of problems. The solution is in the form of infinite series and uses thin wall approximation for the applied magnetic field at the boundaries [18]. Numerical code has been written for the velocity, magnetic field and wall potential distribution for the two sets of problems. The results of velocity, pressure gradient obtained in numerical simulation are then compared with analytical estimations. Observed agreement was satisfactory. However, very slow convergence was noted for the case of insulating channels.

In practical problems the walls of the ducts are of finite thickness for which there is no exact analytical solution. Numerical simulation is then performed in a straight rectangular channel (square channel of side 25 mm) with confining walls of finite thickness (1.5 mm) and electrical conductivity. The results of a fully developed solution are then compared with results from an analytical model based on variational principle [19]. The deviations observed in peak velocity in side layer jet, core velocity and pressure gradient are well within analytical estimates.

In Chapter-3, results of experiments carried out in a test section of multiple 90-degree bends are presented. The main objective is to validate the CFD codes and numerical model at fusion relevant parameters. As the liquid metal flow encounter number of L/U bends path in a typical blanket module, experiments were conducted in stainless steel (SS) test section consisting of multiple 90° bends for various PbLi flow rates and applied magnetic field up to 4T. The measured Hartmann and side wall electric potential distribution at various locations of the test section have been compared with the results of numerical simulation carried out in identical test geometry for different Ha and N. The measured values of side wall and Hartmann wall potential distribution are matching well with the numerical results for all locations including locations very near the bends at low flow rates and high magnetic fields i.e. at high Ha/Re [20]. As the potential on Hartmann wall is the stream function for transverse velocity component core velocity was estimated from the measured Hartmann all potential at locations far away from the bends. Physics of flow distribution at bends where flow turns from parallel to perpendicular and at bends where flow turns in the plane perpendicular to the magnetic field direction is explored from the numerical simulation.

The structural material for fusion blanket systems has been proposed to be reduced activity ferritic martensitic grade steel (RAFMS) which is ferromagnetic in nature. So the liquid metal may experience a lower magnetic field and need to be verified for realistic calculation. In view of this, MHD experiments have been carried out with two identical test sections: one made of SS316L (non-magnetic) and another with SS430 (ferromagnetic), to compare the effect of structural materials on MHD phenomena at various magnetic fields and described in *Chapter-4* [21]. The wall electric potential distribution and total pressure drop is compared for both the structural material with fixed flow conditions. The experiment is also repeated by changing the flow directions. The reduction of applied magnetic field is observed below the saturation magnetization field of SS430 ($M_s \sim 1.4$ T). At higher magnetic fields

deviations are observed for the pressure drops due to higher relative wall electrical conductance ($C = \sigma_w t_w / \sigma a$) of SS 430 than SS 316 material. Here, σ_w , t_w and σ , a are the electrical conductivities and thickness of wall and fluid respectively. In another problem, the influence of the resolution of the Hartmann boundary layer on the flow field variable is studied for a 3D MHD, steady state problem in electrically conducting, straight, rectangular ducts for various Ha [22].

In Chapter-5, the mock up experiments which were carried out with PbLi or NaK in scaled down test sections are presented. The design of the test section is aimed at stimulating different MHD flow aspects expected in general blanket modules. In context to the design of LLCB and various proposed self-cooled TBM concepts, analysis of PbLi liquid metal flow in multiple parallel flow channels under high transverse magnetic fields is of practical interest. MHD experiments have been conducted at high magnetic fields (1-4T) for Lead-Lithium liquid metal flow as well as liquid metal NaK in different model test-sections which have typical features of electrically coupled multiple parallel channels [23]. Theoretical prediction of flow rate distribution in a parallel configuration which is fed from a common inlet header, velocity profile, wall potential and current distribution, pressure drop etc is challenging not only due to liquid metal complex flow path and thin boundary layer at high magnetic fields but also complicated MHD issues at relevant fusion parameters. The level of complexity is further increased due to flow of 3-D currents in liquid metal as well as in the structural walls because of the differential induced potential caused by uneven flow rate and varying direction of the flow. 3D numerical simulation is performed in identical test sections with characteristics Hartmann number up to 1557 at highest magnetic field of 3T and the results are compared with respective experiment data. The fraction of flow rate in individual channels as predicted by the numerical computation is confirmed with the estimated values based on measured side wall potential data. The matching is reasonably well taking into account the correction factor in the

flow meter measured value. It is observed that the degree of agreement between the experiment and numerical data is close to 97% at higher magnetic fields ($B_0 \geq 2T$) and hence proves the validity of numerical models in these flow regimes.

Mock up experiments were carried out at Efremov institute (Russian Federation) using liquid metal NaK in a scaled down test section to simulate the MHD flow in two parallel channels of Indian LLCB TBM. Test-section made of SS is consists of inlet pipe, inlet collector of rectangular cross section, two rows of parallel poloidal (vertical) ducts and outer collector with outlet pipe. Each poloidal duct is further divided into sub-ducts by inserting partition plates to simulate the case of LLCB variants with partition plates in poloidal channels. The flow of NaK experience a transverse magnetic field of varying strength with maximum field strength of 1T. The flow starts with an exponentially varying field at the inlet pipe, then uniform field in the vertical channels up to a certain height and then again exponentially varying in the outlet pipe including outlet header. Numerical simulation is performed in the same test section submerged in complex magnetic field distribution [24]. The results of various flow properties like side wall electric potential distribution, pressure and velocity distribution have been compared with measured values. FLUENT code numerical results are matching well with experimental data and the deviations are less than or close to the experimental errors. Significant deviation for numerical velocity profile predicted by laminar model is observed when compared with measured value using LEVI probe. This deviation was attributed to the presence of residual turbulence at high Reynolds number. It is also observed that flow distribution in parallel channels and sub-ducts is influenced by inlet pipe asymmetry and equivalent thickness of Hartmann walls. The applicability of the numerical model and CFD code is then extended with a user defined magnetic field.

In Chapter-6, Numerical simulation of 3D MHD flow in a full scale variant of India propose Lead-Lithium cooled Ceramic Breeder (LLCB) Test Blanket Module(TBM) for ITER

is presented at realistic parameters ($Ha=17,845$, flow rate= 12 kg/s). The model geometry takes into account the integrated First wall (FW) which is provisioned with internal helium cooling channels for dual cooling purpose. The MHD effects on steady state velocity profile and modification of the wall electric potential distribution due to electrical coupling of parallel channels have been analyzed. Flow rate distribution in electrically coupled parallel channels has been obtained for a fixed PbLi flow rate in the common inlet header. Steady state thermofluid analysis has been performed using user defined heat density data obtained from neutronic estimation in similar variants. Prediction of thermal hot spots in various structural walls and sharing of heat load by coupled PbLi and first wall helium cooling circuit are estimated [25].

Based on the simulation result, flow rate distribution, pressure drop, recirculation zones, velocity and temperature profile is obtained. It has been observed that velocity shoots up dramatically in the side boundary layer of counter current flow configuration channels sharing a common partition wall. Strong electrical coupling is observed in channels of counter flow configuration. In high aspect ratio poloidal channels, where axial currents are converging or diverging, large vortex structures are formed with a reverse flow at the center. Local hot spots are observed in the Hartmann walls of certain high heat deposition regions such as breeder-1 and common partition walls. The higher temperature is attributed to the lower axial velocity and hotter fluid in the corresponding boundary layers. It is also observed that First wall helium cooling has significant effects in limiting the temperature of external as well as internal breeder walls.

In Chapter-7, the MHD effects of the internal poloidal partition plates on thermofluid performance of LLCB variants are presented. The radial, poloidal flow channels in the variants of LLCB are long slotted rectangular ducts having high aspect ratio flow cross section. The higher geometric channel aspect ratio leads to large variation of side layer jet velocity and

hence large temperature variation along the side wall which may lead to significant thermo-mechanical stress. In view of this, it is envisaged to introduce thin vertical plates at the centre of the poloidal flow channels parallel to the Hartmann walls. The addition of a partition wall in the poloidal flow channels will increase the mechanical strength and subdivide the channel into a number of poloidal sub-ducts. However, unlike the external Hartmann wall (part of FW), these plates resemble the internal Hartmann wall where secondary cooling is absent. These internal plates as well as associated boundary layer provide additional path to the flow of induced electric current and hence increases the pressure drop compared to the case without partition. In addition, there is a significant modification in velocity profile across the Hartmann walls due to uneven wall thickness. Thus thermofluid performance is significantly affected due insertion of these partition plates. Numerical study is performed in a full scale variant of LLCB with a partition plate in each poloidal channel. The helium cooled FW is implicitly treated with an effective wall thickness to reduce the computation cost. The effect of buoyancy on velocity profile in plasma facing channels of large varying volumetric heat sources is discussed. Finally, the conclusion and future scope of work is presented in *Chapter-8*.

References

1. IAEA printed ITER Technical basis, ITER EDA documentation, IAEA/ITER EDA/DS/24, IAEA, Vienna, series no-24 (2002)
2. M. Abdou, et.al, Blanket/first wall challenges and required R&D on the pathway to DEMO, Fusion Eng. and Des. 100 (2015)
3. L. Buehler, C. Mistrangelo, et al., Facilities, testing program and modelling needs for studying liquid metal magnetohydrodynamic in fusion blankets, Fusion Eng. and Des.100 (2015)
4. S. Smolentsev, N. B. Morley, et al., Dual-coolant lead–lithium (DCLL) blanket status and R&D needs, Fusion Eng. and Des. 100 (2015)
5. R. Bhattacharyay, Indian TBM Team, Status of Indian LLCB TBM program and R&D activities, Fusion Eng. and Des 89 (2014)
6. I.R. Kirillov, D.A. Pertsev, Investigation of alternative configurations of the LLCB TBM to increase neutronic and thermo-hydraulics performances, Fusion Eng.Des. 85 (2010)

7. U. Muller, L. Buehler, Book: Magnetofluidynamics in channels and containers, Springer-Verlag Berlin Heidelberg, ISBN 3-540-41253 (2001)
8. L. Buehler, Liquid metal flow in arbitrary thin-walled channels under a strong transverse variable magnetic field, *Fusion Eng. and Des.* 17 (1991)
9. J. Priede, T. Arlt, et al., Linear stability of magnetohydrodynamic flow in a square duct with thin walls, *J. Fluid Mech.* 788 (2015)
10. C. B. Reed, B. F. Picologlou, Sidewall flow instabilities in liquid metal MHD flow under blanket relevant conditions, *Fusion Technol.* 15 (1989)
11. A. L. Ting, J. S. Walker, et al., Linear stability analysis for high velocity boundary layers in liquid metal magnetohydrodynamic flows, *Int. J. Engng Sci.* 29 (1991)
12. B. Knaepen and R. Moreau, Magnetohydrodynamic turbulence at low magnetic Reynolds number, *Annu. Rev. Fluid Mech.* 40(2008)
13. S. Smolentsev, R. Moreau, et al., Characterization of key magnetohydrodynamic phenomena in PbLi flows for the US DCLL blanket, *Fusion Eng. Des.* 83 (2008) 771–783
14. S. Ranjithkumar, D. Sharma, et al., Engineering design and analysis of Indian LLCB TBM set, *Fusion Eng. Des.* 109–111 (2016)
15. T. Jayakumar, M.D. Mathew, et al., Reduced activation ferritic martensitic steel and fabrication technologies for the Indian test blanket module in ITER, *Fusion Sci. Technol.* 65 (2019)
16. S. Smolentsev, S. Badia, et al., An approach to verification and validation of MHD codes for fusion applications, *Fusion Eng. Des.* 100(2015)
17. FLUENT 12.0 produced by FLUENT Inc.
18. J.C.R. Hunt, Magneto-hydrodynamics flow in rectangular duct, *J. Fluid Mech.* 21 (1965)
19. S. I. Sidorenko, A.Ya. Shishko, Variational method of calculation of MHD flows in channels with large aspect ratios and conducting walls, *Magnetohydrodynamics* 27 (1991)
20. P.K. Swain, P. Satyamurthy, et al., 3D MHD lead–lithium liquid metal flow analysis and experiments in a test section of multiple rectangular bends at moderate to high Hartmann numbers, *Fusion Eng. Des.* 88 (2013)
21. A. Patel, R. Bhattacharyay, et al., Liquid metal MHD studies with non-magnetic and Ferromagnetic structural material, *Fusion Eng. and Des.* 89 (2014)
22. S. Subramanian, P.K. Swain, et al., Effect of Hartmann layer resolution for MHD flow in a straight conducting duct at high Hartmann numbers, *Sadhana*, 40 (2015)

23. P.K. Swain, A. Shishko, et al., Numerical and experimental MHD studies of Lead-Lithium liquid metal flows in multichannel test-section at high magnetic fields, Fusion Eng. Des. 132 (2018)
24. P. Satyamurthy, P.K. Swain, et al., Experiments and numerical MHD analysis of LLCB TBM test-section with NaK at 1T magnetic field, Fusion Eng. Des. 91 (2015)
25. P.K. Swain, P. Koli, et al., Thermofluid MHD studies in a model of Indian LLCB TBM at high magnetic field relevant to ITER, Fusion Eng. Des. 150 (2020)

8. Conclusion and Future work

The present research is focused to the MHD studies at high Hartmann number relevant to blanket application of ITER. Special attention is given to the development of Indian concept of LLCB TBM for ITER program. Although the studies are closely associated with the development of LLCB variants the obtained results are generic and can also be used for other LM blankets, such as DCLL, HCLL and WCLL. Literature survey is carried out to identify grey areas and key MHD issues at ITER relevant conditions. Numerical modeling of the flow is then carried out in electrically conducting channels of different aspect ratio using CFD code Fluent. Relevant benchmarking studies have been carried out with exact analytical solutions and analytical models at high magnetic fields for the laminar model and electric potential formulation of the FLUENT code. Validation cases such as Hunt's flow, MHD flows in ducts of finite electrical conductivity, flow subject to condition of varying magnetic field, etc have been performed for code benchmarking and model validation. The limitation of the laminar model and predictive capability of the code for steady state flow is ensured through with numerous scaled experiments in complex test sections and at various flow conditions relevant to ITER. The observed reasonably good matching of the experiment data with numerical results testify the code capability for applications in fusion test blankets.

The effect of magnetic properties of the structural material on MHD flow is experimentally verified for reliable modelling of the external magnetic field. The deviation of non-resolved Hartmann layer is quantitatively assessed for numerical simulation in electrically conducting channels. Mock up experiments have been carried out in complex test sections and at high magnetic fields to simulate the flow conditions expected in LLCB variants. After validation of the code, 3-D numerical simulations in identical experiment test sections are successfully

carried out to compare the data and explore various flow features at high Hartmann number. A number of interesting unique features like bend effects, pressure drop variations, flow rate distribution in multichannel configuration, effects of variable magnetic field etc. are observed for MHD flow at different characteristic parameters.

The presented results constitute a very detailed, well-validated study of various MHD phenomena in a LM breeder, which are critically important to not only Indian LLCB TBM but to any LM blanket. Thermofluid simulation is carried out in a full scale variant of Indian LLCB TBM integrated with helium cooled First wall which is a first of kind work. The FW temperature distribution is estimated for a realistic heat deposition profile based on neutronic calculation. MHD effects of the internal poloidal partition plates on thermofluid performance are numerically analysed in a full scale model of LLCB variant. The velocity and flow rate distribution in different channels, zones of recirculation, pressure drop, electrical coupling of parallel flow channels, key structural wall temperatures, the important consequences of buoyancy effects and heat load sharing among helium and PbLi coolant circuits have been estimated. MHD analysis has been further extended to analyse the thermofluid effects of partition plates in the poloidal flow channels of a model LLCB variant. It is observed that the introduction of partition plates has advantages in controlling the recirculation zones in long slotted poloidal flow channels and better heat transfer compared to the case without any partition wall. Also the analysis indicates further scope in optimising the geometry of LLCB variant by varying the number of partition plates and radial width of flow channel for effective use of radiation heat. Although the present research is targeted towards the design of Indian LLCB TBM, the present studies are relevant to generic liquid metal based blanket applications.

Future scope of work

- Numerical modeling in present research is based on the steady state laminar approximation. However, measurement of side wall velocity profiles in some of the experiments indicated spreading of boundary layer with reduced jet velocity at relatively lower magnetic fields. Further, Strong velocity jet with inflexion points in the side wall boundary layers are observed in the flow channel of LLCB variants at high magnetic fields. These inflexion points are potential source of Kelvin-Helmholtz instability even though higher joule dissipation in conducting channels walls. Consequently, presence of turbulence especially Q2D flow regime due to high magnetic fields is highly probable. So the future analysis should be carried out with a suitable Q2D turbulent model and a comparative study can be made with the present laminar analysis.
- The present analysis is based on laminar steady state formulation and unable to capture the instabilities caused by significant buoyancy forces in LLCB model. The performance of the code for time dependent analysis need to be assessed. Transient MHD analysis is also interesting area of research in view of pulsed heat load to TBM modules at initial operation of ITER
- Analysis for electrical insulation failure in the inlet/outlet manifolds under varying magnetic fields is also very relevant in the design of liquid metal based blanket modules
- Experiments to be carried out for estimation of heat transfer coefficient at blanket relevant parameters and its comparison with laminar model analysis

1. CHAPTER

Magnetohydrodynamic Phenomena in Test Blanket Module of ITER

1.1 Introduction

The human race to access fusion energy engaged the scientists and engineers for the last few decades to develop fusion devices for realisation of controlled thermonuclear fusion reaction on Earth, a process which is already providing power to our Sun and prime mechanism of energy source in distant stars of our universe. Fusion of lighter nuclei on Earth with high reaction probabilities is envisaged in isotopes of hydrogen and helium. The easiest one is Deuterium-Tritium (D-T) reaction that require temperature around 150 million 0C to overcome coulomb barrier in contrast to the gravitational confined fusion process (proton-proton cycle) at the core of the Sun where the temperature is around 15 million 0C [1]. To demonstrate fusion as a viable energy source, the energetic particles at such high temperatures (more than 100 million C) need to be confined for a longer duration with sufficient amount of reaction to exceed auxiliary heating power. Significant progress in fusion research and current understanding of the complex plasma behaviour have shown the path to realise such a large temperature in devices that use magnetic field to confine the hot plasma. A charged particle in a strong magnetic field is bound to follow the field lines through action of Lorentz force and remain away from the container walls, otherwise no structural materials at present available to withstand the type of heat flux of fusion plasma. Long way has passed in studying various concepts of magnetically confined fusion (MCF) systems starting from the early years of fusion research with mirror machines, toroidal pinches, stellarators, small tokamak etc. The most promising and contemporary focussed area of research is tokamak concept, a Russian word for a torus shaped magnetic chamber [2]. Frontier tokamak devices currently operating world over that achieved important milestones in fusion research progress are Tokamak Fusion Test

Reactor (TFTR, USA), Joint European Torus (JET, EU), Japanese Torus 60 upgrade (JT-60U, Japan). An important design parameter for a magnetic fusion reactor is its power amplification factor Q , defined as the ratio of fusion power produced to the auxiliary heating power used to heat the plasma to fusion temperature. Higher the Q value more is the closer the state of ignition, a condition of self-sustaining fusion reaction in which plasma temperature is maintained by release of energy by reaction product 3.5MeV alpha (α) without any external heating. However, although controlled ignition is far from reach up to now, modern scientists and engineers are optimistic and inspired by the impressive experimental results recorded in the last couple of decades. The highest Q value registered so far is close to breakeven (for $Q=0.94$) by JET with equal parts of D-T mixture and fusion power of 16MW lasting about 1 second [3]. Another milestone achievement was registered by JT -60 by demonstrating plasma temperature of more than 520 million C and a record value of triple product ($n.\tau.T=1.53 \times 10^{21}$ KeV. S. m⁻³) in a pure deuterium plasma. [4] Number of technological advances and breakthroughs have inspired the fusion communities to strive for realisation of a viable fusion programme. The most ambitious fusion program which is currently being pursued by international collaboration (European Union, India, Japan, Korea, Russia and the US) to build a magnetic confinement based tokamak fusion reactor known as International Thermonuclear Experimental reactor (ITER) [5, 6].

1.2 Test blanket program of ITER

ITER is a unique fusion facility which is currently in the advanced stage of construction phase at Cadarache facility in Saint-Paul-lez-Durance of southern France. The device is equipped with superconducting coils that can produce magnetic fields at the torus axis about 6 T and close to 12 T near the coils and accommodate a magnetic field volume of ~840 m³. The prime objective of this experiment reactor is to demonstrate sustainment of fusion grade plasma by a large fraction of alpha particle heating over a period of 300-500 s. ITER is designed to

produce 500MW of thermal power with a power multiplication factor (Q) of at least 10. The contribution of 3.5 MeV alpha particles generated from the fusion reactions as the plasma heating purpose is intended to be 20% of the total thermal power. ITER is also designed to explore physics basis for steady state operation by means of non-inductive current drive up to several thousand seconds still maintaining power gain by a factor of 5 and is capable of operating in the ignition regime (with power multiplication factor $Q=30$) in the later stage of operation.

Apart from this, ITER is aiming to study another important objective of producing more tritium than consumed as fuel using the lithium breeding blanket concept. It will offer a unique environment to test various concepts of tritium breeding machines conventionally known as Test Blanket Module (TBM) for the technology development and selection of efficient breeding concept for application in future commercial power reactors. The breeding blanket of a particular type is attached with a First wall armour plate towards the plasma facing side, thus serving as the first physical boundary to the plasma volume inside the vacuum vessel, and will be subjected to neutrons and heat flux from plasma radiation. Each blanket module necessarily contains Lithium ($Li6$) either in solid or liquid form for tritium breeding purpose. The volumetric neutronic heat load (neutrons carrying 80% of the energy from the fusion reaction) along with plasma radiation and nuclear heat generated from the exothermic neutron interaction with Lithium-6 will be extracted by a suitable coolant of the specific blanket module. Although ITER is not meant for power production, it will verify and assess the performance of various tritium breeding concepts proposed by different International partners of ITER through their respective Test Blanket.

Since the kind of radiation environment, scale, magnetic field, etc. envisaged in a realistic fusion blanket system is unique, design and testing of a particular concept and its functionality demonstrated in an integrated test facility like ITER is a necessary step towards

the fusion technology development. To accomplish these goals, ITER provides three horizontal equatorial ports each of which can accommodate two isolated blanket types proposed by respective ITER parties to test their concepts through a dedicated Test Blanket Module program. Thorough studies of this Test Blanket Module (TBM) will be the reference for power reactors, specifically in the fusion energy demonstration reactor (DEMO) and further development of efficient machines for future advanced reactors. Several blanket design concepts have been developed world wide since 1970 by the EU, US, Japan and later joined to this program by China, Korea, Russia and India. The blanket test program will demonstrate the performance of design concepts of tritium breeding and extraction process proposed by collaborating partners of ITER. The test also facilitates validation of analytical tools used in the blanket design process including neutronics, electromagnetic and thermal hydraulics.

1.3 Fusion blanket concepts of ITER and worldwide program

In a fusion reactor, the blanket modules are arranged around the plasma and are an integral part of plasma facing First Wall (FW). The main function of a blanket module foreseen in a commercial fusion reactor is tritium self-sufficiency through adequate breeding from lithium or lithium based alloys and extraction of high grade nuclear heat suitable for power generation. To meet this objective, different versions of the blanket are proposed worldwide, each supported by their prospective features along with feasibility issues that would require a dedicated R&D program before coming up with prudent design suitable for reactor operation. A typical blanket assembly in a blanket system is composed of i) First wall: first physical boundary of the plasma and remove surface heat flux of the fusion plasma ii) Breeding unit: breed tritium from lithium or its alloy iii) Shield block: Contribute partly to the shielding requirement of the vacuum vessel (VV) and super-conducting coils. The test blanket program aims for simultaneous testing of all the subsystems functionality including first wall, blanket module and shield block. In a single port of ITER, two Test Blanket Modules (TBMs) are

provisioned for accommodation in the Port Plug (PP) unit which allows for maintenance or replacements of TBMs. The rear part of the Port Plug is mechanically attached with the vacuum vessel through flanged connection and the front part is the TBM frame that provides thermal insulation from other elements of the ITER machine. The schematic layout of blanket assembly with Port Plug in a typical blanket system of ITER is shown in Fig. 1.1. Blanket comparison and selection studies carried out by EU and US have evaluated five type of blanket concepts for commercial fusion applications, i) Water Cooled Lead-Lithium (WCLL) ii) Helium Cooled Lead Lithium (HCLL) iii) Helium Cooled Pebble Bed (HCPB), iv) Dual Coolant Lead Lithium (DCLL), V) Self cooled lead-lithium with Silicon Carbide (SiC) composite as structural material. [7] Each concept has its own advantage with respect to thermal efficiency, design simplicity and also has specific feasibility issues.

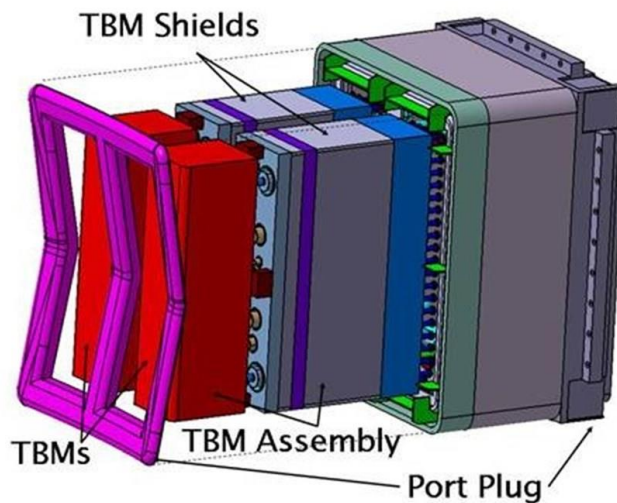


Figure 1.1: Schematic layout of blanket assembly with Port Plug in a typical blanket system of ITER

In general, the blanket modules which are currently pursued worldwide can be classified as two types: 1) Solid breeder concepts, 2) Liquid breeder concepts [8]. In the liquid breeder concepts, pure lithium or alloy of lithium based liquid metal is either utilised as an

exclusive breeder or as a self-cooled breeder that serves the dual purpose of removing self neutronic heat as well as coolant to the structure. When the liquid metal is used as an exclusive breeder, the surface and volumetric heat load in the structure including the first wall is extracted by a separate coolant like Helium/Water. The most advanced version in this category is the HCLL blanket concept as proposed by the EU. Liquid metal moves with very low velocity for facilitating tritium extraction and power conversion is carried by helium. The other promising concept of liquid breeder blanket advocated by the US is the Dual Coolant Lead-Lithium (DCLL) with helium cooled outer structures. The relatively cooled structure is thermally and electrically isolated from the liquid metal by introducing SiC/SiC_f ceramic Flow Channel Inserts (FCI) to achieve higher power conversion efficiency and lower MHD pressure drop. In both the concepts of separately cooled (HCLL) and dual coolant (DCLL) blanket, liquid metal Lead-Lithium (PbLi) eutectic alloy (83Pb17Li enriched with Li⁶) is considered as a promising breeder and prospective coolant because of its potential to achieve high thermal efficiency, lower chemical reactivity than pure lithium and ensure good breeding ratio. The structure is generally preferred to be Reduced Activation Ferritic Martensitic Steel (RAFMS) for low activation due to high energy fusion neutrons. Liquid breeder concept is also advantageous due to least use of toxic beryllium which serves the purpose of neutron multiplication in solid breeders. These blanket concepts are also candidates for ITER Test Blanket and may be the suitable near term solutions in view of available structural material. [9]. Similar variants in these categories are the china proposed Dual Functional Lithium-Lead (DFLL) and Korea proposed Helium Cooled molten Lithium TBM (HC-Li) using Eurofer structure and graphite neutron reflector. Whereas, in self-cooled liquid breeder concept, liquid metal serves the dual purpose of breeding and cooling of structural walls within permissible temperature limit of liquid/solid interface. Since the flow has the additional task of structure cooling that requires higher flow rate and hence more pumping power due to magnetohydrodynamic (MHD) effects

unless the structural walls are electrically decoupled by suitable insulation coating. Example in this category is the Russian Federation proposed Self-Cooled Lithium (SCLi) TBM for ITER. The structural material is vanadium alloy(V-4Cr-4Ti) with ANI insulation coating and porous Be as a neutron multiplier.

The other type of blanket concept is solid breeder concept where a number of ceramic breeding units are arranged either in the form of blocks or pebble bed type for tritium breeding and beryllium is used as a neutron multiplier. Each breeding unit is consisting of alternative layers of ceramic pebbles like lithium-titanate (Li_2TiO_3) or lithium-orthosilicate (Li_4SiO_4) and multiplier beryllium with cooling plates in between for heat removal through high pressure helium. The most active research pursued in the solid breeder category is the Helium Cooled Pebble Bed (HCPB) design as proposed by the EU, Water Cooled Ceramic Breeder blanket (WCCB) proposed by Japan, China Helium Cooled Solid Breeder (CH HCSB), Helium Cooled Ceramic Reflector (HCCR) concept as proposed by Korea for ITER test blanket module and its subsequent upgradation for application in fusion power reactors [10]. India has proposed Lead-Lithium cooled Ceramic Breeder (LLCB) TBM which is a hybrid concept having features of both the solid and liquid breeders. [11] The plasma facing first wall heat due to surface heat flux ($\sim 0.3 \text{ MW/m}^2$) and neutron load (0.5 MW/m^2) is cooled by helium similar to dual/separately coolant concepts and liquid metal Lead-Lithium (PbLi) is utilised for both breeding and coolant to solid ceramic zones in a self-cooled manner. In the absence of full proof electrical insulation technology due to the high radiation environment of fusion reactors, initial stage structural material is considered to be Indian reduced activation ferritic steel (IN-RAFMS) without any electrical insulation.

1.4 Magnetohydrodynamics (MHD) issues in TBM

Liquid metal based breeding blankets are preferred as one of the prospective candidates for the ITER Test Blanket program and have drawn considerable attention to both theoretician

and experimentalists in the fusion communities. The reason for its attractiveness is primarily due to high operating temperature of liquid metal, ensuring good breeding ratio, less susceptibility to radiation damage and potential to achieve high thermal efficiency. However, all liquid metal blanket concepts including DCLL and HCLL, have issues related to the magnetohydrodynamic effects caused by intense toroidal magnetic fields ($\sim 4\text{T}$). Flow of electrically conducting liquid metal under the strong transverse magnetic field that confines the fusion plasma, induces electric current in the flow domain which closes its path either through the boundary layer and/or structural wall depending on the electrical properties of the boundary walls. These induced currents interact with magnetic field results in additional electromagnetic body force in the Navier-Stokes momentum balance equation more often known as Lorentz force density vector which distribution determines the flow field characteristics described by magnetohydrodynamics(MHD). The action of this electromagnetic body force is on an average opposite to the fluid motion but has wide local effects on flow profile depending on the distribution of induced electric current and wall potential. This results in large pressure drop and inhomogeneity in the flow domain as compared to the hydrodynamic counterpart. A typical flow cross section of MHD flow exhibit slow moving core with flat profile, fast moving fluid accompanied with high velocity jets near the side walls (wall parallel to the applied magnetic field) and stiff velocity gradient with exponential profile near the Hartmann walls (wall perpendicular to the applied magnetic field). [12] The high velocity gradients in the base profile are potential sources for generation of instabilities and subsequent transition to turbulence. As the external magnetic field of TBM is strong enough, special type of Q2D turbulence is also expected. All these effects influence the thermofluid performance of the proposed TBMs. The strength of the Lorentz force over the viscous force is measured by a square of the dimensionless parameter known as Hartmann number (Ha) and its strength over inertial force is determined by a parameter known as interaction parameter (N). At ITER blanket conditions

where the strength of the toroidal magnetic field is of 4T, these characteristic non dimensional parameters are of the order of $10^3 - 10^4$ for Hartmann number and $10^2 - 10^3$ for interaction parameters in a typical flow channel and hence intense MHD effects are observed.

The strong opposing nature of the electromagnetic body force results in large pressure drop, especially, in the absence or failure of electrical insulation barriers at the liquid/structure interface. Thermofluid performance is significantly affected by factors like different characteristic boundary layers due to modifications of flow properties and nature of velocity fluctuations due to suppression or modified form of turbulence. For a self-cooled concept, the requirement for a high flow rate to cool the first wall leads to higher pressure drop and in some case pressure stress may exceed the allowable structural limit. In addition to this, 3-D MHD pressure drop occurs in the complex geometric elements like L/U bends, field entrance regions, manifolds with contraction or expansion etc. In a separately cooled concept, even though high flow rate of liquid metal is not required, MHD effects are still there due to slow circulation for the purpose of tritium extraction and purification. Natural convection phenomena are likely to occur in the slow moving fluids which may locally modify the flow profile and can lead to regions of stagnation or back flow. Formation of recirculation zones near the flow turning or middle of the large aspect ratio conducting channels are envisaged as potential thermal hot spots that have significant bearing on thermal performance due to limitation in allowable structural temperature. Large velocity gradients in the characteristic boundary layers coupled with electrical properties of the different structure walls may enhance the corrosion rate. These effects along with tritium permeation due to lower solubility in PbLi are key feasibility issues in the proposed Indian LLCB TBM. The problem is further extended by factors like high PbLi flow rate in some of the poloidal channels to meet the requirement of heat removal from breeder zones, large pressure drop in the inlet manifold, asymmetric M-shaped velocity profile due to varying wall conductance, buoyancy effects associated with large variation of radial heat

deposition etc. So detailed study of MHD flow in various channels/ducts typical to blanket elements at ITER relevant characteristic parameters is essential for reliable, efficient design and quantifying the feasibility of LLCB blanket concept.

1.5 Q2D MHD turbulence

In the limit of small magnetic Reynolds number ($Re_m = \mu_m \sigma u_0 \ell \ll 1$), the actual magnetic field is approximated with applied magnetic field (B_0). Here, ‘ ℓ ’ is characteristics length scale of the flow domain and μ_m, σ, u_0 is the magnetic permeability, electrical conductivity, average velocity of the fluid respectively. So the induced current is determined as per the Ohm’s law $\vec{J} = \sigma(\vec{E} + \vec{U} \times \vec{B}_0)$ and electromagnetic body force density is approximated with $\vec{F}_L = \vec{J} \times \vec{B}_0$. The electromagnetic force term involves a linear retarding term $-\sigma B_0^2 \mathbf{u}_\perp$ for any motion across the field lines. Thus act directly on the dampening of turbulent fluctuations in the plane perpendicular to the magnetic field. As electric currents are induced for an arbitrary eddy subject to magnetic field, the primary mechanism of energy dissipation is the joule dissipation in a characteristic time scale ($\tau_{j_0} = \rho / \sigma B_0^2$) often known as Joule time (τ_{j_0}). Here, ρ is the density of fluid. As the joule time is much smaller than the eddy turns over time ($t_u = \ell / u_0$) and independent of the length scale, strong dissipation occurs for all scales of flow structures subject to high magnetic fields. But the Joule dissipation is responsible for anisotropic flow structures due to the preferential direction set up by the magnetic field. The tendency of the turbulence structure is to become two-dimensional which is a remarkable feature of liquid metal MHD flow at high magnetic fields.

One of the physical interpretations for two-dimensionality is brought by Davidson from the conservation principle of angular momentum as the component of torque in the direction of the field is zero [13]. The Joule dissipation ceases when the variation of flow properties in the direction of the field is absent. In that state, the finite energy of the system is

maintained and overcomes the Joule dissipation. In other words, the flow becomes independent of field aligned coordinates. These 2-D structures in the process of diffusion are elongated to form columnar structures with vortices aligned in the direction of magnetic field as $\ell_{\perp}/\ell_{\parallel} = \sqrt{N}$, whose characteristic time scale is $\tau_{2D} (= \rho a / \sigma B_0^2 \ell_{\perp}^2)$. Here, 'N' is the interaction parameter ($= \sigma a B_0^2 / \rho u_0$), 'a' is length scale in the direction of the magnetic field, ℓ_{\parallel} and ℓ_{\perp} are the length scale of the eddy in parallel and perpendicular direction of the magnetic field respectively. Because of the field aligned elongation, the induced current in the core of the vortex gradually falls as it has to take a longer path for closing. Also the viscous dissipation is insignificant due to large structures. So the weaker viscous and Joule dissipation results in concentration of energy at the large scales, without transferring to smaller eddies due to absence of dissipation mechanism. Although turbulent persists, even of the same order of magnitude as without any magnetic field, its effect on integral characteristics friction coefficient which is evaluated from the measurement of global pressure drop in the experiment test section is insignificant and coincides with laminar behaviour.

However, pure 2-D flow is practically rare in MHD duct flow which can be attributed to two following reasons. First, the Hartmann boundary layers that are developed along the wall normal to the field, velocity profile is exponential and thus large gradients exist across the layer. Another possibility is that flow cannot be 2-D, because of the influence of inertial effects. As the anisotropy increases (2-D structures elongates in the direction of the field) the induced current density as well as Lorentz force falls at the centre of vortices, at some point of time it becomes same order of magnitude as inertial force which tends to restore the isotropy. So there may be alternatives of 2-D and 3-D isotropic turbulence states due to competition of inertial force and joule dissipation. This flow is called Quasi Two- Dimensional (Q2D).

However, the columnar eddies are submitted to Ohmic and viscous dissipation within the Hartmann boundary layers where 3-D effects are still present.

The ends of Q2D eddies are submitted to Hartmann layer or conducting wall where electric currents are short circuited along with viscous dissipation. As a result, eddies suffer from braking which is modelled by Sommeria [14] through a linear drag term in the 2-D Navier-Stokes equation (integrated from one Hartmann wall to another Hartmann wall). For an insulating duct the characteristic time of dissipation in the Hartmann layer is Hartmann damping time ($\tau_H = Ha \tau_{j0}$) which is much larger than Joule time (τ_{j0}) and time scale of Q2D (τ_{2D}). This is a necessary condition for establishment of two-dimensionality and turbulence is then characterised by Q2D turbulence submitted to a linear damping. This flow regime is dependent on a non-dimensional parameter, Re/Ha , which is the ratio of time scale for Hartmann damping to inertial time (τ_H/t_u). Here, ‘ t_u ’ is eddy turnover time. If $\tau_H \gg t_u$, the energy flux towards the large scale is not significantly affected by the Hartmann damping. Thus inverse energy cascade exists without significant dissipation and the cascade still obeys the Kolmogoroff $k^{-5/3}$ spectral law for scales ranging from the largest structures to the forcing mechanism [15]. In contrast when $\tau_H \ll t_u$, the inverse energy cascade is significantly affected by Hartmann damping that results in an energy spectrum that varies with k^{-3} . [16, 17]

1.6 Boundary layer stability in MHD duct flow

The effects of magnetic field on the stability of MHD duct flow for electrically conducting fluid can be thought of as both direct and indirect interactions with flow field variables. Each interaction is accompanied with a competing mechanism for stabilising and destabilising effects. The magnetic field changes the base velocity distribution through the Lorentz force, which flattens the velocity profile in the direction of the magnetic field due to Hartmann effect. On the other hand, it is responsible for instability due to formation of

characteristic boundary layers with high velocity gradients, especially the side layer at the wall parallel to the magnetic field that exhibits jet like structures and point of inflexion. The mechanism of direct action includes suppression of velocity fluctuation through Joule dissipation which restores the stability with increasing field strength. The competing factors are formation of Q2D structures subject to weak dissipation and non-linear growth of finite amplitude disturbances generated due inflexional instability at high shear side walls.

The onset of instability and transition to fully developed turbulence in MHD duct flow is generally investigated from the stability consideration of characteristic boundary layers where velocity gradients are significant. The velocity profile in the Hartmann layer arising along the Hartmann walls is exponential with a thickness of $\delta_H = a/Ha$ and the side layers arise at the parallel walls that pose a complex 3-D velocity profile with jet like structures and point of inflexion. The thickness of the side layer ($\delta_s = a/\sqrt{Ha}$) and magnitude of maximum velocity in the associated jet structure is a function of relative electrical conductance of the Hartmann and side walls and strength of the applied magnetic field in terms of Hartmann number. The stability phenomena of the Hartmann boundary layers are extensively analysed by both theory, experiments and numerical methods because of the simplicity in the base profile. Linear stability analysis performed in an insulated duct by several authors [18, 19, 20] agree to critical Reynolds number that varies linearly with Ha as $Re_c \approx 48000Ha$. Experiments based on the measurement of friction coefficient from global pressure drop revealed transition to turbulence at a much lower critical Reynolds number as $Re_c \approx 380Ha$ [21]. For geometries of different cross section aspect ratio and relative wall electrical conductance, laminarization/transition of the flow is consistent with observed critical Reynolds number in the range of $150 < Re_c < 250$. Direct numerical simulation performed by Krasnov et al. [22] showed excellent agreement with experiments that predicted instability threshold at $Re/Ha=390$. So the stability properties of the Hartmann layers are explained by the critical

Reynolds number based on the Hartmann layer thickness (a/Ha) similar to the instability mechanism for conventional hydrodynamic Poiseuille flow.

The problem of linear stability for MHD flow in a thin rectangular conducting duct with high velocity side layers is numerically analysed by Ting and Walker for the asymptotic limit of Hartmann number [23]. The analysis indicated disturbance vorticity which is perpendicular to the magnetic field decay for all length scales and Reynolds number whereas, disturbance vorticity parallel to the magnetic field becomes unstable at critical Reynolds number (Re_c) at $Re_c=313$, independent of the Ha . The critical disturbance involves short axial scales ($\pi/k_{cr} \cdot Ha^{-1/2}$) and high velocity component in the perpendicular direction to the side walls ($C_{cr} \cdot Ha^{1/2}$). Here k_{cr} and C_{cr} are the critical wave vectors and phase velocity respectively. Asymptotic numerical solution for the linear stability of MHD flow in a square duct with thin conducting wall derived by Priede et al. [24] predict critical Reynolds number and wave number based on the side layer maximum velocity is increasing asymptotically with the magnetic field as $Re_c \sim 110Ha^{1/2}$ and $k_c \sim 0.5 Ha^{1/2}$. The critical disturbances in the transverse field direction travel with a phase velocity close to half of the maximum jet velocity in the side layers. When this critical Reynolds number is rescaled with the average velocity, the critical Reynolds number for the square duct with wall conductance ratio $C \ll 1$ becomes $Re_c \sim 520$, higher than predicted by Ting et al. When the side walls are insulators and Hartmann walls are perfectly conducting as analysed by Hunt, the side layers carry majority of the volume flux and the jet velocity is maximum than any other case of conducting walls. The critical Reynolds number based on maximum jet velocity for the instability in side layer of Hunt's problem is asymptotically increasing with magnetic field ($Re_c \sim 91Ha^{1/2}$) [25]. In contrast, the flow in a perfectly conducting duct where the jet velocity is marginally higher than the core value has a critical Reynolds number $Re_c \sim 642Ha^{1/2}$ [26] The effects of finite conductivity of the Hartmann wall on the stability of the Hunt's flow is analysed by Arlt et al. with different wall conductance

ratio and Hartmann number up to $Ha=10^4$ [27]. They found the stability of the flow is determined by the effective Hartmann wall conductance ratio ($c.Ha$) and critical Reynolds number $Re_c \approx Ha^{-1/2} \tilde{Re}_c(cHa)$ in the asymptotic limit ($Ha > 300$) where, \tilde{Re}_c is the Reynolds number rescaled with $c.Ha$. From these theoretical studies of linear stability analysis, it can be concluded that the stability of the side layer and critical Reynolds number is dependent on the associated jet structure which in turn depends on the magnetic field strength, relative wall electrical conductance and geometric aspect ratio.

Evidence of the side layer instability is further established from the experiment of Reed & Picologlou [28] at Argonne National Laboratory (ANL) for fusion relevant parameters. The authors have measured the stream wise velocity component in the mid plane of the rectangular duct. The instability is first observed in the form of periodic large amplitude fluctuations close to the side walls for Reynolds number in the range $2650 < Re < 5100$ irrespective of the Hartmann number of the experiment varied in the range $2700 < Ha < 5400$. The core region is virtually unaffected and remains laminar. The turbulence in the parallel layer was found experimentally by Burr et al. [29], who reported that for high magnetic fields the critical Reynolds number for the side layer instability is weakly dependent on the Ha as $Re_c \sim Ha^{-1/4}$ and turbulence takes the form of vortex tubes orientated parallel to the field. The pressure drop due to this two-dimensional turbulence is small compared to the losses originating from Joule's dissipation which takes place mostly in the Hartmann layers. All these experiments have shown the critical Reynolds number at least one order more than predicted by linear stability theories. Experimental investigation has been carried by Buehler et al. [30] to study the instability in the side wall boundary layer of a typical Hunt's flow with finite conducting Hartmann wall ($C=0.03$) and insulating side for the Hartmann number up to $Ha= 2700$ and Reynolds number up to $Re= 6. 10^4$. The authors have reported onset of instability and successive transition to turbulence is proceeded through different unstable flow regimes each associated

with a critical Reynolds number. Above the first critical Reynolds number ($Re_{c, I}$), the flow is time dependent and the fluctuations of measurable amplitude are localised close to the side wall without affecting the core. Above the second critical Reynolds number ($Re_{c, II}$), the amplitude of the fluctuation is one or two orders of magnitude larger than the previous regime and the core flow is affected. This transition is attributed to the fully developed turbulence.

Stability of the MHD duct flow is dependent on many factors: the strength of the applied magnetic field, flow rate in terms of Ha and Re , relative wall electrical conductance, duct aspect ratio etc. Identification of a particular flow regime for a given set of parameters is specific interest for fusion blanket design. Although transition to turbulent flow is observed at well-defined critical Reynolds number for a particular duct geometry with specific electrical properties, transient evolution of Q2D turbulent structures and their interaction with confining walls or themselves is less understood. Numerical investigation and modelling of such type of complex flow is required to be supported by thorough understanding of the underlying flow phenomena and means of relevant experiment data. Nevertheless, using theoretical predictions based on linear analysis and available experiment data in literature different flow regimes of a typical blanket element can be approximated to a certain extent. For LLCB variants, the liquid metal flow path is consisting of multiple parallel rectangular channels of electrically conducting walls. The Reynolds number is varied in the range of $Re = 10^4 - 10^5$ for different channels as the flow rate is distributed among the channels from a common header and the characteristic Hartmann number is order of $Ha = 10^4$. Since the $Ha/Re > 380$, the Hartmann layer is unlikely to be unstable. So in this flow regime, the flow characteristic is pure Q2D or laminar. Large columnar vortices with axes parallel to the magnetic field may appear in the flow. The instability may originate from the side walls with jet structure and associated point of inflexion in the velocity profile. To identify different MHD flow regimes depending on the characteristics Hartmann number and Reynolds number, $Ha-Re$ diagram was proposed by

Smolentsev et al. for a duct flow with insulating channel. [31, 32] Although the exact Ha-Re relationship representing the flow transition in electrically conducting ducts depends on additional parameters like relative wall electrical conductance, cross section aspect ratio etc., qualitative transitional flow features can be drawn adopting similar Ha-Re diagrams. Based on the literature data of experiments and theoretical predictions, expected flow regime for LLCB variants is presented in Fig. 1.2.

The sub-regions above the critical transition ($Ha/Re > 380$) the turbulent is essentially 3-D and sustained by unstable Hartmann layer. The component of the velocity in the direction of applied magnetic field is still dampened through Joule dissipation. With the increase of interaction parameter (N), the 3-D turbulent characteristics may exhibit transition to Q2D turbulent flow regime.

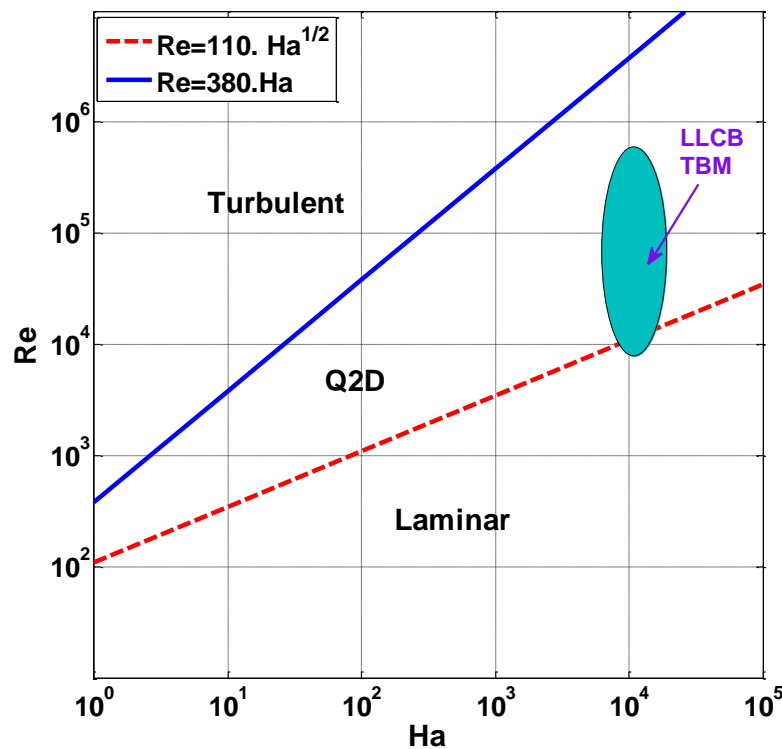


Figure 1.2: Different flow regime of MHD duct flow and expected regime for LLCB variants

1.7 Aim and work plan of the present study

The present research targets the MHD studies at high magnetic fields for the development of Indian concept of Lead-Lithium cooled Ceramic Breeder (LLCB) TBM for ITER program. LLCB TBM is conceptualized with the objective to assess both liquid and solid breeder features simultaneously and attempt to address thermofluid MHD issues that are encountered in generic self-cooled and separately cooled TBM concepts. Research is under progress in different variants to achieve an optimised configuration. In the LLCB variants liquid metal Pb-Li flows in long slotted parallel poloidal channels formed by interspaced solid ceramic breeder blocks [33]. The Indian reduced activity ferritic martensitic steel (IN-RAFMS) is the structure material including plasma facing 'U' shaped First Wall (FW) that encloses internal PbLi channels and Li_2TiO_3 breeder blocks. Helium cooling channels are embedded in the double wall type U-shaped first wall (see Fig. 1.3). Liquid breeder PbLi flows at a moderate velocity around the solid breeder zones encapsulated in RAFMS box structure to extract the nuclear heat generated in the breeder materials. A model of the representative LLCB TBM variant with helium cooled FW is shown in Fig. 1.3. Liquid metal PbLi flow path in the poloidal-radial plane is shown in Fig. 1.4. The flow of PbLi experiences strong transverse toroidal magnetic field ($\sim 4\text{T}$) of small spatial variation in the radial direction. Since there is no electrical insulation at PbLi and RAFMS interface, MHD effects are dominating over the viscous and inertial contribution. As the poloidal flow channels are fed from a common inlet header, flow rate distribution among these channels is not uniform because of the influence of flow inertia. The degree of electrical coupling among these parallel channels are different due to not only unequal flow rates but the MHD effects also associated with counter flow and co-flow configuration in neighbouring channels. As a result, small variation in the flow resistance of a particular channel will lead to imbalance in desired flow rate distribution. 3-D pressure drop is also expected due to multiple L/U bends and regions of expansion and contraction along the flow path. In addition, radial variation of volumetric heat density, the presence of toroidal-

poloidal components of magnetic field, long developing flow length by the generated axial currents due to change in flow cross section or change in flow direction leads to complex thermofluid MHD phenomena. The effect of buoyancy in channels with large radial variation of heat deposition and hence large temperature gradient has to be considered as it may lead to stagnation zones or back flow regions. Successful design of the blanket module relies on the accurate prediction of the flow field variables at fusion relevant conditions.

The present studies are primarily concerned with MHD phenomena and conjugate heat transfer issues anticipated in a generic liquid metal blanket. Based on these studies, thermofluid MHD simulation has been carried out in a baseline variant of Indian LLCB TBM for ITER application. The understanding is essential in the pathway to develop efficient blanket modules and is a first of kind work as far as Indian LLCB TBM design is concerned. In view of this objective, the primary task is to qualify the numerical code and its applicability in fusion relevant conditions. Benchmarking studies are carried out with available exact analytical solutions or theoretical models using CFD code FLUENT. Experiments are planned at Institute of Physics University of Latvia(IPUL) in different test sections (test section of multiple bends, scale down multichannel test section) subject to high magnetic fields (1-4 T). Numerical simulation is then performed in identical experiment test sections to validate the model and understanding of various MHD effects foreseen in the blanket applications. The effects of varying magnetic fields in the inlet manifold is studied by both numerical and experiment analysis in a multichannel test section experiment carried out at Efremov Institute of Russian Federation. The effects of magnetic structural material on MHD flow at high magnetic fields is investigated by comparing the results obtained in both magnetic and nonmagnetic identical test sections. Finally, 3-D numerical computation is performed in a full scale variant of Indian LLCB TBM integrated with helium cooled first wall. Thermofluid performance of the LLCB is evaluated at ITER relevant parameters. Further, the thermofluid MHD effects of partition

plates which are envisaged to enhance the mechanical strength are investigated in a model variant through numerical simulation.

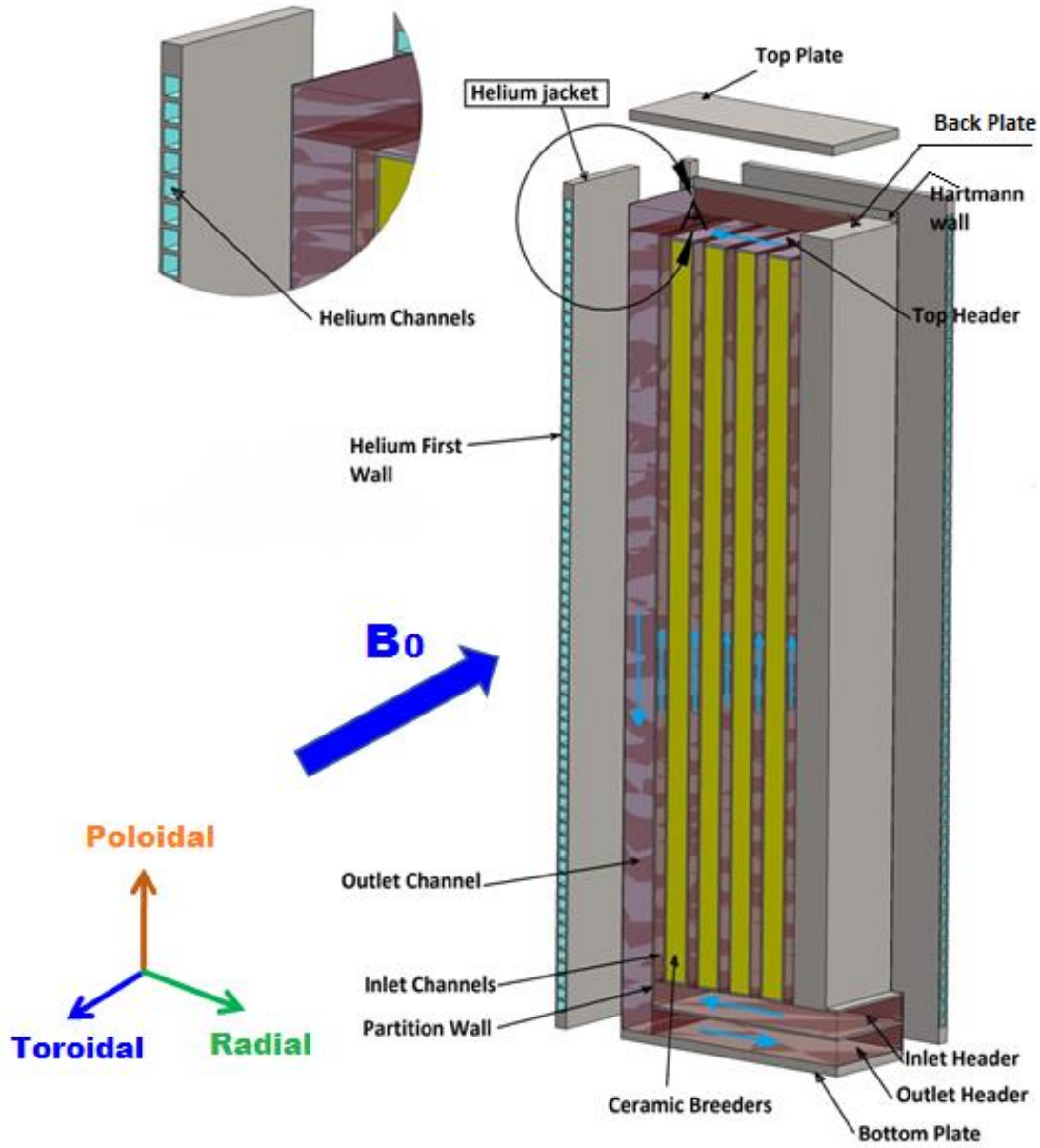


Figure 1.3: Model of representative LLCB TBM variant with helium cooled First wall

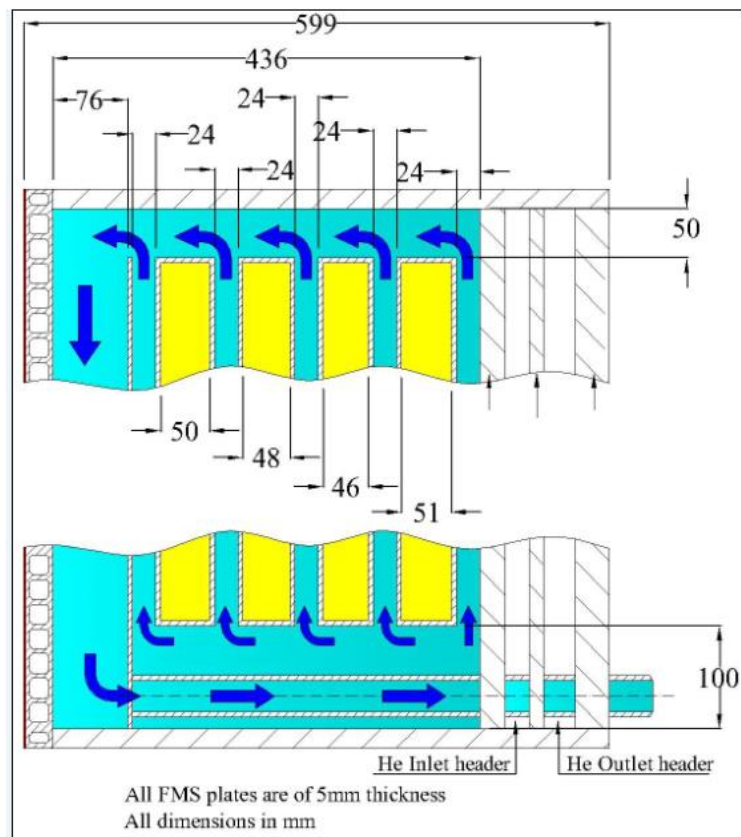


Figure 1.4: PbLi flow path in a poloidal-radial plane of LLCB TBM

1.8 References

1. S. Glasstone, Controlled Nuclear Fusion, AEC Washington, D.C. office of Information Service ED 107 520 (1974)
2. J. Ongena, R. Koch, et al., Magnetic-confinement Fusion, Nature Physics 12, (2016)
3. M.L.Watkins et al., Overview of JET Results, Proc. 21st IAEA Fusion Energy Conference, Chengdu, China 2006
4. H. Shirai, P. Barabaschi, et al., Recent progress of the JT-60SA project, Nucl. Fusion, 57 (2017)
5. ITER Technical basis, ITER EDA Documentation Series no-24, IAEA Vienna (2002)
6. O. Motojima, The ITER project construction status, Nuclear Fusion 55, (2015)
7. Mohamed Abdou, et.al, Blanket/first wall challenges and required R&D on the pathway to DEMO, Fusion Eng. and Des. 100 (2015)

8. L. Giancarli, V. chuyanov, et al., Breeding blanket modules testing in ITER: An international program on the way to DEMO, *Fusion Eng. And Des.* 81 (2006)
9. L. Buehler, C. Mistrangelo, et al., Facilities, testing program and modelling needs for studying liquid metal magnetohydrodynamic in fusion blankets, *Fusion Eng. and Des.* 100 (2015)
10. L. Giancarli, V. chuyanov, et al., Test blanket modules in ITER: An overview on proposed designs and required DEMO relevant materials, *Journal of Nuclear Materials*, 367 (2007)
11. C. Paritosh, S. Ranjithkumar, et al., Progress in engineering design of Indian LLCB TBM set for testing in ITER, *Fusion Eng. and Des.* 89 (2014)
12. U. Muller, L. Buehler, Book: *Magnetofluidynamics in channels and containers*, Springer-Verlag, ISBN 3-540-41253 (2001)
13. P.A Davidson, The role of angular momentum in the magnetic damping of turbulence, *J. Fluid Mech.*, 336 (1997)
14. J. Sommeria, R. Moreau, Why, how, and when, MHD turbulence becomes two-dimensional. *J. Fluid Mech.*, 118 (1982)
15. J. Sommeria, Experimental study of the two-dimensional inverse energy cascade in a square box, *J. Fluid Mech.*, 170 (1986)
16. T. Alboussiere, V. Uspenski, et al., Quasi 2D MHD turbulent shear layers, *Exp.Therm.Fluid Sci.* 20 (1999)
17. K. Messadek, R. Moreau, An experimental investigation of MHD quasi-2D turbulent shear flows, *J. Fluid Mech.* 456 (2002)
18. R. J. Lingwood, T. Alboussiere, On the stability of Hartmann layers, *Physics of Fluids*, 11(1999)
19. M. Takashima, The stability of the modified plane Poiseuille flow in the presence of a transverse magnetic field, *Fluid Dyn. Res.* 17, (1996)
20. M. Takashima, The stability of the modified plane Couette flow in the presence of a transverse magnetic field, *Fluid Dyn. Res.* 22, (1998)
21. P. Moresco, T. Alboussiere, Experimental study of the instability of the Hartmann layers, *J. Fluid Mech.* 504, (2004)
22. D. S. Krasnov, E. Zienicke, et al., Numerical study of the instability of the Hartmann layer, *Journal of Fluid Mechanics*, 504, (2004)

23. A. L. Ting and J. S. Walker, Linear stability analysis for high velocity boundary layers in liquid metal magnetohydrodynamic flows, *Int. J. Engng. Sci.* 29, (1991)
24. J. Priede, T. Arlt, et al., Linear stability of magnetohydrodynamic flow in a square duct with thin conducting walls, *J. Fluid Mech.* 788 (2016)
25. J. Priede, S. Aleksandrova, et al., Linear stability of Hunt's flow, *J. Fluid Mech.* 649, (2010)
26. Y. S. Uflyand, Flow stability of a conducting fluid in a rectangular channel in a transverse magnetic field, *Sov. Phys.* 5 (1961)
27. T. Arlt, J. Priede, et al., The effect of finite-conductivity Hartmann walls on the linear stability of Hunt's flow, *J. Fluid Mech.* 822, (2017)
28. C. B. Reed, B. F. Picologlou, Sidewall flow instabilities in liquid metal MHD flow under blanket relevant conditions. *Fusion Technol.* 15, (1989)
29. U. Burr, L. Barleon, et al., Turbulent transport of momentum and heat in magnetohydrodynamic rectangular duct flow with strong sidewall jets, *J. Fluid Mech.* 406, (2000)
30. L Buehler, T. Arlt, et al., Magnetically induced instabilities in duct flows, *IOP Conf. Ser: Mater. Sci. Eng.* 228 (2017)
31. S. Smolentsev, R. Moreau, et al., MHD thermofluid issues of liquid-metal blankets: phenomena and advances, *Fusion Eng. Des.* 85, 1196-1205 (2010)
32. S. Smolentsev, S Badia, et al., An approach to verification and validation of MHD codes for fusion applications, *Fusion Eng. Des.* 100, 65-72 (2015)
33. R. Bhattacharyay, IndianTBM Team, Status of Indian LLCB TBM program and R&D activities, *Fusion Eng. and Des.* 89 (2014)

2 CHAPTER

Benchmarking Studies with Linear Analytical Solutions

2.1 Introduction

Liquid metal flow in rectangular ducts exposed to transverse magnetic field has wide applications in many engineering problems. Specifically, it has drawn considerable interest in tritium breeding blankets of fusion reactors where the flow is subject to high toroidal magnetic fields(4T) and the flow dynamics are governed by magnetohydrodynamics(MHD) equations. In MHD flow, the current induced by the interaction of non-magnetic conducting fluid with the externally applied magnetic field in the fluid domain is closed through the boundary layer and/or through the confining channel walls. The induced current interacts with an external magnetic field that gives rise to an electromagnetic body force which is spatially distributed depending on the magnitude and direction of the induced current density vector. The presence of electromagnetic body force in the momentum balance equation leads to large pressure drop and significant modification in the flow pattern in contrast to the conventional hydraulic flow. The non-dimensional parameters that characterizes the MHD flow are basically the Hartmann number ($Ha = B_0 a \sqrt{\sigma/\mu}$) which square is a measure of the ratio of electromagnetic force to the viscous force and the interaction number ($N = \sigma a B_0^2 / \rho u_0$) which is a measure of the ratio of electromagnetic force to the inertial force and the relative wall electrical conductance parameter ($C = \sigma_w t_w / \sigma a$). Here, u_0 is the average velocity, σ_w , t_w , and σ , a is the electrical conductivity, thickness of Hartmann walls and fluid respectively. There are stiff gradients with exponential velocity profile in the Hartman boundary layer of thickness ($\delta_h = a/Ha^{-1}$) near the Hartmann walls (The walls at which B_0 is normal) of and strong side layer jets of thickness ($\delta_s = a/Ha^{-1/2}$) near the side walls (The walls at which B_0 is parallel) and gradient less flat profile

in the core region that makes a complex flow distribution. Schematic of the distinctive regions in a typical flow cross section is shown in Fig. 2. 1.

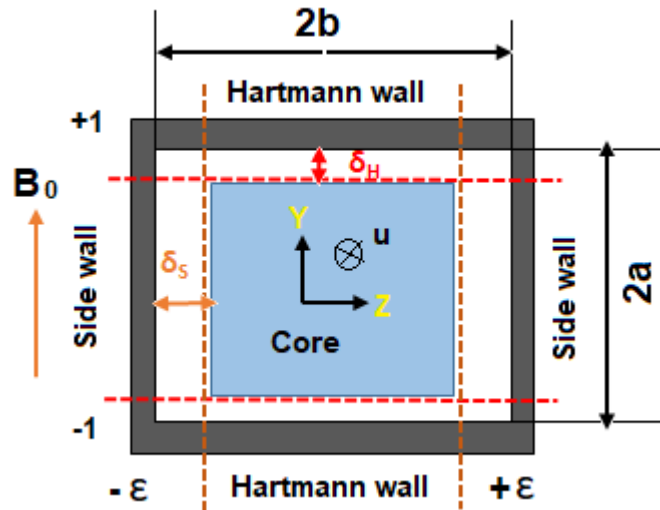


Figure 2.1: Characteristic flow regions in a cross section of typical MHD flow

Numerical simulation of this complex MHD flow through discretisation of computation volume and time is suitable to predict flow field solutions irrespective of the shape of geometry and parameter range. But the cost of computation is enormous due to the requirement of resolving thin boundary layers expected at high Hartmann numbers and sometimes impossible to simulate a real problem. On the other hand, analytical solutions neglecting the non-linear terms of Navier-Stokes equation is fast, reliable and handy to many engineering problems without any need of expensive computation. Unfortunately, an exact analytical solution for the problem of MHD flow in ducts of conducting walls with finite electrical conductivity and arbitrary thickness is rarely found in literature. However, analytical solutions exist for certain classes of problems which are essential for the benchmarking of numerical codes to assess their limitations. Analytical solutions for a rectangular duct with unsymmetrical walls of arbitrary conductivity and finite wall thicknesses are reported by Z.Tao et al., for two case studies; case-1) Insulating side walls and unsymmetrical Hartmann wall of arbitrary conductivity and case-

2) Unsymmetrical arbitrary conducting side walls with infinitely conducting Hartmann walls [1]. In the limiting case of symmetrical walls and thin wall approximations, the problems coincide with the class of problem addressed by J.C.R Hunt [2]. In this chapter, theoretical work of J.C. R Hunt is presented for which exact analytical solutions exist in the asymptotic limit of $Ha \gg 1$ for specific boundary problems as mentioned in the case-1 and case-2 studies of Z. Tao et al. Then an analytical model based on the variational approach for a duct with finite wall thicknesses and arbitrary electrical conducting walls, theoretical work carried by Sidorenkov & Shisko is presented. Numerical simulation in 3D is carried out to benchmark the MHD module of CFD code for both the analytical solutions. Subsequently, comparison is made for both the models at very high Hartmann numbers relevant to fusion applications.

2.2 Benchmarking with Hunt's Exact Analytical solution

The exact analytical solution for the steady state fully developed flow of a laminar viscous conducting fluid, driven by a constant pressure gradient in a rectangular duct under uniform transverse magnetic field has been derived by J.C.R Hunt [2] for two classes of problems. In one case (i) the Hartmann walls (The wall perpendicular to applied magnetic field B_0) are perfectly conducting and the side walls (The wall parallel to the B_0 field) are of arbitrary conductivity. In other case (ii) The Hartman walls are of arbitrary conductivity and the side walls are insulating. The flow field variables in a flow cross section(2D) is obtained from the solution of governing magetohydrodynamic equations for axial velocity(U_z) induced magnetic field (H_z) coupled with Lorentz force term determined by Maxwell's equations as described in Eqn (2.1)1to Eqn (2.5). The problem solving is then proceeded with the assumption of thin wall approximation for the induced magnetic field and no slip condition for velocity field at the boundary.

$$\frac{\partial P}{\partial z} = B_0 \frac{\partial H_z}{\partial y} + \mu \left(\frac{\partial^2}{\partial x^2} + \frac{\partial^2}{\partial y^2} \right) U_z \quad \text{Eqn(2.1)}$$

$$0 = B_0 \frac{\partial U_z}{\partial x} + \frac{1}{\sigma} \left(\frac{\partial^2}{\partial x^2} + \frac{\partial^2}{\partial y^2} \right) H_z \quad \text{Eqn(2.2)}$$

$$j_x = -\sigma \frac{\partial \phi}{\partial x} - U_z B_0 ; j_y = -\sigma \frac{\partial \phi}{\partial y} \quad \text{Eqn(2.3)}$$

$$\frac{\partial j_x}{\partial x} + \frac{\partial j_y}{\partial y} = 0 \quad \text{Eqn(2.4)}$$

$$j_x = \frac{\partial H_z}{\partial y} ; j_y = -\frac{\partial H_z}{\partial x} \quad \text{Eqn(2.5)}$$

Here, j_x, j_y are the current density components; ϕ is the electric potential; B_0 is the applied magnetic field induction; σ, μ, P are electrical conductivity, viscosity and pressure of the fluid respectively.

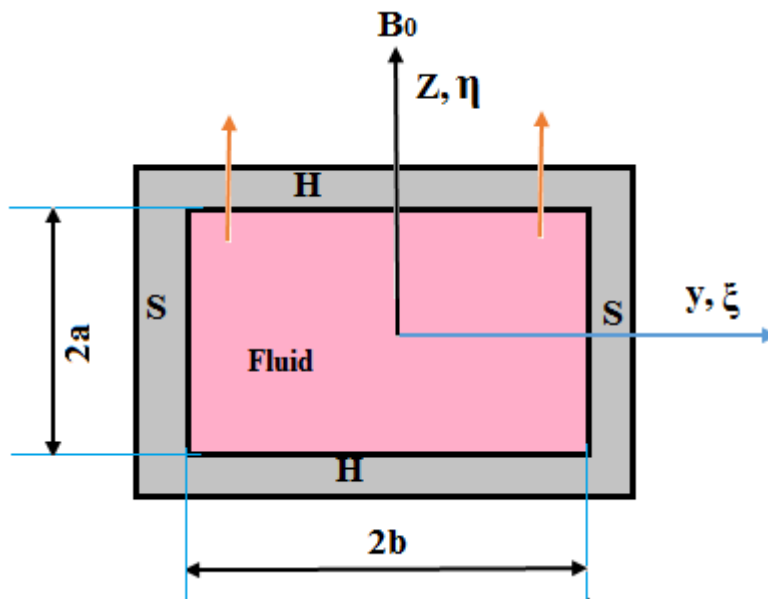


Figure 2.2: Non dimensional co-ordinates in a 2D flow plane of Hunt's problem

Governing equations are then normalized by scaling the variables in terms of pressure gradient to give two second order coupled partial differential equations.

$$\frac{\partial^2 V}{\partial \xi^2} + \frac{\partial^2 V}{\partial \eta^2} + \text{Ha} \frac{\partial H_z}{\partial \eta} = -1 \quad \text{Eqn(2.6)}$$

$$\frac{\partial^2 H_z}{\partial \xi^2} + \frac{\partial^2 H_z}{\partial \eta^2} + Ha \frac{\partial V}{\partial \eta} = 0 \quad \text{Eqn(2.7)}$$

Similarly, the equation for non-dimensional electric potential can be derived as follows;

$$\frac{\partial \varphi}{\partial \xi} = \frac{\partial H}{\partial \eta} + Ha V \quad \text{Eqn(2.8)}$$

Where,

$$V = \mu U_z / \left(-\frac{\partial P}{\partial z} \right) a^2$$

$$H = H_z \mu^{1/2} / \left(-\frac{\partial P}{\partial z} \right) a^2 \sigma^{1/2}$$

$$\varphi = \phi(\sigma \eta^{1/2}) / \left(-\frac{\partial P}{\partial z} \right) a^2$$

$$Ha = B_0 a \sqrt{\sigma / \mu}$$

$$\xi = x/a ; \eta = y/a$$

The solution is in the form of infinite series and applicable to any value of Hartmann number (Ha). Numerical code has been written for the velocity and magnetic field distribution to get an idea of the basic flow features at high Ha and for the purpose of comparing the analytical solution with results of numerical simulation. The code is also extended to obtain the electric potential distribution in the fluid domain for completeness, the solutions of dimensionless velocity and induced magnetic field induction obtained by the original author for case of infinite conducting Hartmann wall and arbitrary conducting side wall is presented in Eqn. (2.9) and Eqn. (2.10). The solution for electric potential is further extended that has been derived from solution of velocity and magnetic field is presented in Eqn. (2.11).

$$V = \sum_{j=0}^{j=\infty} \frac{2(-1)^j \cos \alpha_j \eta}{\alpha_j (\alpha_j^2 + \beta_j^2)} \left[1 - \frac{C_j(\xi) - (Ha/\alpha_j) D_j(\xi)}{K_j} - \frac{d_A \{ \beta_j E_j(\xi) - \gamma_j F_j(\xi) \}}{K_j} \right] \quad \text{Eqn(2.9)}$$

$$H = \sum_{j=0}^{\infty} \frac{2(-1)^j \sin \alpha_j \eta}{\alpha_j(\alpha_j^2 + \beta_j^2)} \left[-\frac{Ha}{\alpha_j} + \frac{(Ha/\alpha_j)C_j(\xi) + D_j(\xi)}{K_j} + \frac{d_A\{\gamma_j E_j(\xi) + \beta_j F_j(\xi)\}}{K_j} \right] \quad \text{Eqn(2.10)}$$

Where, $\beta_j, \gamma_j = \left(\frac{1}{2}\alpha_j\right)^{1/2} [\pm\alpha_j + (\alpha_j^2 + Ha^2)^{1/2}]^{1/2}$ and $\alpha_j = (j + \frac{1}{2})\pi$

$$K_j = \cosh 2\beta_j l + \cos 2\gamma_j l + d_A(\beta_j \sinh 2\beta_j l - \gamma_j \sin 2\gamma_j l)$$

Nomenclatures are followed as per the original author's convention except the Hartmann number presentation is 'Ha' instead of 'M' and characteristic Hartmann length is "a" instead of "b" as used by the original author. From these solutions the equation for dimensionless electric potential is derived as follows,

$$\Phi = \int d\xi \left(\frac{\partial B}{\partial \eta} + Ha V \right)$$

$$\Phi = \sum_{j=0}^{\infty} \frac{2(-1)^j \cos \alpha_j \eta}{(\alpha_j^2 + \beta_j^2)} \left[\left\{ -\frac{Ha}{\alpha_j} + \frac{(Ha/\alpha_j) \int C_j(\xi) d\xi + \int D_j(\xi)}{K_j} + \frac{d_A\{\gamma_j \int E_j(\xi) d\xi + \beta_j \int F_j(\xi) d\xi\}}{K_j} \right\} + \left(\frac{Ha}{\alpha_j} \right) \left\{ 1 - \frac{\int C_j(\xi) d\xi - (Ha/\alpha_j) \int D_j(\xi) d\xi}{K_j} - \frac{d_A\{\beta_j \int E_j(\xi) d\xi - \gamma_j \int F_j(\xi) d\xi\}}{K_j} \right\} \right] \quad \text{Eqn(2.11)}$$

Where,

$$\int C_j(\xi) d\xi = \left(\frac{1}{(\gamma_j^2 + \beta_j^2)} \right) \left[\beta_j \{ \cos \gamma_j(l - \xi) \sinh \beta_j(l + \xi) - \cos \gamma_j(l + \xi) \sinh \beta_j(l - \xi) \} - \left\{ \gamma_j \{ \sin \gamma_j(l - \xi) \cosh \beta_j(l + \xi) - \sin \gamma_j(l + \xi) \cosh \beta_j(l - \xi) \} \right\} \right]$$

$$\int D_j(\xi) d\xi = \left(\frac{1}{(\gamma_j^2 + \beta_j^2)} \right) \left[\beta_j \{ \sin \gamma_j(l - \xi) \cosh \beta_j(l + \xi) - \sin \gamma_j(l + \xi) \cosh \beta_j(l - \xi) \} - \left\{ \gamma_j \{ -\cos \gamma_j(l - \xi) \sinh \beta_j(l + \xi) + \cos \gamma_j(l + \xi) \sinh \beta_j(l - \xi) \} \right\} \right]$$

$$\int E_j(\xi)d\xi = \left(\frac{1}{(\gamma_j^2 + \beta_j^2)}\right) \left[\beta_j \{ \cos \gamma_j(l - \xi) \cosh \beta_j(l + \xi) - \cos \gamma_j(l + \xi) \cosh \beta_j(l - \xi) \} \right. \\ \left. - \{ \gamma_j \{ \sin \gamma_j(l - \xi) \sinh \beta_j(l + \xi) - \sin \gamma_j(l + \xi) \sinh \beta_j(l - \xi) \} \} \right]$$

$$\int F(\xi)d\xi = \left(\frac{1}{(\gamma_j^2 + \beta_j^2)}\right) \left[\beta_j \{ \sin \gamma_j(l - \xi) \sinh \beta_j(l + \xi) - \sin \gamma_j(l + \xi) \sinh \beta_j(l - \xi) \} - \right. \\ \left. \{ \gamma_j \{ -\cos \gamma_j(l - \xi) \cosh \beta_j(l + \xi) + \cos \gamma_j(l + \xi) \cosh \beta_j(l - \xi) \} \} \right]$$

The above mentioned solutions are coded in a computer program to generate profiles for arbitrary Ha and wall conductance ratio (d_A). The code is used for benchmarking the results of numerical studies carried out in different aspect ratio ducts described in subsequent sections. Non dimensional velocity profile in a side layer at different height ($\eta=0$ for centre and $\eta=1$ for top Hartmann wall) is shown in Fig. 2.3. As can be seen, the profile exhibits point of inflexion.

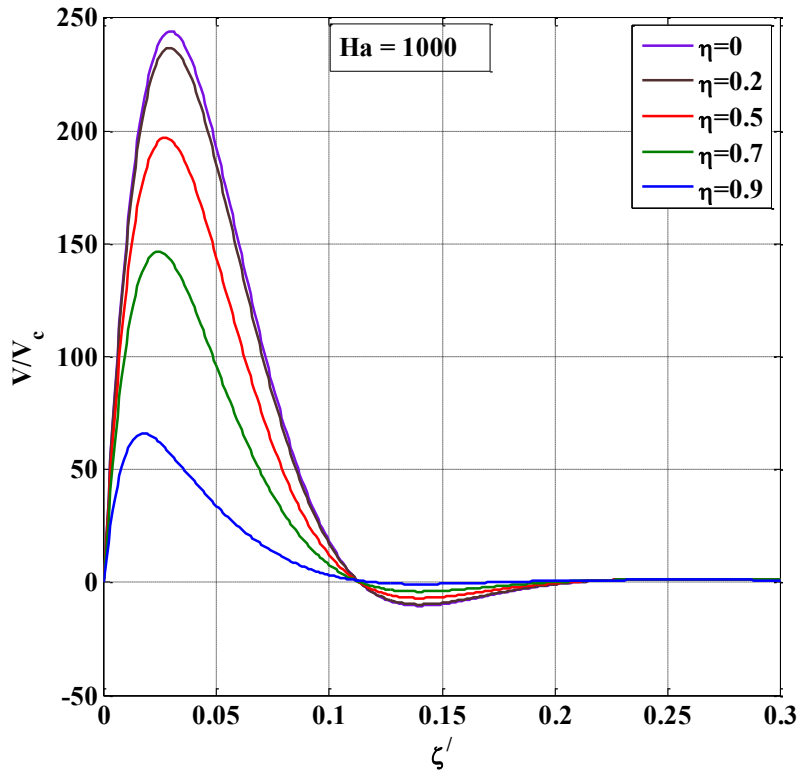


Figure 2.3: Non dimensional velocity profile in the side layer at different height

2.3 Numerical simulation for benchmarking with Hunt's analytical solution

For the purpose of benchmarking studies 3D numerical simulation is carried out for a laminar, incompressible, steady state MHD flow in a straight rectangular duct using CFD code FLUENT [3]. Liquid metal Lead-lithium (PbLi) is assumed to be the working fluid subject to uniform transverse magnetic field. The aspect ratio of the flow cross section $\epsilon (=a/b)$ (see Fig. 2.4) in computation geometry as well as applied magnetic field strength(B_0) is varied to simulate different characteristic Hartmann number (Ha). Unlike thin wall boundary condition as considered in analytical problem, finite thickness of the confining walls is resolved in numerical simulation. In a first case the square geometry ($\epsilon=1$) with flow cross section of 25 mm x 25 mm and wall thickness of 2mm and in the second case rectangular geometry of half aspect ratio with flow cross section of 25 mm x 50 mm with longer side parallel to applied magnetic field is considered. In both the cases the length of the channel is 1000mm long and wall thickness is of 2mm. To simulate the infinite conductivity of the Hartmann, wall as in the Hunt's case study large electrical conductivity is assumed (1.0×10^{10} mho-m⁻¹) in the numerical simulation. The fully developed solution obtained in each case at a certain axial distance from the inlet depending on the Hartmann number (Ha) is then compared with analytical solutions. The relative wall electrical conductance of Hartmann wall ($C_{hw} = \sigma_{hw}t_{hw} / \sigma a$) and side walls ($C_{sw} = \sigma_{sw}t_{sw} / \sigma a$), Hartmann number (Ha) of the model geometry is used for the computation of analytical profile. Here σ_{hw}, t_{hw} and σ_{sw}, t_{sw} are the electrical conductivity and wall thickness of Hartmann and side walls; σ, a is the electrical conductivity of the liquid metal PbLi and characteristic length scale respectively.

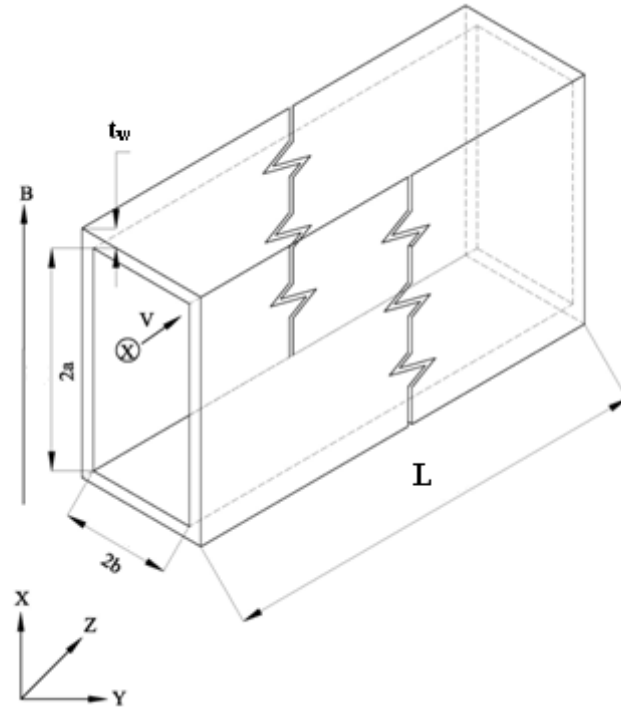


Figure 2.4: Schematics of geometry for 3D numerical computation of Hunt's problem

Governing Equation

The following system of equations governing the MHD flow of incompressible, electrical conducting fluid under the influence of external magnetic field has been solved in FLUENT. The effect of induced magnetic field is neglected and electromagnetic source term in the momentum equation is modelled based on electric potential formulation.

Modified Navier-Stokes equation:

$$(\vec{U} \bullet \vec{\nabla})\vec{U} = \frac{-\vec{\nabla}P}{\rho} + \nu \nabla^2 \vec{U} + \frac{\vec{J} \times \vec{B}_0}{\rho} \quad \text{Eqn. (2.12)}$$

Conservation of mass

$$\vec{\nabla} \bullet \vec{U} = 0 \quad \text{Eqn. (2.13)}$$

Generalised Ohm's law:

$$\vec{J} = \sigma (-\vec{\nabla}\phi + \vec{U} \times \vec{B}_0) \quad \text{Eqn. (2.14)}$$

Conservation of charge:

$$\vec{\nabla} \cdot \vec{J} = 0 \quad \text{Eqn. (2.15)}$$

Here, ρ , \vec{U} , ν , σ are density, velocity, kinematic viscosity, electrical conductivity of the fluid whereas p , \vec{J} , \vec{B}_0 , ϕ are pressure, electric current density, magnetic field induction, and electric potential respectively.

Eqn(2.14) and Eqn(2.15) is combined in potential method formulation to solve electric potential ϕ from the following equation,

$$\nabla^2 \phi = \vec{\nabla} \cdot (\vec{U} \times \vec{B}_0) \quad \text{Eqn. (2.16)}$$

Here, B_0 is the strength of applied magnetic field.

In the solid domain the following equation is solved for the electric potential

$$\nabla^2 \phi_w = 0 \quad \text{Eqn. (2.17)}$$

Here ϕ_w is the potential distribution in the walls. At the fluid-wall interface, in addition to no-slip condition for the velocity, continuity of the normal component (to the walls) of current density ($J_n = J_{nw}$) have been applied. Here J_n refers to the normal component of current density on the fluid side and J_{nw} corresponds to the wall side.

Boundary conditions

For velocity field, no-slip condition is being used at the solid surface. At the inlet uniform velocity and at the outlet, a homogenous Dirichlet pressure condition ($p=0$) is applied. For electric potential, the outer wall is assumed insulator and a homogeneous Neumann condition $\frac{\partial \phi}{\partial n} = 0$ is applied. For internal wall boundaries, that are the boundaries between fluid/solid or solid/solid zones, a coupled boundary condition is applied.

Solving methodology

The MHD module of FLUENT is a finite volume and pressure based segregated solver. The electric potential equation is solved through user-defined scalar transport equation. All the

flow variables are computed with double precision in a multiple processor (8 nodes) executed on the same computer. SIMPLE algorithm for pressure-velocity coupling and first order upwind method for spatial discretization of momentum and least squares cell based algorithm for evaluation of gradient was used in computation. The computation process begins with a very low magnetic field and then gradually increased to the required value. The converged solution was verified by checking the residuals of velocity, pressure and current distribution and monitoring the residuals for a sufficient number of iterations until there were no significant changes between successive iterations. The converged solution is also verified by checking the velocity, and conservation of current in a fully develop location. As additional source terms are added to the momentum and energy equations, the under relaxation factors for these equations should generally be reduced to improve the rate of convergence. For the electric potential equation, the convergence is generally slow and under relaxation factors for these equations was set to 0.7 to 0.9. For other variables such as pressure and momentum the under relaxation parameters were taken as 0.3 and 0.7 respectively.

Mesh

The variable O-type structured mesh in the cross section of square geometry ($\varepsilon=1$) and rectangular geometry ($\varepsilon=1/2$) is shown in Fig. 2.5(a) and Fig. 2.5(b) respectively. The Hartmann and side wall boundary layers are adequately resolved. The grid spacing is gradually increased from the walls towards the core region where gradient of flow properties is relatively lower. The details of the geometrical parameters are summarized in Table-2.1.

Fig. 2.5(a)

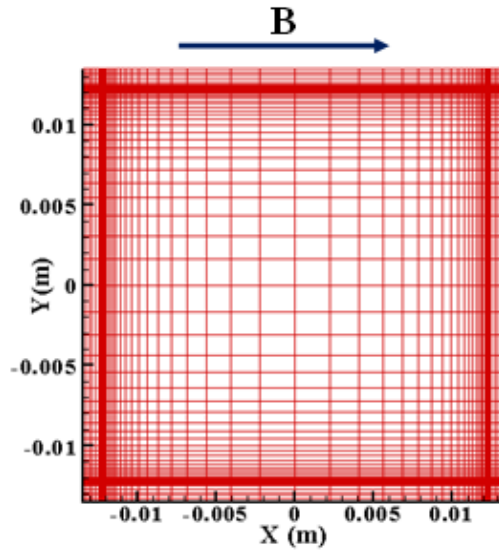


Fig. 2.5 (b)

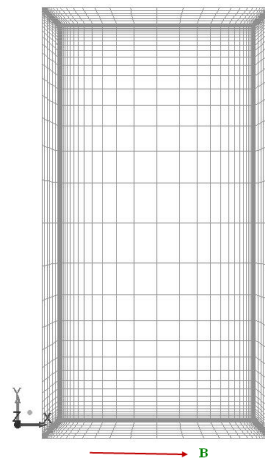


Figure 2.5: View of grid structure in a flow cross section, for square geometry ($\epsilon=1$) in Fig. 2.5(a) and for rectangular geometry ($\epsilon=1/2$) in Fig. 2.5(b) cross section

Table 2-1: Details of grid structure used for numerical computation of Hunt's case

Geometric parameters	Square($\epsilon=1$)	Rectangular($\epsilon=1/2$)
Relative conductance of Hartmann wall (C_{hw})	2061	1030
Relative conductance of side wall (C_{sw})	0.206	0.103
Minimum spacing near the Hartmann wall(m)	4×10^{-7}	4×10^{-7}
Minimum spacing near the side wall(m)	6.7×10^{-6}	7.7×10^{-6}
Maximum grid space in core(m)	2.88×10^{-3}	5.0×10^{-3}
Total number of vol. elements	535000	576000
No. of elements in the wall	06	06

Physical properties

Hartmann wall :

- i. Density (ρ) : 8000 kg/m³
- ii. Electrical Conductivity (σ) : 1.0 X 10¹⁰ mho-m⁻¹ (To simulate infinite electrical conductivity)

Side wall :

- i. Density (ρ) : 8000 kg/m³
- ii. Electrical Conductivity (σ) : 1.0 X 10⁶ mho-m⁻¹

Fluid Pb-Li :

- i. Density (ρ) : 9402 kg/m³
- ii. Viscosity (μ) : 0.0018 pa-sec
- iii. Electrical Conductivity (σ) : 0.77616X10⁶ mho-m⁻¹

Results of numerical simulation

In this section the results of velocity and electrical potential distribution for magnetic field $B= 2.0$ T ($Ha=519$) and $B= 4.0$ T ($Ha=1038$) obtained by numerical computation is compared with the analytical estimations for a mean velocity is 0.01m/s. The deviations in results of intermediate magnetic field are within the same range of reported cases. So those cases are not explicitly presented. As the analytical expressions are in dimensionless form, numerical results of velocity and electric potential is normalized as per Eqn (2.18) and Eqn (2.19) for ease of comparison.

$$V^* = \frac{V}{(a^2 \frac{\partial P}{\partial z} / \mu)} \quad \text{Eqn(2.18)}$$

$$\phi^* = \frac{\phi}{(a^2 \frac{\partial P}{\partial z} / \sqrt{\sigma \mu})} \quad \text{Eqn(2.19)}$$

Here characteristics length 'a' is half the width between Hartmann walls.

For the case square duct($\epsilon=1$) the non-dimensional velocity across side wall, Hartmann wall and electric potential distribution in a fully developed flow at the centre of the flow cross section is compared with the analytical profiles and is shown in Fig. 2.6, Fig. 2.7 and Fig. 2.8

respectively for $Ha=519$ ($B_0 = 2.0$ T). Similarly, for the case of $Ha=1038$ ($B_0 = 4.0$ T) and for square duct ($\epsilon=1$), fully develop non dimensional velocity profile across side wall, Hartmann wall and electric potential at the centre of the flow cross section is compared in Fig. 2.9 Fig. 2.10 and Fig. 2.11 respectively. The fully develop length, deviation in side layer peak velocity, core velocity, magnitude of core current each case study is summarized in Table-2. Numerical analysis carried out for rectangular duct ($\epsilon=1/2$) for $Ha=519$ and $Ha=1038$ are also presented in Table-2.2. In the fully develop region, the current conservation is verified by integrating the net core current along the field direction ($j_y \cdot a$) and current in the Hartmann wall ($j_w \cdot t_w$). It is observed that deviation in the current conservation is less than 5% in any case and thus ensuring fully develop flow profiles.

Table 2-2: Comparison of numerical results with Hunt's analytical estimation

	Square duct ($\epsilon=1$)		Rectangular duct ($\epsilon=1/2$)	
	Ha=519	Ha=1038	Ha=509	Ha=1038
Fully develop length(m)	0.12	0.09	0.15	0.12
Deviation in peak velocity (%)	2.46	1.54	2.29	0.76
Deviation in core velocity (%)	0.46	0.82	0.2	0.1
Transverse core current (A/m^2)	157	302	224	441

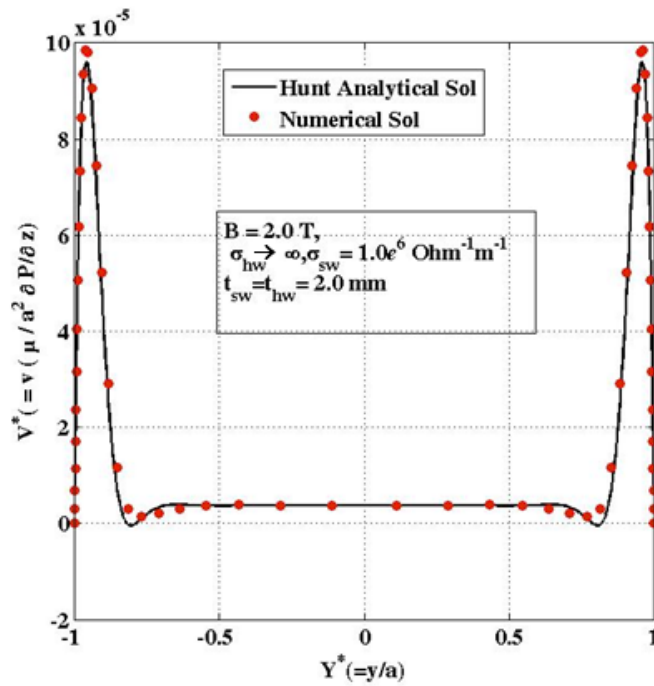


Figure 2.6: Comparison of velocity profile across the side walls at the centre of flow cross section for $Ha = 519$ and $\epsilon = 1$

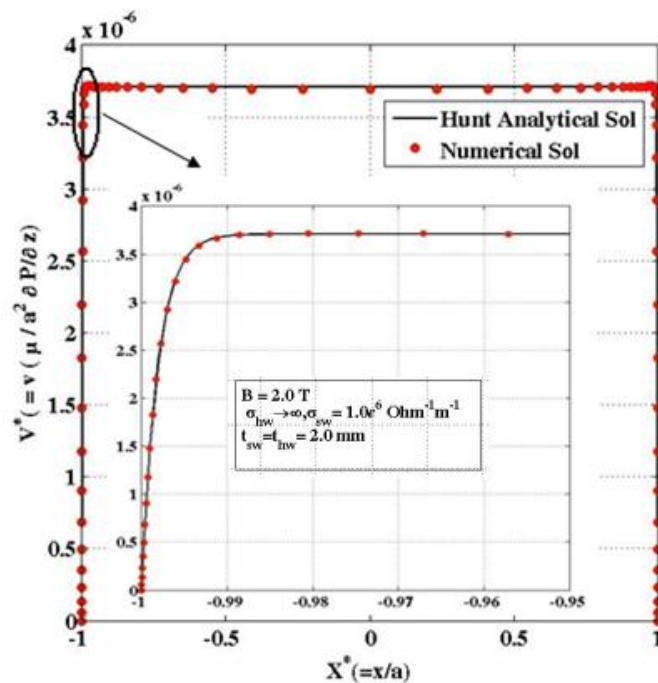


Figure 2.7: Comparison of velocity profile across the Hartmann walls at the centre of flow cross section for $Ha = 519$ and $\epsilon = 1$. Hartmann layer profile is zoomed in the embedded picture

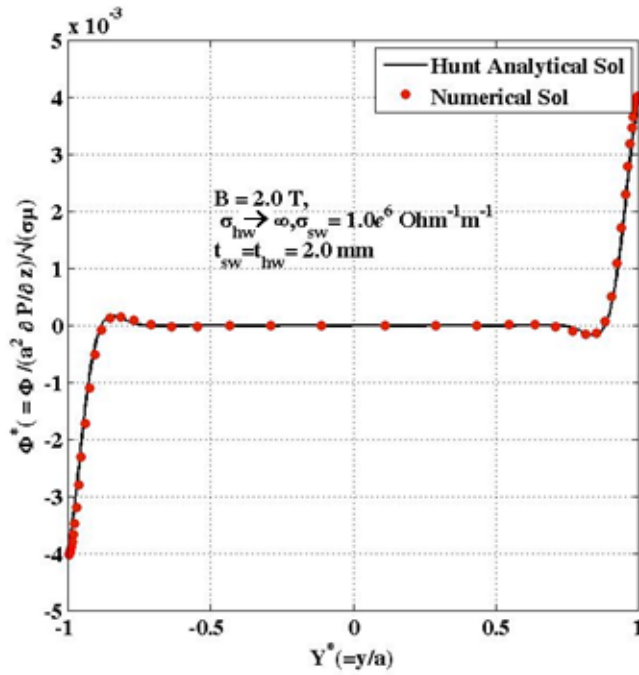


Figure 2.8: Comparison of electric potential distribution across the side walls and at the centre of the duct cross section for $Ha=519$ and $\varepsilon=1$.

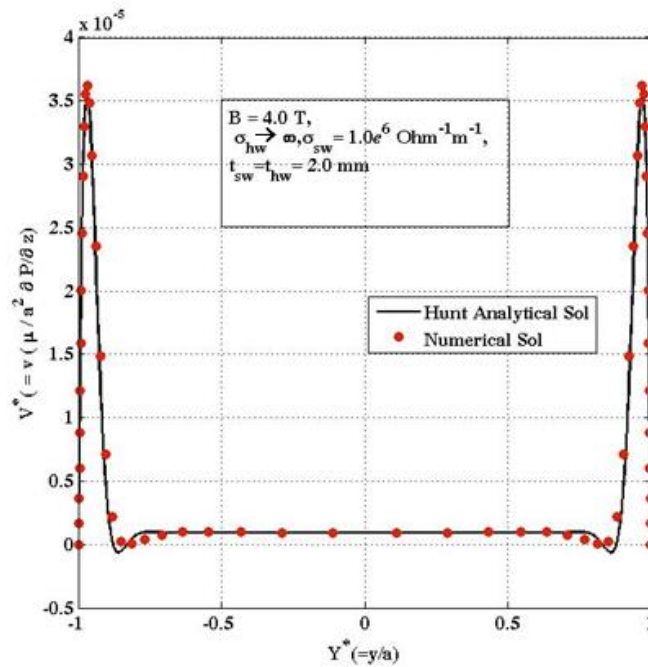


Figure 2.9: Comparison of velocity profile across the side walls at the centre of flow cross section for $Ha = 1038$ and $\varepsilon=1$

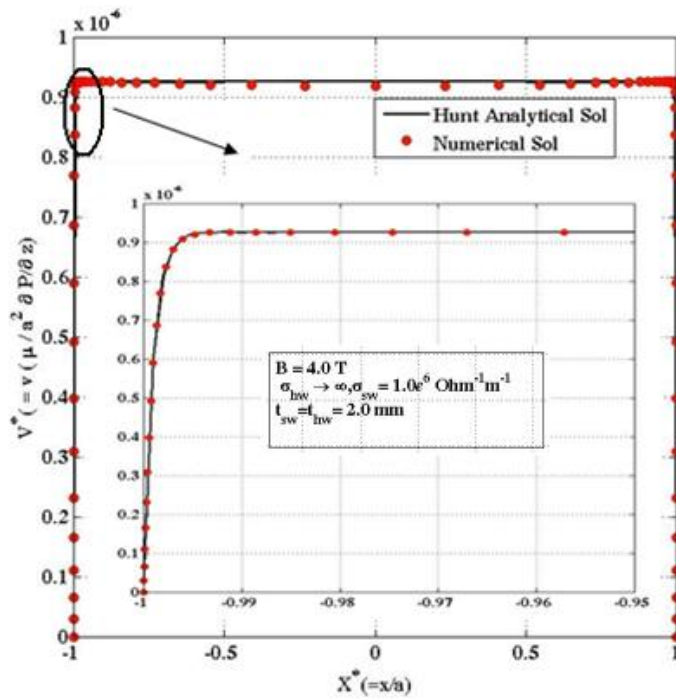


Figure 2.10: Comparison of velocity profile across the Hartmann walls at the center of flow cross section for $Ha = 1038$ and $\varepsilon = 1$. Hartmann profile is zoomed in the embedded picture

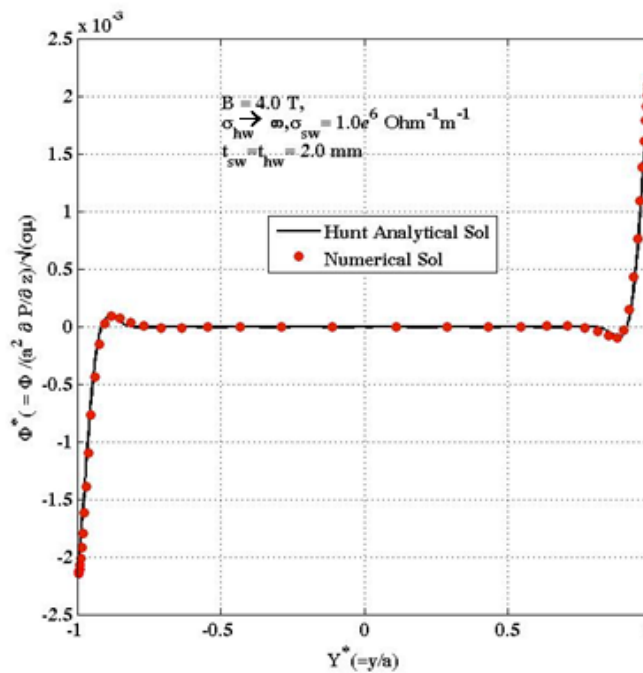


Figure 2.11: Comparison of electric potential distribution across the side walls and at the center of the duct cross section for $Ha = 1038$ and $\varepsilon = 1$

2.4 Benchmarking problems recommended by International team for verification and validation of MHD codes

To establish a framework for benchmarking database of various MHD codes used by international fusion communities, five set of problems are recommended covering wide range of MHD flows relevant to fusion applications. One of the suggested problem is to benchmark 2D flow of electrically conducting fluid in a straight rectangular duct subject to uniform magnetic field. In view of this proposed activity on verification and validation of MHD code [4], numerical computation is carried out in rectangular duct using CFD code FLUENT for two cases as proposed, caseA1: Insulating duct [5] and caseA2: conducting Hartmann walls with relative wall conductance ratio C_w of 0.01 ($C_w = \sigma_w t_w / \sigma a$) and insulating side walls. Here σ_w , t_w is the electrical conductivity and wall thickness of the Hartmann wall, σ , a is the electrical conductivity of the fluid and characteristic length scale respectively. The rectangular channel considered for computation is of length 300 mm with a flow cross section 25 mm x 50 mm and wall thickness of 1.0 mm. The electrically conducting fluid is sodium-potassium alloy (NaK) flowing with a mean velocity of 0.01 m/s. Applied transverse magnetic field is parallel to the longer side (see Fig. 2.12) and uniform throughout. The numerical analysis is performed for Hartmann number $Ha=500$ and $Ha=5000$ and the normalized results are compared with Hunt's analytical solution [2] in the fully developed regime. The Hartmann boundary layer of thickness ($\delta_h = a / Ha$) and Shercliff layer thickness ($\delta_s = a / \sqrt{Ha}$) at the side wall is properly resolved with adequate grid points. The details of the number of points in these boundary layers are presented in Table-2.3.

Table 2-3: Boundary layer thickness and number of elements in each boundary layer used in computation for different Hartmann number

Grid Resolution	Hartmann number (Ha)	Thickness of Hartman layer δ_h (m)	Number of element in δ_h	Thickness of Side layer δ_s (m)	Number of element in δ_s
90 x 50 x 40	500	5×10^{-5}	19	1.118×10^{-3}	12
	5000	5×10^{-6}	9	3.5355×10^{-4}	7

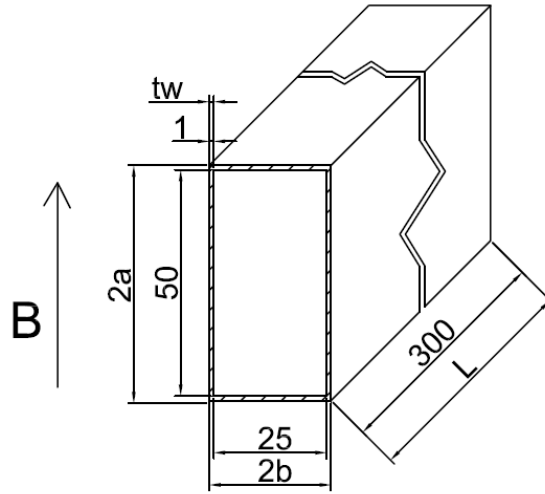


Figure 2.12: Computation geometry for Hunt's benchmarking problem

2.4.1 Results of numerical study

The numerical simulations have been carried out in 3D to get fully developed flow (2D) configurations near the outlet. The fully developed flow is ensured by checking constant pressure gradient, current conservation and no change in velocity distribution. The duct length of 300 mm is chosen in this regard seems adequate for the present case studies. The properties of the NaK are taken as 857.6 kg/m^3 , $2.691 \times 10^6 \text{ S/m}$, $7.131 \times 10^{-4} \text{ Pa.s}$, for density (ρ), electrical Conductivity (σ) and dynamic viscosity (μ) respectively. The electrical conductivity (σ_w) of Hartmann walls are set 672750 S/m for $C_w=0.01$ (case A-2) and Side walls are taken as $1.00 \times 10^{-10} \text{ S/m}$ to simulate insulating wall condition. Numerical convergence for mass, X, Y,

Z component of velocity, mass continuity and electric potential have been achieved up to 5.58×10^{-9} , 2.06×10^{-9} , 3.25×10^{-7} , 1.49×10^{-5} , and 2.86×10^{-8} respectively.

The analytical flow rate (\bar{Q}_{Analyt}) in dimensionless form is estimated as follows,

$$\bar{Q}_{Analyt} = \int_{-\ell}^{+\ell} \int_{-1}^{+1} \bar{u}_z(\bar{x}, \bar{y}) d\bar{x} d\bar{y} \quad \text{Eqn(2.20)}$$

Where, $\bar{x} = x/a$, $\bar{y} = y/a$, $\ell = b/a$

$\bar{u}_z(\bar{x}, \bar{y})$ is the dimensionless z-component velocity field solution obtained by Hunt.

Since the numerical simulation is carried out in dimensional form, for comparison with analytical estimation, the flow rate in dimensionless form (\bar{Q}_{Num}) is computed from the following equation.

$$\bar{Q}_{Num} = \frac{4 U_0 \mu \ell}{(-\partial P / \partial Z)_{num} a^2} \quad \text{Eqn (2.21)}$$

Here, U_0 is the average velocity and $(\partial P / \partial Z)_{num}$ is the numerical pressure gradient in fully developed flow region. The comparison of dimensional pressure gradient in fully developed flow region and non-dimensional flow rate for different Hartmann number is summarized in Table 2-4.

Table 2-4: Comparison of pressure gradient and non-dimensional flow rate for different Ha

Cases	Hartmann number (Ha)	Dimensional pressure gradient (Pa/m)		Non dimensional flow rate (\bar{Q})	
		Numerical	Analytical	Numerical ($\bar{Q}_{Num.}$)	Analytical (\bar{Q}_{Analyt})
A1	500	6.371	6.1876	3.5817×10^{-3}	3.6879×10^{-3}
A2	500	31.1	31.1158	7.3374×10^{-4}	7.3336×10^{-4}
A2	5000	2053	2045.9	1.1115×10^{-5}	1.1154×10^{-5}

The numerical velocity profile across the side walls at the centre of the duct in dimensionless form has been compared with the corresponding analytical solution. The normalization factor for the velocity field is defined as follows,

$$\bar{u}_z(\bar{x}, \bar{y}) = \mu u_z(x, y) / (-\partial P / \partial z)_{\text{num}} a^2 \quad \text{Eqn (2.22)}$$

Fully developed normalized velocity profile across the side walls and at the centre of the duct for $Ha=500$ and $Ha= 5000$ of case A2 ($C_w=0.01$) are shown in Fig. 2.13(a) and 2.13(b) respectively. For the case of insulating walls, the normalized velocity profile (normalized with average velocity U_0) across the side walls and at the centre of the duct is shown in Fig. 2.14.

Fig. 2.13(a)

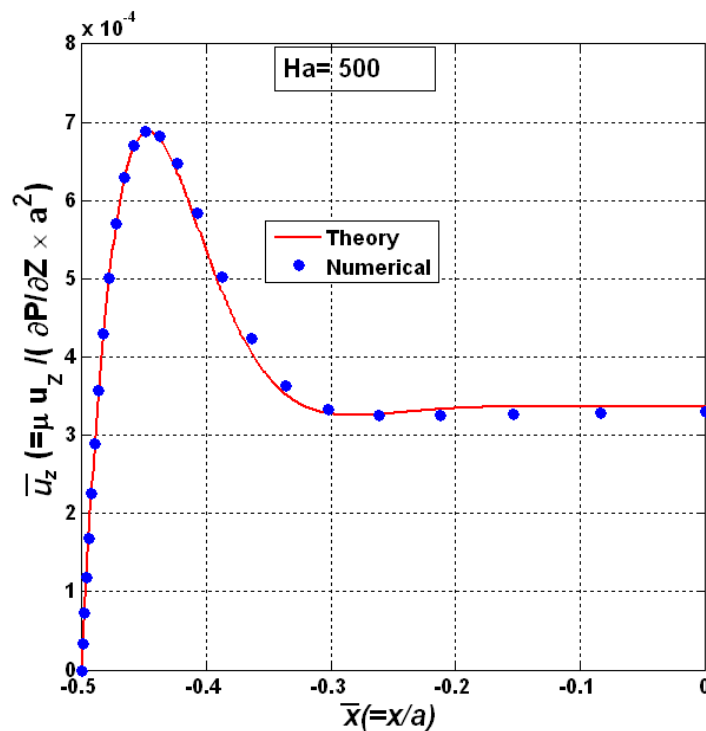


Fig. 2.13(b)

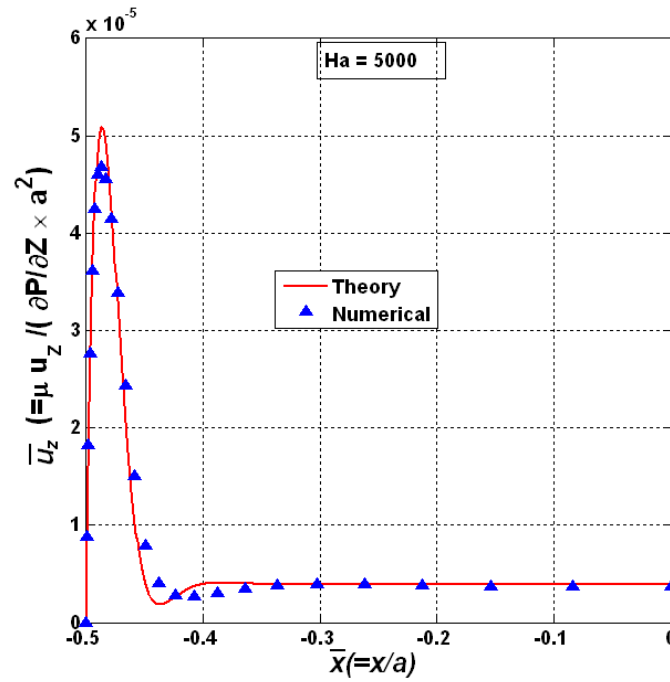


Figure 2.13: Non dimensional velocity distribution across the centre of side walls for case A2 with $C_w=0.01$, at $Ha=500$ in Fig. 2.13 (a) and at $Ha=5000$ in Fig. 2.13(b)

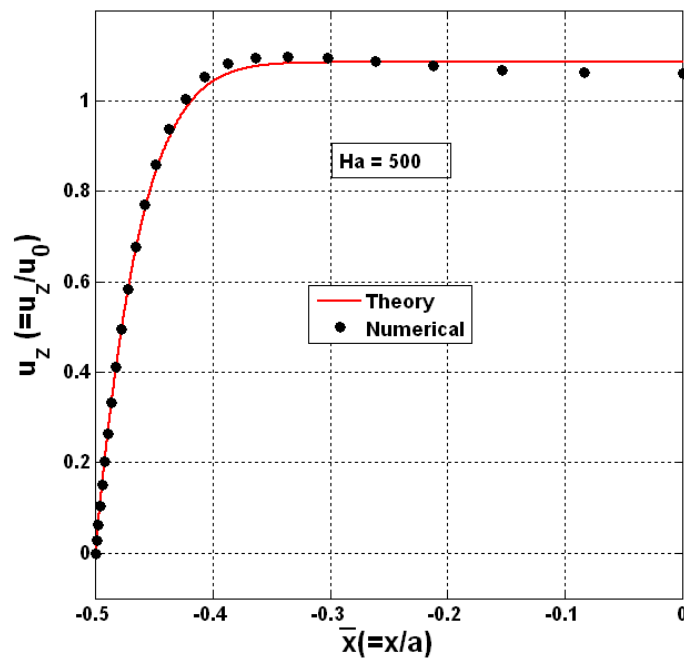


Figure 2.14: Non dimensional velocity distribution across the center of side walls for case A1 (Insulating walls, $C_w = 0$) and $Ha=500$

2.5 Summary of the key results of benchmarking studies with Hunt problem

- i. The fully developed length is decreasing with increasing Hartmann number for a given aspect ratio channel.
- ii. On the other hand, for a fixed Ha , the fully developed length is higher for smaller aspect ratio (longer width along the applied field direction) ducts.
- iii. The core current for a given Ha is larger for a smaller aspect ratio which will lead to larger pressure drop due to higher electromagnetic drag.
- iv. The deviation in estimation of core velocity and the peak velocity in the side layer is less than 1% and 2.5 % respectively in any case.
- v. The maximum deviation in electric potential distribution is of less than 1% from Hunts analytical solution in all the cases.

The results of 3D numerical simulation of MHD flow at high Hartmann number in rectangular ducts of different aspect ratio and wall conditions is reasonably matching well with the corresponding analytical estimations derived by Hunt. The deviations observed can be attributed to two facts. First is the finite electrical conductivity of Hartmann walls in numerical calculation as opposed to the infinite assumption in theory. Second is the numerical computation in the finite wall thickness in contrast to the theoretical estimation based on thin wall approximation. The deviations are expected to be reduced further by improving the grid points in the boundary layer and with the expense of longer computational time. It is to be noted that convergence of the numerical solution becomes slow as the electrical conductivities of walls are decreased. For insulating channels, the convergence is extremely slow that requires prolonged computation for several months.

2.6 Benchmarking studies with analytical model based on variational approach

Analytical solutions developed by Hunt for liquid metal MHD channel flows are restricted to specific boundary conditions of the channel walls. In the limit the solution can be extended to i) insulating side wall and infinitely conducting Hartmann wall, ii) both walls are insulating, and iii) both walls are infinitely conducting. However, in real systems both the Hartmann and side walls will have arbitrary finite conductivities. Hunt's solution cannot be applied for these realistic cases. So the solution of the MHD flow problem relies on numerical methods only. Although numerical methods are suitable for any arbitrary conditions (including taking into account finite thickness of the channel walls, flow in L and U bends, flow in diverging and converging channels etc.), CFD codes are still to be bench marked with analytical solutions. To my knowledge, there are no exact analytical solutions for a simple practical case in which all the walls are of identical thickness and electrical conductivity. However, some of the analytical models exist that assume fully developed flow for linear Navier-Stokes equation and finite conductivity of the confining walls. These models are handy for benchmarking purposes. In view of this, the benchmarking studies in a model developed by Sidorenkov and Shisko [6] based on variational approach is presented. The solutions were obtained for a fully developed velocity profile and electric potential distribution in a channel of arbitrary wall conductivity and valid for arbitrary Hartmann number. Numerical simulation is carried out and comparison is made with those analytical estimations.

2.6.1 Description of analytical model

Consider the steady state flow of a viscous incompressible conducting fluid perpendicular to a uniform external applied magnetic field in a rectangular channel of cross section $|y| \leq b/2$ and $|z| \leq a/2$. The flow is driven by a constant pressure gradient ($\partial p / \partial x = \text{con.}$) in \mathbf{x} direction and the applied magnetic field $\mathbf{B} = B(0, 0, B_0)$ in \mathbf{z} direction (see Fig. 2.15). The flow is assumed fully developed and all the walls of the channel (Hartmann and side walls)

have finite conductivity. The electrical conductivity of the fluid (σ) is assumed constant and there is no contact resistance at the fluid wall interface. The governing equation for the axial component of velocity $u_x=u_x(y, z)$ and induced magnetic field $B_x=B_x(y, z)$ were obtained simplifying the Maxwell equations and generalized Ohm's law.

$$\nabla^2 u_x + \frac{B_0}{\mu \rho \nu} \frac{\partial B_x}{\partial z} = \frac{1}{\rho \nu} \frac{\partial p}{\partial x} \quad \text{Eqn(2.23)}$$

$$\nabla^2 B_x + \mu \sigma B_0 \frac{\partial u_x}{\partial z} = 0 \quad \text{Eqn(2.24)}$$

Where,

μ is the permeability of the fluid ($H \cdot m^{-1}$), ρ is the density of the fluid (kg/m^3), ν is the kinematic viscosity of the fluid (m^2/s), σ is the conductivity of the fluid ($Ohm^{-1}m^{-1}$), p is the pressure of the fluid ($Newton/m^2$).

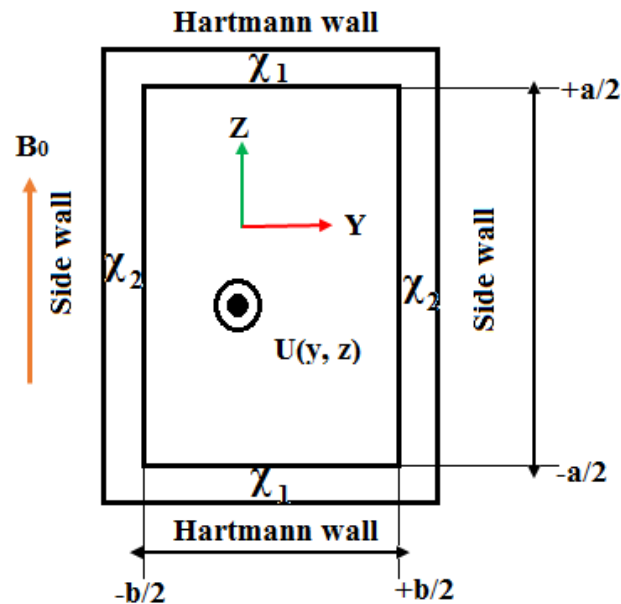


Figure 2.15: Analytical problem geometry(2D) considered by variational model

The boundary value problem was solved using no slip condition for the flow field and thin wall approximation for the induced field at the fluid-wall interface as follows,

For velocity field:

$$\vartheta(\pm 1/2, z) = \vartheta(y, \pm \lambda/2) = 0 \quad \text{where, } \lambda=a/b$$

For induce magnetic field:

$$b \pm \chi_1 \frac{\partial b}{\partial z} = 0; \quad \chi_1 = \frac{\sigma_{w1} a_{w1}}{\sigma b} \quad \text{at the Hartmann walls i.e, } z = \pm \lambda/2$$

$$b + \chi_{2+} \frac{\partial b}{\partial z} = 0; \quad \chi_{2+} = \frac{(\sigma_{w2+}) a_{w2+}}{\sigma b} \quad \text{at the side wall i.e, } y = + 1/2$$

$$b - \chi_{2-} \frac{\partial b}{\partial z} = 0; \quad \chi_{2-} = \frac{(\sigma_{w2-}) a_{w2-}}{\sigma b} \quad \text{at the side wall i.e } y = - 1/2,$$

The original system of Eqn(2.25) and Eqn(2.26) were reduced to homogeneous form through substitution of approximate solution displayed in Eqn(25) and Eqn(26).

$$\vartheta(y, z) = \frac{P}{t Ha} \left\{ 1 - \frac{\cosh(Ha z)}{\cosh(Ha \lambda/2)} - \bar{\vartheta}(y, z) \right\} \quad \text{Eqn(2.25)}$$

$$b(y, z) = -\frac{P}{t Ha} \left\{ tz - \frac{\sinh(Ha z)}{\cosh(Ha \frac{\lambda}{2})} + \bar{b}(y, z) \right\} \quad \text{Eqn(2.26)}$$

Where, $t = (1 + \chi_1 Ha) / (\lambda + 2\chi_1)$, $P = \frac{p}{p^*}$, $p^* = \frac{b^2}{\rho \nu u_0} \frac{\partial p}{\partial x}$

The detail derivation of the above said problem can be found in the reference of Sidorenkov and Shisko[6]. The final solution for velocity, induced field and electric potential they have obtained is presented in Eqn (2.27), Eqn (2.28) and Eqn (2.29) respectively for completeness.

$$\vartheta(y, z) = \frac{P}{t Ha} \left[\left\{ (1 - \vartheta_1(y)) \left(1 - \frac{\cosh(HaZ)}{\cosh\left(\frac{Ha\lambda}{2}\right)} \right) \right\} - \left\{ \vartheta_2(y) \left(1 - \frac{4z^2}{\lambda^2} \right) \right\} \right] \quad \text{Eqn (2.27)}$$

$$b(y, z) = \frac{P}{tHa} \left[\left\{ \left(tz - \frac{\cosh(Haz)}{\cosh(Ha\lambda/2)} \right) (1 + b_1(y)) \right\} + \left\{ z \left(1 - 4\eta \frac{z^2}{\lambda^2} b_2(y) \right) \right\} \right] \quad \text{Eqn (2.28)}$$

$$\begin{aligned} \varphi(y, z) = -\frac{P}{tHa} & \left[\left(1 - \frac{\cosh(Haz)}{\cosh(Ha\lambda/2)} \right) (y - \tilde{Q}_1(y)) - \left(1 - \frac{4z^2}{\lambda^2} \right) \tilde{Q}_2(y) \right. \\ & - \left. \left(\frac{1}{Ha} (y + \tilde{Q}_3(y)) \left(t - \frac{Hacosh(Haz)}{\cosh(Ha\lambda/2)} \right) \right) \right. \\ & \left. - \frac{1}{Ha} \left(1 - \frac{4\eta z^2}{\lambda^2} \right) \tilde{Q}_4(y) \right] \quad \text{Eqn(2.29)} \end{aligned}$$

Where,

$$\tilde{Q}_{1,2,3}(y) = \sum_{k=1}^4 C_k \tilde{\Delta}_{1,2,3}(\alpha_k) \frac{\sinh(\alpha_k y)}{\alpha_k \cosh(\alpha_k/2)}$$

$$\tilde{Q}_4(y) = \sum_{k=1}^4 C_k \frac{\sinh(\alpha_k y)}{\alpha_k \cosh(\alpha_k/2)}$$

2.7 Numerical simulation of 3D MHD flow in electrically conducting square duct

The MHD flow of PbLi for various Hartmann number (Ha) is simulated in a square duct having all the walls electrically conducting and submerged in a uniform applied magnetic field. The flow cross section is 25 mm x 25 mm and a flow length of 500 mm which is sufficient to achieve a fully develop profile. All the channels walls are of 1.5 mm thick SS plate and electrical conductivity of 1.0 E+6 S/m that correspond to a relative wall conductance ratio of ~0.15. The schematic view of the geometry is shown in Fig. 2.16. The flow is assumed to be steady, incompressible and laminar for a mean velocity of 0.01 m/s. The strength of the applied magnetic field is fixed at $B_0=3.85257$ which corresponds to the value of $Ha=1000$ for this given geometry and properties of PbLi. The numerical solution is obtained using Electric potential formulation of CFD code FLUENT and same governing equations as described in section 2.3.1 (Numerical simulation of Hunt's case). The converged results of velocity, electric potential,

pressure gradient and current distribution in a fully developed flow region is compared with the analytical estimations based on variational principle described in section 2.6.

2.7.1 Results of numerical simulation and comparison with analytical model

In the present case the relative conductance of the side wall (0.15) is higher than the relative conductance of the side wall boundary layer. As a result, the majority of the induced transverse current enters into the side wall crossing the side wall boundary layer from the core flow region. Because the currents add up linearly in the direction of the magnetic field, the potential distribution is parabolic with maximum at the centre. Since the parallel component of electric field is continuous, electric potential and transverse electric field follow the same parabolic distribution at the fluid solid interface. But there is no variation of electric potential and its gradient along the field direction outside the side wall boundary layer. So there exists a potential jump across the side wall boundary layer. The potential jump is associated with the jump in the transverse electric field component which gives rise to increased velocity as per the generalized Ohm's law. So the characteristic M-type profile is observed for velocity profile across the side walls with decreasing jet velocity in the direction of applied magnetic field. However, the velocity in the Hartmann layer exhibits as usual an exponential profile. For clear presentation, 3D velocity profile and path line of current in a flow cross section is shown in Fig. 2.17 and Fig. 2.18 respectively. For pressure, the gradient along the axis of the flow is shown in Fig. 2.19 from which fully developed length is identified from the region of constant pressure gradient. The fully developed region is obtained beyond 0.065 m from the inlet of uniform velocity.

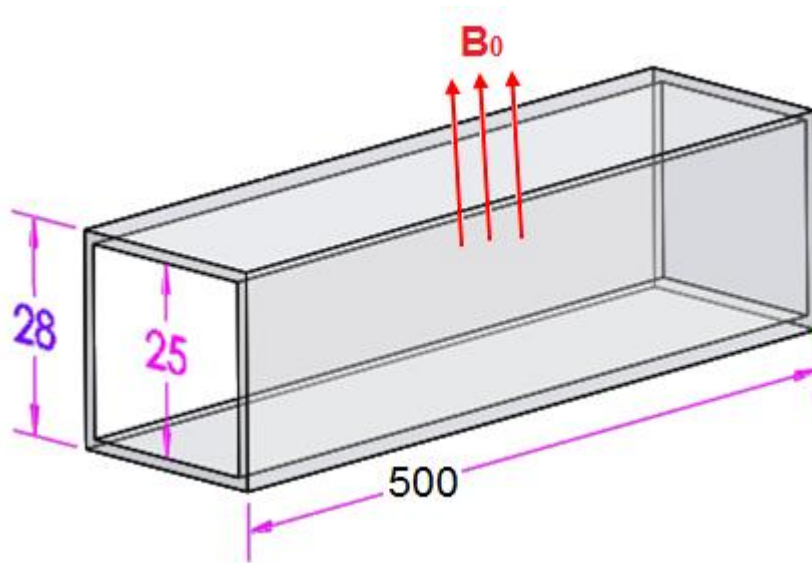


Figure 2.16: Computation geometry for benchmarking study with variational model. All the dimensions are in mm unit

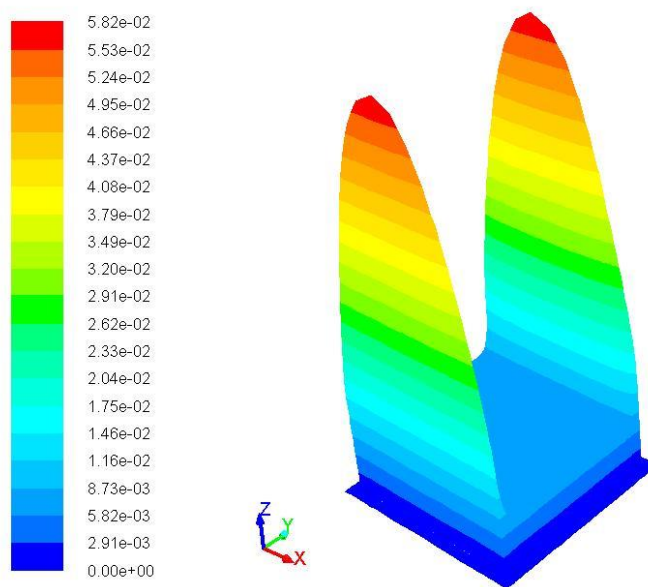


Figure 2.17: 3D axial velocity profile for a conducting square duct at $Ha = 1000$ and mean velocity 0.01 m/s

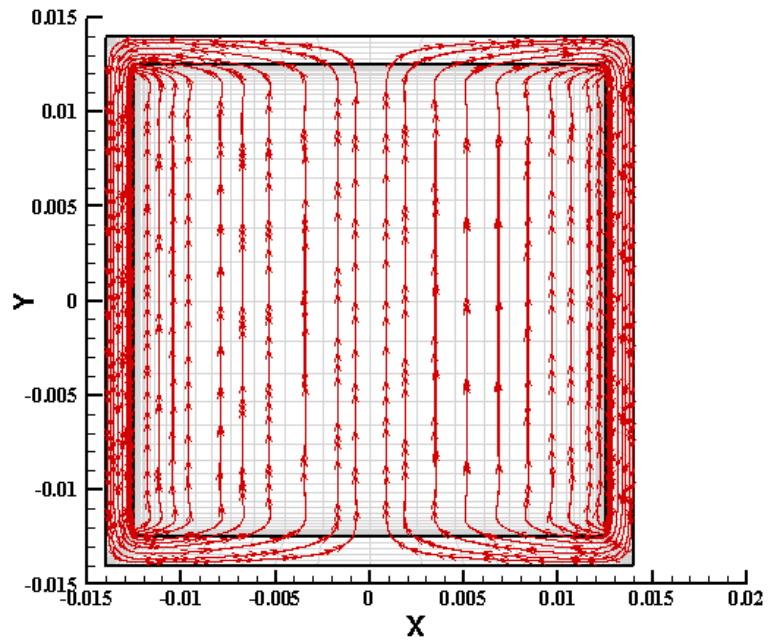


Figure 2.18: Pathlines of electric current in a flow cross section of conducting square duct

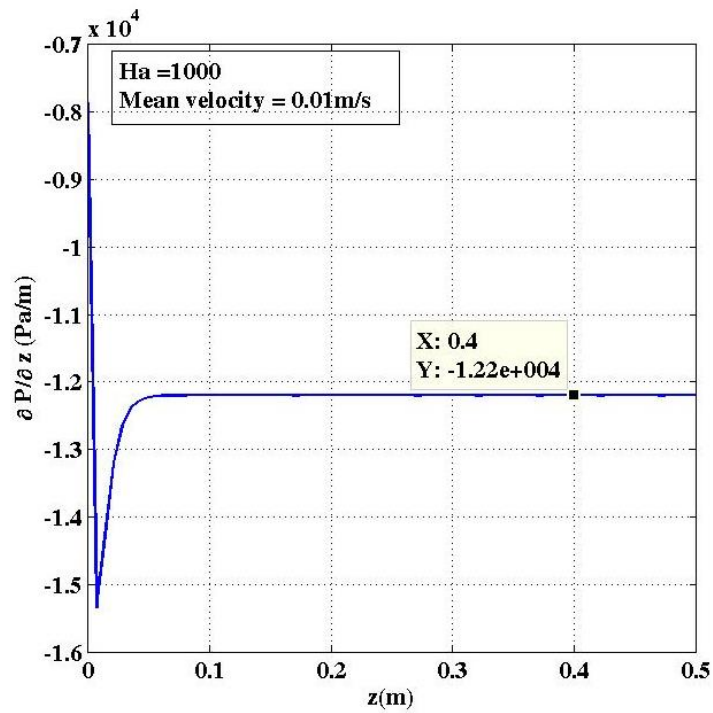


Figure 2.19: Pressure gradient along the flow length of a conducting square duct for $Ha = 1000$ and mean velocity 0.01 m/s

2D velocity and electric potential distribution across the side wall at the centre of the duct cross section is shown in Fig. 2.20 and Fig. 2.21. Comparison with analytical models indicates numerical value of the peak velocity in the side layer jet and core velocity is matched well with the analytical estimations. The deviation for core and peak velocity is within 0.4 and 1.25% respectively. However, relatively higher deviation is observed at the point of inflexion. Similarly, for the electric potential distribution across the side walls (see Fig. 2.21), the deviation is within 1%. In experiment, the measured potential difference across the side walls is a measure of the average flow rate in the duct cross section. So the distribution of side wall potential difference along the applied field direction is of interest for real application. Numerically obtained potential difference across the side walls is compared with the analytical distribution. As can be seen in Fig. 2.22, numerical distribution is matching well with the corresponding analytical profile with maximum deviation at the center is within 1%.

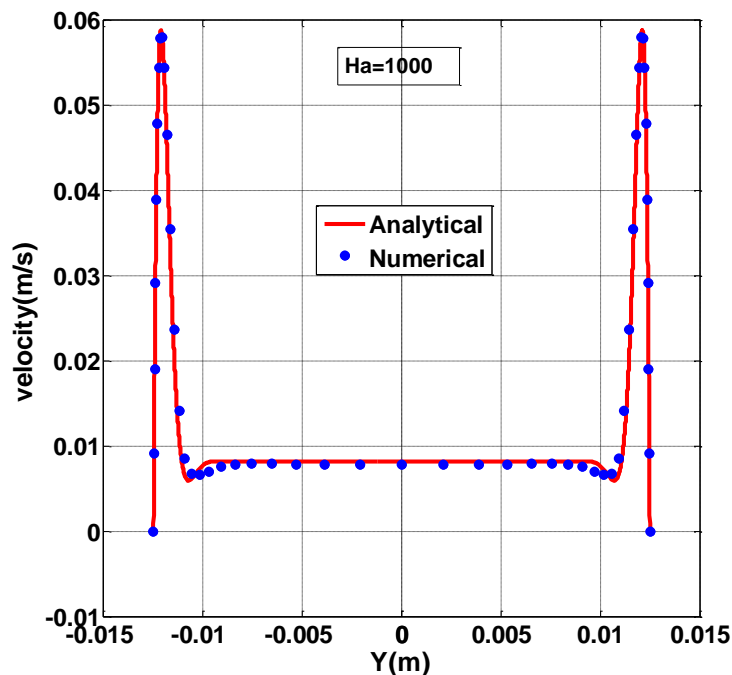


Figure 2.20: Comparison of numerical velocity distribution across the center of side walls in a conducting square duct for $Ha = 1000$ and mean velocity 0.01 m/s with the corresponding analytical profile

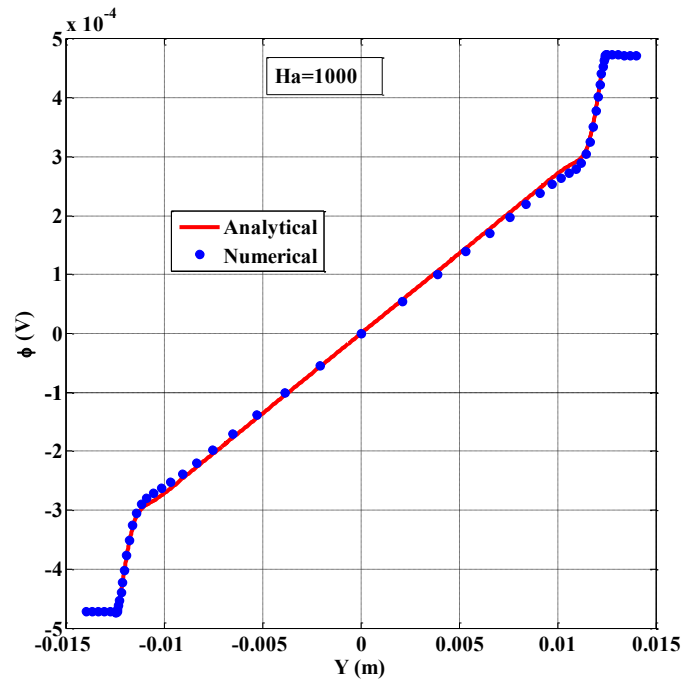


Figure 2.21: Comparison of numerical electric potential distribution across the center of side walls in a conducting square duct for $Ha = 1000$ and mean velocity 0.01 m/s with the corresponding analytical profile

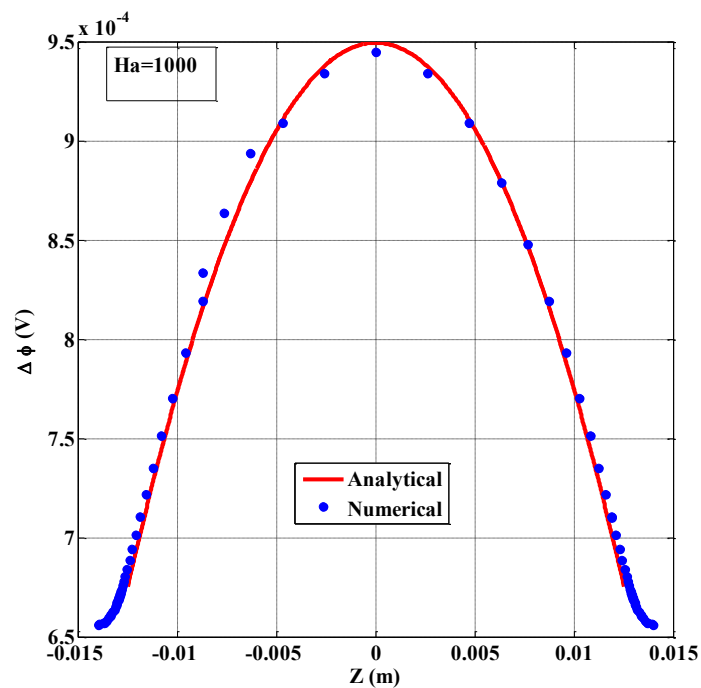


Figure 2.22: Distribution of side wall electric potential difference along the applied field for a conducting square duct at $Ha=1000$ and mean velocity of 0.01 m/s

A comparison of various parameters estimated from analytical and corresponding numerical counterpart is summarized in Table 2-5.

Table 2-5: comparison of parameters estimated from numerical and analytical solution for a conducting square duct at $Ha=1000$ and mean velocity of 0.01 m/s

Ha=1000	Analytical	Numerical	Deviation (%)
Peak velocity(m/s)	0.05878	0.058045	1.25
Core velocity(m/s)	0.008133	0.0081	0.4
Maximum side wall potential (mV)	0.95	0.94	1.05
Pressure gradient(Pa/m)	1.263E4	1.22E4	3.4

2.8 Comparison of variational model with Hunt's exact analytical solution

Following the benchmarking analysis for both the model with numerical solution, a comparison is made for both the analytical solutions for quantitative assessment of their performances at high Hartmann number. For this purpose, a single poloidal flow channel of LLCB TBM is considered. The typical flow cross section of a LLCB channel is 428 mm (toroidal)x 24 mm(radial). Because of the high toroidal magnetic field ($B_0=4T$) and large channel aspect ratio of the flow channel, the characteristic Hartmann number is ~ 18000 for a liquid metal flow in a poloidal direction. The thickness of the Hartmann and side walls is assumed to be 11.67 mm and 5mm respectively. Due to high electrical conductivity of the structural walls ($\sigma_w=1.31E6$ S/m), the electrical conductance of the Hartmann wall is relatively larger ($Ch_w=0.0929$) than side walls ($C_{sw}=0.04$). The mean velocity is assumed 0.014 m/s and physical properties of PbLi is assumed 9402 kg/m³, 0.00177 Pa. s, 7.692E5 S/m for density(ρ), viscosity(μ) and electrical conductivity(σ) respectively. The fully developed velocity profile estimated by variational model and Hunt's solution at the centre of the flow cross section is shown in Fig. 2.23. As can be seen, small deviation is observed for the peak velocity in a side layer jet. The deviation is attributed to the infinite conductance of the Hartmann wall assumed

by Hunt's solution rather than finite conductivity of the variational model. It is interesting to see that the negative velocity is predicted by both the analytical solution at the point of inflection of the side wall boundary layer.

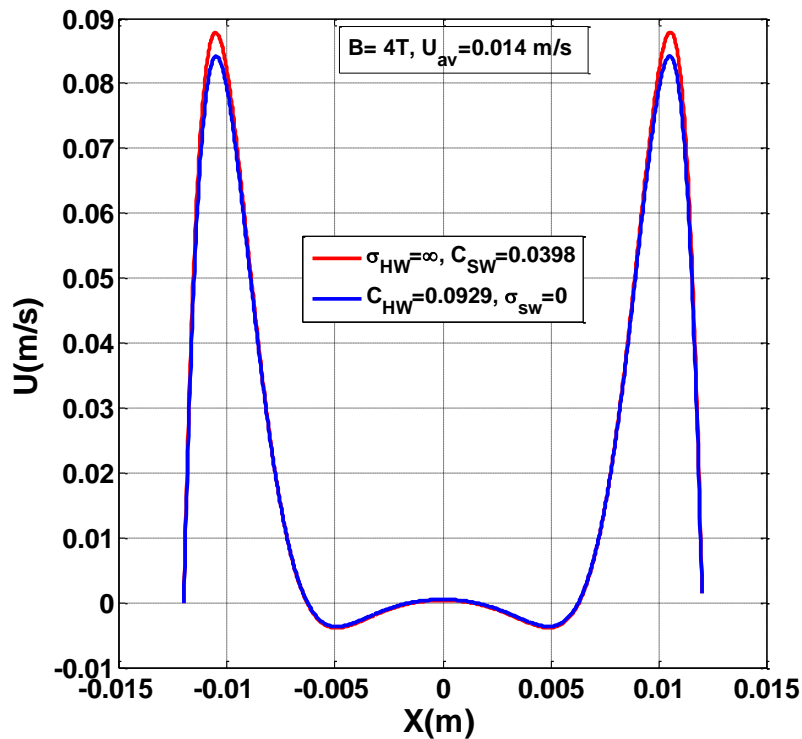


Figure 2.23: Comparison of side wall velocity profile predicted by Hunt and Variational analytical solution in a channel of LLCB at Ha=18000

2.9 Summary of the benchmarking studies with analytical model

The present benchmarking studies are limited in a broad spectrum MHD flow as foreseen for generic LM blanket applications. The capability of MHD solver of CFD code FLUENT is tested for steady state laminar incompressible flow at high magnetic fields. Numerical results of FLUENT code for velocity, electric potential, and pressure drop are matching reasonably well with analytical estimations based on variational method. The maximum deviation in peak velocity of side layer and core velocity is within 1.25 %. However, relatively higher deviation is observed at the region of point of inflexion. This region may be further investigated with

improved grid resolution. A comparison of the model estimation with Hunt's exact solution at high Hartmann number indicates a fair matching of both the predictions. Hence the model can be used as a tool for analysis of data in experiment test sections with finite wall electrical properties at arbitrary Hartmann number.

However, the present studies lack in addressing unsteady benchmarking problems. As envisaged, the MHD flow in a typical LM blanket exhibits unsteady phenomena due to instabilities associated with high velocity gradients in the side layer jets, buoyancy driven convection flows and many other 3-D effects associated with geometry and verity of flow configurations. Further, considering the electrically conducting channels and high numerical values of relevant characteristic parameters of the present studies; Hartmann number ($Ha \sim 10^4$), Grashof number ($Gr \sim 10^8-10^{10}$) and Reynolds number ($Re \sim 10^4-10^5$) the turbulence is foreseen to evolve to the form of quasi-two-dimensional(Q2D) state. The results of various test-section experiments carried with Lead-lithium (PbLi) and Sodium-potassium (NaK) at high magnetic fields which are presented in subsequent chapters of the present study also indicate limitation of laminar model approach due to possible turbulence effects. Measurement of velocity in the side layer jet as obtained from the RF test section experiment (chapter-5, section 5.17) indicated a reduced peak velocity and increased thickness of the side layer. The origin of the instability was probably related to the inflexional instabilities in the side layer jet structure. So the analysis points to the necessity of extending flow and heat transfer characteristics beyond the laminar flow regime which has not been addressed in the present studies.

2.10 References

1. Z. Tao, M. Ni, Analytical solutions for MHD flow at a rectangular duct with unsymmetrical walls of arbitrary conductivity, Science China Physics, Mechanics & Astronomy 58, 024701 (2015).

2. J. C.R. Hunt, Magneto-hydrodynamics flow in rectangular duct, J. Fluid Mech. 21 (1965)
3. FLUENT code produced by FLUENT Inc.
4. J. A. Shercliff, Steady motion of conducting fluids in pipes under transverse magnetic fields, Proc. Camb. Phil. Soc., 49 (1953)
5. S. Smolentsev, S. Badia, et al., An approach to verification and validation of MHD codes for fusion applications, Fusion Eng. and Des.100 (2015)
6. S. I. Sidorenko, A.Ya. Shishko, Variational method of calculation of MHD flows in channels with large aspect ratios and conducting walls, Magneto-hydrodynamics, 27 (1991)

3 CHAPTER

Numerical Model Validation with Experiment at High Magnetic Field

3.1 Introduction

Liquid metal PbLi enriched with ${}^6\text{Li}$ (83% Pb and 17 % Li enriched by 90% with Li^6) is considered to be prospective coolant and tritium breeder or as an exclusive breeder for the fusion blanket program of many international partners including India. [1, 2] Typically, in the blanket module, the liquid metal flows in electrically conducting channels which are consisting of multiple L/U bends. In the plane of 90° turning the flow is subject to high toroidal magnetic fields. 3-D axial currents that are generated at the flow turning and expansion/contraction regions along the flow path lead to modification in the base flow structure and increased pressure drops. MHD flow properties are also affected if the orientation of the legs of the bend is different with respect to magnetic field. Thus liquid metal flows in ducts of multiple bends have various interesting MHD phenomena, especially in the absence of electrical insulation between the liquid metal and structural components. Development of efficient blanket modules relies on the understanding of these phenomena encountered in such types of basic elements of the general blanket system. Some of these thermo-fluid MHD issues including instabilities, turbulence, buoyancy effects have been studied by Smolentsev et al. [3, 4] Analysis of MHD flow in a conducting rectangular U bends, where the flow turns from perpendicular to parallel direction of the applied magnetic field has been carried out by Molokov and Buehler [5] for high Hartmann number ($\text{Ha} \gg 1$) and in the inertia less limit ($\text{N} > \text{Ha}^{1/2}$). Here, Ha is the Hartmann number ($\text{Ha} = B_0 a \sqrt{\sigma/\mu}$) and N is the interaction parameter ($\text{N} = \sigma a B_0^2 / \rho U$) and the symbols used in the definition of Ha and N have their usual meaning as described earlier. MHD duct flows at blanket conditions are complex and experimentally validated MHD codes

are needed for the design of TBMs as well as future DEMO Blankets. In this regard Ming-Jiu Ni et.al. [6] and Smolentsev et.al. [7] have developed advanced computational techniques for MHD flow simulation at high Hartmann number relevant to fusion systems. The present work aims to verify the applicability of the MHD module of CFD code FLUENT in an experiment test model at high magnetic fields relevant to fusion blanket conditions.

Experiments were carried out in the lead-lithium loop of Institute of Physics University of Latvia (IPUL) integrated with the solenoid superconducting magnet which can provide uniform axial magnetic field up to 4 T in a circular region of diameter of 280 mm. The test section channel consists of four rectangular L-bends and made up of 3 mm thick SS316 plates. [8] The experiments were carried out with different characteristic non dimensional parameters by varying the flow rates (0.1221 m/s to 0.3222 m/s) and magnetic field strength (1 to 4 T). The experiment could achieve maximum Hartmann number $Ha=2060$ for the test section geometry and interaction parameter (N) in the range 25-270 for the above said flow rates. Pressure drop and wall electric potential distribution at various locations of the test section is measured to generate an experiment database. The measured data of Hartmann and side wall electric potential distribution is used for validation of numerical models and code applicability for fusion relevant conditions. With help of developed analytical techniques, the measured side wall potential data at a location of the test section free from bend effects is also used for estimation of flow rate in the loop.

3D numerical simulation is carried out in a half symmetry of the experiment test section using the MHD module of FLUENT. The test section model for numerical study is consisted of multiple 90° bends with different orientation of the applied magnetic field with respect to the flow direction at different legs of the bend (parallel to perpendicular, and perpendicular to perpendicular direction with respect to the applied magnetic field). Electric potential (induction less approximation) method is used while modeling the flow. The magnetic field is steady and

spatially uniform during each run. The maximum Hartmann number $Ha (= B_0 a \sqrt{\sigma/\mu})$ is 2060 corresponding to the 4T field. The interaction parameter $N (= \sigma a B_0^2 / \rho U)$ is varied from 25 to 270. Here B_0 , a , σ , μ is the applied magnetic field, characteristic length scale, electrical conductivity of the liquid metal and dynamic viscosity respectively. Characteristic length scale 'a' is considered as half the length alongside walls (For present test section, $a = 0.025$ m). Numerical simulation results of two sets of data ($Ha=1030$, $N=25, 40, 67$ for $B=2T$ and $Ha=2060$, $N=129, 161, 270$ for $B=4T$) is compared with the corresponding measured values to assess the code performance at various flow condition covering the full range of experiment.

3.2 Experiment set up

3.2.1 Liquid metal (Lead-lithium) experiment loop

PbLi (see Fig. 3.1) experiment loop at IPUL is a pressurized closed loop system to perform the high temperature isothermal liquid metal MHD experiment. Working fluid, Pb-Li is maintained under argon cover gas to minimize the formation of oxides. The magnet used in this experiment is a cryogen-free liquid helium cooled superconducting solenoid magnet that can provide maximum magnetic field 5T at the center of the solenoid. The cylindrical space of the magnet available for experiment had a diameter of 280mm. The test section is placed in the central zone of the SCM (superconducting magnet) where the magnetic field uniformity is maximum and connected to the loop outside. An electromagnetic pump with a maximum pressure head of 5.0 bar is used to circulate Pb-Li at temperature 350°C. In the loop, liquid metal is circulated through pipes of inner diameter of 28 mm. An electromagnetic flow meter is used in order to determine the flow rate in the loop.

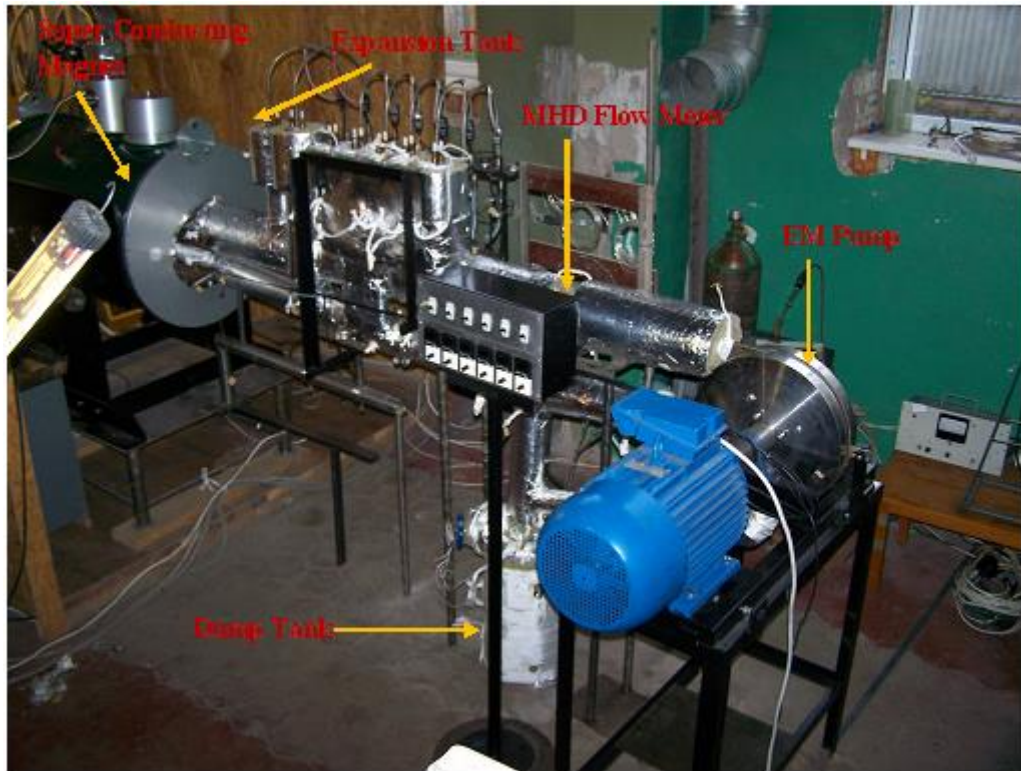


Figure 3.1: Photograph of Experimental loop with various components

The overall system consists of the following major sub-systems:(i) Pb-Li loop (ii) Argon cover gas system (iii)Vacuum and leak detection system (iv) Instrumentation and DAS (v) Helium cooling system (vi) Flow meter (vii) Super conducting magnet (viii) Heating system

3.2.2 Experiment test section

Experimental test section consists of multiple 90° rectangular bends and the orientation of the applied magnetic field with respect to the flow direction is changing at different legs of the bend (parallel to perpendicular, and perpendicular to perpendicular direction of the applied magnetic field). Two 90° channel bends were in the parallel plane where the flow turns from parallel to a transverse direction of the applied magnetic field and vice versa with sudden expansion/contraction (flow cross-section changing from 0.025 m × 0.025 m to 0.0247 m × 0.0496 m) and another two 90° bends in the plane perpendicular to the magnetic field (see Fig. 3.2a). All the confining walls of the test section are made from 3 mm thick SS plates of 316L.

Liquid metal at 350 °C enters into the test section through a square inlet duct of cross section 0.025 m × 0.025 m which is parallel to the axial magnetic field and then becomes perpendicular to the magnetic field after taking a 90° turn from the square inlet duct. The flow cross section where it is transverse to the applied magnetic field is 0.0247 m (between side walls) × 0.0496 m (between Hartmann walls). The flow further experiences two sharp 90° bends in the plane perpendicular to magnetic field before coming out of the test section through an outlet square duct of same flow cross section as that of inlet duct. So the flow is experiencing sudden expansion or contraction at the inlet/ outlet section of the test section respectively as the flow cross section is changing from square to rectangular arm of the 90° bend with magnetic field aligned along the axis of inlet/outlet square duct. Inlet and outlet duct of the test section is integrated to rest of the loop piping through circular to square transition pieces (see Fig. 3.2b). Electric potential sensors and pressure tubes are welded at various locations of the test section for diagnostics. Heating cables are wrapped in the intermediate spacing of diagnostic locations (see Fig. 3.2c) to maintain the liquid metal temperature. The height of the test section is limited by the available space of superconducting magnet bore. Detail dimension of the experiment test section is shown in Fig. 3.3. It is to be noted there are small deviations in the cross section dimension of the actual test section with respect fabrication drawing (Fig. 3.3). In order to ensure proper electrical isolation of the potential pins from the heater coils, heater cables were covered with ceramic beads wrapped over the test section surface through an intermediate layer of fiberglass insulated tape. Finally, the test sections with wrapped heaters were thermally insulated with surrounding by covering ceramic wool insulation.

Fig. 3.2(a)

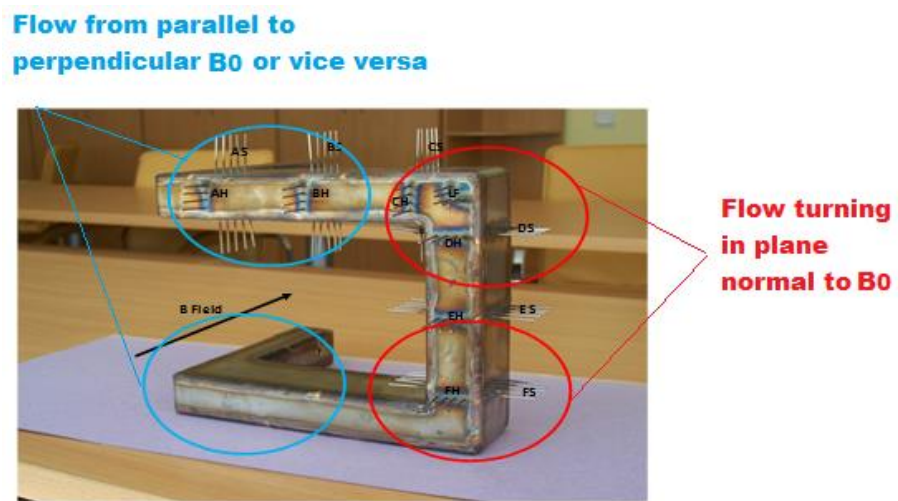


Fig. 3.2(b)



Fig. 3.2(c)

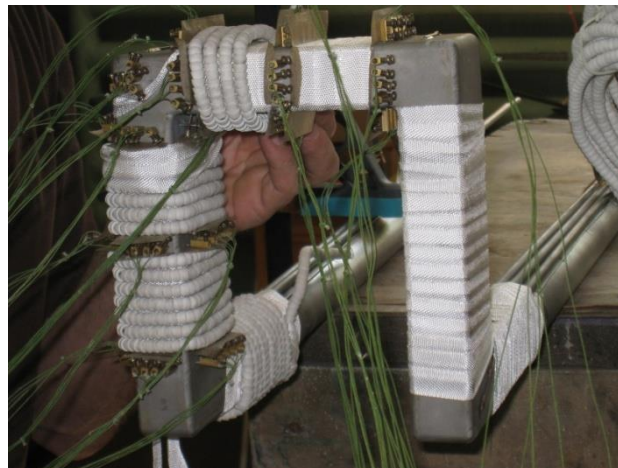


Figure 3.2: Photograph of the multiple bend test section, Orientation of different 90° bends with respect to applied B_0 in Fig. 3.2(a), connection of test section inlet/outlet to loop pipes through transition pieces in Fig. 3.2(b), arrangement of heaters in Fig. 3.2(c)

3.3 Diagnostics and Instrumentation

3.3.1 Potential measurement

The wall potential in the test-section was measured by multiple arrays of potential sensors placed at different locations of the test section (see Fig. 3.4(a)). Potential pins made from SS wires of dia 1.2 mm were connected on both the side walls as well as Hartmann wall of the TS. At any of the location named A, B, C, D, E, F: there were 5 potential pins in a row on the inner and outer side walls facing back to back and 4 potential pins are placed in the same array on the Hartmann wall. Arrangement of pins in an array 'A' is illustrated in Fig. 3.4(b). Similar pin configuration for B to F in the side walls were done as shown in position A and in the back side of corner location. The distances between two consecutive pins on the side wall (Δl_s) is 8mm and distances between two consecutive pins on the Hartmann wall is (Δl_h) 5mm. Owing to the symmetry of the test section, placement of potential arrays was decided for half of the total flow length perpendicular to magnetic field.

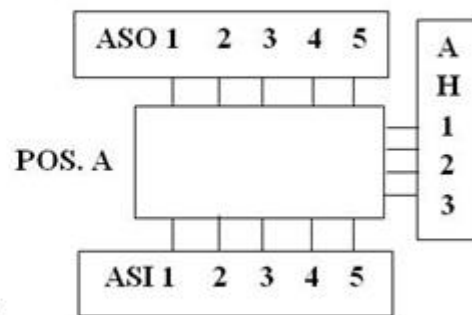
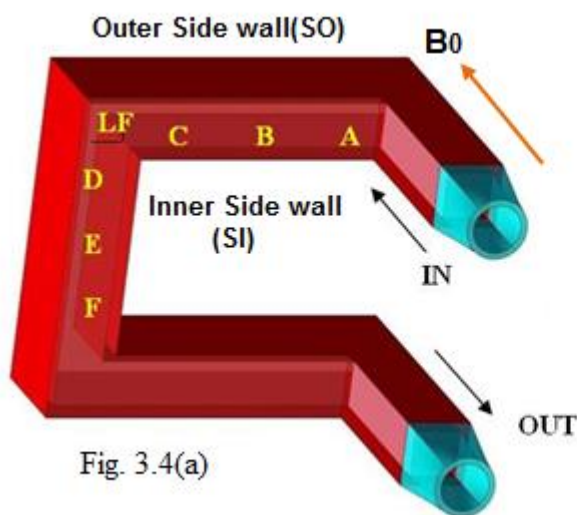


Figure 3.4: Labelling of potential sensors in the multiple bend test section, locations in Fig. 3.4(a), arrangement of pins for an array 'A' in Fig. 3.4(b)

The electrical connection for the potential pins were made before putting it inside the SCM, as it was practically impossible to make in situ electrical connections for potential pins. The total

number of potential pins were 94 and electrical connections accommodated in four connectors, each of which having a maximum no. of 25 channels. Experimental test section with attached potential pins at various locations before integration into the MHD loop is shown in Fig. 3.5.

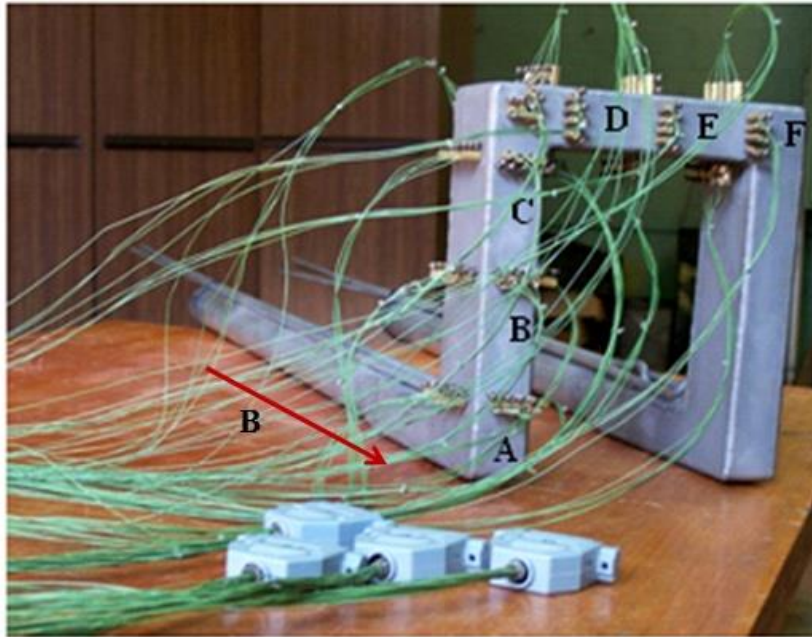


Figure 3.5: Experimental test section with attached potential pins at various locations before integration into the MHD loop

According to the inlet and outlet flow direction, following connection scheme was adopted

Connection scheme for potential pins:

Connector A:

Pins AH1 – AH4 ----- A1 – A4
 Pins BH1 – BH4 ----- A5 – A8
 Pins CH1 – CH4 ----- A9 – A12
 Pins DH1 – DH4 ----- A13 – A16
 Pins EH1 – EH4 ----- A17 – A20
 Pins FH1 – FH4 ----- A21 – A24

Connector AI:

Pins ASO1 – ASO5 -- AI1 – AI5 ; Pins ASI1 – ASI5 ----- AI6 – AI10
 Pins BSO1 – BSO5 – AI11 – AI15 ; Pins BSI1 – BSI5 ----- AI16 – AI20
 Pins CSO1 – CSO5 – AI21 – AI25.

Connector BI:

Pins FSO1 – FSO5 -- BI1 – BI5 ; Pins FSI1 – FSI5 ----- BI6 – BI10
 Pins ESO1 – ESO5 – BI11 – BI15 ; Pins ESI1 – ESI5 ----- BI16 – BI20
 Pins DSO1 – DSO5 – BI21 – BI25.

Connector B: Pins CSI1 – CSI5 -- B1 – B5; Pins DSI1 – DSI5 ----- B6 – B10

Pins LF1 – LF5 – B11 – B15 ; Pins LB1 – LB5 ----- B16 – B20.

Following the above mentioned philosophy, electrical cable was connected to each of the potential pin and was tightened with the help of screw. Only the potential pins at the inner side walls of the L-Bend were connected through brazing. All the Hartmann wall pins were connected to one connector. The side wall pins (except inner L-bend) were distributed in two other connectors and the fourth connector accommodates the inner wall pins of both the side walls along with pins from both the Hartmann walls of L-bends.

3.3.2 *Pressure measurement*

Liquid metal pressure at different locations of the test section and total pressure in the loop were measured through indirect means of cover gas pressure of expansion tanks attached with pressure measurement line. Five pressure transmitter tubes (ϕ ~6mm and 1 mm thick) of length ~600-700mm were welded to the Hartmann wall where potential pin array was absent. Expansion tank (size: O. D=72 mm, I. D=69 mm, Height=150 mm) with space for cover gas was connected to each of the pressure tube. The locations at which pressure transmitter tubes were welded to the test section is shown in Fig. 3.6. Since there was no space available inside the SCM, expansion tanks were located outside the SCM. In addition, there were two more expansion tanks, one in the incoming pipeline at inlet side line and the other in the outgoing pipeline at outlet side. These two expansion tanks were meant for measurement of integral pressure drop in the test section and extended pipelines associated with inlet/outlet section before integration into rest of the loop. All these expansion tanks were pressurized by argon gas through a common distribution gas line. For thermocouples connections at different locations, TIG welding and resistance micro welding was adopted. Schematics of the MHD loop with all the expansion tanks for pressure measurement is shown in Fig. 3.7.

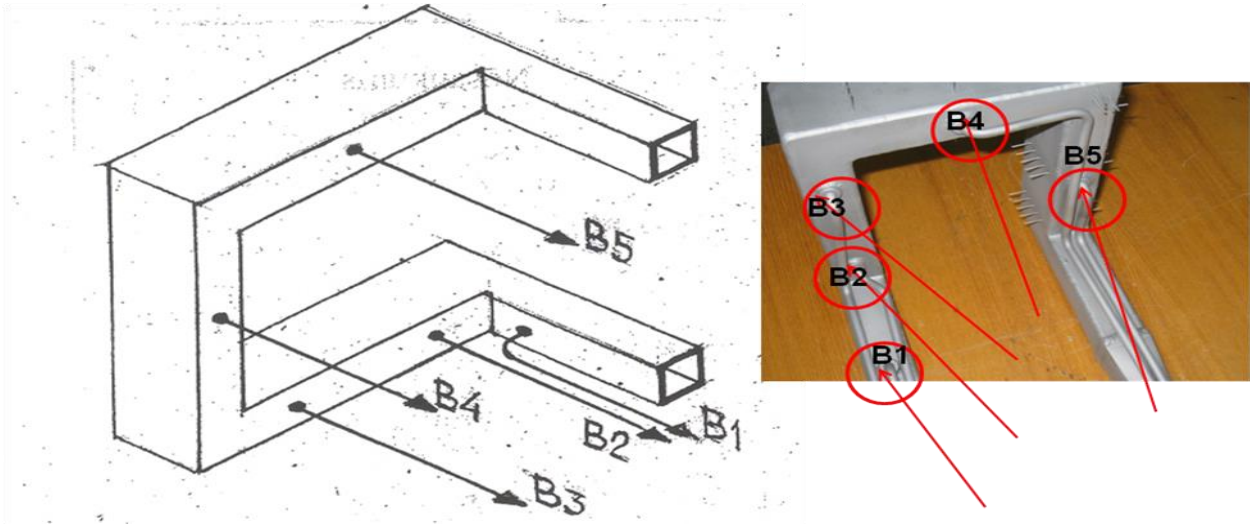


Figure 3.6: Locations of the pressure transmitters in test section of multiple bends

The five expansion tanks which measure pressure at location B1 to B5 of the test section are having same area of cross section and approximately same length. Other two expansion tanks (A1 and A2) which were connected to the inlet and outlet pipeline of the loop have the same size (O. D=102 mm, ID=98 mm, Height=188 mm) but different from B1 to B5. Schematic that indicates the level of liquid metal, gas column and geometric height of the expansion tanks is shown in Fig. 3.8

3.3.3 Methodology for the measurement of pressure drop

Let h_{1ig} and h_{2ig} be initial height of the gas column for the tank A1 and tank A2 respectively and P_{1ig} and P_{2ig} are the initial gas pressure in the respective tanks for no flow condition. P_{1fg} and P_{2fg} are the final gas pressure reading in the tank A1 and tank A2 at a particular flow rate and magnetic field and h_{1fg} and h_{2fg} are the corresponding gas column height of respective pressure P_{1fg} and P_{2fg} . Then expression for the pressure drop between A1 and A2 ($h_{1ig} \neq h_{2ig}$) is given by Eqn(3.1)

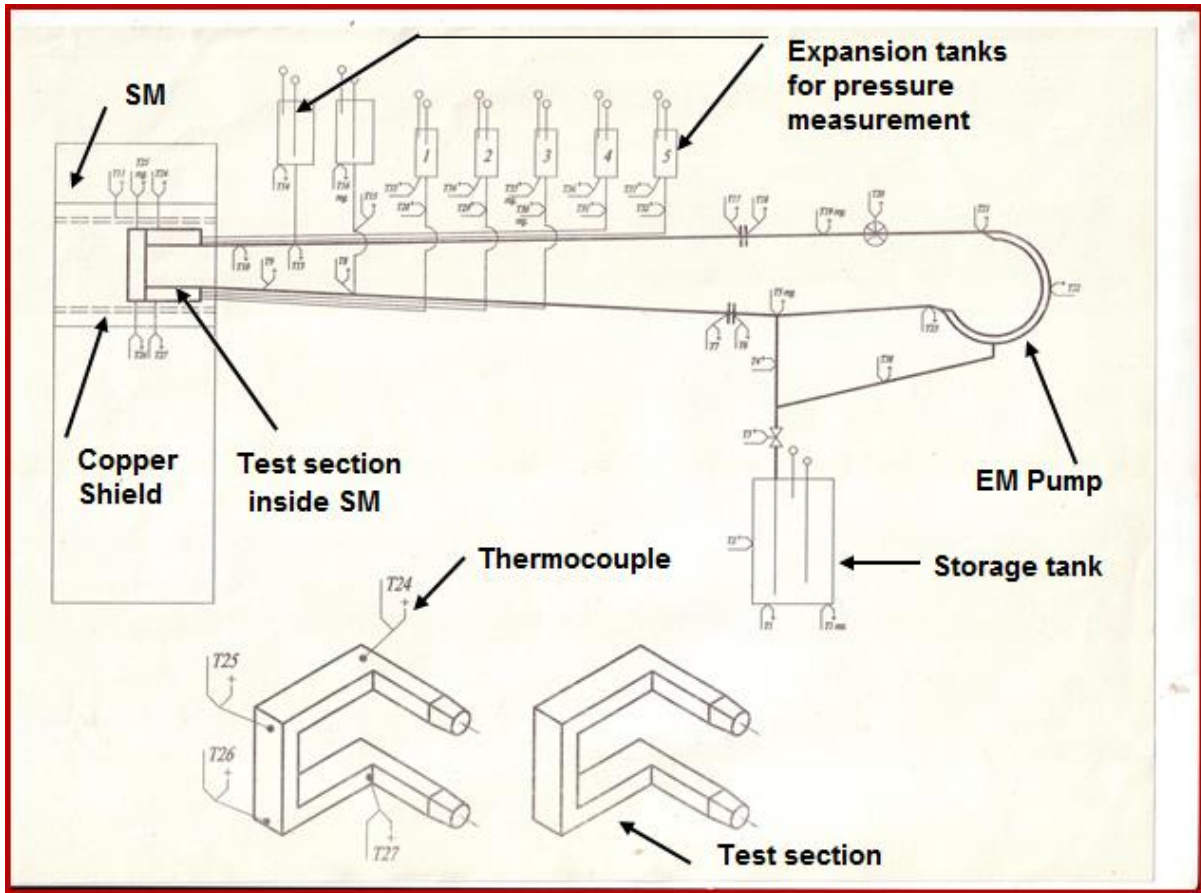


Figure 3.7: Schematic of the integrated MHD loop with arrangement of expansion tanks for pressure measurement in test section of multiple bends

$$\Delta P = P_{1fg} - P_{2fg} + \rho g 10^{-5} \left[\left\{ h_{1ig} \left(1 - \frac{P_{1ig}}{P_{1fg}} \right) \right\} - \left\{ h_{2ig} \left(1 - \frac{P_{2ig}}{P_{2fg}} \right) \right\} \right] \quad \text{Eqn(3.1)}$$

And the expression for MHD pressure drop between two ports of the test section (B1 to B5) ($h_{1ig} = h_{2ig}$) is given in Eqn(3.2)

$$\Delta P = P_{1fg} - P_{2fg} + \rho g 10^{-5} \left[\left\{ h_{2ig} \left(\frac{P_{2ig}}{P_{2fg}} \right) \right\} - \left\{ h_{1ig} \left(\frac{P_{1ig}}{P_{1fg}} \right) \right\} \right] \quad \text{Eqn(3.2)}$$

Here, the pressure reading P_{1fg} and P_{2fg} are in units of bar. The initial gas column height of tank A1 and A2 is $h_{1ig}=125m$, $h_{2ig}=155mm$ respectively.

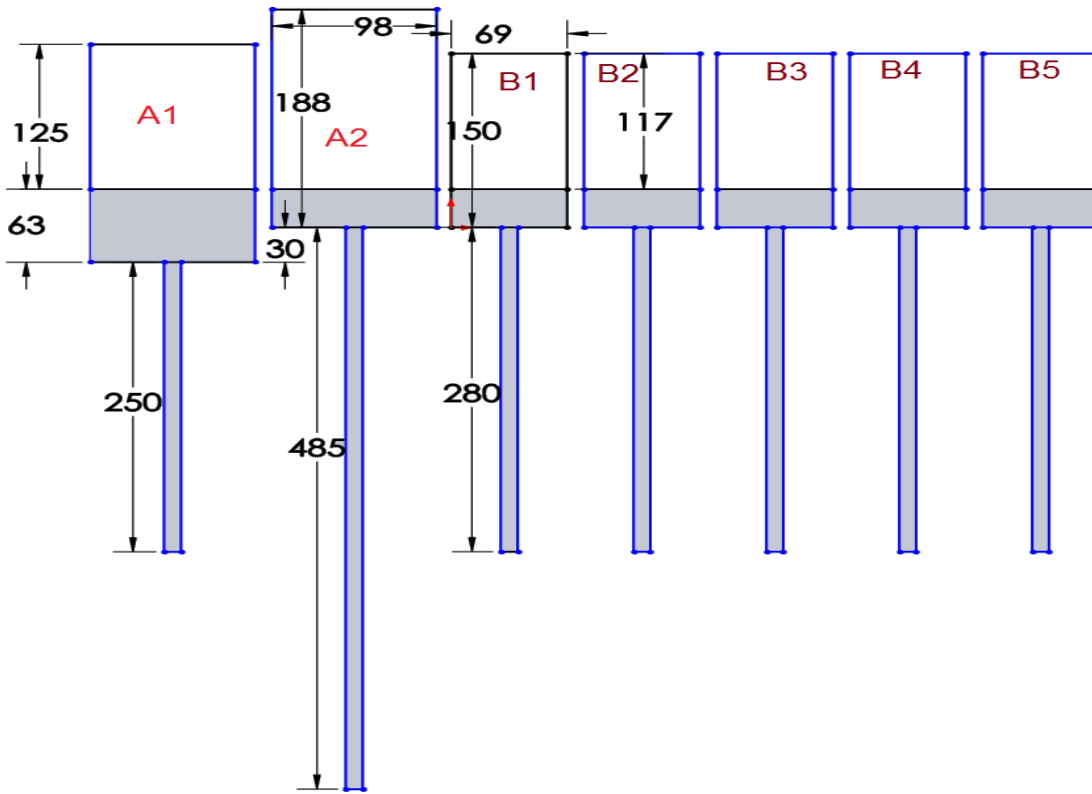


Figure 3.8: Liquid metal and gas column level (mm unit) schematic in expansion tanks for measurement

3.4 Analysis of Experimental Data

3.4.1 Mean velocity estimation from side wall potential distribution

Using the analytical models and experiment data of measured side wall potential, mean velocity in the test section is estimated. Based on this flow rate in the loop and calibration of the flow meter is obtained. For a fully develop flow in Y-Z plane and applied magnetic field in the Z- direction, axial velocity $u_x(y,z)$ integrated across the side wall (y direction) at certain height (z-direction) is directly linked with the side wall potential difference at that height [9]. Mathematically the relation in dimensionless form is given in Eqn(3.3)

$$\langle u(z) \rangle_y = \Delta\phi(z) \quad \text{Eqn(3.3)}$$

$$\text{Where, } \langle u(z) \rangle_y = \int_{-1}^{+1} u(y,z) dy$$

Referring to [9], in the case of a fully developed MHD flow, the distribution of the electrical potential $\phi(y,z)$ in a flow cross section of the test section ($|y| \leq 1/2$, $|z| \leq \lambda/2$), can be presented as:

$$\begin{aligned} \phi(y,z) = & -\frac{1}{F} \cdot \left\{ \left[y - \sum_{k=1}^4 C_k \cdot \tilde{\Delta}_1(\alpha_k) \cdot \frac{\text{sh}(\alpha_k \cdot y)}{\alpha_k \cdot \text{ch}(\alpha_k/2)} \right] \cdot \left[1 - \frac{\text{ch}(\text{Ha} \cdot z)}{\text{ch}(\text{Ha} \cdot \lambda/2)} \right] - \right. \\ & - \left[\sum_{k=1}^4 C_k \cdot \tilde{\Delta}_2(\alpha_k) \cdot \frac{\text{sh}(\alpha_k y)}{\alpha_k \cdot \text{ch}(\alpha_k/2)} \right] \cdot \left[1 - \frac{4z^2}{\lambda^2} \right] - \\ & - \left[y + \sum_{k=1}^4 C_k \tilde{\Delta}_3(\alpha_k) \frac{\text{sh}(\alpha_k y)}{\alpha_k \text{ch}(\alpha_k/2)} \right] \cdot \left[\frac{t}{\text{Ha}} - \frac{\text{ch}(\text{Ha} \cdot z)}{\text{ch}(\text{Ha}\lambda h(\text{H}))} \right] - \\ & \left. - \frac{1}{\text{Ha}} \cdot \sum \left[C_k \frac{\text{sh}(\alpha_k y)}{\alpha_k \text{ch}(\alpha_k/2)} \right] \cdot \left[1 - \frac{12\eta z^2}{\lambda^2} \right] \right\} \end{aligned}$$

Eqn(3.4)

Where,

$$F = \left(1 - \frac{2}{\lambda \text{Ha}} \right) \cdot (1 - Q_1) - \frac{2}{3} Q_2, \quad Q_{1,2} = 2 \cdot \sum_{k=1}^4 C_k \tilde{\Delta}_{1,2}(\alpha_k) \frac{\text{th}(\alpha_k/2)}{\alpha_k},$$

$$\text{Ha} = aB_0 \sqrt{\sigma / \rho \nu}$$

The width across the side wall ‘a’ is used for normalization of the cross section dimension and calculation of Hartmann number (Ha). μ ($\text{H} \cdot \text{m}^{-1}$) is the permeability of the fluid, ρ (kg/m^3) is the density of the fluid, ν (m^2/s) is the kinematic viscosity of the fluid, σ ($\text{Ohm}^{-1} \text{m}^{-1}$) is the conductivity of the fluid, $\kappa = \sigma_w h_w / (\sigma a)$ is relative wall electrical conductance, and all other symbols corresponds to those used in [9]. The expression for $\phi(y, z)$ is good enough to describe the distribution of the potential over the whole cross-section of the channel, except for the areas close to the corner points. For a given flow cross section, potential difference per unit velocity can be computed theoretically at different heights using above mentioned Eqn(3.4). Since the observed potential difference is linear with velocity and proportional to theoretical estimation of non-dimensional value as per Eqn(3.4), average velocity in that cross section can be estimated as described in the following.

Let's consider i^{th} pair of potential pins for which theoretical value of the potential difference is obtained from Eqn(3.5)

$$\Delta\phi_i^{\text{theory}} = B_0 a V_i G_i \quad \text{Eqn(3.5)}$$

Here G_i is the non-dimensional electric potential estimated from the theoretical relation given in Eqn(3.4) at a height represented by i^{th} pair of potential pins. B_0 is the external magnetic field and 'a' is the width across side walls.

Equating Eqn(3.5) with the measured value $\Delta\phi_i^{\text{exp}}$ from the experiment unknown average velocity V_i at i^{th} location can be estimated using Eqn (3.6)

$$V_i = \frac{\Delta\phi_i^{\text{exp}}}{B_0 a G_i} \quad \text{Eqn(3.6)}$$

Since the electric potential difference has a parabolic distribution along the applied field direction, average velocity estimated using Eqn(3.6) at different channel height(corresponding to respective i^{th} pair pins) has a similar distribution. So the average velocity in the cross section can be computed using the Eqn(3.7) which is derived from the condition of minimum of the root mean square deviation of the experiment values from the theoretical counterpart.

$$V = \frac{\sum_{k=1}^5 \Delta\phi_k^{\text{exp}} \cdot G_k}{(aB_0 \sum_{k=1}^5 G_k^2)} \quad \text{Eqn(3.7)}$$

Here, the index k corresponds to the 5-pair of pins fixed in the side wall along the magnetic field direction. Using Eqn(3.7), average velocity in the model and hence the corresponding flow rate Q is estimated from Eqn(3.8)

$$Q = VA \quad \text{Eqn(3.8)}$$

Here 'A' is the area of flow cross section and for the present test section it is 12.5 cm^2

In this experiment, the flow appears to be fully developed at location 'E' (see Fig. 3.9) which is situated at least 60 mm away from the bend and lies in the plane perpendicular to the

nearly uniform solenoid magnetic field. The inertia phenomena in the vicinity of such bend are suppressed effectively enough that allows to assume the existence of an MHD flow close to a fully developed one near the cross-section E. [10] The symmetrical distribution of experimentally measured side wall potential difference at that location also confirms the existence of fully developed flow. So the measured data obtained from potential sensors placed at this location is suitable for flow meter calibration. The average velocity at this location is estimated at highest magnetic field 4T for various operated flow rate and calibration factor is calculated from the measured voltage of flow meter.

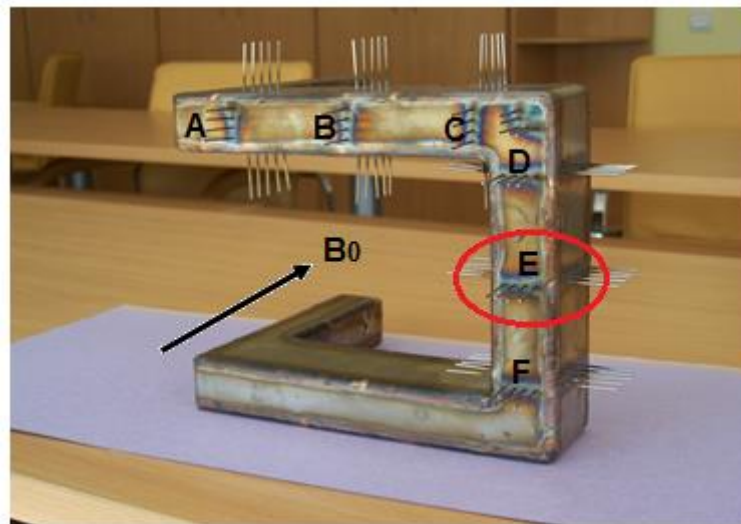


Figure 3.9: Assumed location of fully develop flow in the test section of multiple bends

At location 'E' there are 5 pair of uniformly spaced potential sensors (distance between consecutive pins is 8 mm) arranged back to back in the side walls along the applied magnetic field direction. The potential difference distribution is parabolic and symmetric for various flow rate and applied magnetic field. For illustration, measured side wall potential difference by 5 pair of pins for various flow rate and 4T magnetic field is shown in Fig. 3.10. For each flow rate the corresponding analytical profiles are shown in dotted lines.

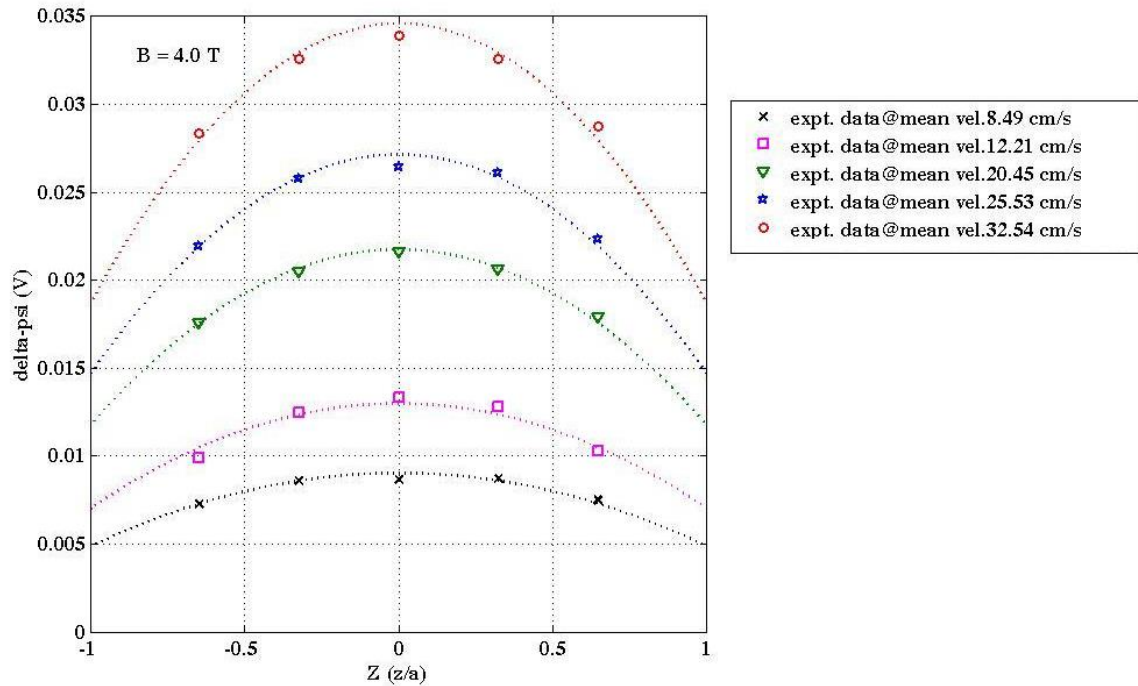


Figure 3.10: Measured side wall potential difference along the applied magnetic field direction for various mean velocity at $B_0 = 4.0$ T.

Average velocity at i^{th} locations are estimated using Eqn (6) from the respective measured voltage of i^{th} pair of pins. Estimated values for various flow rates are summarized in Table 3-1. The average velocity in the cross section is the arithmetic mean of the velocities estimated by 5 pair of pins. Then the actual flow rate in the loop which is used for flow meter calibration is estimated using Eqn(3.8).

Table 3-1: Estimation of mean velocity at location 'E' from the measured potential

AT , B=4T, At E location , Mean velocity V=8.47 cm/s					
i^{th} location	1(z/a= -0.648)	2 (z/a= -0.324)	3 (z/a= 0)	4(z/a= 0.324)	5(z/a= 0.648)
$\Delta\phi_i^{exp}$ [mV]	7.266	8.603	8.664	8.692	7.45
G_i	0.869	1.024	1.076	1.024	0.869
V_i ,[cm/s]	8.461	8.504	8.15	8.592	8.734
AT , B=4T, At E location , Mean velocity V= 12.45cm/s					
i	1(z/a= -0.648)	2 (z/a= -0.324)	3 (z/a= 0)	4(z/a= 0.324)	5(z/a= 0.648)
$\Delta\phi_i^{exp}$ [mV]	10.976	12.662	12.473	12.781	11.064
G_i	0.869	1.024	1.076	1.024	0.869
V_i ,[cm/s]	12.782	20.238	20.337	20.394	20.83
AT , B=4T, At E location , Mean velocity V= 20.42cm/s					
i	1(z/a= -0.648)	2 (z/a= -0.324)	3 (z/a= 0)	4(z/a= 0.324)	5(z/a= 0.648)
$\Delta\phi_i^{exp}$ [mV]	17.542	20.475	21.62	20.633	17.887
G_i	0.869	1.024	1.076	1.024	0.869
V_i ,[cm/s]	20.43	20.238	20.337	20.394	20.83

Once the actual flow rate in the loop is known, calibration factor(S) can be obtained from Eqn (3.9) using the measured voltage signal of the MHD flow meter. Calibration curve generated from the measured flow meter voltage and actual estimated flow rate is presented Fig. 3.11. Mean value of calibration factor(S) obtained from the slope of Fig. 3.11 is $S=28.23 \text{ cm}^3/\text{s.mV}$. This method of standardization of flow meter is an alternative approach for estimation of actual flow rate in high temperature applications.

$$S = \frac{Q}{U} \quad (\text{cm}^3/\text{s.mV}) \quad \text{Eqn(3.9)}$$

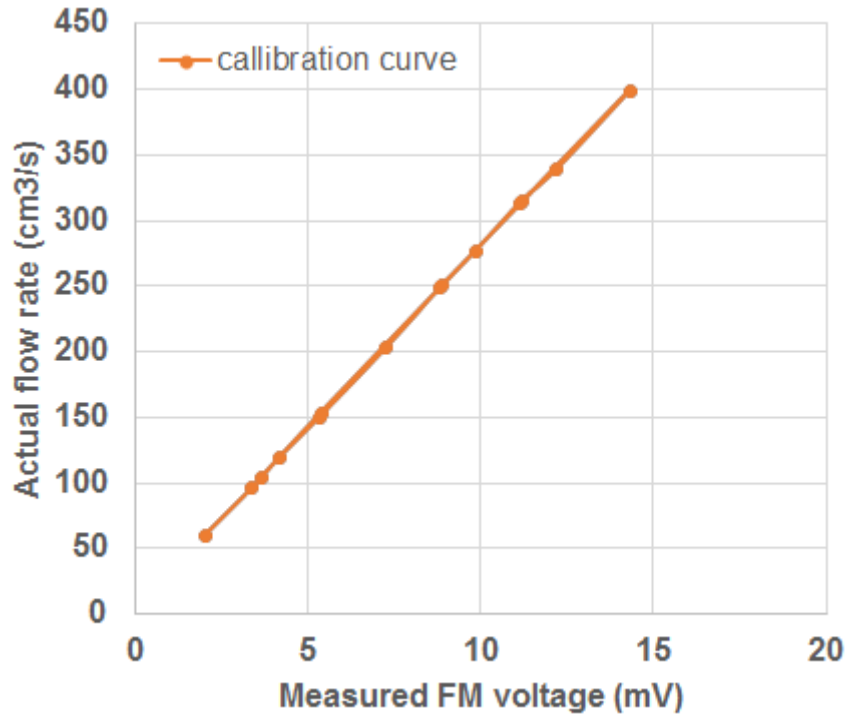


Figure 3.11: Calibration curve of the MHD flow meter

3.4.2 Estimation of Core Velocity from Hartmann Wall Potential Distribution

The velocity in the core is governed by the current density J through generalized Ohm's law given by

$$J = \sigma(-\nabla\phi + u \times B) \quad \text{Eqn (3.10)}$$

Let's suppose that, the core velocity $u = \bar{u} \hat{x}$ and applied external field $B = B_0 \hat{z}$. Here, \bar{u} is the average velocity in channel and B_0 is the uniform applied magnetic field strength. Then from the above equation the axial component of current in y-direction (J_y) follows the relation

$$\frac{J_y}{\sigma} = -\frac{\partial\phi}{\partial y} - \bar{u}B_0 \quad \text{Eqn (3.11)}$$

The magnitude of current density J in the core of fully developed MHD duct flow is proportional to $C+1/Ha$ (C is the relative wall electrical conductance of Hartmann wall defined by $C = \sigma_w t_w / \sigma a$; a is the half the distance between Hartmann walls) and σ is the electrical conductivity of fluid. Since the value of σ is very high, LHS of Eqn(3.11) can be neglected for

most the liquid metal applications in strong magnetic field. Thus by measuring the open circuit voltage in the core region, which is of course not convenient always, the axial component of the core velocity can be estimated from Eqn(3.12)

$$u_c \approx \frac{-\frac{\partial\phi}{\partial y}}{B_0} \quad \text{Eqn(3.12)}$$

At higher magnetic field and electrical conducting walls ($C \gg 1/Ha$) the variation of core current density and electric potential in the direction of applied magnetic field is negligible. Assuming a fully develop flow the core current density (J_y) can be estimated from the Eqn (3.13) which is derived from the conservation of current in the core and Hartmann wall.,

$$J_y = -\frac{C}{1+C} \sigma \bar{u} B_0 \quad \text{Eqn(3.13)}$$

Plugging Eqn(3.13) in Eqn (3.11), the average velocity becomes

$$\bar{U} = -\left(\frac{1+C}{B_0}\right) \left(\frac{\partial\phi}{\partial y}\right)_{\text{core}} \quad \text{Eqn(3.14)}$$

As the core potential does not vary along the magnetic field direction, neglecting the potential drop in thin Hartmann layer ($O \sim 1/Ha^2$) and across the thickness of the Hartman wall ($O \sim (t_w/a)^2$), the potential distribution in the Hartmann wall is a good measure of the core potential and serve as a stream function for the core velocity. So assuming the gradient of potential in the core and in the Hartmann wall is same, core velocity can be estimated from measured Hartmann wall potential gradient from Eqn(3.15)

$$\left(\frac{\partial\phi}{\partial y}\right)_{\text{core}} = \left(\frac{\partial\phi}{\partial y}\right)_{\text{Hartmann wall}}$$

$$U_c = -\left(\frac{1+C}{B_0}\right) \left(\frac{\partial\phi}{\partial y}\right)_{\text{Hartmannwall}} \quad \text{Eqn(3.15)}$$

In this experiment there are 4 uniformly spaced potential sensors are arranged in a row perpendicular to the solenoid magnetic field on the Hartmann wall. The gradient of potential has is obtained by a linear least square fit of the measured Hartmann wall potentials for these

4 sensors. The estimated core velocity using Eqn(3.12) (neglecting J) & Eqn(3.14) (considering J) for different applied magnetic field is compared with theoretical predictions based on analytical model and summarized in Table 3-2. The distribution of measured Hartmann wall potential at location ‘E’ and 4T magnetic field is shown in Fig. 3.12

Table 3-2: Estimation of core velocity from measured Hartmann wall potential at location ‘E’

U(cm/s)	EH1 (mV) y/a=- 0.3024	EH2 (mV) y/a=- 0.1008	EH3 (mV) y/a=0.100 8	EH4 (mV) y/a=0.302 4	Slope $\frac{\partial\phi}{\partial y}$	Core Velocity Uc (cm/s), considering J	Core Velocity Uc (cm/s), Neglecting J	Uc (cm/s) Theoretic al
For B₀=4.0 T								
12.51	1.945	0.977	-0.833	-1.975	-0.2725	8.5	6.81	8.37
20.45	3.652	1.049	-1.426	-3.328	-0.4702	14.52	11.75	13.68
25.53	4.583	1.366	-1.824	-3.928	-0.5768	17.87	14.42	17.08
32.54	5.959	1.881	-1.964	-5.048	-0.7404	22.91	18.51	21.77
For B₀=3.0 T								
13.21	1.761	0.706	-0.729	-1.383	-0.2182	9.06	7.27	8.91
20.32	2.753	0.791	-0.994	-2.382	-0.3452	14.26	11.51	13.7
25.71	3.608	1.087	-1.219	-3.105	-0.4507	18.5	15.02	17.33
31.96	4.468	1.331	-1.645	-3.979	-0.5687	23.28	18.96	21.55
38.23	5.409	1.647	-1.849	-4.714	-0.6801	27.84	22.67	25.77
For B₀=2.0 T								
12.31	1.177	0.379	-0.378	-0.920	-0.1415	8.74	7.07	8.41
20.38	1.888	0.625	-0.718	-1.687	-0.2424	14.88	12.12	13.92
32.22	3.096	0.83	-1.167	-2.813	-0.3961	24.16	19.8	22.01
46.11	4.457	1.281	-1.731	-4.013	-0.5708	34.78	28.54	31.5
57.98	5.755	1.79	-2.009	-4.965	-0.7221	43.95	36.1	39.61
64.82	6.483	1.955	-2.272	-5.635	-0.815	49.52	40.75	44.28
For B₀=1.0 T								
13.81	0.686	0.309	-0.283	-0.585	-0.08826	10.69	8.83	9.71
*18.21	0.792	0.476	0.362	0.182	-0.03904	6.37	3.9	12.8
31.77	1.579	0.392	-0.77	-1.621	-0.2161	25.91	21.60	22.33
45.08	2.181	0.439	-1.251	-2.473	-0.3143	37.53	31.43	31.68
57.3	2.774	0.528	-1.584	-3.124	-0.3977	47.52	39.77	40.27
84.43	4.028	0.703	-2.518	-4.832	-0.5985	71.27	59.85	59.33

* The measure potential data corresponding to mean velocity 18.21 cm/s appears to be malfunctioned

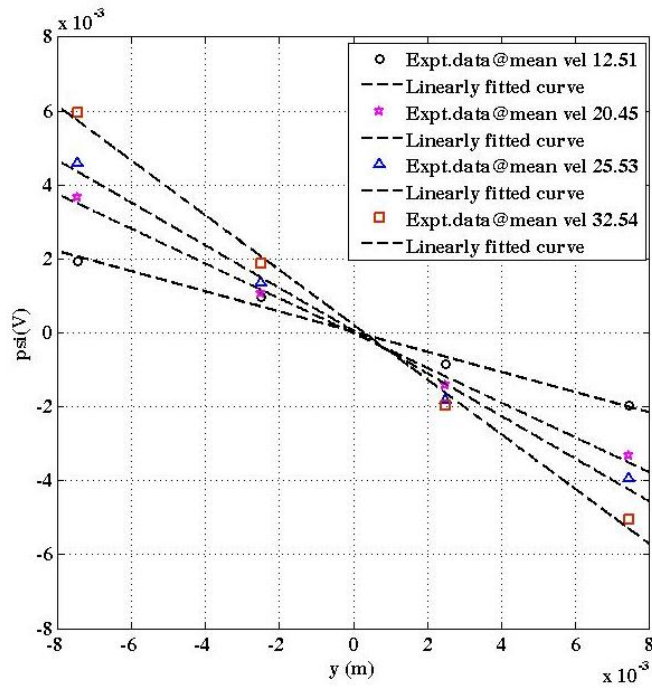


Fig. 3.12(a)

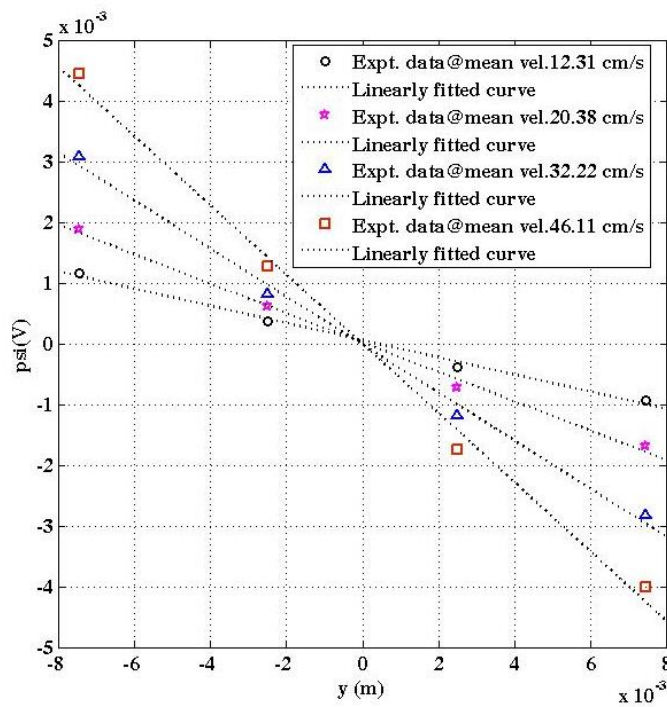


Fig. 3.12(b)

Figure 3.12: Measured Hartmann wall potential distribution at location ‘E’ for various flow rates; for applied magnetic field of 4T in Fig. 3.12(a) and for applied magnetic field of 2T in Fig. 3.12(b)

3.5 Pressure drop

3.5.1 Pressure drop in bend where flow turns from parallel to perpendicular direction

The pressure difference between pressure transmitter B1 in the horizontal duct (axis of the duct parallel to the magnetic field) and B3 in the vertical branch (flow axis normal to the applied magnetic field) measures the mhd pressure drop in right angle bend where the flow turns from a direction parallel to perpendicular direction of the applied magnetic field (see Fig. 3.6). The flow experiences sudden expansion at this bend as the cross section changes from 25 mm x 25 mm in the square duct to 25 mm x 50 mm in the test section. The variation of measured pressure drop with flow rate for different magnetic field is shown in Fig. 3.13. It is observed that the pressure drop increases linearly with the flow rate for each magnetic field (1T, 2T, 4T) and the rate of increase is more with increasing strength of the field. The pressure measurement data at 3T magnetic field appears to be erroneous. So the analysis for pressure measurement data at 3.0 T is not presented.

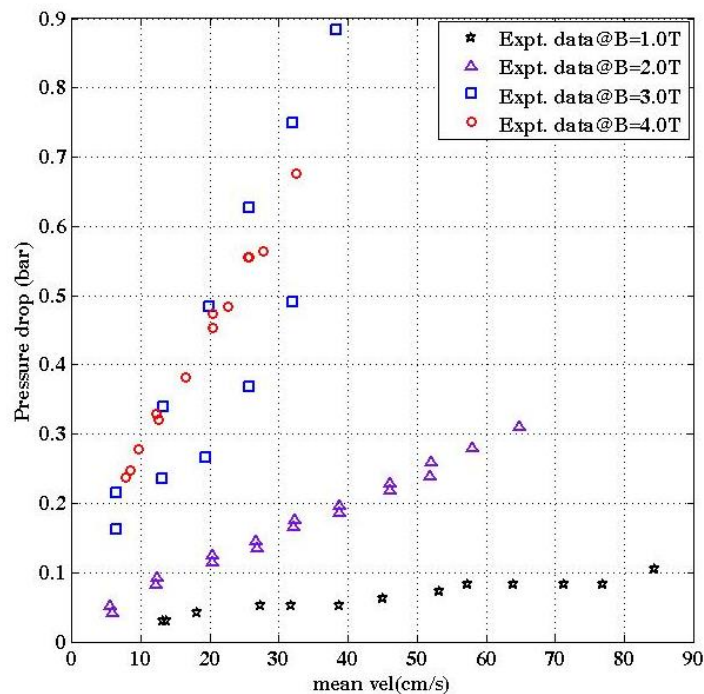


Figure 3.13: Measured pressure drop verses flow rate in the bend of parallel to perpendicular flow at different magnetic field strength

The excess pressure drop due to 3-D effects [11] over the fully developed MHD pressure drop at this bend is estimated from Eqn (3.16) and normalized with pressure scaling factor.

$$\Delta P^{3-D} = \frac{\Delta P - \Delta P_{FD}}{\sigma a U_0 B_0^2} \quad \text{Eqn (3.16)}$$

Where,

$$\Delta P_{FD} = \frac{\sigma U_0 B_0^2 L}{\frac{C+1}{C+Ha^{-1}} + \frac{\varepsilon \sqrt{Ha}}{3(1+C\sqrt{Ha})}} \quad \text{Eqn(3.17)}$$

Here σ , U_0 , B_0 , a , ε , are the electrical conductivity of fluid, mean velocity in the larger duct, applied magnetic field, and characteristic length scale (half the distance between Hartman walls), aspect ratio and L is the flow length. ΔP is the measured pressure drop in the bend and ΔP_{FD} corresponds to the MHD pressure drop assuming the flow to be fully developed in a straight channel of length L (corresponds to flow length transverse to the magnetic field ~ 100 mm after the bend up to pressure Port B3 in the present test section) and is computed using Eqn (3.17) for a straight conducting channel of arbitrary wall conductance ratio. [12]

The additional pressure drop, ΔP_1^{3-D} , as defined in the Eqn (16) is found to be linearly increasing with N for a given Hartmann number (see Fig. 3.14). The increase in the pressure loss with N can be partly attributed to 3D effects associated with the sudden expansion coupled with parallel to perpendicular flow turning and partly to the physics of residual turbulence in the upstream (square duct) where the field is parallel to the magnetic field. Further, the rate of increase is less with increasing the strength of Hartmann number (Ha) which indicate the strength of 3-D axial current due to bend effects is less at higher Ha .

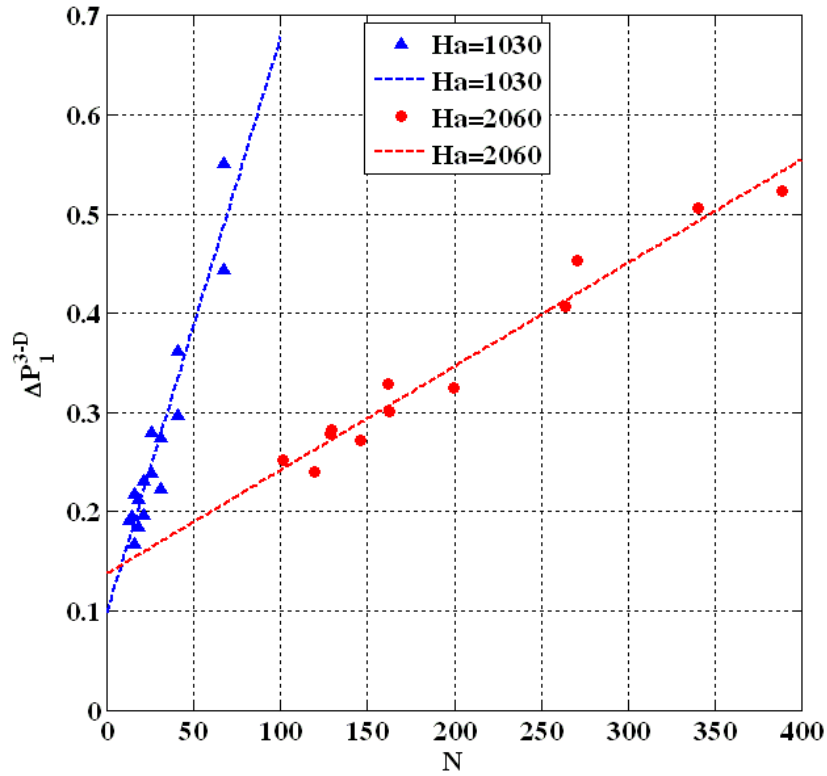


Figure 3.14: ΔP_I^{3-D} as a function of interaction parameter (N) for different Hartmann number (Ha) at the bend where the flow is turning from parallel to perpendicular direction of the applied field with sudden expansion

3.5.2 Pressure drop in bend where flow turns from perpendicular to parallel direction of the applied magnetic field

When the direction of flow is reversed the flow turns from perpendicular to parallel direction of the applied magnetic field with a sudden contraction. The pressure drop between B3 and B1 pressure Transmitter shows a linear variation with flow rate for each magnetic field but the value of the pressure drop is lesser as compared to the parallel to perpendicular direction of the flow configuration (see Fig. 3.15). The variation of non-dimensional pressure drop (normalized by dimensional quantity $\sigma\mu LB_0^2$) as presented in Eqn (3.18) shows the linear variation with $N^{-0.3644}$ for most of the data point (see Fig. 3.16).

$$\Delta P^* = 0.0429 + 0.3021 N^{-0.3644} \quad \text{Eqn(3.18)}$$

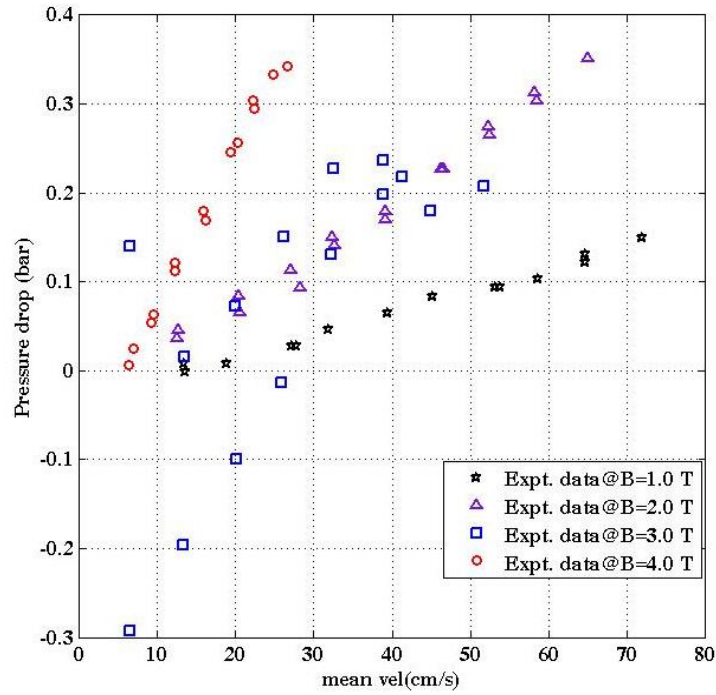


Figure 3.15: Measured pressure drop versus flow rate for different magnetic field at the bend where flow turns from perpendicular to parallel direction of the applied magnetic field

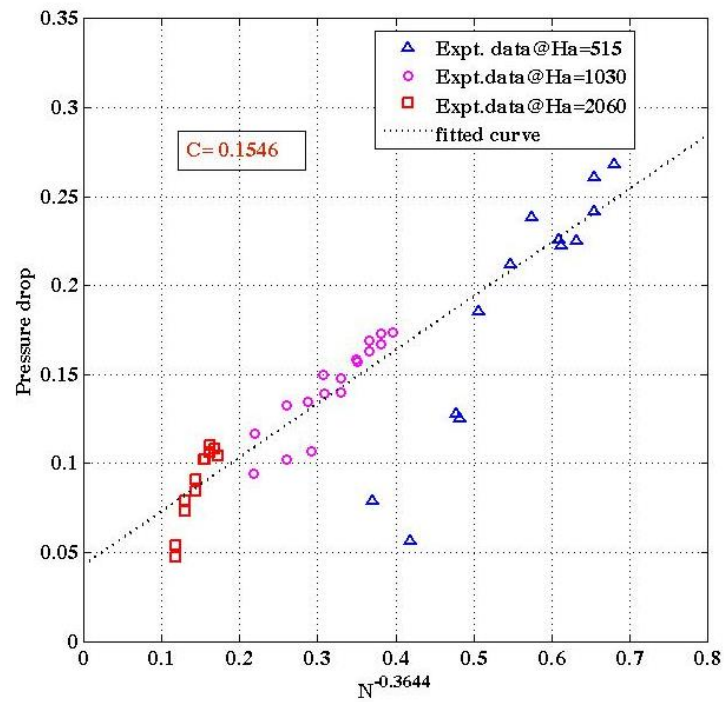


Figure 3.16: Non dimensional pressure drop as a function of N at the bend where flow turns from perpendicular to parallel direction of the applied magnetic field.

In contrast to the previous case (flow turning from parallel to perpendicular), the dimensionless pressure drop decreases with N for a given Ha . This is in agreement with $N^{-1/3}$ variation of pressure drop due to interaction of the flow with internal layer of thickness $\sim N^{-1/3}$. A similar relationship for pressure drop with N and Ha is reported by Stieglitz et al. [10] that shows pressure drop varies with $N^{-0.337}$. Since the present test section has a higher wall conductance ratio ($C = \sim 0.15$) the slope is higher as compared to the slope predicted by Stieglitz for a C value of 0.052. However, some of the experimental data points are deviating significantly from $-1/3$ power law at lower flow rates. The analysis indicates physics of energy dissipation mechanism when the flow turns from parallel to perpendicular is different from the case when flow turns perpendicular to parallel direction of the magnetic field.

3.5.3 Pressure drop at the bend where flow is normal to the magnetic field in both the legs

The pressure difference between pressure port B3 and B4 measures the mhd pressure drop in a bend where the flow is perpendicular to the applied magnetic field in both the legs. The measured pressure drop versus flow rate is shown in Fig. 3.17. The dimensionless pressure drop ΔP_2^{3-D} due to 3-D effects at this bend is defined similar to Eqn(16). In contrast to 3-D loss when the flow turns from parallel to perpendicular direction, ΔP_2^{3-D} is negative, i.e the fully develop pressure drop is more than the observed pressure drop. Also ΔP_2^{3-D} is decreasing with increasing interaction parameter (N) for a given Hartmann number (see Fig. 3.18) and the rate of decrease is more at a lower Ha . Since the cross section in both the arms of the bend are same ($0.025 \times 0.05 \text{ m}^2$), the decrease in 3-D pressure loss may be attributed to the suppression turbulence at higher N . [13] It is anticipated that at lower Ha , the flow may exhibit transitional features from 3D turbulence to Q2D turbulence state with increasing N . So the pressure fall is relatively more than the case with higher Ha where the turbulence may exist in pure Q2D or laminar flow.

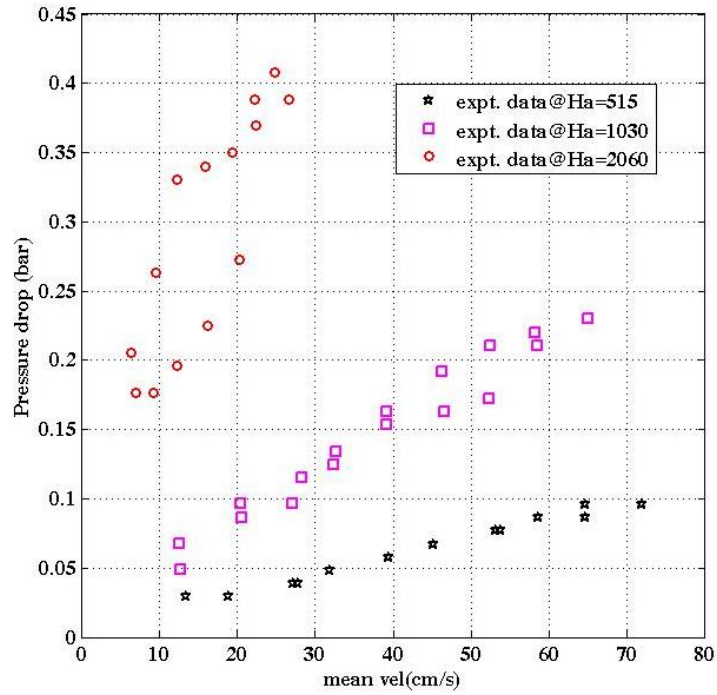


Figure 3.17: Measured pressure drop variation with flow rate at the bend where flow is normal to the applied magnetic field in both legs.

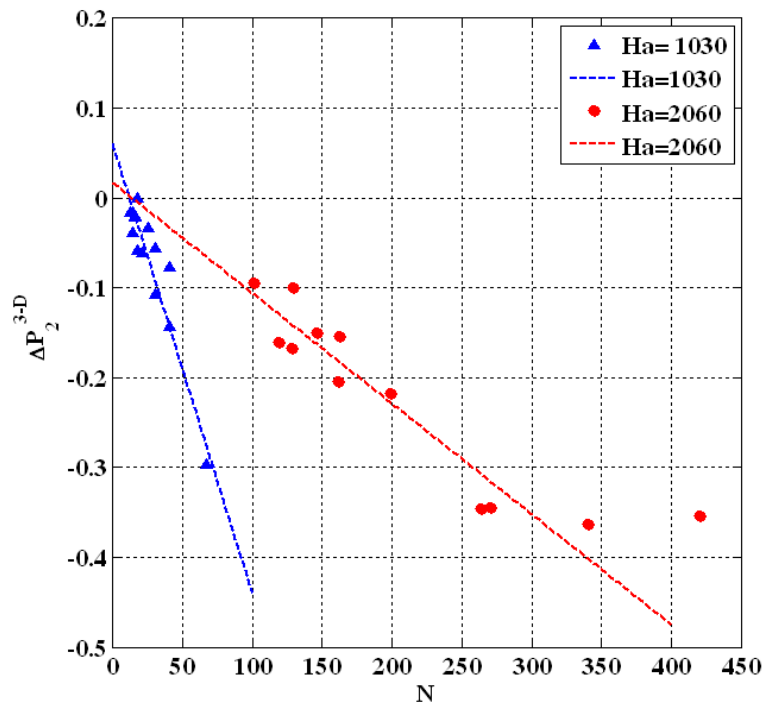


Figure 3.18: ΔP_2^{3-D} as a function of interaction parameter (N) for different Hartmann number (Ha) at the bend where the flow is normal to the applied magnetic field in both the legs of bend

3.6 Brief summary of experimental data analysis in the test section of multiple bends

Analysis is carried out based on the measurement of wall potential and pressure data at different location of the test section with multiple bends. The main outcome of the analysis is summarized as follows;

1. The symmetrical distribution of side wall potential difference at location 'E' of test section and fair agreement with analytical model predictions confirms that the flow is fully developed at this location. The average velocity and actual flow rate in the loop is estimated from on the side wall potential data and analytical model. Based on this the calibration coefficient (S) of flow meter is established.
2. The core velocity is estimated from the measured Hartmann wall potential data by taking into account the induced transverse current from the conservation of current in a fully develop plane. The estimated values are matching reasonably well with the analytical model prediction.
3. Non dimensional 3D pressure drop at the bend where flow turns from parallel to perpendicular direction of the applied magnetic field is increasing with interaction parameter (N). The trend is observed to be opposite for the bend where flow is transverse in both the legs of the bend.
4. When the flow turns from perpendicular to parallel direction of the applied magnetic field, the non-dimensional pressure drop varies with $N^{-1/3}$ for most of the data point which is in line with the earlier experimental observation available in literature.

3.7 3D numerical study of MHD flow in test section of multiple bends

Numerical simulation in the experiment test section is performed using MHD module of CFD code FLUENT based on electric potential formulation (induction less approximation) [14] and laminar model approximation. Steady state results are obtained for two set of Hartmann number (Ha) with different interaction parameter (N) as presented in Table 3-3. The governing equations and boundary conditions are same as described in previous chapter for benchmarking with Hunt's analytical solution. Numerical results of electric potential distribution are compared with the experiment data to assess the applicability of numerical model and code capability for MHD flow simulation at high magnetic fields. Velocity profile and electric current path at different bends is presented.

Table 3-3: Non Dimensional parameters for the Numerical simulation

B_0 (T)	U_{av} (m/s)	Ha	N	Re	Ha/Re
2	0.123	1030	67	16087	0.064
2	0.204	1030	40	26612	0.039
2	0.322	1030	25	42073	0.024
4	0.122	2060	270	15944	0.129
4	0.204	2060	161	26704	0.077
4	0.255	2060	129	33337	0.062

3.7.1 Model Geometry and Mesh

In view of symmetry in the test-section and to reduce computation, numerical simulation is carried out up to 3rd 90° channel bend of experimental test-section and flow is assumed fully developed at the exit (Fig. 3.19). The domain of the computation is limited to $0 \leq x \leq 0.149$ m, $0 \leq y \leq 0.2$ m and $0 \leq z \leq 0.16$ along with uniform magnetic field B in the **z** direction (see Fig. 3.19). Similar to the experiment flow configuration, PbLi enters into the model geometry through inlet square duct (25mm × 25mm) in a direction parallel to applied

magnetic field B_0 and then enters in the vertical rectangular duct having cross section of 25mm \times 50mm where the flow was perpendicular to B_0 . At the other bend, the flow is in the plane transverse to the applied field in both the legs having same cross section of 25 mm \times 50 mm. The walls of the channel are of 3 mm thick SS316 plates having electrical conductivity of 1.01×10^6 S/m which corresponds to wall conductance ratio ($C = \sigma_w t_w / \sigma a$) of 0.156. Here characteristic length ' a ' is half the distance between Hartmann walls. The properties of the Pb-Li are taken as 9402 kg/m^3 , $7.7616 \times 10^5 \text{ S/m}$, $0.0018 \text{ Pa}\cdot\text{s}$, for density, electrical conductivity and dynamic viscosity respectively [15].

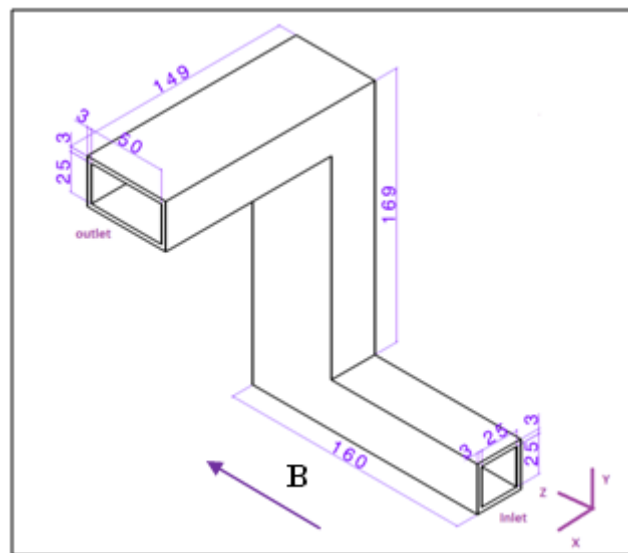


Figure 3.19: Computation geometry for simulation of multiple bend test section

A variable structured mesh ensuring adequate number of grid points in the Hartmann boundary layer (dimensionless thickness $O(\text{Ha}^{-1})$) and side boundary layer (dimensionless thickness $O(\text{Ha}^{-1/2})$) is used for computation. [16] There are 40×50 nodes in a flow cross section and total of 645541 nodes in the entire geometry having minimum spacing in Hartmann layer and side layer is $8.0 \times 10^{-6} \text{ m}$ and $2.0 \times 10^{-5} \text{ m}$ respectively. The maximum grid spacing in

the core region is 3.033×10^{-3} m. Different views of the geometry with mesh are shown in Fig.

3.20

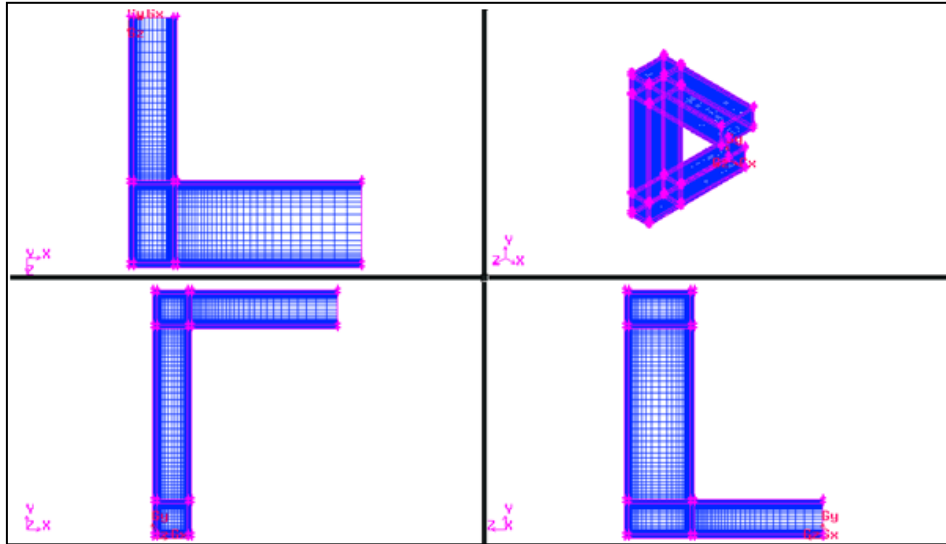


Figure 3.20: Grid structure in computation geometry for test section of multiple bends

3.8 Comparison of numerical simulation results with experiment

Experimental results for three different flow velocities and magnetic field 2.0 T and 4.0 T are compared with the respective CFD values. The convergence criterion for dependent variables (velocity components, electric potential) is based on the absolute value of residuals. The residuals for continuity, x, y and z component of velocities and electric potential have reached less than 5.0×10^{-6} , 1.0×10^{-6} , 1.0×10^{-6} , 2.0×10^{-7} and 5.0×10^{-7} respectively further which there was no reduction in residuals.

3.8.1 Side wall electric potential distribution

The numerically obtained potential difference ($\Delta\phi$) between the side walls along the direction of the applied field (along z) at different cross sections are compared with the experimentally measured values. At the location A, which is situated ~ 10 mm away from the junction ($y=0.041$ m), the measured values are matching well with the numerical results for low

flow rates and higher magnetic fields (mean velocity $U_{av} = 0.122$ m/s and $B_0 = 4.0$ T which corresponds to $N = 270$) (see Fig. 3. 21). As can be seen, with the increase of flow rate, the deviation from the numerical value is also increasing. This may be due to the presence of residual turbulence in the flow near the bends at higher Reynolds number. Although the ratio of Ha/Re in this experiment is in the laminar flow regime, (Ha/Re varies from 0.024 to 0.129 $> 1/300$) there may be 2D turbulence due to bend effects which is not accounted in the numerical simulation [17].

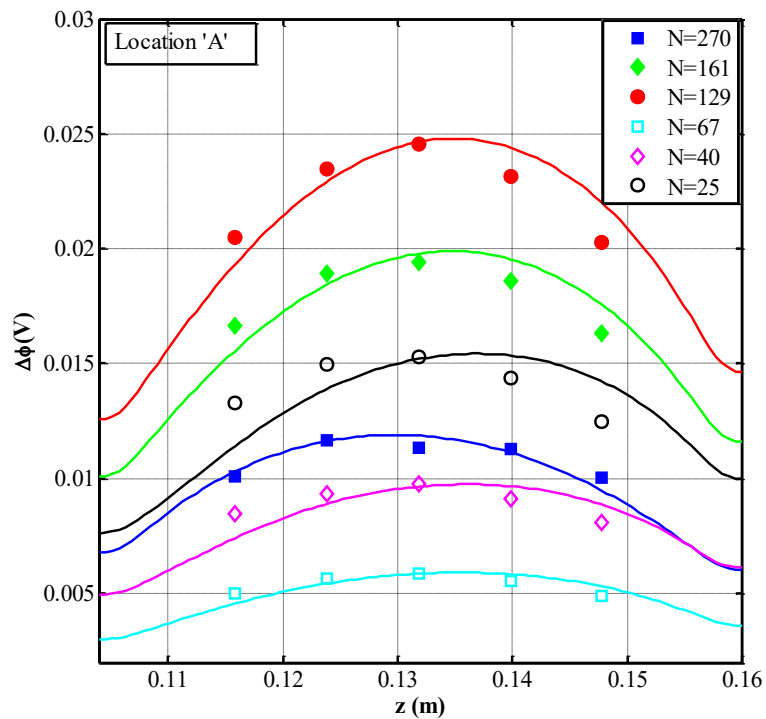


Figure 3.21: Comparison of measured side wall potential difference with numerical profile (continuous line) at location ‘A’ for different N

At the location C, which is situated 74 mm away from the junction ($y=0.105$ m), the measured potential difference is matching well with the numerical results for all the flow rates and magnetic fields (see Fig. 3.22). This indicates that laminarization of the flow after bend due to stronger MHD forces. In the Fig. 3.23, results at location D, which is ~ 11 mm away from the bend ($x = 0.042$ m), is presented. As can be seen the deviation is less as compared to

the results at the location A. This indicates that smaller length is required for laminarization of the flow after the bend when the magnetic field is perpendicular to both the legs of the bend.

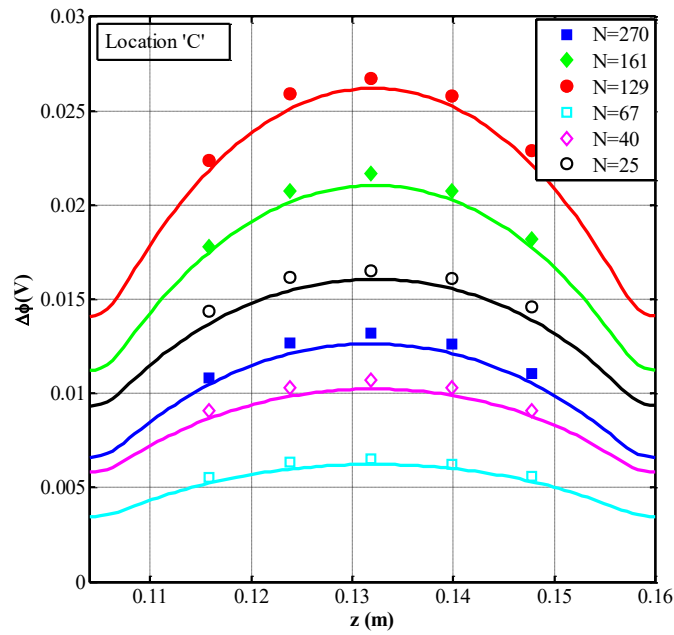


Figure 3.22: Comparison of measured side wall potential difference with numerical profile (continuous line) at location 'C' for different N

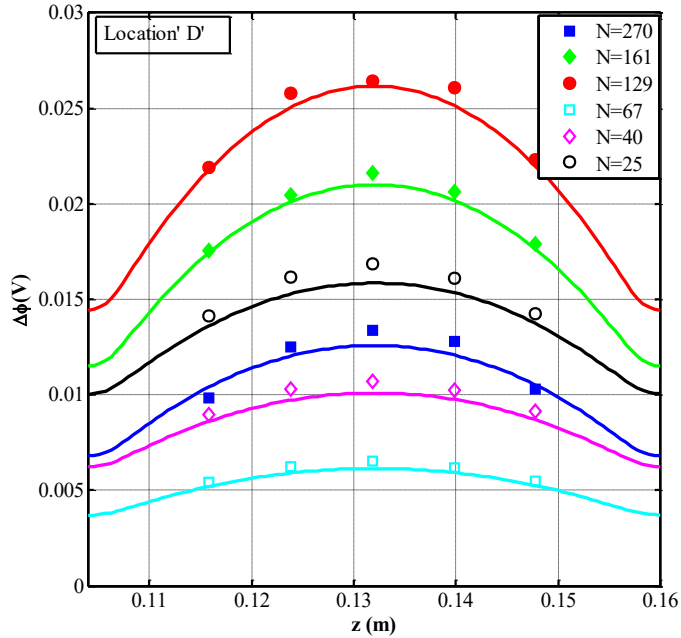


Figure 3.23: Comparison of measured side wall potential difference with numerical profile (continuous line) at location 'D' for different N

At the location E which is situated 65 mm away from the junction ($x=0.097$ m), the measured values are matching well with the numerical results for all the flow rates and the applied fields and is shown in Fig. 3.24. The filled symbols in Fig. 3.21 to Fig. 3.24 correspond to the experiment data for magnetic field of 4T.

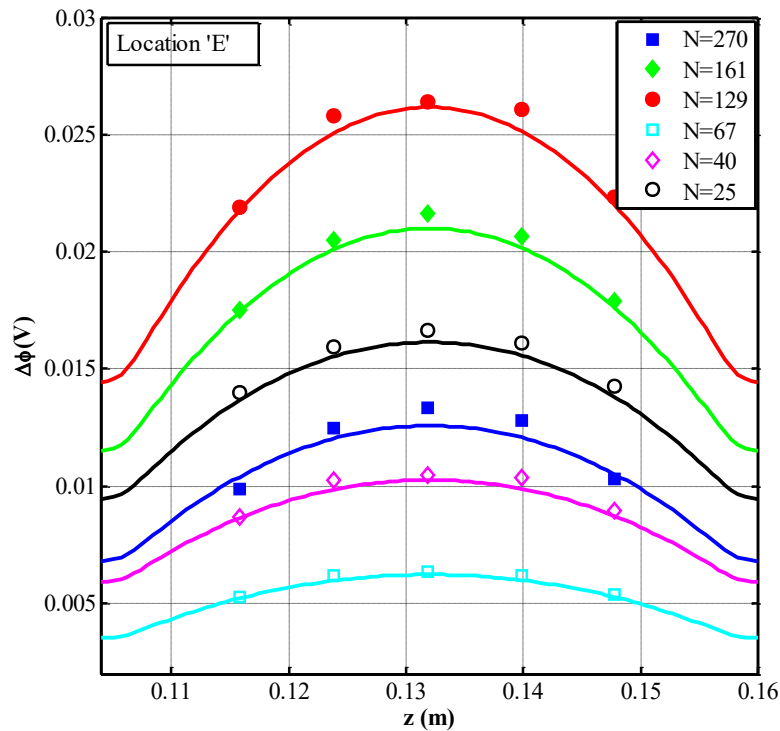


Figure 3.24: Comparison of measured side wall potential difference with numerical profile (continuous line) at location ‘E’ for different N

3.8.2 Hartmann wall potential distribution

The potential distribution on the Hartmann wall is compared with measured values. The reference potential for calculation of difference is the value at $x=7.85$ mm on the Hartmann wall. At the location ‘A’ for high flow rates, there is significant deviation between the numerical and the experimental values (see Fig. 3.25). But at low flow rates, with higher Ha/Re ratio ($Ha/Re > 0.06$), the numerical results are agreeing well with the corresponding experimental values.

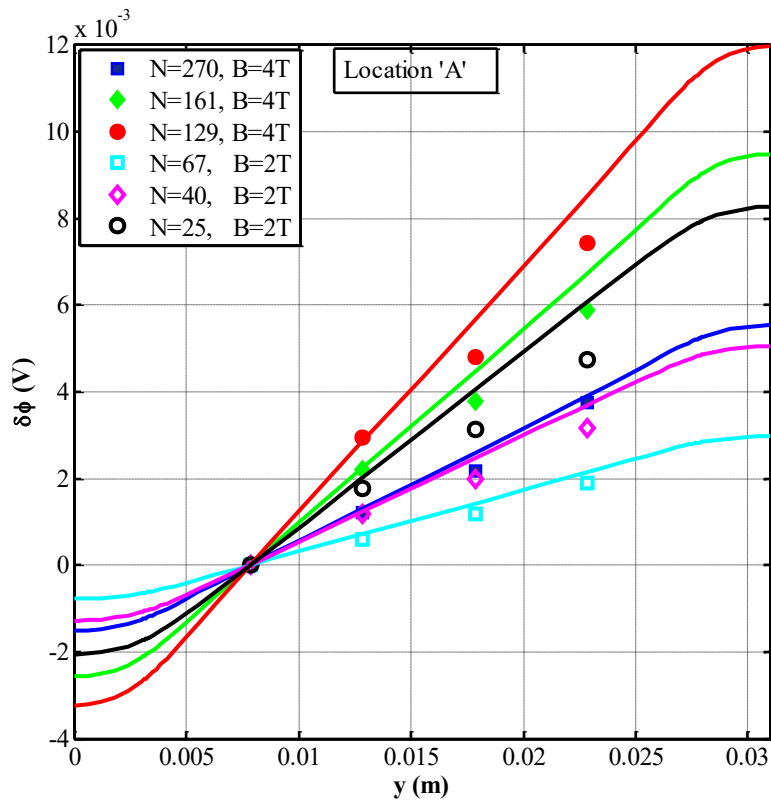


Figure 3.25: Comparison of measured Hartmann wall potential distribution with numerical results (continuous line) at Location ‘A’ for different N

At the location ‘C’ the matching is good for all the cases (see Fig. 3.26). This may be again attributed to the laminarization of the flow. At the location ‘D’ the results are similar to the location ‘A’ but the deviation is less (Fig. 3.27). It may be concluded that even in the case of sharp 90° bends, laminar flow approximation is valid at higher magnetic field and low flow rates. At the location E, where the flow becomes symmetric at higher interaction parameter $N > 67$ ($U_{av} = 0.123\text{m/s}$ and $B = 2.0\text{ T}$), experimental results are matching well with the numerical estimations (Fig. 3.28).

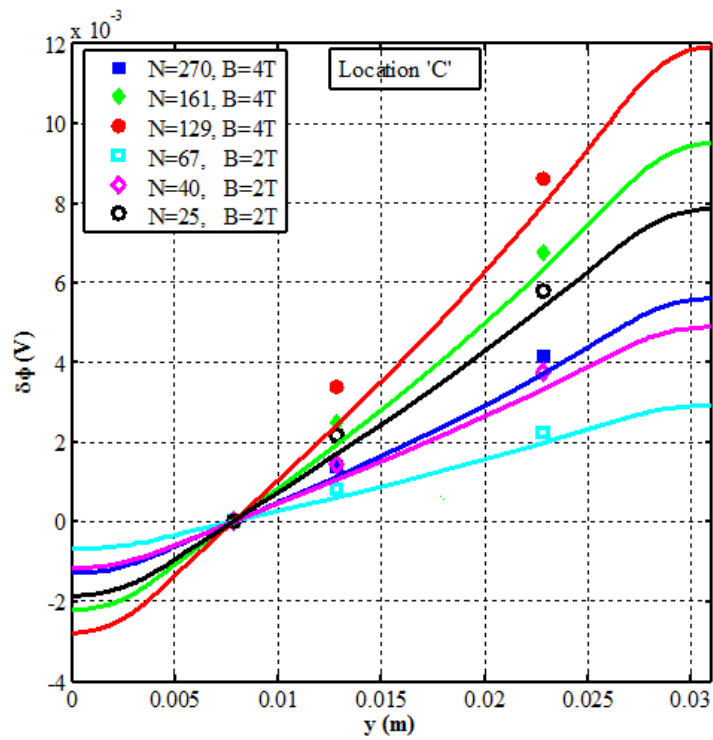


Figure 3.26: Comparison of measured Hartmann wall potential distribution with numerical results (continuous line) at Location ‘C’ for different N

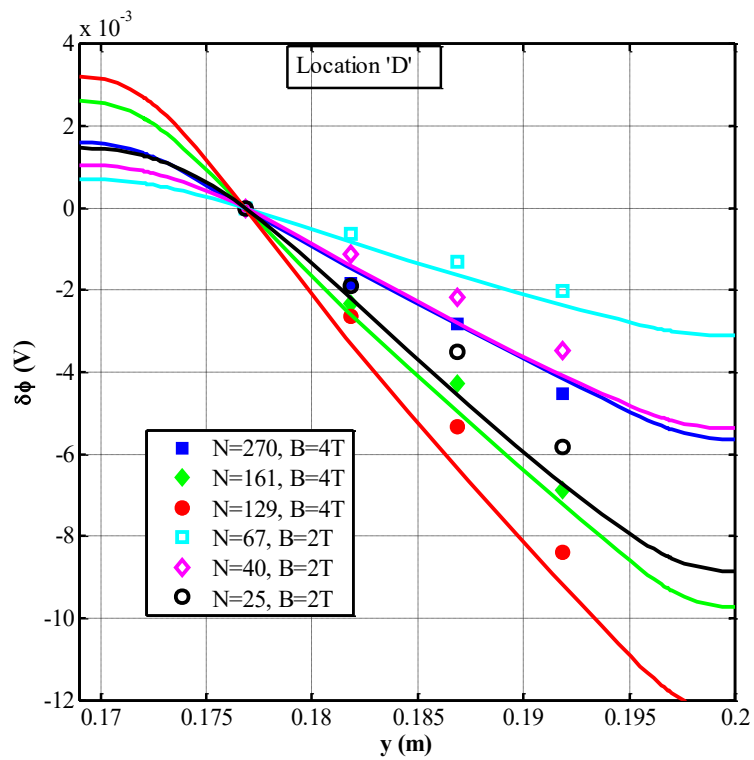


Figure 3.27: Comparison of measured Hartmann wall potential distribution with numerical results (continuous line) at Location ‘D’ for different N

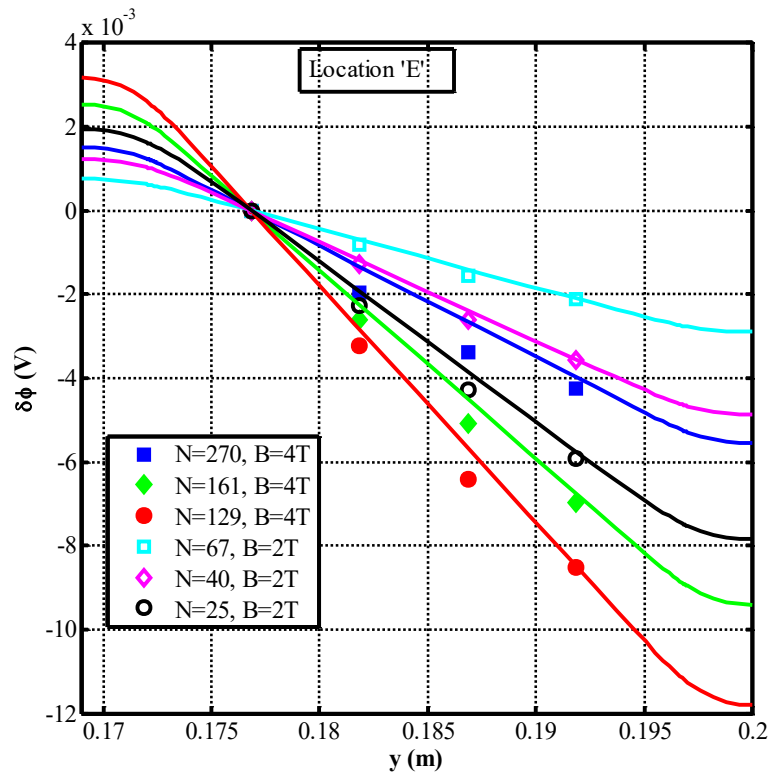


Figure 3.28: Comparison of measured Hartmann wall potential distribution with numerical results (continuous line) at Location ‘E’ for different N

3.9 Flow distribution in the bends based on numerical simulation

3.9.1 Velocity distribution in the inlet duct ($0 \leq x \leq 0.031m$, $0 \leq y \leq 0.031m$ and $0 \leq z \leq 0.104$)

As the flow is parallel to the applied field in this duct (see Fig. 3.19), opposing electromagnetic force flow is absent. Still the flow can be assumed laminar due to the suppression of the turbulence by strong magnetic field [18]. As the walls are electrically connected to the walls of vertical duct, where the flow induces electrical currents due to interaction of the transverse magnetic field, there exist potential difference between the walls of the inlet square duct and vertical rectangular duct. These potential differences drive current which are closed through the fluid leading to MHD forces which modify the flow distribution. The velocity profile and current vector for Hartmann number of 2060 and mean velocity of 0.122 m/s in the plane perpendicular to B_0 at $z = 0.08$ m is shown in Fig. 3.29 & Fig. 3.30.

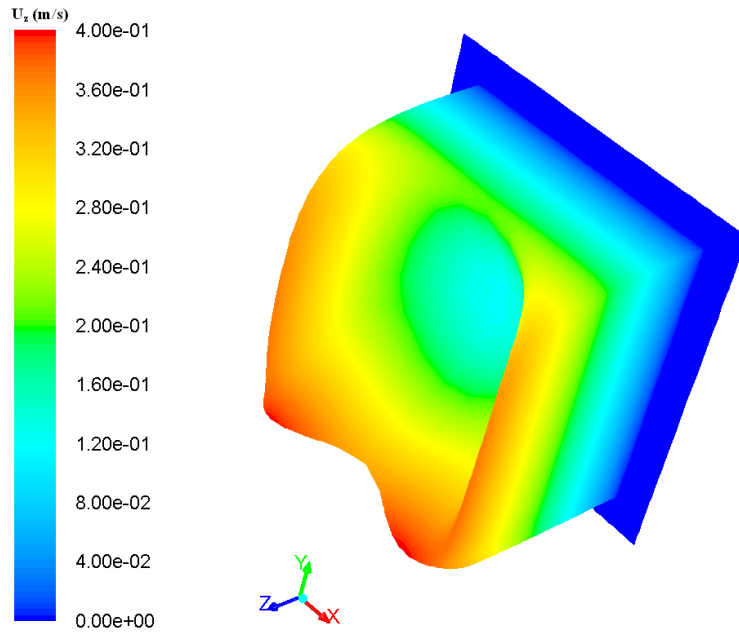


Figure 3.29: Velocity profile in the square duct with flow axis parallel to the magnetic field at $z = 0.08$ m for $Ha = 2060$ and mean velocity 0.244 m/s

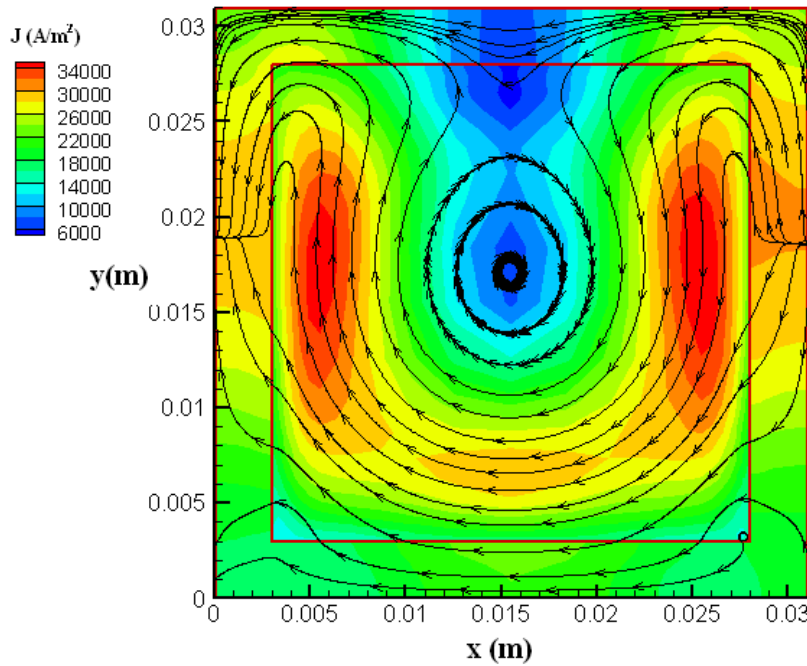


Figure 3.30: Current density vector at $z = 0.08$ m for $Ha=2060$ and mean velocity 0.1221 m/s

Near the walls of square duct which are connected to the side walls of the vertical duct there is a velocity peaking at higher Hartmann number ($Ha > 200$). The peaking of velocity near the walls is due to interaction of J_y current with applied magnetic field leads to MHD force that

pushes the core fluid towards the walls. The velocity distribution is symmetric about the y-z plane passing through the centre of the duct because of the symmetrical distribution of current (see Fig. 3.30). However, the velocity profile is asymmetric about the x-z plane (passing through the centre of the duct). This is due to the inertial effect caused by sharp bending at $z = 0.104$ m and the variation of the axial current (J_z) component in y-z plane. The asymmetry in the velocity distribution has been observed even in the absence of the applied magnetic field and is decreasing with increasing of Hartmann number.

3.9.2 *Velocity distribution in the vertical duct ($0 \leq x \leq 0.031$ m, 0.028 m $\leq y \leq 0.169$ m and 0.104 m $\leq z \leq 0.16$)*

In the vertical duct, the flow is transverse to the applied magnetic field and the induced current is 3-D due to the prolong bend effects and developing flow. The induced current loop in the vertical duct loses its symmetry at the bend ($y = 0.028$ m) and the transverse current component J_x becomes opposite in the region $y < 0.012$ m. This leads to a MHD pumping action at the bottom of the vertical duct. The larger portion of the fluid flows in the side wall boundary layer. Near the bends, the asymmetry in axial velocity component $U_y(x,z)$ (Fig. 3.31) along \mathbf{z} increases at lower interaction number ($N=25$, $U_{av} = 0.322$ m/s). This is due to the stronger inertial effects and variation in axial current component J_y (Fig. 3.32). However, the flow distribution is relatively symmetrical along the \mathbf{x} (see Fig. 3.33). This is due to the action of the transverse magnetic field as soon as it enters into the vertical duct. As the flow advances, $U_y(x,z)$ becomes gradually symmetric along \mathbf{z} (Fig. 3.34). Also, at the exit of vertical duct, the peak velocity at the inner side wall jet is increasing with increasing interaction parameter before taking a 90° turn (see Fig. 3.35). However, it appears that the length of the vertical duct was

not adequate for the flow to be fully developed even at the maximum value of Interaction parameter ($N=270$, $B=4.0$ T mean velocity 0.122 m/s).

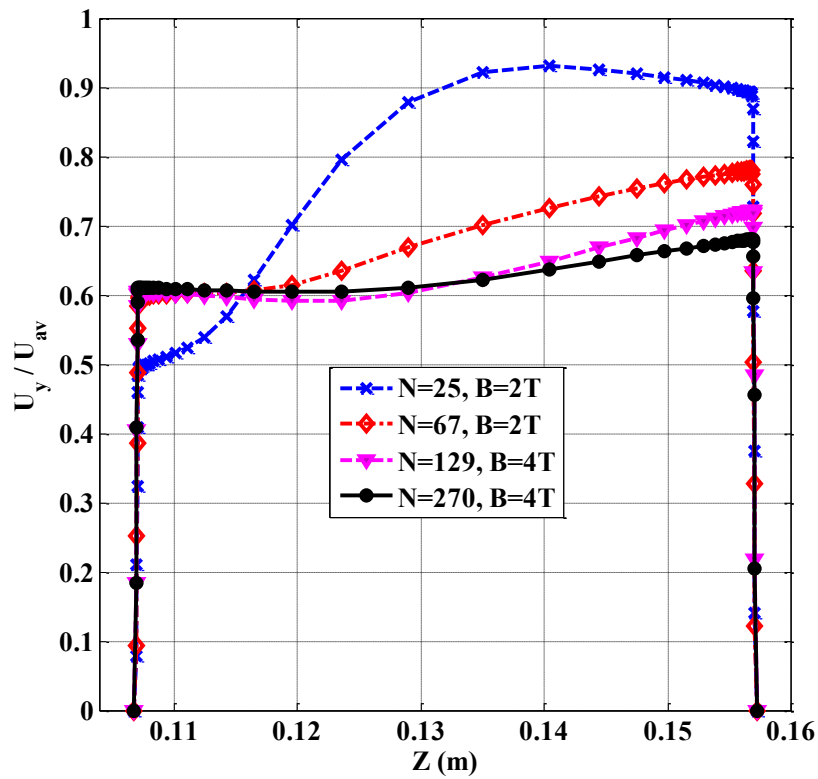


Figure 3.31: Normalized U_y velocity profile across the center of Hartmann walls (along z) at $y=0.039$ m for various N

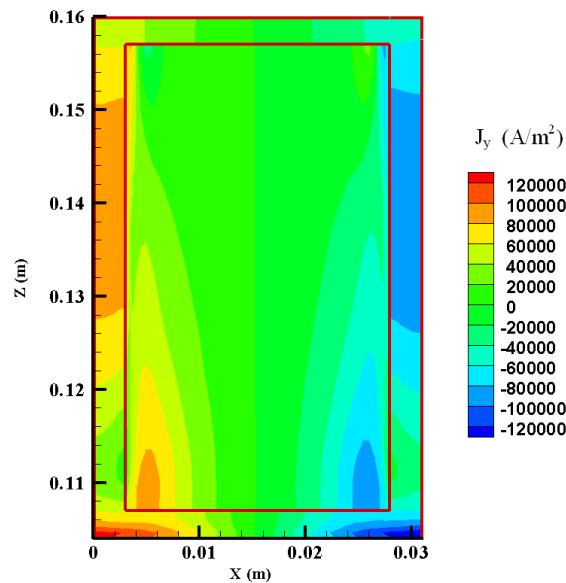


Figure 3.32: Contours of axial current component (J_y) in a plane at $y = 0.032$ m for $Ha=2060$ and mean velocity (U_{av}) of 0.322 m/s

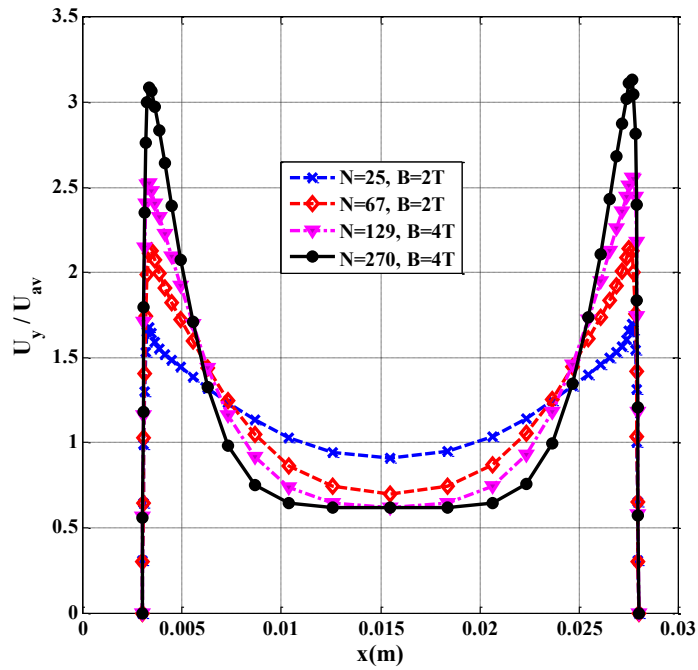


Figure 3.33: Normalized U_y velocity profile across the side walls (along x , centre of the duct) at $y=0.039$ m for various N

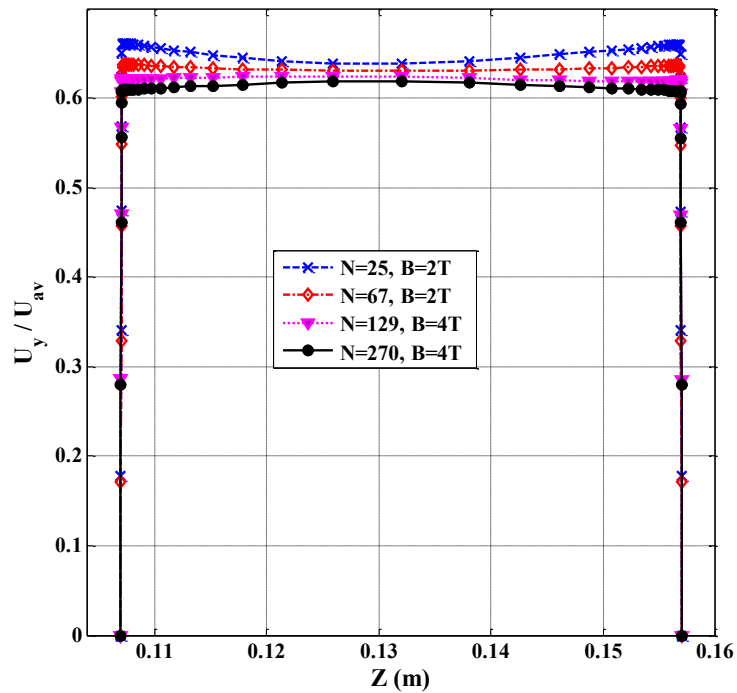


Figure 3.34: Normalized U_y velocity profile across the side walls (along x , centre of the duct) at $y=0.161$ m for various N

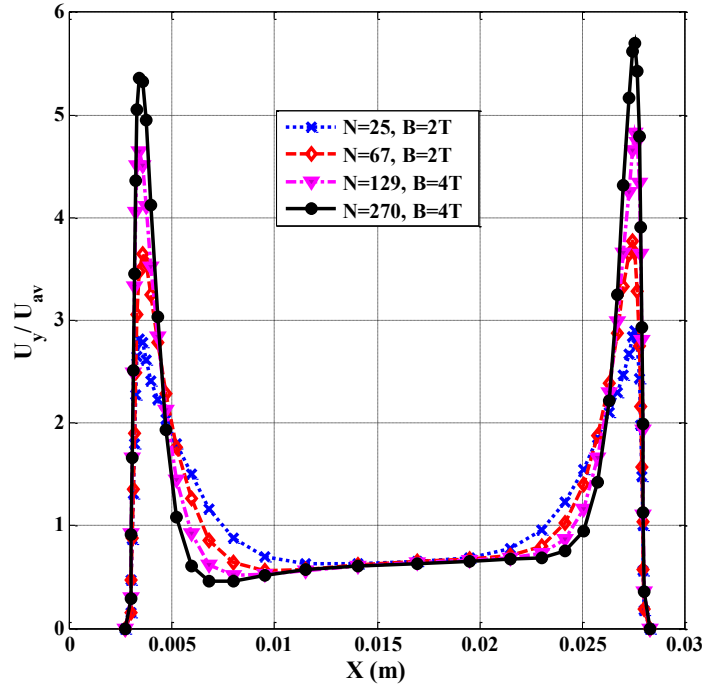


Figure 3.35: Velocity profile across the side walls in a plane just after the bend ($x=0.032$ m) for different N

3.9.3 Velocity distribution in the horizontal duct ($0.031m \leq x \leq 0.149m$, $0.169 m \leq y \leq 0.2$ m and $0.104m \leq z \leq 0.16$ m)

After a turn of 90° from the vertical duct, the flow enters into the horizontal duct. So flow is transverse to the applied field in both the legs of the bend. Just after the bend ($y = 0.028$ m), there is a complex flow distribution. More liquid enters through inner side layer in a jet like structure and the jet velocity increases with increasing interaction parameter (see Fig. 3.36). The current stream lines bend near the inner side wall due to axial current (J_x component) and thus decreasing the transverse J_z component. This in turn, reduces the opposing MHD force at the inner side wall. The side layer jet is associated with a region of recirculation at the inner side wall the boundary layer. The reverse flow also exists in this region even in the absence of external magnetic field due to the boundary layer separation by bend effect. But with the increase of the interaction parameter, the region of reverse flow narrows down with increasing magnitude of peak velocity (see Fig. 3.36). Thus the flow is asymmetric about the plane parallel to the side wall (along y).

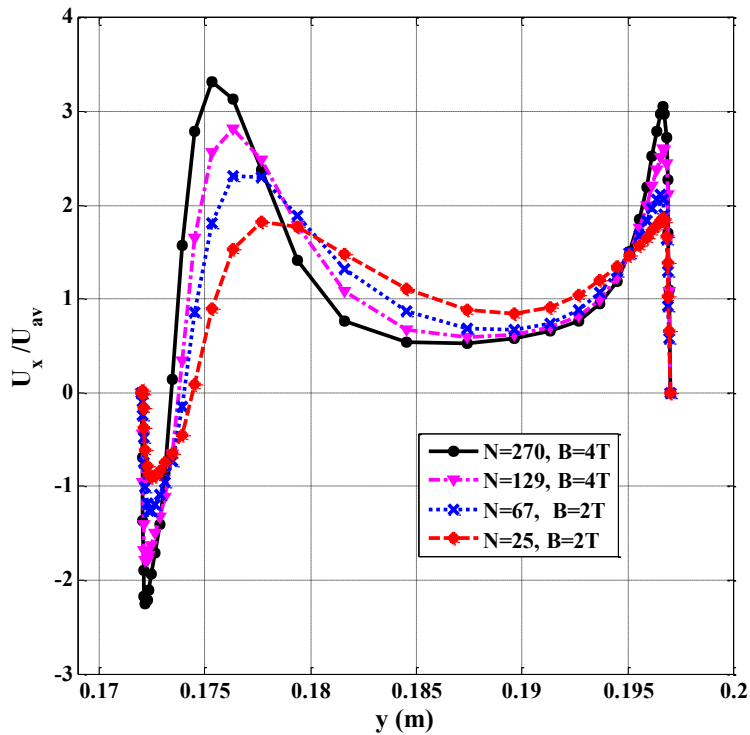


Figure 3.36: Velocity distribution across the side walls in a plane just after the bend ($x=0.032$ m) for different N

As the flow advances along x further from the bend, the flow tends to restore the symmetry along y direction. As flow proceeds past the bend, it becomes almost symmetric at a shorter length for higher interaction number and appears to be fully developed at the exit. Normalized fully develop velocity distribution in a flow cross section of the present test section is shown in Fig. 3.37 which is computed from the analytical solution for comparison of the numerical model prediction. [9] A comparison of numerical velocity profile across the side walls at the middle and exit of the horizontal duct along with the theoretical fully developed profile is shown in the (Fig. 3.38). As can be seen, although the numerical flow profile is approaching to be symmetric at the assumed outlet, fully developed profile is not yet achieved as imposed in the present simulation. This is expected to contribute some error in the numerical simulation.

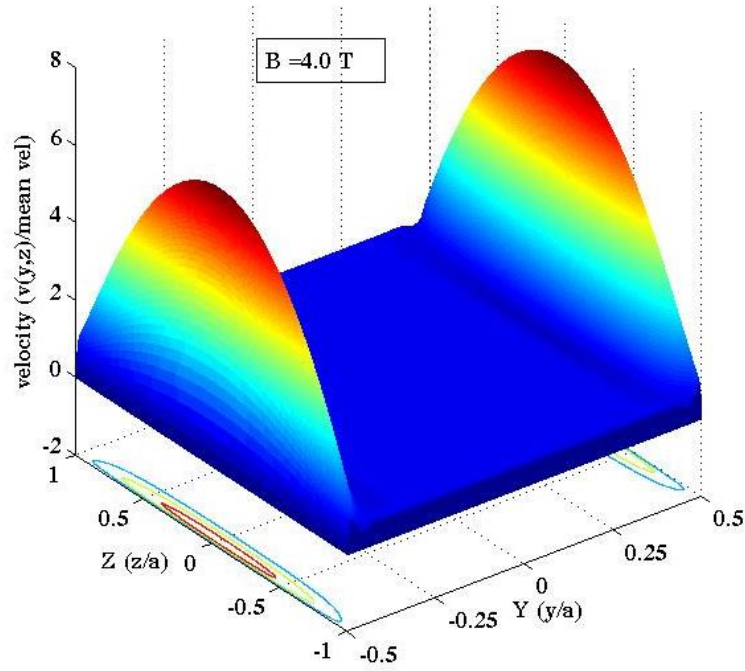


Figure 3.37: Analytical estimation of normalised velocity distribution in a flow cross section of the test section. A contour plot is shown beneath the mesh.

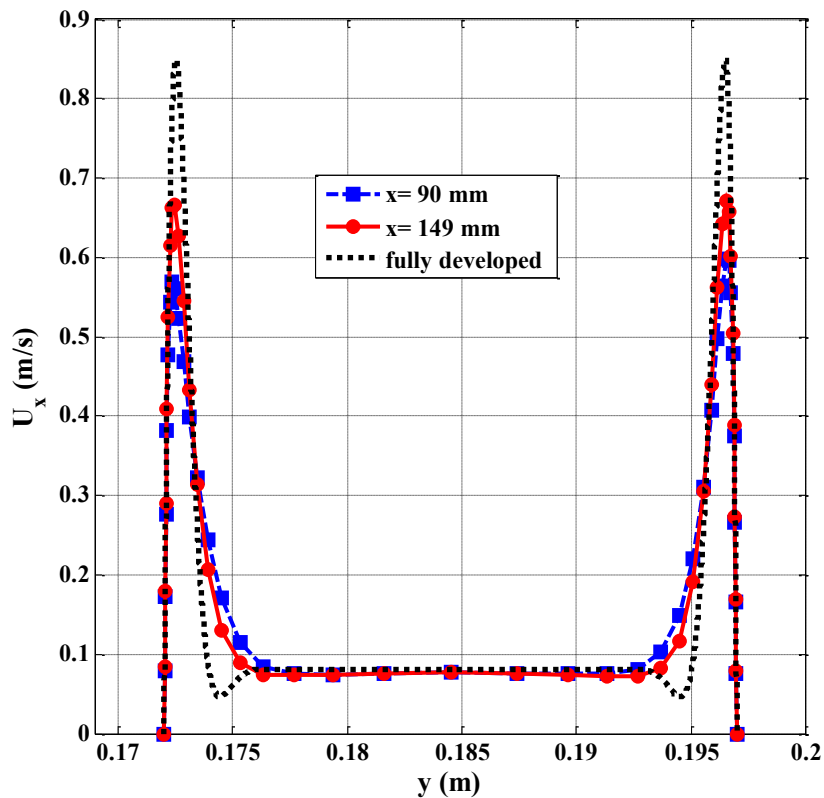


Figure 3.38: Comparison of U_x velocity distribution across the side walls (centre of the duct) with fully developed profile for $B_0 = 4\text{T}$ and mean velocity 0.122m/s

3.10 Pressure distribution

Numerical results of pressure distribution along the central flow path (ζ) of the model test section are shown in Fig. 3.39 for various flow rates and applied magnetic field of 4T. The linear flow path (ζ) equivalent to the total flow length in the test section is obtained by adding the flow length in horizontal and vertical elements of various bends of the model geometry. The corresponding fully developed pressure profile along the flow coordinate ' ζ ' based on analytical calculation is shown in the dotted line. Since numerical simulation is carried out in half symmetry, the measured fluid pressure between the ports B1-B4 is also plotted in Fig. 3.39. As can be seen the pressure drop is negligible in the inlet duct where flow is parallel to the applied field. At the bends where the flow turns from parallel to perpendicular direction of the applied field the pressure increases at first due to sudden expansion and then linear up to 2nd bend. In contrast to the first bend, the increase in pressure drop is less at the second bend where the flow is in the plane normal to the field without any change in flow cross section. So it can be concluded that additional 3-D pressure drop is more at the bend where the flow turns from parallel to perpendicular direction of the applied magnetic field. Numerical values of pressure are always more than the measured values at locations B1-B4. However, the fully developed pressure gradient (represented by dotted lines) is more or less agreement with the numerical results in the region of test section free from bend effects. The total pressure drop in the test section estimated by numerical simulation is compared with the experimental results and is presented in Table 3-4. The observed deviation is found to be within 20% in most of the cases.

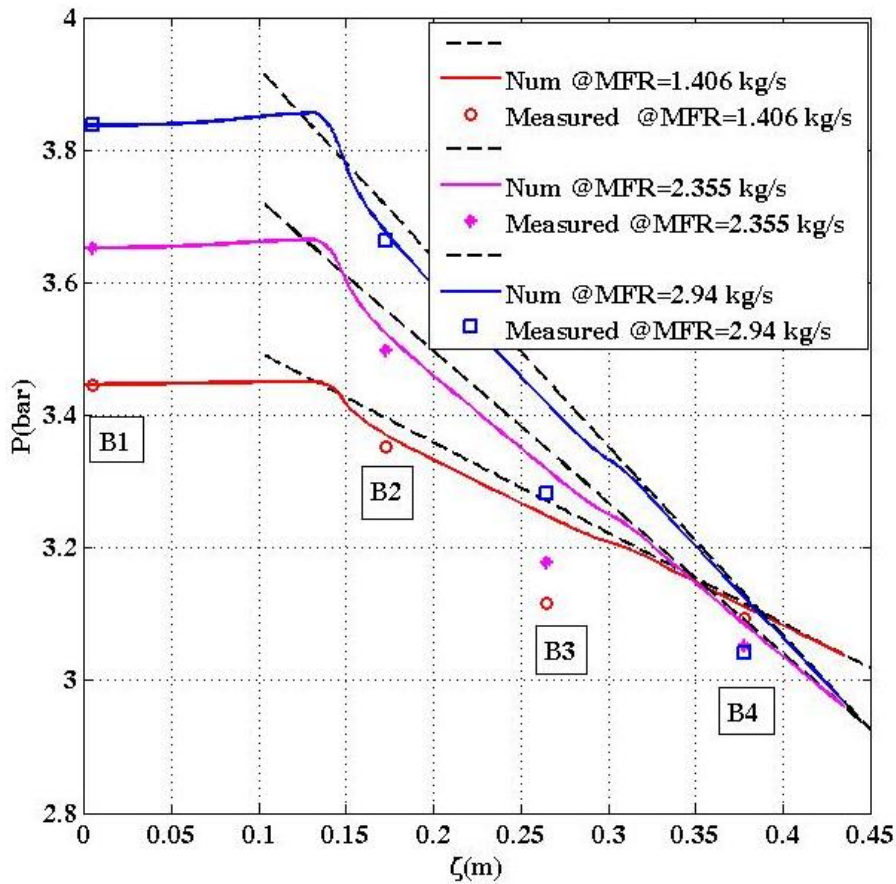


Figure 3.39: Comparison of numerical pressure profile with experiments in the test section of multiple bends for various flow rate and $B_0= 4$ T. The dotted lines are the corresponding theoretical prediction based on fully developed flow

Table 3-4: Comparison of total pressure drop in the model test section obtained by numerical simulation and experiment

B_0 (T)	Mass Flow Rate (kg/s)	ΔP (bar)		
		B1 – B4		
		Numerical	Experiment	Deviation(%)
2.0	1.418	0.09	0.09	0
2.0	2.347	0.14	0.17	17.6
4.0	1.406	0.23	0.35	34.2
4.0	2.355	0.56	0.7	0.2
4.0	2.941	0.7	0.79	11.4

3.11 Brief qualitative comparison of the present results with the simulation using other MHD codes

The test section consisting of multiple 90-degree bends (in fact the same test section is used for the present study) was also used for the purpose of benchmarking of CFD codes HIMAG/FLUIDYN at high Ha and Re [19]. 3-D numerical computations were performed in full test section geometry in contrast to the present numerical study with half symmetry. Numerical results of side wall electric potential difference distribution and pressure drop at different sections obtained from both the codes (FLUIDYN/HIMAG) were compared with corresponding experiment for two set of non-dimensional control parameters ($Ha=515$, $N=3.2$ and $Ha=2059$, $N=63.8$). It was reported by the authors that side wall potential distribution predicted by both the codes were matching reasonably well with experiment. However, the deviation with pressure drop was significant which was attributed to the measurement error at low absolute value of the pressure for set of control parameters and possible amplification of the errors due to low resolution of the indirect pressure measurement technique adopted in the experiment. Similar inference can be drawn for the performance of the FLUENT code qualitatively as a direct comparison is not possible due to different set of control parameters undertaken for the two independent numerical studies and comparison with experiments. It appears that numerical results of electric potential distribution obtained by FLUENT code (in the present study) is very close to the results predicted by FLUIDYN & HIMAG. At locations which are \sim three times characteristics length away from the 90-degree bends (location 'C', 'E'), the maximum deviation was within 3.5% for all the flow control parameters. For numerical pressure drop, the deviation with experiment increases with increasing flow rate for a given applied magnetic field strength. This may be attributed to the presence of increased residual turbulence at higher flow rates. Analysis of 3-D pressure drop at different oriented bends with respect to the applied magnetic field indicated much deviation from the general

trend at lower interaction parameters. The higher deviation at low N also indicates possible measurement error at low absolute value of pressure with indirect measurement technique.

3.12 Summary of numerical simulation in test section of multiple bends

Experiments and 3D numerical simulations are carried out for PbLi liquid metal MHD flow in a test section consisting of multiple 90° bends for various flow rates and applied magnetic field up to 4T. The maximum characteristics Hartmann number (Ha) of the study is $Ha=2060$. The measured electric potential in both Hartmann and side walls of the test section at various locations are compared with numerical results. It is observed that numerical results of wall potential data based on laminar model are matching well with the measured values of at all the locations including locations very near the bends at low flow rates and high magnetic fields. There is significant deviation near the bends at higher flow rates and low magnetic field (lower Ha/Re ratio) which may be attributed to the residual turbulence in the flow that is not accounted in the present simulation. However, at far away from the bend the agreement of side wall and Hartmann wall potential distribution with numerical prediction is within a maximum deviation of 3.5% for all the flow rates and applied magnetic fields.

The analysis indicates that the flow distribution becomes rapidly symmetric after the bends where the flow is in the plane perpendicular to the applied magnetic field in both the legs of bend. In contrast, flow distribution remains asymmetric for a longer distance when it turns from parallel to perpendicular direction of the applied field. As the numerical results are in good agreement with experimental data at higher Ha/Re ratio, it illustrates the capability of the numerical code to predict MHD flows in channels of a typical blanket module consisting of sharp L/U bends where the flow characteristics are governed by high Hartmann number ($Ha \sim 10^3$ to 10^4) and interaction parameter ($N \sim 10^3$). The applicability of the code is limited to laminar flow regime and needs further development to include turbulence effects. Even though the code is predicting reasonably well for MHD parameters relevant to Blanket Modules for

single channel flows with bends, further validation of the code is needed for its applicability in electrically coupled parallel/anti-parallel channel flows associated with multiple rectangular bends.

3.13 References

- [1] C. Paritosh, E. Rajendra Kumar, et al. Status and progress of Indian LLCB test blanket systems for ITER, *Fusion Eng. and Des.* 87 (2012)
- [2] S. Smolentsev, R. Moreau, et al., Characterization of key magnetohydrodynamic phenomena in PbLi flows for the US DCLL blanket, *Fusion Eng. and Des.* 83 (2008)
- [3] S. Smolentsev, R. Moreau, et al., MHD thermofluid issues of liquid metal blankets: Phenomena and advances, *Fusion Eng. and Des.* 85 (2010)
- [4] L. Buehler, H. J. Brinkmann, et al., Magnetohydrodynamic Flow in a Mock-up of a HCLL Blanket: Part-11-Experiments, FZKA-7424 (2008)
- [5] S. Molokov and L. Buehler, Liquid metal flow in a U bend in a strong uniform magnetic field, *J. fluid mech.*, 267 (1994)
- [6] M. J. Ni, M. Ramakanth, et.al, A current density conservative scheme for incompressible MHD flows at a low magnetic Reynolds number Part I: On a rectangular collocated grid system, *Journal of computational physics* 227 (2007)
- [7] S. Smolentsev, N. Morley, et al., Code development for analysis of MHD pressure drop reduction in a liquid metal blanket using insulation technique based on a fully developed flow model, *Fusion Eng. and Des.* 73 (2005)
- [8] P. K. Swain, P. Satyamurthy, et al., 3D MHD lead–lithium liquid metal flow analysis and experiments in a Test-Section of multiple rectangular bends at moderate to high Hartmann numbers, *Fusion Eng. and Des.* 88 (2013)
- [9] S. I. Sidorenko, A. Ya. Shishko, Variational method of calculation of MHD flows in channels with large aspect ratios and conducting walls. *Magnetohydrodynamics*, 27 (1991)
- [10] R. Stieglitz, R. Barleon, et al., Magnetohydrodynamics flow through a right-angle bend in a strong magnetic field, *Journal of Fluid Mech.* 326, (1996)
- [11] I. R. Kirillov, C. B. Reed, et al., Present understanding of MHD and heat transfer phenomena for liquid metal blankets, *Fusion Eng. and Des.* 27 (1995)
- [12] Alice Y. Ying, Mark S. Tillack, MHD heat transfer in elongated rectangular ducts for liquid metal blankets, *Fusion Tech.*, 19 (1991)
- [13] R. Bhattacharyay, A. Patel, et al., Liquid metal MHD experimental activities for LLCB TBM development, *Fusion Eng. and Des.* 88 (2013)
- [14] L. Buhler, Liquid metal flow in arbitrary thin-walled channels under a strong transverse variable magnetic field, *Fusion Eng. and Des.* 17 (1991)

- [15] E. M. Valls, L. A. Sedano, et al., Lead- lithium eutectic material database for nuclear fusion technology, *Journal of Nuclear Materials*, 376 (2008)
- [16] A. Sterl, Numerical simulation of liquid-metal MHD flows in rectangular ducts, *J . Fluid Mech.*, 216 (1990)
- [17] S. Smolentsev, R Moreau, One-equation model for quasi-two-dimensional magnetohydrodynamic flows, *Physics of Fluids* 19, (2007)
- [18] U. Muller, L. Buehler, Book: Magnetofluidynamics in channels and containers, Springer ISBN 3-540-41253 (2001)
- [19] A. Patel, G. Pulugundla, et al., Validation of numerical solvers for liquid metal flow in a complex geometry in the presence of a strong magnetic field, *Theor. Comput. Fluid Dyn.* (2017)

4 CHAPTER

Effects of Magnetic Properties of the Structural Material and Non-resolved Hartmann Layer on Liquid Metal MHD Flow

4.1 Effects of magnetic properties of the structural material on PbLi MHD flow

The structural material for the generic blanket module of ITER is likely to be Reduced Activity Ferritic Martensitic Steel (RAFMS). Many ITER partners have developed their own Ferritic-Martensitic grade steel (FMS) not only for ITER but for potential applications in subsequent commercial fusion reactors (DEMO). IN-RAFMS material is considered by India for its proposed LLCB TBM. FMS grade has an advantage in high temperature radioactive environment because of its potential for relatively low activation, low swelling and high heat resistance properties [1-4]. But these materials are magnetic in nature with high magnetic permeability ($\mu_r > 1$) in comparison to the austenitic grade steel like SS316 ($\mu_r = 1$). When the electrically conducting liquid metal is flowing in channels of FMS exposed to an external magnetic field, the strength of the field experienced by liquid metal is expected to be affected by the magnetic properties of the material. For numerical simulation of the MHD flow and validation purpose, the actual magnetic field is to be taken into account for accurate prediction of the flow field variables. To study these effects, MHD experiments have been conducted in test sections of SS430 ($\mu_r \approx 800$) and SS316 ($\mu_r = 1$) subject to different strengths of magnetic field induction ($B_0 = 1-4T$) at IPUL, Latvia. Liquid metal PbLi at a temperature of $350^\circ C$ is considered as working fluid to simulate the MHD flow at different flow rates. The maximum characteristic Hartmann number (Ha) and interaction parameter (N) achieved in this experiment is $Ha \sim 1047$ and $N = 300$ respectively for $B_0 = 4T$ and flow rate of $34.4 \text{ cm}^3/\text{s}$. In view of similar saturation magnetization ($M_s \sim 1.4T$) of IN-RAFMS and SS430, the range of applied magnetic field induction of the present experiment is very relevant to the ITER blanket applications.

4.2 Test section and diagnostics

Two identical test sections in the form of square loop are made with 3mm thick walls of SS316L non-magnetic structural material and SS430 ferromagnetic structural material. The schematic of the layout the test section is shown in Fig. 4.1. Each of the test section consists of two symmetric U-bends of square duct with a flow cross section of 25 mm x 25 mm. The flow of PbLi is normal to the applied magnetic field throughout the square path. Liquid metal enters into the test section from a square inlet header (25 mm x 25 mm) that distributes the flow symmetrically in two branches of the square loop via a baffle plate. In the test section the flow experiences two 90° bends in the plane perpendicular to the magnetic field and comes out of the test section through outlet header with similar arrangement as that of inlet.

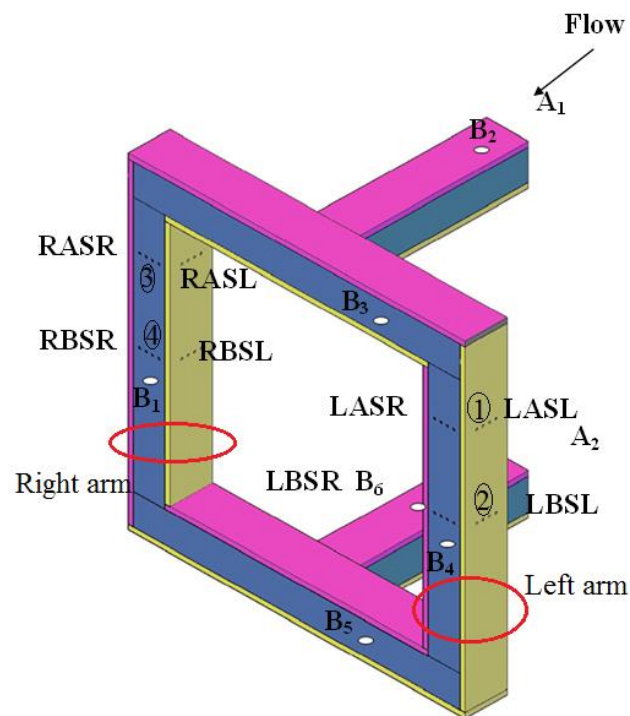


Figure 4.1: Schematic lay out of the square loop test section with locations of diagnostics

The test section with geometrical symmetry is considered to minimize the induced magnetic torque while placed in the solenoid of super conducting magnet used for experiment. As the material properties are concerned the two test section are different with respect to the wall electrical conductivity and relative magnetic permeability. Test section made of SS430 has

comparatively ~8% higher wall electrical conductivity and ~800-time higher relative magnetic permeability than SS316 test section.

The liquid metal pressure at various locations of the test section is indirectly measured through cover gas (Argon) pressure of expansion tanks linked with the diagnostic pressure tubes. [5] Pressure tubes (B₂-B₆) are connected to the identical expansion tanks at fixed height and have the identical liquid level at rest condition. Each expansion tank is equipped with two level indicators (10 mm height difference) for liquid metal level measurement. Above the free surface of Pb-Li, space is located for inert gas argon, whose pressure is measured through room temperature gas manometers GDH of 14 AN (Piezo resistive pressure sensors). First the initial cover gas pressure (in the range of 1-2 bar) in each expansion tank is recorded before the circulation of liquid metal. The change in cover gas pressure is measured during experiments for various flow conditions. Usually, for one set up experiment the applied magnetic field is kept fixed and the flow rate is varied. At the completion of one set, the pump is stopped and the cover gas pressure on each expansion tank is recorded again and compared with initial gas pressures. The maximum difference is found to be less than 0.1 bar. This suggests that, experimental error bar is within 10 % for this pressure measurement.

Several numbers of potential pins are welded to different walls in identical manner for each test section to measure the wall potential and comparison of the results. For side walls (the wall which parallel to magnetic field) 4 pairs of pin are placed along the applied field direction with uniform spatial gap at locations named LAS, LBS, RAS and RBS. Here the letter 'L' and 'R' is used for left and right leg convention of square loop. Photograph of the experiment test section with diagnostic instrumentation is shown in Fig. 4.2. Potential difference is also measured in the absence of magnetic field or in the magnetic field without circulation of Pb-Li. In both the cases, the difference is found to be negligible (max ~0.1 mV) as compared to the measured wall electric potential difference in presence of magnetic field

with the motion of Pb-Li. The experimental error bar in the wall electric potential difference measurements are expected within 5%.

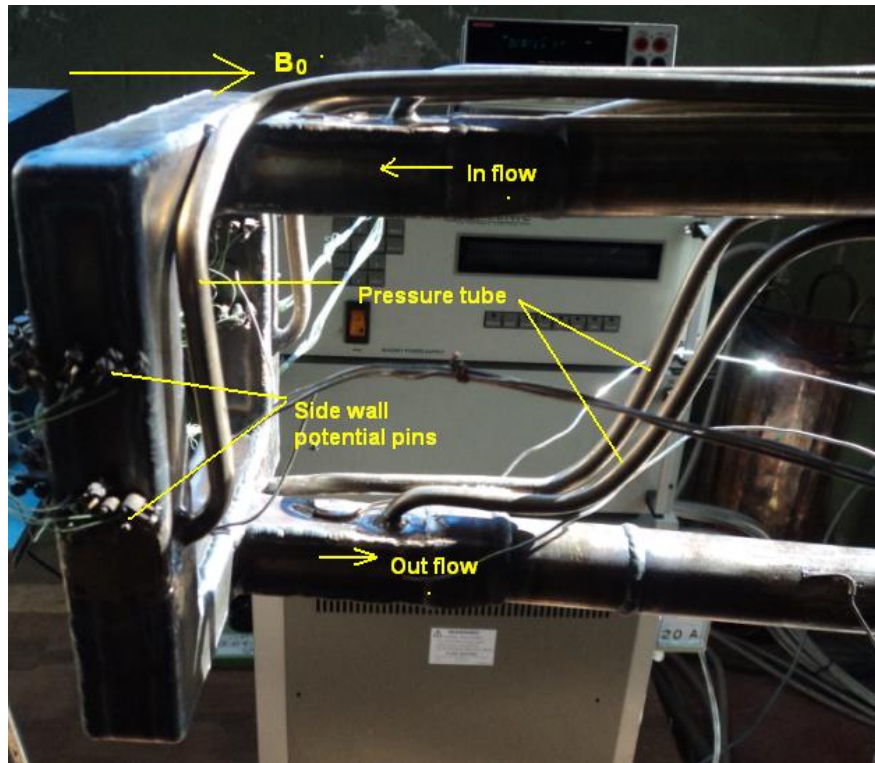


Figure 4.2: Photograph of the test section of square loop with diagnostic instrumentation

4.3 Analysis of Experiment result

4.3.1 Comparison of side wall voltage

The voltage measured across the side walls at locations LBS and RBS is considered for comparison of the results obtained in two test cases of the present analysis. These locations are at the middle of the vertical ducts of two branches and are expected to be free from the bend effects. Assuming a developed flow at this location, The voltage measured by a pair of pin is governed by Eqn(4.1)

$$\Delta\phi = \frac{\sigma u_{av} B_0}{1 + C} \quad \text{Eqn(4.1)}$$

Here, u_{av} is the average velocity in each leg of the test section square loop, C is the relative wall conductance ($C = \sigma_w t_w / \sigma a$), σ is the electrical conductivity of PbLi, t_w is the thickness of Hartmann wall and B_0 is the applied magnetic field induction.

Since the relative wall electrical conductance of SS430 is higher than the SS316 the measured voltage is anticipated to be higher for SS316 test section for a given flow rate and applied magnetic field strength. It is to be noted that the voltage measured by the 3rd or 2nd pair of pin is higher than the other pair as they are close to the center of the flow cross section at LB location. In this present analysis, data of the 3rd pair of pins is compared to reduce the error due to higher voltages. In Fig. 4.3, the measured voltage by a pair of pins (3rd pair) at location LB is shown for applied magnetic field of 4T. As can be seen the observed voltage is little higher for SS316 than SS430 and follows Eqn(4.1). But at lower magnetic field of 1T as shown in Fig. 4.4, the difference is relatively larger than the case for $B_0=4T$. Also the slope of the curve which is a measure of the sensitivity (mV/cm^3s^{-1}) is higher for SS316 than SS430. Nevertheless, the measured voltage is higher for SS316 at both lower and higher magnetic field. The larger difference at lower field is attributed to the shielding effects of PbLi by magnetic material (SS430 test section) that lead to further lowering of voltage than non-magnetic SS316 test section.

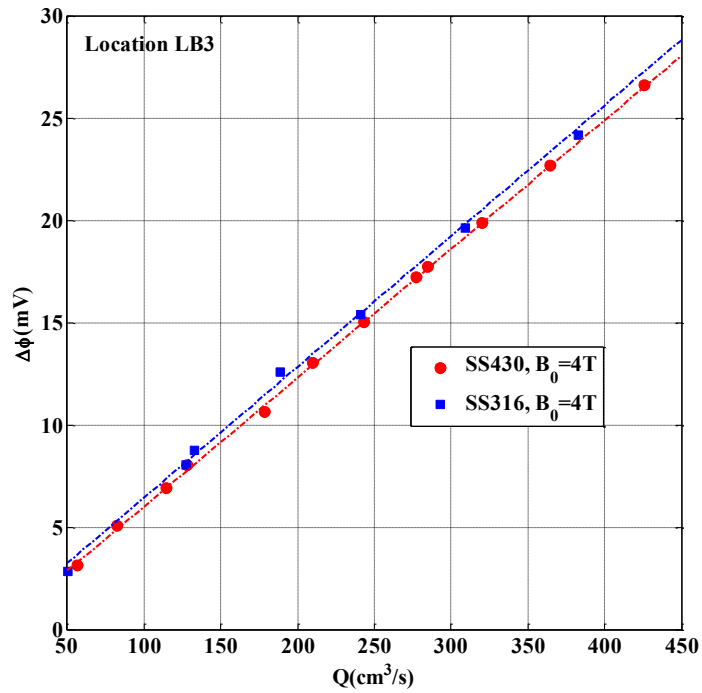


Figure 4.3: Comparison of observed voltage with flow rate for SS430 and SS316 test section at location LB and $B_0=4T$

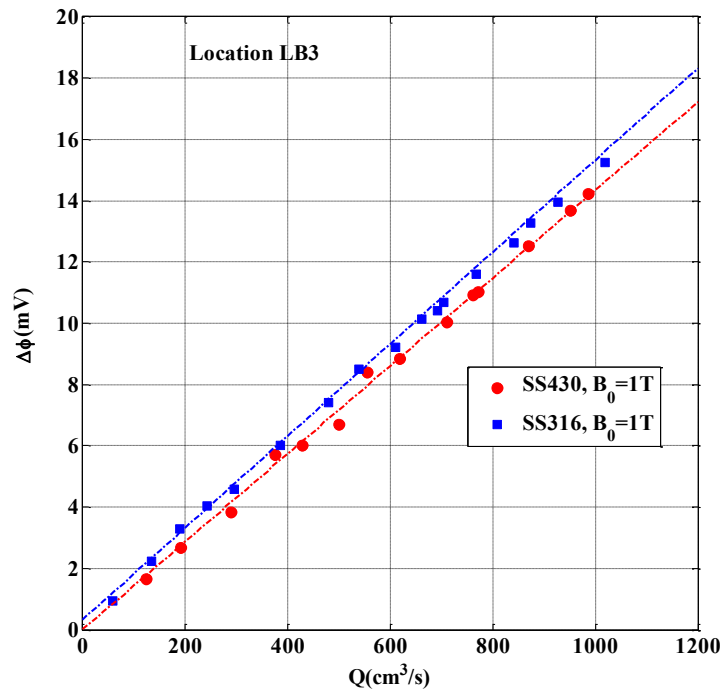


Figure 4.4: Comparison of observed voltage with flow rate for SS430 and SS316 test section at location LB and $B_0=1T$

Because of geometrical symmetry in the test section, the experiment is repeated by reversing the flow direction. Similar observations are made for the electrical potential measurement. The observed voltage with flow rate at the same location is shown in Fig. 4.5 and Fig. 4.6 for applied magnetic field of 4T and 1T respectively. It is concluded from Fig. 4.3 to Fig. 4.6 that when the applied magnetic field strength is lower (1T), the voltage measured by the test section is affected by the shielding effects whereas at high magnetic field (more than the saturation field) the observed voltage is determined by the relative wall conductance of structural wall.

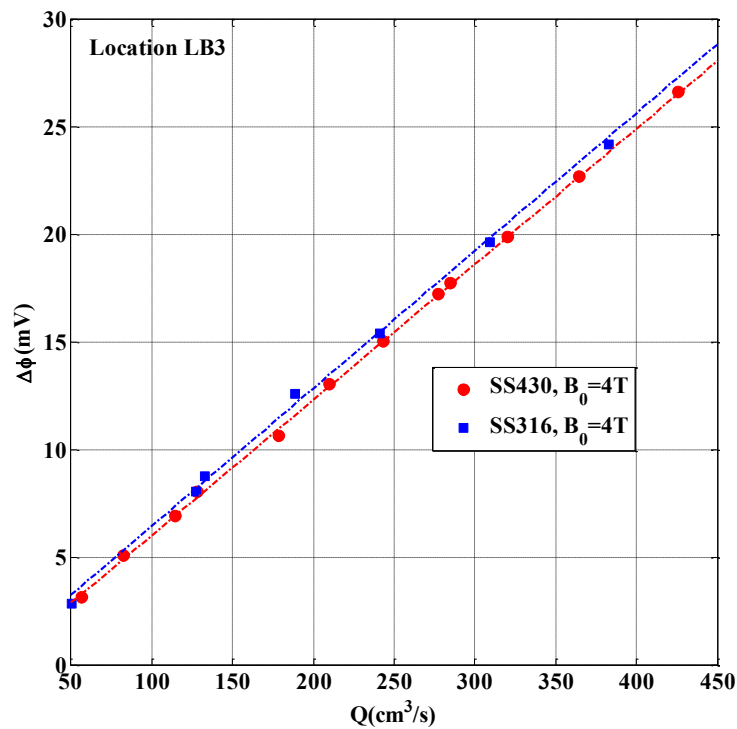


Figure 4.5: Comparison of observed voltage with flow rate for SS430 and SS316 test section at location LB and $B_0=4T$ for reverse flow condition

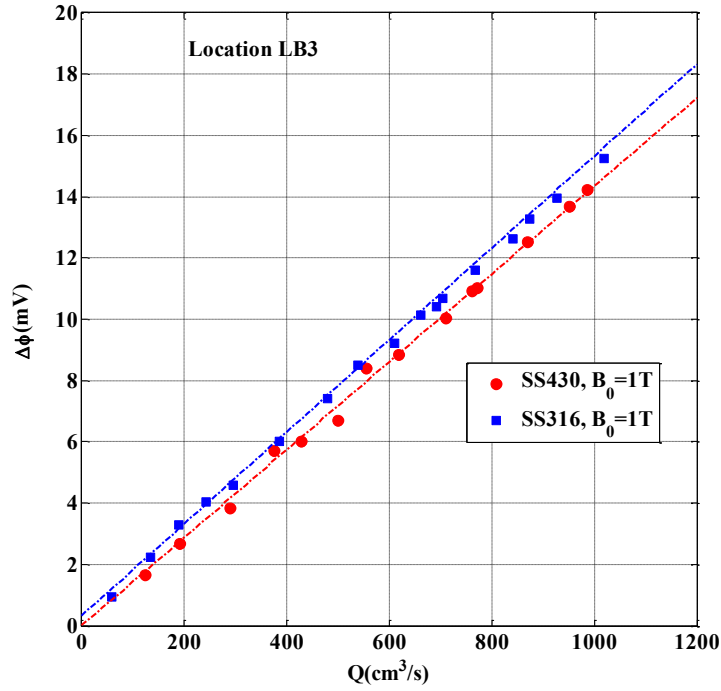


Figure 4.6: Comparison of observed voltage with flow rate for SS430 and SS316 test section at location LB and $B_0=1T$ for reverse flow condition

4.3.2 Comparison of pressure drop

The pressure difference between the port B2 and B6 (see Fig. 4.1) is a measure of the total pressure drop in the test section. For MHD flow in electrically conducting channel, the dependence of pressure drop with wall conductance ratio in most of the practical problem is well predicted by Eqn (4.2).

$$\Delta p = \frac{C}{1+C} (\sigma u_{av} B_0^2 L) \quad \text{Eqn(4.2)}$$

Here, L is the total flow length in the test section from point B1 to B6. In Fig. 4.7 and Fig. 4.8 the observed pressure drop for various flow rate is compared for both the test section at different magnetic field strength. As can be seen in Fig. 4.7, for higher magnetic field (4T) the pressure drop is higher for SS 430 than SS316 for a fixed flow rate. This is because C value is higher for SS430 than SS316 and the pressure drop follows Eqn(4.2). The pressure drop trend is linear with respect to the flow rate as expected in a typical MHD flow.

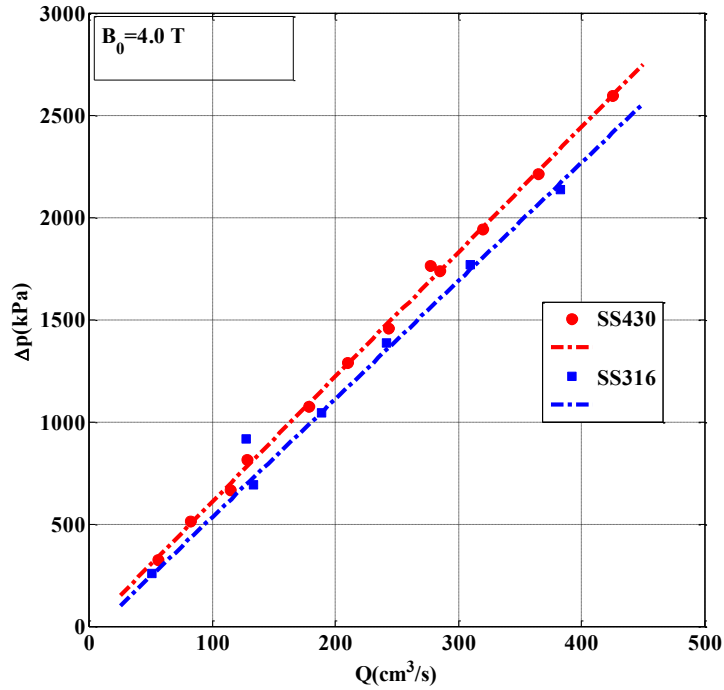


Figure 4.7: Comparison of total pressure drop with flow rate for SS430 and SS316 test section at applied magnetic field strength of $B_0=4T$

But when the applied magnetic field strength is lower (say 1T) as can be seen in Fig. 4.8, the pressure drop in both the test sections is identical and follows a nonlinear trend. The nonlinear trend is analogous hydrodynamic counterpart where variation of pressure drop with flow rate

is quadratic ($\Delta p = \frac{1}{2} \lambda L \rho u_{av}^2$). It is believed that the effective field strength experienced by

the SS430 test section is reduced when the external magnetic field strength is low (below saturation). Even the pressure drop varies with square of the magnetic field strength; the reduced pressure drop for the case of SS430 appears to be compensated by the increased pressure drop due to higher relative wall conductance. So the pressure drop curve for both the test sections is similar. But at higher magnetic fields, the deviation is observed due to difference in electrical conductivity only and there is no change in the strength of the applied magnetic field. Similar trend for the total pressure drop is observed when the flow direction is reversed in the test section and is presented in Fig. 4.9.

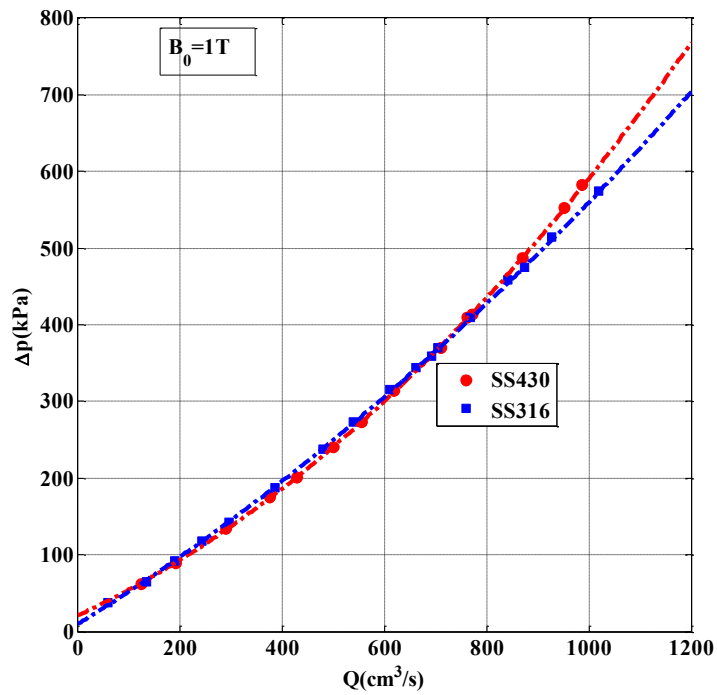


Figure 4.8: Comparison of total pressure drop with flow rate for SS430 and SS316 test section at applied magnetic field strength of 1T

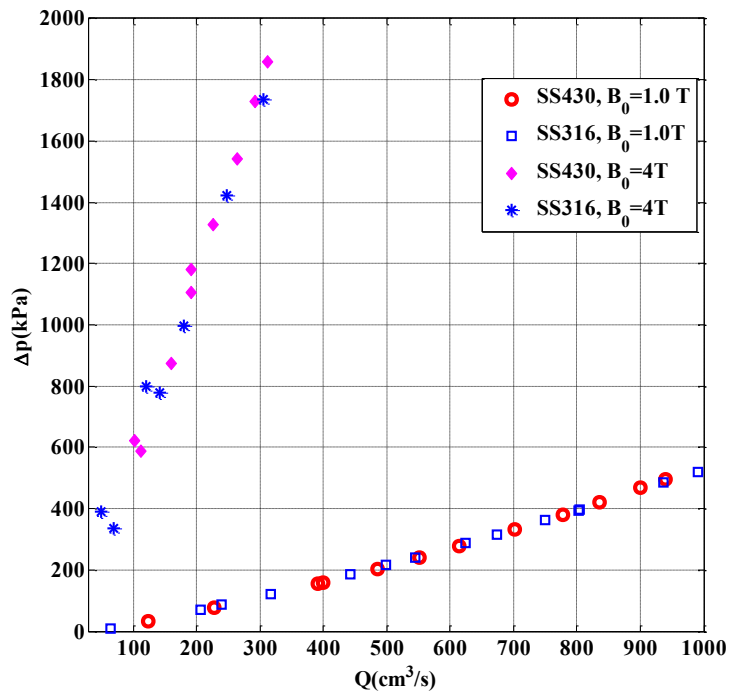


Figure 4.9: Comparison of total pressure drop with flow rate for SS430 and SS316 test section at different magnetic field for reverse flow condition

4.4 Summary of the effects of magnetic properties of the material on MHD flow

In summary it may be concluded that when the external magnetic field strength is below saturation, the magnetic field strength experienced by the liquid metal is affected by the magnetic properties of the structural wall. Whereas, at higher field strength the structural material is transparent to the magnetic field and flow physics is governed by the relative electrical properties of the structural material with respect to the liquid metal. So the MHD flow simulation of blanket module of ITER where the liquid metal flow is subject to high toroidal magnetic field is not affected by the magnetic properties of the RAFMS structural material

4.5 Numerical study for quantifying effects of non resolved Hartmann layer on MHD flow in electrically conducting channel

Hartmann layer is the characteristic boundary layer in a typical MHD flow which is developed at the walls normal to the external magnetic field. The velocity field in this layer is exponential with the dimensional thickness (δ_H) determined by inverse of Hartmann number ($Ha = B_0 a \sqrt{\sigma/\mu}$) times the characteristic length(a), usually half the width of the duct cross section along the magnetic field. Here B_0 , μ , σ denote the external magnetic field induction, dynamic viscosity and electrical conductivity of the fluid respectively. One of the important aspects of this boundary layer is part of the induced currents due to interaction of flow field with the external magnetic field is closed through this layer depending on the resistance offered by Hartmann wall and associated Hartmann layer. Resolving these layers for numerical solution is necessary to get an estimation of accurate current density in the flow cross section which ultimately influence the flow field solution through electromagnetic source term ($J \times B_0$) in Navier-Stokes momentum balance equation. For MHD flows involving high Hartmann numbers, the boundary layer becomes thinner ($\delta_H = a/Ha$) and enormous computational efforts are required for resolving this layer. However, in case of electrically conducting walls,

the majority of the current loops are closed through the walls. As the Hartmann layer contributes a lesser fraction to global current path for high Hartmann number flows, there may be less impact on obtaining a solution of the flow field even if it is not numerically resolved. The present study attempts at understanding the effect of resolution of the Hartmann Layer on various flow properties like core current, velocity and pressure gradient. Comparisons have been carried out for a well resolved and unresolved Hartmann layer at different magnetic fields. The numerical results are also compared with relevant analytical solutions based on fully developed flow models.

Limitation of analytical solutions for simple geometries like ducts with finite electrical conductivity or asymmetric wall thickness has led to development of a number of numerical schemes to provide solutions for practical 3D MHD problems. A Boundary Element Method for the steady MHD flow through a cylindrical duct was developed by Adrian Carabineanu et al. (1995) [6]. Nizar Ben Salah et al. developed a finite element technique to solve 3D, incompressible MHD flows [7]. 3-D finite volume based MHD solver HIMAG developed by HyPerComp in collaboration with UCLA has shown promising results for MHD flow simulation at high Hartmann number as the code employs a consistent charge conservation scheme for current density interpolation in inductionless formulation of the Lorentz force [8]. 3-D thermofluid MHD simulation in a single channel has been performed using the MHD solver of the general purpose CFD code FLUIDYN developed by Transoft International Ltd in collaboration with IPR, India [9]. MHD thermofluid simulation in channels subject to uniform thermal load has been demonstrated using open source code OpenFOAM by OpenCFD Ltd [10]. Benchmarking studies were performed using MTC-H 1.0 developed at UCAS (China) which employ conservative scheme for computation of induced current density similar to HIMAG and showed good accuracy for $Ha \sim 10^2$ [11]. But, for realistically computing the flow field, most methods require the Hartmann and side boundary layers through which the induced

current paths are closed to form a loop, to be well resolved. For geometries like the Test Blanket Module (TBM) of the International Thermonuclear Experimental Reactor (ITER), the Hartmann wall is a part of double wall type U shaped thick First wall is subject to high magnetic field (4T) and encloses high aspect ratio flow channels. The boundary layers with thickness in the micron scale are developed at the FW component where the magnetic field is normal to the wall. Numerical solution of such problems necessitates extensive computer memory and time. The present study attempts at understanding the effect of coarsening and not resolving the Hartmann boundary layer thickness ($\delta_a \sim a/Ha$) on the overall solution. Only straight conducting channels with square and rectangle cross-sections are studied and an FVM solution is employed using ANSYS FLUENT. Lead lithium (PbLi) is taken as the working fluid. Hartmann Number ($Ha = Ba\sqrt{\sigma/\mu}$) of the flow is varied from 550 to 2080 by changing the magnetic field from 1T to 4T. Quantitative effects on various flow parameters due to coarsening of the mesh in Hartmann layer is investigated for rectangular ducts and envisaged as a possible technique for obtaining fast hand numerical solution in complex geometries.

4.6 Description of geometry and grid

A square and a rectangle duct having a 25x25 mm and 25x50 mm cross-section, and length of 500 mm have been analyzed. Fig. 4.10 shows the rectangular cross-section geometry. The wall thickness (t_w) was 1.5 mm and the field is applied along the Y-Axis. The flow of Pb-Li along the channel occurs along the Z-Axis.

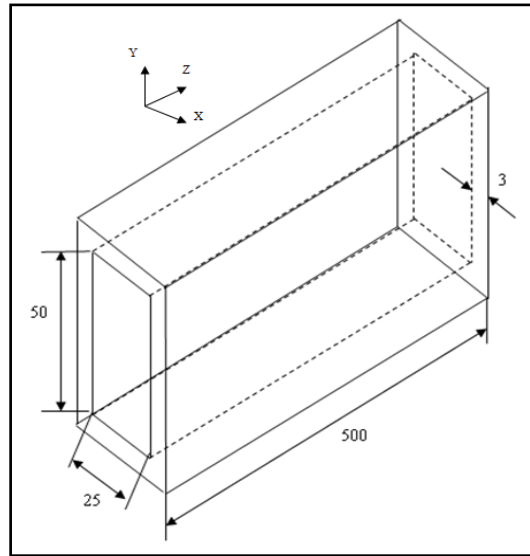


Figure 4.10: Rectangular model geometry for numerical experiment of effects of Hartmann layer resolution

For both geometries, three grid systems: Grid 1, Grid 2, Grid 3 are designed, having 3, 1 and no points in the Hartmann boundary layer respectively at the highest magnetic field of 4T. For all grid systems, the side wall boundary layer thickness ($\sim a/\sqrt{Ha}$) is resolved with 9 points at 4T field to capture the side layer jet. A fourth system, Grid 4, is created for both geometries, having no grid point in the Hartmann boundary layer at 1T. As the Hartmann layer thickness goes on decreasing with increase in field strength, this system provided a completely unresolved Hartmann layer at all fields higher than 1T. A structured, non-uniform coarse grids in the core region of the flow and progressively finer towards the walls is employed (See Fig. 4.11). Meshing along the channel length was kept uniform, using a total of 70 grid points. The coarseness of the grid systems with respect to Grid 1 is summarized in Table 4-1.

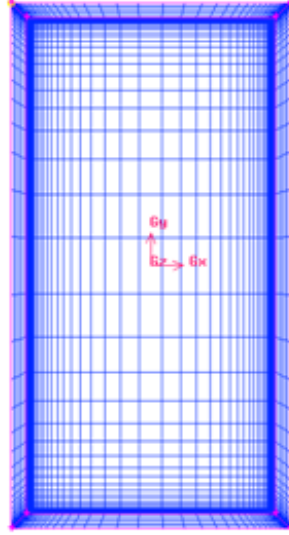


Figure 4.11: Mesh structure in the cross section of model geometry for numerical experiment of effects of Hartmann layer resolution

Table 4-1: Meshing details of various grid systems in the model geometry for numerical experiment of Hartmann layer resolution

Geometry	Square				Rectangle			
Grid	Grid 1	Grid 2	Grid 3	Grid 4	Grid 1	Grid 2	Grid 3	Grid 4
No of Cells	336980	285390	257250	177520	369810	318220	290080	196280
% Coarseness with respect to Grid 1	-	15.31	23.66	47.32	-	13.95	21.56	46.92

4.7 Governing equations

MHD flows are described by coupling the equations governing fluid flow with Maxwell's equations of electrodynamics. The resulting, steady state, incompressible MHD equations are [12] displayed in following equations.

$$\vec{\nabla} \cdot \vec{U} = 0 \quad (\text{Continuity of mass}) \quad \text{Eqn (4.3)}$$

$$(\vec{\nabla} \cdot \vec{J}) = 0 \quad (\text{Current conservation}) \quad \text{Eqn (4.4)}$$

$$\vec{J} = -\sigma(-\vec{\nabla}\phi + \vec{U} \times \vec{B}) \quad (\text{Ohm's Law}) \quad \text{Eqn (4.5)}$$

$$(\vec{U} \cdot \vec{\nabla})\vec{U} = -\frac{\vec{\nabla}P}{\rho} + \nu \nabla^2 \vec{U} + \frac{\vec{J} \times \vec{B}}{\rho} \quad (\text{Momentum balance}) \quad \text{Eqn (4.6)}$$

ρ , \vec{U} , ν , P , \vec{J} , σ , \vec{B} , ϕ are density, velocity, kinematic viscosity, pressure, current density, electrical conductivity, applied magnetic field, and electric potential respectively.

Since magnetic Reynolds number ($R_m = \mu_m \sigma u_0 a$) is $\ll 1$, the induced field is neglected and electric potential method is used to solve Eqn(4.6). Using Eqn (4.4) and Eqn (4.5), a Poisson equation for electric potential Eqn (4.7) is formed and solved within the flow field and structural wall with zero velocity.

$$\nabla^2 \phi = \vec{\nabla} \cdot (\vec{U} \times \vec{B}) \quad \text{Eqn (4.7)}$$

For the geometries under study, since $Ha/Re \gg 1/300$, the laminar model is chosen for the numerical solution. A Pressure based solver is employed and the *SIMPLE* algorithm [13] is provided Pressure-Velocity coupling. Second order upwind scheme is used for the discretization of electrical potential and momentum equations.

4.7.1 Boundary Conditions

The inlet velocity for all cases is 0.01m/s and is specified via a Velocity Inlet boundary condition and a Pressure Outlet boundary condition is used to set the channel outlet gauge pressure to 0 Atm. At all the inner wall surfaces, No-slip boundary condition is applied and these walls were treated as coupled walls to ensure continuity of the normal component (to the walls) of current density ($J_n = J_{nw}$) and that of electric potential ($\phi = \phi_w$). The outer surfaces of the wall are modeled as insulating surfaces to ensure that no electric current passes through these boundaries.

4.8 Results and discussion

The channel walls are considered to be of stainless steel having electrical conductivity (σ_w) 1.01×10^6 S/m. The density of Pb-Li is taken as 9776.9 kg/m^3 , its electrical conductivity

7.7616×10^5 S/m. Its dynamic viscosity (μ) and magnetic permeability (μ_m) are taken as 0.0018 Pa.s and 1.257×10^{-6} H.m⁻¹ respectively. The results of the numerical simulation are discussed in the subsequent sub-sections where comparisons are made between grid systems to determine effect of coarsening, and with existing analytical and numerical schemes for model validation.

4.8.1 Comparison for induced electrical current density

Table-4.2 & Table-4.3 compares the currents in Hartmann layer, core and walls for fully developed flow, for both the geometries and the overall current conservation for each grid system is also tabulated. At every magnetic field, the core current density, the core current and the wall current for the four grid systems agree well with each other and their variation with respect to Grid 1 does not exceed 1.5% for both geometries. Since Grid 4 of both geometries has no points in the Hartmann layer even at 1T, no value is obtained for Hartmann layer current.

At 1T, the ratio of currents in Hartmann layer to the Hartmann wall is less than 2% for Grids 1, 2, 3 of both the geometries (Tables 4-2 & 4-3). As the magnetic field is increased, the Hartmann layer becomes thinner and offers higher resistance to the global current path. This causes most of the current loops to close through the Hartmann walls instead of the boundary layer, reducing the Hartmann layer current. In fact, the ratio of current in Hartmann layer to the Hartmann wall is less than 0.5% even for the finest grid system (Grid 1) at 4T.

For a given magnetic field, the number of grid points in the Hartmann layer reduces from Grid 1 to Grid 4, resulting in a lower estimation of Hartmann layer currents for both the geometries. The deviations of Hartmann layer current for Grid 2, 3, 4 with respect to Grid 1 for 1T and 4T fields are documented in Table 4-4. Although the Hartmann layer current is totally neglected in Grid 4 and high deviations are observed in Grid 2 and 3, overall current balance for the system is maintained (Tables 4-2 and 4-3). This is because the Hartmann layer current

accounts for not more than ~2% of the total current. Thus, coarsening of the Hartmann layer does not affect the induced currents developed in the system.

Table 4-2: Comparison of the induced currents in different grid system for square geometry

Property	Magnetic Field (T)	Grid 1	Grid 2	Grid 3	Grid 4
Core current density (A/m ²)	1	-883.59	-883.16	-882.81	-876.16
*Integral core current (A/m)		-21.83	-21.81	-21.8	-21.52
Hartmann wall Current (A/m)		21.48	21.49	21.49	21.51
Current in Hartmann Layer (A/m)		0.36	0.36	0.35	0
Hartmann layer current to Hartmann wall current ratio		0.0168	0.0169	0.0162	0
Deviation in current conservation (percentage)		0.933	1.094	1.342	1.774
Core current density (A/m ²)	4	- 3296.31	-3296.71	-3297.2	-3285.31
Integral core current (A/m)		-82.15	-82.12	-82.09	-82.02
Hartmann wall Current (A/m)		82.05	82.02	81.98	82.03
Current in Hartmann Layer (A/m)		0.33	0.3	0.15	0
Hartmann layer current to Hartmann wall current ratio		0.0041	0.0037	0.0019	0
Deviation in current conservation (percentage)		1.114	2.115	3.038	0.002

*The integral core current is estimated by integrating the core current along the applied magnetic field. Similarly, the Hartmann wall current and current in the Hartmann layer is integrated over their respective thickness.

Table 4-3: Comparison of the induced currents in different grid system for rectangular geometry

Property	Magnetic Field (T)	Grid 1	Grid 2	Grid 3	Grid 4
Core current density (A/m ²)	1	-414.8	-414.85	-414.96	-411.87
Integral core current (A/m)		-20.59	-20.59	-20.59	-20.35
Hartmann wall Current (A/m)		20.24	20.24	20.23	20.29
Current in Hartmann Layer (A/m)		0.40	0.4	0.39	0
Hartmann layer current to Hartmann wall current ratio		0.0198	0.0197	0.0194	0
Deviation in current conservation (percentage)		0.78	0.99	1.30	1.20
Core current density (A/m ²)	4	-1499.15	-1499.02	-	-
Integral core current (A/m)		-74.81	-74.80	-74.72	-74.19
Hartmann wall Current (A/m)		74.54	74.54	74.57	74.95
Current in Hartmann Layer (A/m)		0.37	0.31	0.19	0
Hartmann layer current to Hartmann wall current ratio		0.005	0.0042	0.0025	0
Deviation in current conservation (percentage)		1.22	2.03	2.70	1.03

Table 4-4: Deviation of Hartmann layer current in different grid system w. r. t Grid-1

Physical quantity	Magnetic Field (T)	Percentage error with respect to Grid 1					
		square			rectangle		
		Grid 2	Grid 3	Grid 4	Grid 2	Grid 3	Grid 4
Hartmann Layer Current	1	0.66	3.66	100	0.75	2.19	100
	2	5.13	14.45	100	1.41	15.11	100
	3	11.32	44.98	100	5.20	18.31	100
	4	10.5	54.65	100	15.16	48.89	100

The core current (J_{xc}) for grid systems of both geometries assuming a fully developed flow is estimated using the relation Eqn (4.8) [14].

$$J_{xc} = -\frac{C}{1+C} \sigma W_c B_0 \quad \text{Eqn (4.8)}$$

Where, $C = \sigma_w t_w / \sigma a$ This comparison is shown in Table 4-5 for the two extreme cases- Grid 1 and Grid 4 of both geometries at 1T and 4T fields. The variation in the core current between numerical and analytical relation is within 2.5%, thus validating the model used.

Table 4-5: Comparison of numerical and analytical fully developed core current density

Magnetic Field (T)	Core Current Density (A/m ²)	Square		Rectangle	
		Grid 1	Grid 4	Grid 1	Grid 4
1	Numerical	-883.6	-876.16	-414.8	-411.87
	Analytical	-863.16	-862.69	-409.74	-410.56
4	Numerical	-3296.31	-3285.31	-1499.15	-1485.27
	Analytical	-3282.87	-3280.53	-1488.89	-1495.83

4.8.2 Comparison for core velocity

Due to the strong breaking effect of the Lorentz force, the central portion of the duct experiences a constant core velocity. A comparison among the grids with regard to core velocity is summarized for 1T and 4T magnetic field in Table 4-6. Errors are to the tune of 0.5% or lesser for both geometries. The above obtained values of core velocities are compared with the values from analytical relation [14] given in Eqn (4.9) and is shown in Table-4.7 for Grid 1 and Grid 4 of both geometries.

$$w_c = \left(-\frac{1+C}{C} \right) \frac{\partial \phi_h}{\partial x} \quad \text{Eqn (4.9)}$$

The value $\partial \phi_h / \partial x$ represents the transverse electric potential gradient in the Hartmann wall, in a fully developed flow regime.

Table 4-6: comparison of core velocity in different Grid system

Magnetic Field (T)	Core velocity (m/s), square				Core velocity (m/s), rectangle			
	Grid 1	Grid 2	Grid 3	Grid 4	Grid 1	Grid 2	Grid 3	Grid 4
1	0.0082 3	0.0082 3	0.0082 3	0.0082 3	0.0072 9	0.0072 9	0.0072 9	0.0073 0
4	0.0078 3	0.0078 3	0.0078 2	0.0078 2	0.0066 2	0.0066 2	0.0066 2	0.0066 5

The general trend observed is that the errors between the numerical and analytical solution reduces with increase in the magnetic field. This can be attributed to the fact that at higher magnetic fields, due to reduced Hartmann layer thickness, the jump in electric potential through boundary layer is less. So, the error in estimation of electric potential gradient in the Hartmann wall is close to the transverse potential gradient in the core. At lower magnetic field, due to thicker boundary layer the potential gradient in the wall will be lower. Lower potential gradient will lead to under estimation of core velocity estimated from Eqn(4.9) at lower magnetic fields thereby, increasing the error as shown in Table 4-7. Variation in the grid system, however, does not give any appreciable change when compared with the analytical estimation of core velocity, for both geometries. As similar trends are observed for intermediate fields, only 1T and 4T are tabulated.

Table 4-7: Comparison of numerical and analytical core velocity

Magnetic Field (T)	Grid System	Core Velocity (m/s) Square			Core Velocity (m/s) Rectangle		
		Numerical	Analytical	% Error	Numerical	Analytical	% Error
1	Grid 1	0.00823	0.00820	0.44	0.00729	0.00720	1.18
	Grid 4	0.00823	0.00821	0.27	0.00730	0.00722	1.13
4	Grid 1	0.00783	0.00783	0.03	0.00662	0.00663	0.11
	Grid 4	0.00782	0.00782	0.01	0.00665	0.00667	0.20

4.8.3 Comparison for side layer jet velocity

Formation of current loops leads to a parabolic distribution of electric potential along the length of the side wall, with maximum potential difference developed at the centre. Since the electric potential beyond the side wall boundary layer is constant along the applied field direction, the maximum potential at the centre of the side wall leads to higher electric field and hence as per Ohm's law Eqn (4.5), the local velocity in side layer increases. The variation in the velocity profile within the side layers is shown in Fig. 4.12. The comparison is done at 1T and 4T, between Grid 1, Grid 4 and a solution that is obtained from analytical model based on variational principle [15]. The intermediate fields have not been shown due to similarity in trends. Fig. 4.12(a) and Fig.4.12(b) shows a close agreement for the side layer peak velocity between the fine and the coarse grid systems for both square and rectangular geometry. The fine grid system also matches with the analytical solution. However, higher deviations of about 5% are observed for Grid 1 of the Rectangle channel on comparison with analytical solution, indicating that Grid 1 may have to be further refined to increase of accuracy.

Fig. 4.12(a)

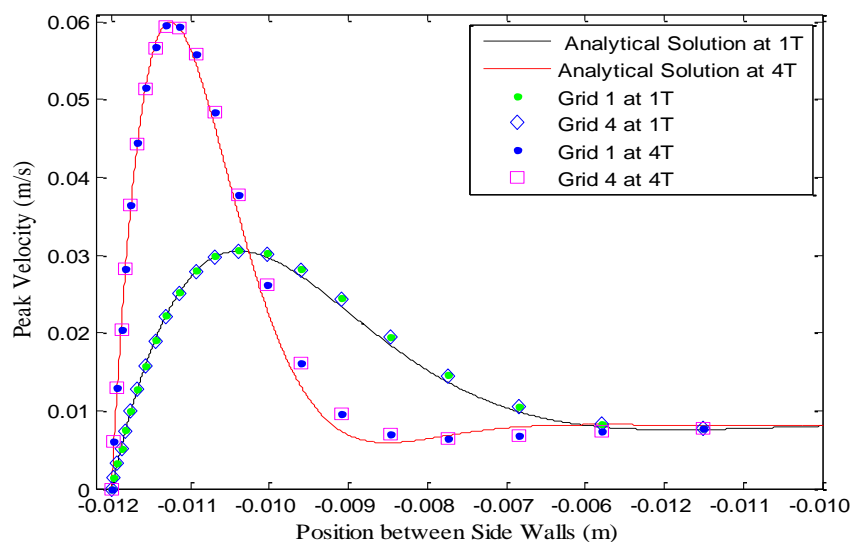


Fig. 4.12(b)

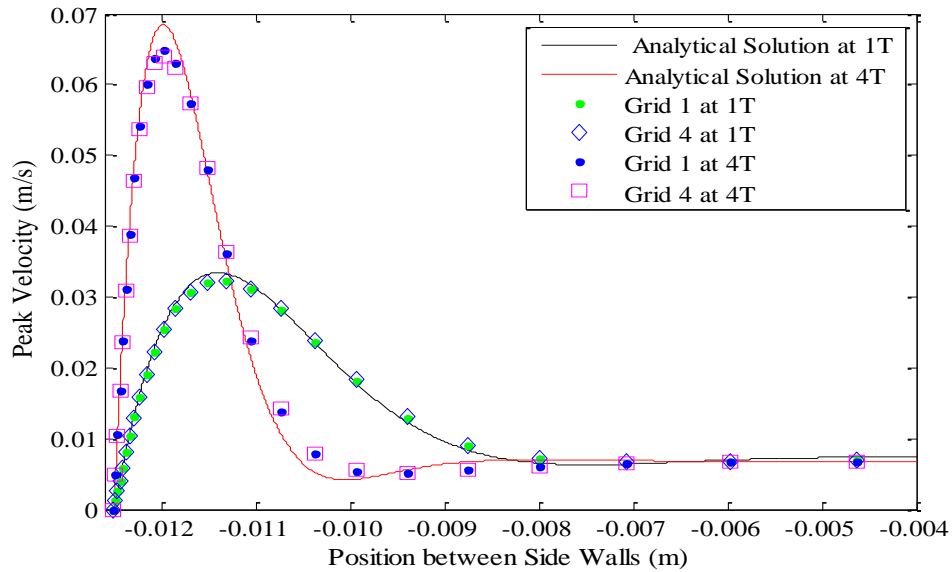


Figure 4.12: Comparison for side layer peak velocity in different grid system; for square channel in Fig. 4.12(a) and for rectangular channel in Fig. 4.12(b)

4.8.4 Pressure drop comparison

Fig. 4.13 shows the total pressure drop developed at different magnetic fields, for the grid systems under study. From these values, the developed flow pressure gradient is also calculated. The percentage deviations, in both the pressure drop and developed flow pressure gradient with respect to Grid 1 do not exceed 1%. The pressure drop is directly affected by the electromagnetic force that opposes the flow, which in turn depends on the induced current developed. As the error obtained in induced current generation due to unresolved Hartmann layer is negligible, pressure distribution is not affected significantly

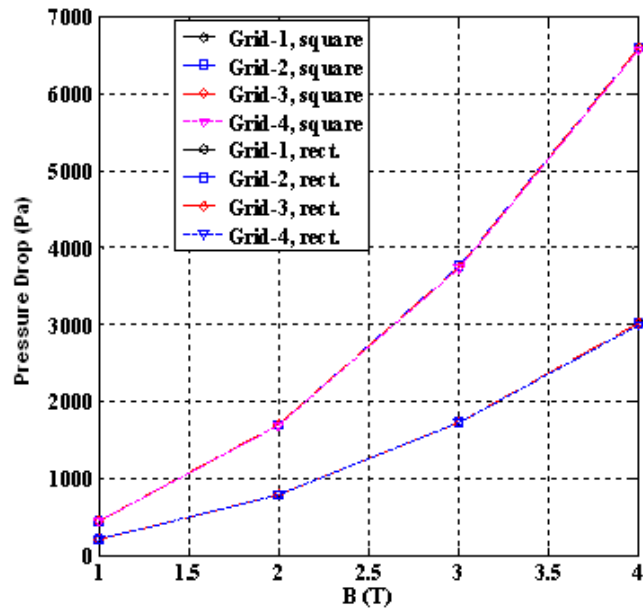


Figure 4.13: Variation of pressure drop with applied magnetic field for various grid system

4.9 Summary of the numerical studies for non-resolved Hartmann layer

The study quantifies the influence of the resolution of the Hartmann boundary layer on the flow field variables in electrically conducting, straight, rectangular ducts. The maximum error obtained in core current and wall current estimation for ~48% coarser mesh in square or rectangular geometry with respect to a finely resolved system is around 1.5% for square cases and around 1.2% for the rectangular geometry. For both the geometries, peak and core velocities are deviated by ~1.5% and ~0.5% respectively, with respect to the fine system. Variations in pressure drop and developed flow pressure gradient is to the tune of 1% when compared with the fine system for both geometries. It has also been established that coarsening the grid up to 50% by not resolving the Hartmann layer in a straight duct of electrically conducting walls gives at least first hand results and is a promising means for reducing the computational time and resources, for complex geometry MHD simulations. For insulating walls however, all the currents will close through the Hartmann layer, and if the layer is not sufficiently resolved, realistic capturing of the flow phenomena will not be possible. Resolution of the Side layer must be adequate for a proper mapping of the local velocity peaks that are

produced in them. However, the effect of coarsening the grid in Hartmann layer of electrically coupled channels consisting of multiple perpendicular bends has to be studied for generalization of this result for a general, arbitrary geometry of conducting confining walls.

4.10 References

1. A. Kimura, Current status of reduced activation ferritic/martensitic steels R&D for fusion energy, *Material Transactions*, 46 (2005)
2. B. V. Schaaf, D. S Gelles, et al., Progress and critical issues of reduced activation ferritic / martensitic steel development. *Journal of nuclear material*, 283 (2000)
3. L. Giancarli, V. Chuyanov, et al., Breeding blanket modules testing in ITER: An international program on the way to DEMO, *Fusion Eng. and Des.* (2006)
4. L. M. Giancarli, M. Abdou, et al., Overview of the ITER TBM program, *Fusion Eng. and design* 87 (2012)
5. R. Bhattacharyay, A. Patel, et al., Liquid metal MHD experimental activities for LLCB TBM development, *Fusion Eng. and Des* (2013)
6. A. Carabineanu, A. Dinu, et al., The application of the boundary element method to magnetohydrodynamic duct flow, *Zangew Math Phys* 46 (1995)
7. N. B. Salah, A. Soulaïmani, et al., A finite Element Method for Magnetohydrodynamics, *Comput. Methods in Appl. Mech. Engg.*, 190 (2001)
8. Ni, M.J., et al., A current density conservative scheme for incompressible MHD flows at low magnetic Reynolds number. Part II: on an arbitrary collocated mesh. *J. Comput. Phys.* 227, (2007)
9. FLUIDYN-MP: Ver. 5.2.1: User's guide. FLUIDYN (2011)
10. E. Mas de les Valls, et al., MHD thermofluid flow simulation of channels with a uniform thermal load as applied to HCLL breeding blankets for fusion technology, *Magnetohydrodynamics*, 48 (2012)
11. T. Zhou, Z. Yang, et al., Code development and validation for analyzing liquid metal MHD flow in rectangular ducts, *Fusion Eng. Des.* 85 (2010)
12. P.A. Davidson, Book: *An Introduction to Magnetohydrodynamics*, Cambridge University Press, (2001)
13. Patankar, Suhas V, Book: *Numerical Heat Transfer and Fluid Flow*, Taylor & Francis, (2011)

14. P. K. Swain, P. Satyamurthy, et al., 3D MHD lead–lithium liquid metal flow analysis and experiments in a Test-Section of multiple rectangular bends at moderate to high Hartmann numbers, *Fusion Eng. and Des.*, 88 (2013)
15. S.I. Sidorenko, A. Ya. Shishko, Variational method of calculation of MHD flows in channels with large aspect ratios and conducting walls, *Magnetohydrodynamics*, 27 (1991)

5 CHAPTER

Mock-up Experiments and Numerical Studies for LLCB TBM Variants

5.1 Introduction

For TBM program of ITER, MHD experiments and numerical simulation in scaled test sections at high magnetic fields is useful for generating database and to understand various flow phenomena at fusion relevant conditions. In particular, test sections with features of electrically coupled multiple channels are of practical interest to many international partners including India. The Indian concept of LLCB variant, where liquid metal Pb-Li serves dual purpose of coolant and tritium breeder is flowing in multiple parallel channels and are fed from a common header which enable to reduce overall MHD pressure drop [1, 2]. Distribution of flow rate and profile in individual channels in such type of parallel configuration is a function of characteristics Hartmann number ($Ha = B_0 a \sqrt{\sigma/\mu}$) and interaction parameter ($N = \sigma a B_0^2 / \rho U_0$) and associated geometric parameters like orientation of inlet axis with respect to the applied magnetic field, relative wall conductance ratio and channel layout [3]. Here, B_0 , σ , μ , ρ are the strength of the applied magnetic field, electrical conductivity, dynamic viscosity and density of Pb-Li. Variables 'a' and 'U₀' are characteristics length and velocity scale. Prior prediction of flow rate distribution, velocity profile, wall potential distribution etc. is extremely difficult due to complicated MHD issues at relevant fusion conditions and complex flow path that consists of multiple L/U bends. The level of complexity is even more in the case of conducting channels, as the difference in induced potential caused by uneven flow rate and varying direction of the flow that drive 3-D currents in liquid metal as well as in the structural walls and consequently modify the flow behaviour [4]. As the strength of the applied magnetic field, scale and kind of neutronic environment of ITER is unique, laboratory

experiments in full scale version of TBM is near impossible. However, mock up experiments with scaled down test sections are essential to provide valuable insight into the various MHD issues typically encountered in blanket applications.

Some of the complex issues encountered in generic blanket elements, number of experiments and computational studies have been performed earlier in scaled down test-sections not only to generate engineering data base but to validate numerical model also and possible extrapolation of the numerical code performances at fusion relevant conditions. MHD experiments with NaK at high Hartmann number (up to $Ha=4000$) have been studied by K Starke, et al. in a scaled mock of HCLL TBM to study the effect of poloidal manifolds on flow partitioning in breeder units. Each breeder unit is consisting of electrically coupled multiple parallel radial channels formed by internal walls [5]. Numerical simulations have also been carried out for fully developed flow in the same geometry by C. Mistrangelo, L. Buhler using modified CFX code [6]. For US DCLL TBM, numerical simulation of Pb-Li MHD flow in poloidal running parallel flow channels connected with toroidally oriented manifold has been carried out by N. B. Morley, et al. using advanced HIMAG computer code based on a consistent and conservative scheme for determination of current density [7]. Analysis of 3-D MHD pressure loss in a prototype non-conducting manifold consisting of rectangular feeder duct with sudden expansion in the direction of the magnetic field were numerically simulated using MHD code HIMAG for a wide range of flow parameters and correlations were proposed based on the numerically computed 3-D pressure loss in the manifold [8].

In this chapter, numerical and experimental studies of PbLi MHD flow carried out in a multichannel test section subject to high magnetic fields are presented. In another study, numerical simulation performed in a mock-up test section at Efremov scientific institute of Russian Federation (RF) for liquid metal NaK MHD flow is presented. The RF experiment test section simulated two electrically coupled parallel channels of LLCB TBM with variable

number of partition plates and flow was subject to variable magnetic field along the flow path. Numerical studies performed in this RF-test section address the effects of inlet manifold on flow rate distribution among parallel channels and their sub channels formed by partition plates. The studies also include comparison of the experiment and numerical results for velocity, wall electric potential distribution at different locations and pressure drop for such type of complex magnetic field distribution [9].

5.2 Numerical and experimental MHD studies in a multichannel test section

In context to the LLCB flow configuration, experiments have been performed at high magnetic fields (1-3 T) to study the MHD assisted molten Lead-Lithium (PbLi) flow in a model test-section which has typical features of multiple parallel channel flows with number of L/U bends. The experiment is carried out in PbLi liquid metal loop at Institute of Physics University of Latvia (IPUL) and test section dimensions are scaled down in view of accommodating it in the superconducting magnet bore of 300 mm diameter. In addition to reduction in the size of the channels, only two channels of parallel flow (as against 5 channels proposed in the Indian TBM [1]) and a parallel counter flow channel and thus a total of 3 electrically coupled poloidal channels are provided due to the constraint of the magnet dimension. The characteristics Hartmann number ($Ha = B_0 a \sqrt{\sigma/\mu}$) of the presented case study is up to 1557 which is relevant to typical fusion blanket conditions. Symbols B_0 , a , σ , μ in the definition of Hartmann number are strength of the applied magnetic field, characteristic length scale which is half the channel width parallel to the magnetic field, electrical conductivity and dynamic viscosity of PbLi respectively.

3-D numerical simulation has been performed for the exact physical model based on the laminar approximation and is presented in this section. Numerical prediction of flow rate distribution in parallel channels for different applied magnetic field strength is compared with the estimated values from the measured side wall potential difference data. The validity of

numerical results of wall potential distribution based on laminar model is verified by a proposed similarity coefficient. Non dimensional numerical profile for side wall potential distribution is used to estimate the flow rate in each channel instead of using a fully developed model. A qualitative discussion on flow profile asymmetry in parallel channels as obtained by the numerical solution is presented. The dominance of electromagnetic flow regime with variation of Ha/Re ratio is identified from total pressure drop in the test section. The comparison of such calculations with the experimental data makes it possible to decide, to a certain extent, on the applicability of the laminar approach.

The three parallel flow channels of the test section are separated by dummy breeder boxes in which no heat source is provided. Working fluid PbLi is supplied to the two parallel flow channels from a common inlet header at the bottom, recombine again at the top header and then return through a similar parallel duct of larger width which is connected to the outlet through bottom outlet header. Liquid metal enters or exits from the bottom inlet/outlet header of the test-section through pipes oriented parallel to the axial magnetic field of the superconducting magnet. Schematic of liquid metal PbLi flow path in the multichannel experiment test section is shown in Fig. 5.1.

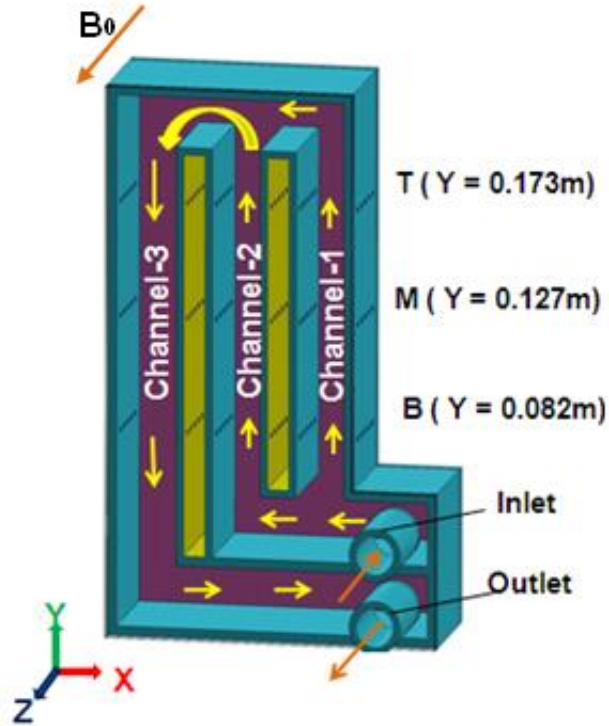


Figure 5.1: Schematic PbLi flow path in multichannel experiment test section

Although the test section model is not exactly the scaled down replica of LLCB TBM, the PbLi flow path in the experiment simulates some of the features of LLCB TBM flow configuration. As the strength of the applied magnetic field that determine the Hartmann layer thickness and imposes constraint in numerical modelling, the present experimental data and numerical simulation up to $B_0=3T$ is considered to be relevant for assessment of test blanket scenario. Further, in the present experiment, the 3D flow field is similar to that of the actual LLCB TBM.

5.3 Experiments in multichannel test section

Experiments have been carried out in the multichannel mock up test section at IPUL with Pb-Li as working fluid. Pb-Li flows at $350\text{ }^{\circ}\text{C}$ in the test section experiences a transverse magnetic field up to $3T$ produced by a cylindrical superconducting magnet of 300 mm diameter and 1000 mm length. The test section is placed at the central bore region of the superconducting magnet where the magnetic field is uniform both in axial and radial direction. Liquid metal

circulation is achieved through a variable speed MHD pump and the flow rate in the loop is measured by a DC electromagnetic flow meter placed outside the superconducting magnet. The flow meter is equipped with detachable permanent magnets and provides a linear relationship between flowrate Q (m^3/s) and potential difference U (mV) measured across its channel width. The photograph of the experimental loop and schematics of flow path in the test-section is shown in Fig.5.2. Experiments are carried out at different magnetic fields (maximum up to 3T) and the flowrate has been varied at each magnetic field so that characteristics MHD flow parameters of Hartmann number (Ha) and interaction parameter (N) is achieved in the range of 519-1557 and 3- 431 respectively. Physical value of the characteristic length scale is 0.025 m which is half the channel width along the direction of applied magnetic field and characteristic velocity U_0 is considered as the average velocity in channel-3.

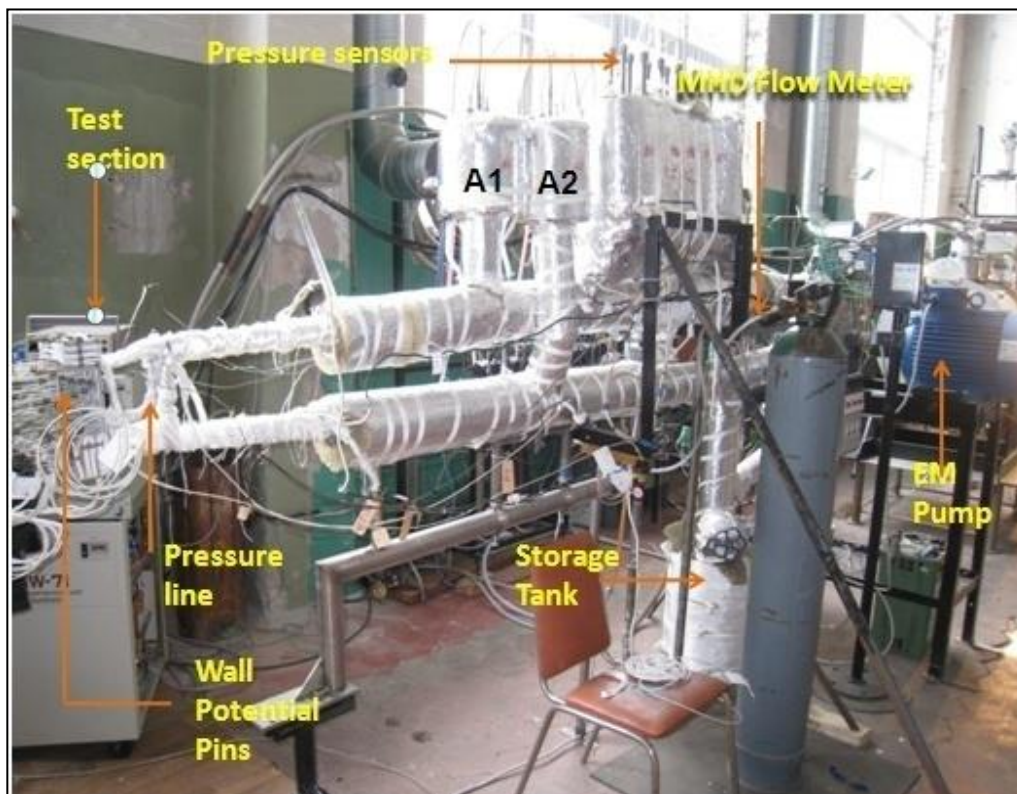


Figure 5.2: Photograph of the Pb-Li liquid metal experiment loop integrated with multi-channel test section at IPUL, Latvia

5.3.1 Details of test section

Test-section, made of SS316 material, consists of vertically oriented two electrically coupled parallel rectangular channels with a common inlet collector duct attached with inlet pipe and a similar return channel of counter flow path connected to the outlet pipe through bottom collector duct (see Fig. 5.3). The parallel flow channels are separated by 9 mm thick dummy breeder zones encased with 3mm thick SS plates. Design of the test section flow path is envisaged to simulate the flow configurations of scaled down Indian LLCB TBM. Liquid metal PbLi is supplied to the test section through inlet pipe (1/2" schedule 40) parallel to the axial magnetic field of superconducting magnet. After taking a 90° turn at the exit of inlet pipe the flow spreads into the bottom inlet collector duct (25mm × 50 mm) of the vertically oriented test-section and enters into two parallel rectangular channels each having a flow cross section of 20 mm × 50 mm. Then the flow combines at the top collector duct (20mm × 50mm) and returns through a rectangular duct of flow cross section 25mm × 50mm which is parallel to the other two vertical channels. Similar to the inlet pipe, the flow comes out from the test section through outlet pipe connected to the bottom outlet collector duct of same cross section as in the return channel. Bottom inlet and outlet collector ducts are separated by a 3mm thick partition plate. Flow path of Pb-Li is transverse to the applied magnetic field in the entire test geometry except at the inlet/outlet pipe. All the outer walls of the test-section are made of 4 mm and internal partition walls are of 3mm thick SS316 plates.

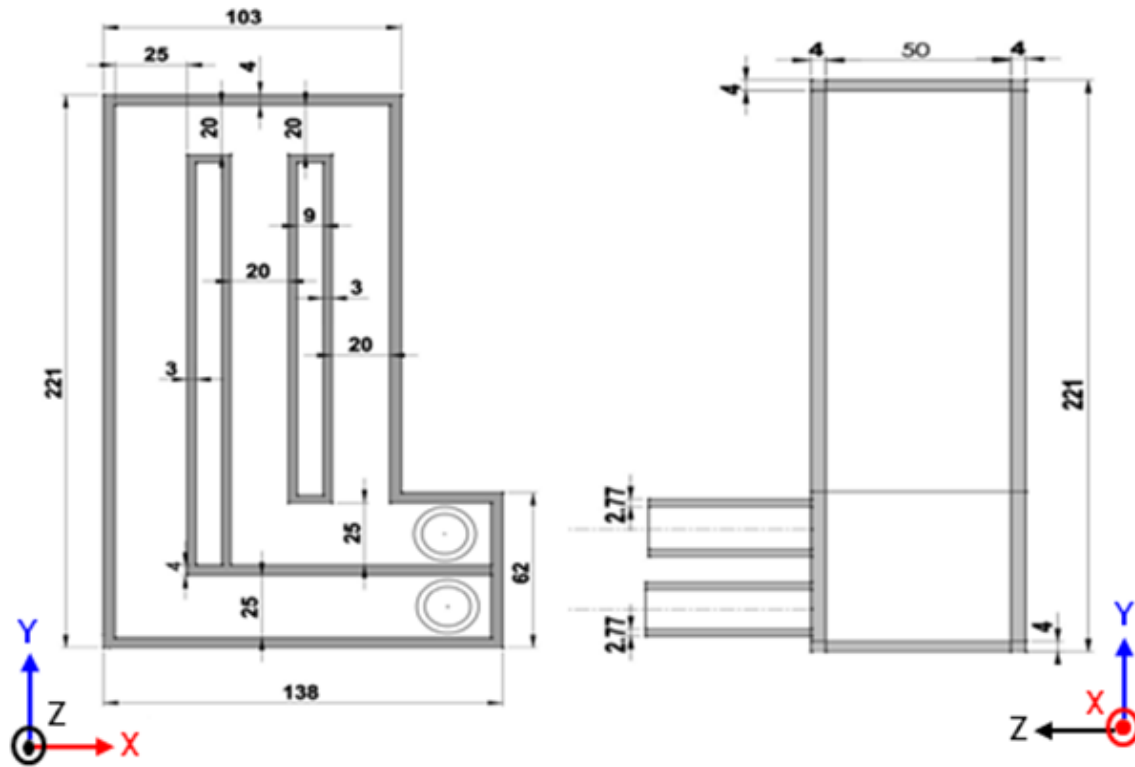


Figure 5.3: Dimensional details of various flow channels in multichannel test geometry

5.3.2 Diagnostics in multichannel test section

Wall electric potential distribution are measured with potential pins welded at various locations of the test section. Side wall potential difference along the applied magnetic field direction is measured by an array of 5 pairs of potential pins at 3 different heights (B, M & T) of the parallel channels. Photograph of the test section with various diagnostic locations and channel nomenclature is shown in Fig. 5.4. Five pairs of potential pins are uniformly placed with 8mm gap over 50 mm width of the side wall. Measured signals were in the range 0.6-36 mV depending on the flow rate and magnetic field strength. Prior to the experiment, spatial variation of the magnetic field is measured with a Hall probe. The variation of magnetic field strength in the test-section including the inlet/outlet pipe is less than 0.1%. Pressure drop in the test section with extended inlet outlet pipe line is measured with pressure transmitter located at A1 and A2 (see Fig. 5.2). Liquid metal pressure is obtained by measuring the cover gas pressure

of expansion tanks provided at these locations. Change in gas pressure with variation of liquid metal level in the expansion tank is assumed isothermal. Along the flow path the pressure is also recorded at various locations from the pressure sensors attached with B1, B2, B3, B4 and B5 expansion tanks. These expansion tanks are located outside the superconducting magnet and attached to the test-section through connecting pipes.

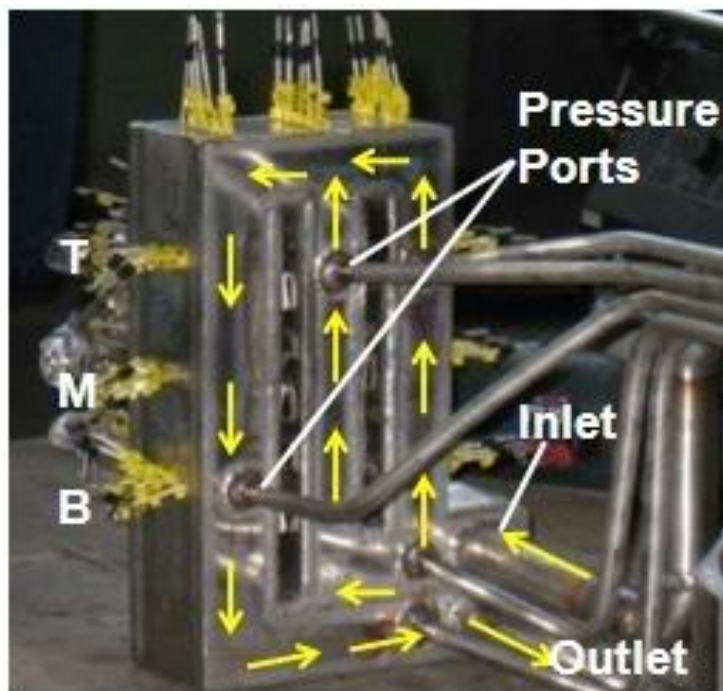


Figure 5.4: Photograph of multi-channel test section and diagnostic locations labelled with B, M, T at different channel of the test section

5.4 Flow modelling

5.4.1 Governing Equations

The following system of equations governing the steady state MHD flow of incompressible, electrical conducting fluid under the influence of external magnetic field has been solved in FLUENT [10] code. The effects of induced magnetic field are neglected due to small magnetic Reynolds number ($Re_m < 1$) [11] and the electromagnetic body force, as source term in the momentum equation is coupled with other equations based on electric potential

formulation. In view of electrical conducting channels and moderate characteristic parameters ($Ha > 1038$, $N > 20$) the flow is expected to be laminar as Ha/Re value is above the critical number of transition ($Ha/Re > 0.02$) from turbulent to laminar regime [12].

$$(\vec{U} \cdot \vec{\nabla})\vec{U} = \frac{-\vec{\nabla}P}{\rho} + \nu \nabla^2 \vec{U} + \frac{\vec{J} \times \vec{B}_0}{\rho} \quad \text{Eqn(5.1)} \quad [\text{Modified Navier-Stokes equation}]$$

$$\vec{\nabla} \cdot \vec{U} = 0 \quad \text{Eqn(5.2)} \quad [\text{Conservation of mass}]$$

$$\vec{J} = \sigma (-\vec{\nabla}\phi + \vec{U} \times \vec{B}_0) \quad \text{Eqn(5.3)} \quad [\text{Generalised Ohm's law}]$$

$$\vec{\nabla} \cdot \vec{J} = 0 \quad \text{Eqn(5.4)} \quad [\text{Conservation of charge}]$$

Here, ρ , \vec{U} , ν , σ are density, velocity, kinematic viscosity, electrical conductivity of the fluid whereas P , \vec{J} , \vec{B}_0 , ϕ are pressure, electric current density, magnetic field induction, and electric potential respectively.

Equations (3) and (4) are combined in potential method formulation to solve electric potential ϕ from the following equation,

$$\nabla^2 \phi = \vec{\nabla} \cdot (\vec{U} \times \vec{B}_0) \quad \text{Eqn(5.5)}$$

Here, B_0 is the strength of applied magnetic field.

In the solid domain the following equation is solved for the electric potential

$$\nabla^2 \phi_w = 0 \quad \text{Eqn(5.6)}$$

Here ϕ_w is the potential distribution in the walls. At the fluid-wall interface, in addition to no-slip condition for the velocity, continuity of the normal component (to the walls) of current density ($J_n = J_{nw}$) have been applied. Here J_n refers to the normal component of current density on the fluid side and J_{nw} corresponds to the wall side.

5.4.2 Boundary conditions

For velocity field, no-slip condition has been used at the solid surface. At the inlet uniform velocity and at the outlet, a homogenous Dirichlet pressure condition ($P=0$) is applied. For the electric potential, insulation is assumed beyond the outer walls and a homogeneous Neumann condition $\partial\phi/\partial n=0$ is applied.

5.5 Numerical model geometry and mesh

Numerical simulations in the test model is carried out in the CFD facility of VJTI, Mumbai, India using FLUENT code to obtain the flow field solutions and compared with experimental values. Benchmarking and model validation of the code has already been reported for a straight duct (with Hunt's analytical model), for a test-section consisting of multiple 90° bends (with experiments at high Hartmann number up to $Ha=2060$) [13] and also MHD flow in parallel channels at 1T field [9]. Dimensional limits of the test-section computation domain are confined to $0 \leq X \leq 0.138$ m, $0 \leq Y \leq 0.221$ m and $0 \text{ m} \leq Z \leq 0.098$ m (see Fig. 5.3). Uniform magnetic field is applied along \bar{z} direction. Two vertical channels with co-current flow (channel-1 & channel-2) start at $Y=0.057$ m from bottom inlet collector duct ($0.033 \leq Y \leq 0.057$ m) and subsequently combines at top collector duct extends from $0.057 \leq Y \leq 0.077$ m. The return channel (channel-3) extends from $0.033 \leq Y \leq 0.219$ along with the bottom collector duct starts from $0.004 \leq Y \leq 0.029$ m. For computation, the length of the inlet and outlet pipe is taken as 40 mm ($0.058 \leq Z \leq 0.098$ m).

5.5.1 Grid details and Physical properties

The geometry is meshed with multi-block hexahedral structure grid with total number of volume elements ~ 2.05 million. Hartmann layers and side layers (Shercliff boundary) are resolved with 3 elements ($\delta_H \approx 1.6 \times 10^{-5}$ m) and 12 elements ($\delta_s \approx 0.63 \times 10^{-3}$ m) respectively for maximum Hartmann number of 1557. The optimum grid structure is obtained by performing the grid independent analysis for 3 different grid structures as shown in Appendix A. To

optimize the computation, the flow cross section is meshed with variable spaced grid points and structural walls are meshed with uniform spacing for 5 numbers of elements along the thickness. The properties of the PbLi are taken as 9402 kg/m^3 , $7.7616 \times 10^5 \text{ S/m}$, $1.8 \times 10^{-3} \text{ Pa-s}$, for density (ρ), electrical conductivity (σ) and dynamic viscosity (μ) respectively and electrical conductivity (σ_w) of the structural wall are taken as $1.01 \times 10^6 \text{ S/m}$ in present numerical simulation [14].

5.6 Numerical results in multi-channel test model and comparison with experiment

Although experiments are carried with different flow rates at each magnetic field (1-3 T), numerical analyses have been presented for higher magnetic fields (2 & 3 T) and for two flow rates for each case. Flow parameters of different numerical case studies and respective non dimensional parameters are shown in Table-5.1. The characteristics non dimensional value for Reynolds number (Re) and interaction parameter (N) as presented in Table 5-1 corresponds to the channel-3 (Return path) of the test section. For individual channel, these values will be different since the mean velocity in respective channel varies from case to case. The flow rate in the test section used for numerical simulation is based on readings of flow meter integrated in the loop.

Table 5-1: Characteristics parameters of numerical model geometry of multi-channel test section

B_0 (T)	Volume flowrate (cm^3/s)	Mass flowrate (kg/s)	Ha	N	Re	Ha/Re
2.0	242.2	2.278	1038	42.6	25310	0.041
2.0	492.5	4.631	1038	20.95	51454	0.02
3.0	240.2	2.259	1557	96.7	25096	0.062
3.0	490.7	4.614	1557	47.4	51263	0.03

5.6.1 Numerical wall electric potential distribution and comparison with experiment

The measured side wall electric potential difference ($\Delta\phi_j, j = 1 - 5$) at location ‘M’ and location ‘T’ of all Channels is shown in Fig. 5.5(a) and Fig. 5.5(b) respectively for different

flow rates and applied magnetic field strength. Results of numerical estimations as shown by continuous lines in Fig. 3 and Fig. 4 are compared with corresponding measured values. For convenient presentation of the potential difference profile of all the channels, the Z-coordinate is linearly shifted to new coordinate ζ as defined by $\zeta = Z + 0.07 \times (3 - i)$, where $i=1, 2, 3$ for channel-1, 2 and channel-3 respectively. In all these cases the measured profile of side walls potential difference distribution at each location (B, M and T) is lower than the corresponding numerical estimations (see Fig. 5.5 and Fig. 5.6). This indicates the assumed flow rate in the numerical calculation based on the flow meter reading is higher than the actual flow rate in the loop.

Fig. 5.5(a):

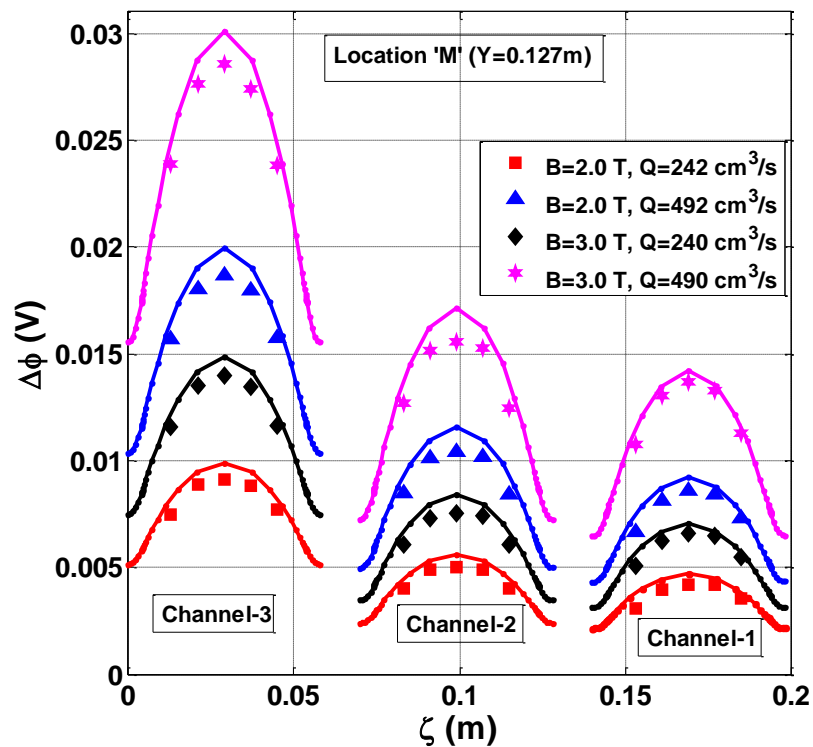


Fig. 5.5(b):

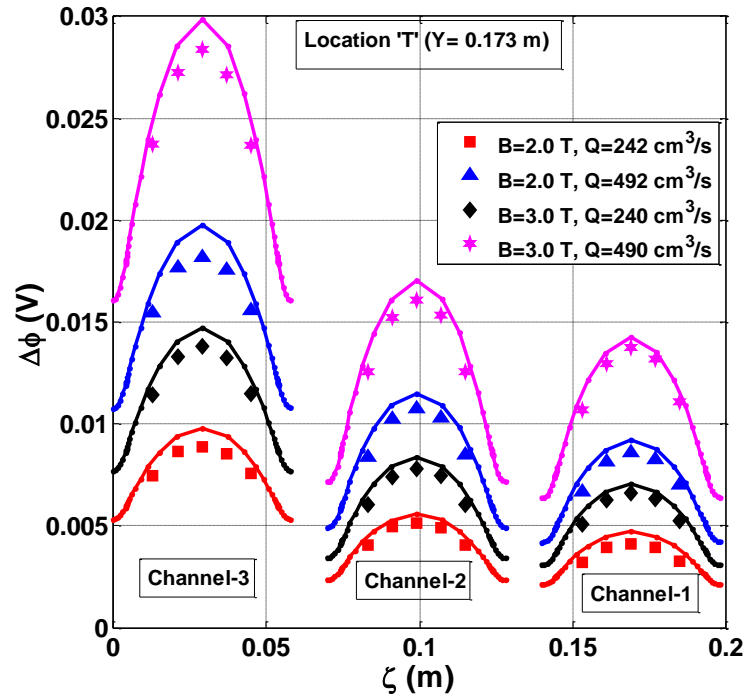


Figure 5.5: Comparison of measured side wall electric potential difference data with the corresponding numerical counterpart (represented by continuous lines) in each channel for different flow rates and applied magnetic field strength; at location ‘M’ in Fig. 5.5(a) and at location ‘T’ in Fig. 5.5(b)

Since the actual flow rate is different from the numerical flow rate, the values of measured wall potential at various locations of the test sections is consistently deviating with the numerical simulation. In order to establish the degree of similarity between the numerical and experimental picture of wall potential distribution, a similarity coefficient for numerical data ($K_{i,j}^{num}$) and experiment data ($K_{i,j}^{expt}$) have been proposed as defined in Eqn. (5.7)

$$K_{i,j}^{num,expt} = \frac{\Delta\phi_{i,j}^{num, expt}}{\Delta\phi_{3,j}^{num, expt}} \quad \text{Eqn(5.7)}$$

Where, $i = 1, 2$ for channel-1 and channel-2 and $j = 1-5$ for five pair of pins at each location (B, M and T) and $\Delta\phi_{3,j}$ is the potential difference data of j^{th} pair pins of channel-3 (return channel).

The abbreviation ‘num’ and ‘expt’ corresponds to the numerical and experimental data respectively. The closeness of $K_{i,j}^{num}$ and $K_{i,j}^{expt}$ will determine the degree of similarity

between the numerical and experiment model. Comparison of the similarity coefficients ($K_{i,j}^{num,expt}$) at each location (B, M and T) for a specific case of $B=3T$ and $Q=240.2 \text{ cm}^3/\text{s}$ is shown in Table 5-2. As can be seen with the proposed version of similarity coefficient for electric potential distribution $\phi(x, y, z)$, $K_{i,j}^{num}$ of individual channel-1 & channel-2 has excellent agreement with the measured values ($K_{i,j}^{expt}$) and more or less close to the numerical average ($\langle K_i^{num} \rangle$).

Table 5-2: Similarity coefficients of numerical and experimental data for case of $B_0=3T$ and $Q=240.2 \text{ cm}^3/\text{s}$ in multi-channel test section

B=3T, Flow rate (Q) = 240.2cm³/s, Locations: B // M // T					
j^{th} pair $\Delta\phi$ at locations B// M// T	J=1, Z=0.013m B // M // T	J=2, Z=0.021m B // M // T	J=3, Z=0.029m B // M // T	J=4, Z=0.037m B // M // T	J=5, Z=0.045m B // M // T
$\Delta\phi_{1j}^{num}$ [mV]	5.78 // 5.81 // 5.81	6.73 // 6.87 // 6.88	7.08 // 7.25 // 7.27	6.74 // 6.87 // 6.88	5.8 // 5.81 // 5.81
$\Delta\phi_{2j}^{num}$ [mV]	6.51 // 6.51 // 6.51	7.73 // 7.79 // 7.79	8.16 // 8.25 // 8.25	7.73 // 7.79 // 7.79	6.52 // 6.51 // 6.51
$\Delta\phi_{3j}^{num}$ [mV]	12.26 // 12.26 // 12.25	14.24 // 14.19 // 14.09	14.95 //14.89 // 14.75	14.24 // 14.19 // 14.09	12.26 // 12.26// 12.25
$\Delta\phi_{1j}^{expt}$ [mV]	5.00 //5.05 // 5.09	6.10 // 6.26 // 6.27	6.46 // 6.62 // 6.6	6.37 // 6.5 // 6.33	5.46 // 5.49 // 5.22
$\Delta\phi_{2j}^{expt}$ [mV]	6.18 //6.07 // 6.04	7.19 // 7.31 // 7.39	7.54 // 7.55 // 7.78	7.18 // 7.43 // 7.43	5.97 // 6.05 // 6.05
$\Delta\phi_{3j}^{expt}$ [mV]	11.47 // 11.58 // 11.43	13.5 // 13.52 // 13.30	14.05 // 13.97 // 13.82	13.47 // 13.42//13.22	11.53 // 11.60 // 11.5
$K_{1,j}^{num}$	0.471 // 0.474//0.474	0.473 // 0.484//0.488	0.474 // 0.487// 0.493	0.473// 0.484//0.488	0.473// 0.474//0.474
$K_{1,j}^{expt}$	0.436// 0.436//0.445	0.452 // 0.463//0.471	0.46 // 0.474//0.478	0.473 // 0.484//0.479	0.473 // 0.473//0.454
$K_{2,j}^{num}$	0.531 // 0.531//0.531	0.543 // 0.549//0.553	0.546 // 0.554//0.559	0.543 // 0.549//0.553	0.532 // 0.531//0.531
$K_{2,j}^{expt}$	0.539 // 0.524//0.528	0.533 // 0.541//0.556	0.537 // 0.540//0.563	0.533 // 0.554//0.562	0.518 // 0.522//0.526

The root mean square deviation of the similarity coefficients at each location $\sigma_i^{B,M,T}$ and overall deviation σ_i for the individual channel-1 and channel-2 have been estimated using equation Eqn (5.8) and Eqn(5.9) as shown in Table 5-3 for all the cases studies. The overall deviation σ_1 and σ_2 for channel-1 and channel-2 with the average numerical similarity coefficient is within 5% in most of the places except at bottom location of channel-1. Hence it may be concluded that results of numerical calculation based on laminar approximation is satisfactory in the bulk of the flow domain. However, higher deviation of in channel-1 indicates possible measurement error at low voltages and limitation of the laminar model to account the presence of larger residual turbulence near the bends at higher flow rates and lower magnetic fields. The proposed version of the similarity coefficient eliminates the systematic error due to inaccuracy in flow rate measurement and is a unique way of validating the numerical model.

$$\sigma_i^\ell = \sqrt{\frac{\sum_{j=1}^5 (K_{i,j}^{\ell, \text{num}} - K_{i,j}^{\ell, \text{expt}})^2}{5}} \quad \text{Eqn (5.8)}$$

$$\sigma_i = \sqrt{\frac{\sum_{\ell=1}^3 \sum_{j=1}^5 (K_{i,j}^{\ell, \text{num}} - K_{i,j}^{\ell, \text{expt}})^2}{15}} \quad \text{Eqn (5.9)}$$

Here index ℓ corresponds to location 'B', 'M' and 'T' and $i=1, 2$ for channel-1 & channel-2 respectively.

Table 5-3: Root mean square deviation of similarity coefficients in multichannel experiment

Case B=3T Q=240.2 cm³/s						
	σ^B	σ^M	σ^T	σ	$\langle K^{num} \rangle$	Deviation (%)
channel-1	0.012873	0.013826	0.008047	0.011855	0.465467	2.55
channel-2	0.018955	0.019652	0.00912	0.01662	0.5527	3.0
Case B=3T Q=490.7 cm³/s						
channel-1	0.011875	0.01068	0.011313	0.0113	0.47754	2.4
channel-2	0.010402	0.00911	0.005292	0.00855	0.5424	1.6
Case B=2T Q=242.2 cm³/s						
channel-1	0.035179	0.033599	0.036666	0.03517	0.476036	7.38
channel-2	0.038707	0.033006	0.018094	0.009977	0.546403	1.83
Case B=2T Q=492.5 cm³/s						
channel-1	0.03804	0.0224	0.0185	0.0276	0.4715	5.85
channel-2	0.0077	0.0058	0.0134	0.0095	0.5536	1.72

5.6.2 Estimation of flow rate using numerical profile of wall electric potential distribution

At the location 'M' ($Y=0.127$ m) which is ~ 2.8 times the characteristic length ($a=0.025$ m) from the bottom and top manifold, the flow under single channel flow configuration is expected to be fully developed due to stronger electromagnetic forces at high Hartmann number. However, because of top and bottom wall of the test section and flow turning at the nearby 90° bends ($Y=0.197$ m) in upstream and downstream generates 3-D electrical currents. These additional current loops are closed through the liquid metal and breeder walls of parallel channels and modify the flow distribution continuously and hence does not attain fully developed configuration. To ascertain this, the normalized wall electric potential distribution for various flow rates and higher applied magnetic field strength (2T and 3T) are compared with the corresponding theoretical estimations based on fully developed theory [15] as shown in Fig. 5.6(a) and Fig. 5.6(b).

Fig. 5.6 (a):

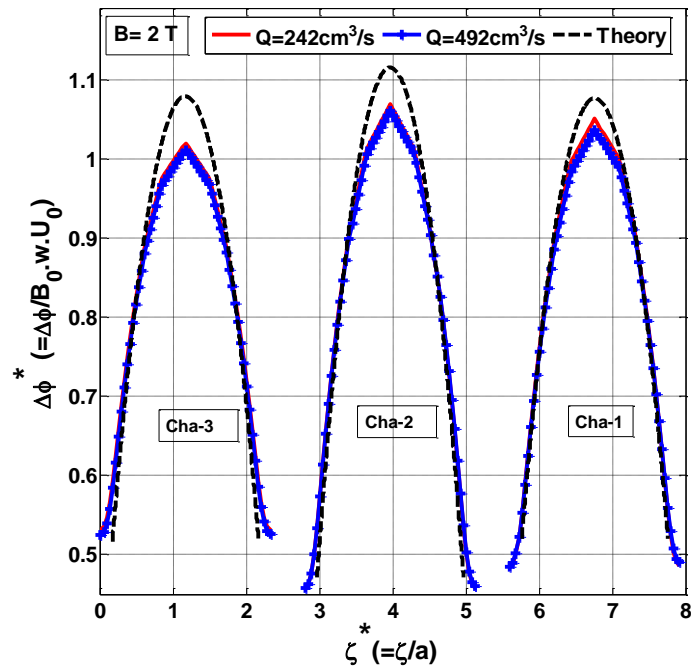


Fig. 5.6 (b):

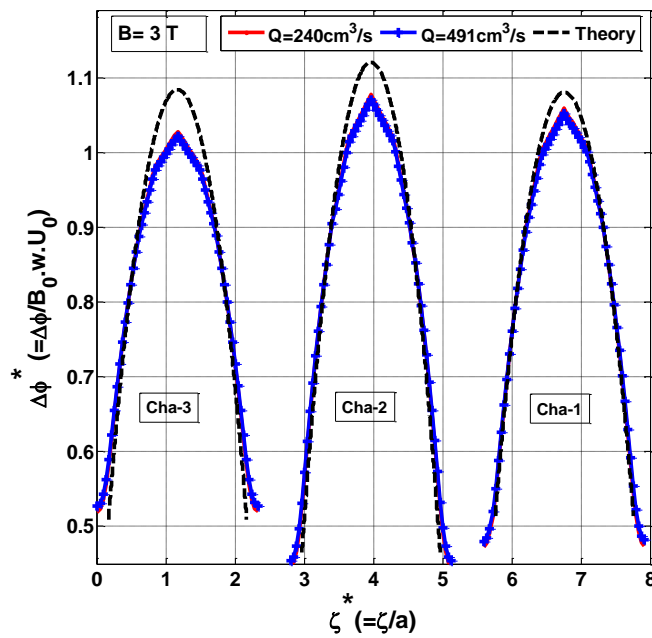


Figure 5.6: Normalized side wall electric potential difference distribution and comparison with corresponding theoretical profile (dotted line) in all the channels at location 'M' for different flow rates; for $B_0 = 2 \text{ T}$ in Fig. 5.6(a) and for $B_0 = 3 \text{ T}$ in Fig. 5.6(b)

As can be seen, although the side wall potential distribution is symmetric, it is significantly deviated from the asymptotic profile even at higher magnetic field strength of 3T. So the conventional approach of estimating the flow rate in individual channels from side wall potential data, assuming the flow to be fully developed, [16, 17] may not be applicable for the present experimental test-section. However, we can use non dimensional numerical profile of side wall potential distribution as a reference profile to estimate the flow rate provided the variation is insignificant in that range of flow rates and applied magnetic field strength. The assumption holds true at locations free from bend effects and at large interaction parameter. As can be seen in Fig. 5.6(a) and Fig. 5.6(b), the non-dimensional electric potential ($\Delta\phi_i / wU_{0i}B_0$) profiles are nearly identical with maximum deviation of less than 1% for various flow rates at each applied magnetic field. Here U_{0i} , ($i=1-3$) is the average velocity in the i^{th} Channel estimated from the numerical simulation and ‘w’ is the respective channel width (20 mm for channel-1 and channel-2) along the transverse direction of applied magnetic field. Since the non-dimensional reference potential difference profile which accounts all the geometrical coupling factors and is nearly independent of flow rate, it can be used to estimate the flow rate in individual channel from the measured side wall distribution of respective channels.

The induced voltage measured by pair of potential sensors across the side walls of a given flow cross section is proportional to the local average velocity. Unlike the open-circuit configuration where proportionality constant is one, correction factors must be included in determining the voltage signal as function of flow velocity to account return currents in the finite thickness of side walls. In present case of electrically coupled walls, numerical values of local non dimensional side wall electric potential difference ($\Delta\phi_j^{*num}$) is used as the proportionality constant to estimate the local average velocity. The average velocity in the cross section may be calculated by averaging the velocities estimated by each pair of side wall

potential pins in that cross section. Using this assumption, the measured flow rate in each channel is estimated from the side wall potential difference data $\Delta\phi_j^m$ ($j=1-5$) measured by j^{th} pair of potential pins across the channel width. The average velocity (U_j^i , $j=1-5$) at j^{th} location of cross section ‘M’ of i^{th} channel is estimated from the following relation.

$$U_j^i = \Delta\phi_j^m / (B_0 w_i \Delta\phi_j^{*num}) \quad \text{Eqn (5.10)}$$

Where, $\Delta\phi_j^{*num}$ is the non-dimensional potential difference at j^{th} location obtained from the numerical simulation, ‘ B_0 ’ is the applied magnetic field intensity, ‘ w_i ’ is the channel width transverse to the applied field direction.

The average velocity (U_i) in respective channel cross section is estimated as follows,

$$U_i = \frac{1}{5} \sum_{j=1}^5 U_j^i \quad \text{Eqn (5.11)}$$

Here, $i=1, 2, 3$ for channel-1, channel-2 and channel-3 respectively.

Using Eqn (5.10) & Eqn (5.11), the average velocity and corresponding flow rate in each channel is estimated. For illustration, the local average velocity ($j =1-5$) estimated from numerical non dimensional potential difference for channel-1 is shown in Table 5-4 for various case studies. The estimated flow rate (Q_E) is then compared with corresponding numerical counterpart (see Table 5-5). It should be noted that numerical flow rate (Q_{num}) in the channel-3 is based on Flow meter measured value. As can be seen in Table 5-5, the estimated flow rate (Q_E) based on the measured side wall potential of channel-3 is always lower than the flow meter measurement. The integral of estimated flow rate in channel-1 and channel-2 is close to the estimation in channel-3 with maximum deviation of less than 2.7% which may be attributed partly to the error in side wall potential measurement at low voltages. Thus, the consistent

estimation of a lower flow rate from the side wall potential data necessitates calculation of actual flow rate by some other alternative mean. However, as far as flow rate distribution is concerned, the fraction of flow in individual channel as predicted by numerical model and evaluated from the side wall potential measurement is more or less same. The fraction of flow rate in channel-2 for various case studies as shown in Table 5-5 is matching within 1% deviation. Thus the numerical model can be used to predict the flow rate distribution in coupled parallel channels of a typical blanket module at ITER relevant conditions.

Table 5-4: Local average velocity at Location ‘M’ of channel-1 estimated from measured side wall potential for various case studies

B₀=2T, flow rate = 242.2 cm³/s, mean velocity in channel-1 (U₁) =9.92cm/s					
j th location	j =1 (Z=0.013 m)	j =2 (Z=0.021m)	j = 3 (Z=0.029m)	j = 4 (Z=0.037 m)	j = 5 (Z=0.045 m)
$\Delta\phi_j^m$ [mV]	3.061	3.94	4.17	4.18	3.57
$\Delta\phi_j^{*num}$	0.8515	1.0003	1.0551	1.0025	0.8537
U _j [cm/s]	8.98	9.85	9.88	10.42	10.45
B₀=2T, flow rate = 492.5 cm³/s, U₁ = 20.52 cm/s					
j th location	j = 1	j = 2	j = 3	j = 4	j = 5
$\Delta\phi_j^m$ [mV]	6.67	8.11	8.58	8.39	7.27
$\Delta\phi_j^{*num}$	0.8515	0.9987	1.0515	0.9998	0.8526
U _j [cm/s]	19.58	20.3	20.4	20.98	21.32
B₀=3T, flow rate = 240.2 cm³/s, U₁ =10.93 cm/s					
j th location	j = 1	j = 2	j = 3	j = 4	j = 5
$\Delta\phi_j^m$ [mV]	5.05	6.26	6.62	6.5	5.49
$\Delta\phi_j^{*num}$	0.8097	0.961	1.0143	0.9624	0.8126
U _j [cm/s]	10.39	10.86	10.88	11.26	11.26
B₀=3T, flow rate= 490.7 cm³/s, U₁ =21.63 cm/s					
j th location	j = 1	j = 2	j = 3	j = 4	j = 5
$\Delta\phi_j^m$ [mV]	10.74	13.01	13.68	13.26	11.28
$\Delta\phi_j^{*num}$	0.8521	1.0033	1.059	1.0048	0.8543
U _j [cm/s]	21.01	21.61	21.52	21.99	22.01

Table 5-5: Estimated flow rate distribution based on the measured side wall potential data and comparison with numerical prediction for different case studies

B₀ (T)	*Numerical flow rate (cm³/s) based on Flow meter(Q_{num})				Estimated flow rate (cm³/s) using measured potential data (Q_E)			
	<i>cha-3</i>	<i>cha-2</i>	<i>cha-1</i>	<i>% flow in cha-2</i>	<i>cha-3</i>	<i>cha-2</i>	<i>cha-1</i>	<i>% flow in cha-2</i>
2.0	242.2	128.2	114.2	52.9	223.1	117.8	99.2	52.8
2.0	492.5	265	227.5	53.8	462.4	248.3	205.2	53.7
3.0	240.2	124.7	115.5	51.9	227.3	116.5	106.1	51.3
3.0	490.7	260.1	230.6	53	467.2	246	216.3	52.6

5.7 Discussion on of flow distribution in two parallel channels

Assessment of factors affecting the flow rate distribution in parallel channels is required to foresee the blanket performance at ITER condition. Apart from the effects of flow inertia and applied magnetic field strength, the present simulation indicates axial currents also play a key role in distributing the flow in parallel channels. These axial currents are generated by the complex flow path and various geometrical constraints like top and bottom plate, partition plate at the bottom inlet/outlet collector duct of the test-section. For a given magnetic field strength, percentage of flow in channel-2 is rising with increase in total flow rate. Even though fluid enters into parallel channels from the common inlet header after a 90 degree turn from the inlet pipe, effects of inertia lead to uneven flow distribution. However, with increasing N, flow distribution tends to saturate depending upon the coefficient of resistance (R_H^i) of the individual channel as defined in the following relation.

$$R_H^i = \nabla P_i / \sigma U_i B_0^2 \quad \text{Eqn(5.12)}$$

Here, ∇P_i is the pressure gradient in the i^{th} channel assuming the flow to be fully developed.

Since the effective thickness of the side walls of the channel-1 is more (3.5mm) as compared to the channel-2 (3 mm), the coefficient of resistance (R_H) is less ($R_H^2=0.0964$) for channel-2 as compared to the channel-1 ($R_H^1=0.102$) for $B_0=3T$ and hence draw more flow in channel-2.

The unequal flow distribution in the parallel channels can be explained by analysing the axial currents (J_y) generated in the inlet collector header where the flow turns from parallel (In the inlet pipe) to perpendicular direction (in the test section) of the applied magnetic field. 3D currents are generated by the top wall and bottom partition plate which is common to inlet/outlet collector ducts. Also, the difference in induced wall potential in different channel due to difference in average velocity and flow turning at bends leads to generation of 3D currents. The contour of electric potential in different walls of the test section is shown in Fig. 5.7. Since there is a gradient of potential in the upper as well as lower side wall of the extended inlet/outlet header region with opposite polarities, 3D currents are generated in this region that closes the path in the bottom inlet header. The axial current (J_y) induced in this region in the presence of transverse magnetic field ($B_0\vec{z}$) give rise to electromagnetic forces that redistribute the flow in channels depending upon its strength and direction. The profile of J_y current along the centre of the channel-1 including the bottom inlet header region is shown in Fig. 5.8. As can be seen, the magnitude J_y current increase with increasing the field strength which gives electromagnetic force in \vec{x} direction and hence draws more flow towards the channel-1. For a given applied magnetic field, as the flow rate increases the current J_y increases and consequently balances the inertial force.

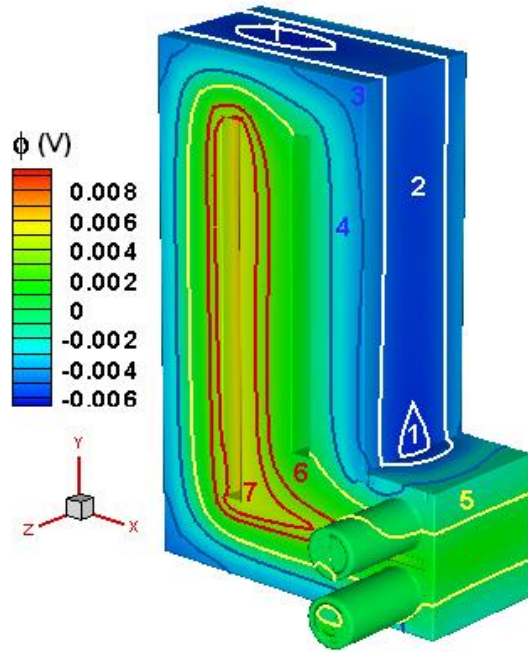


Figure 5.7: Contours of electric potential and iso-surfaces in various walls of the multi-channel test section. Level-1, 2, 3, 4, 5, 6 and 7 corresponds to potential value (mV) of -6, -5, 4, 2, 0, 3 and 4 mV respectively

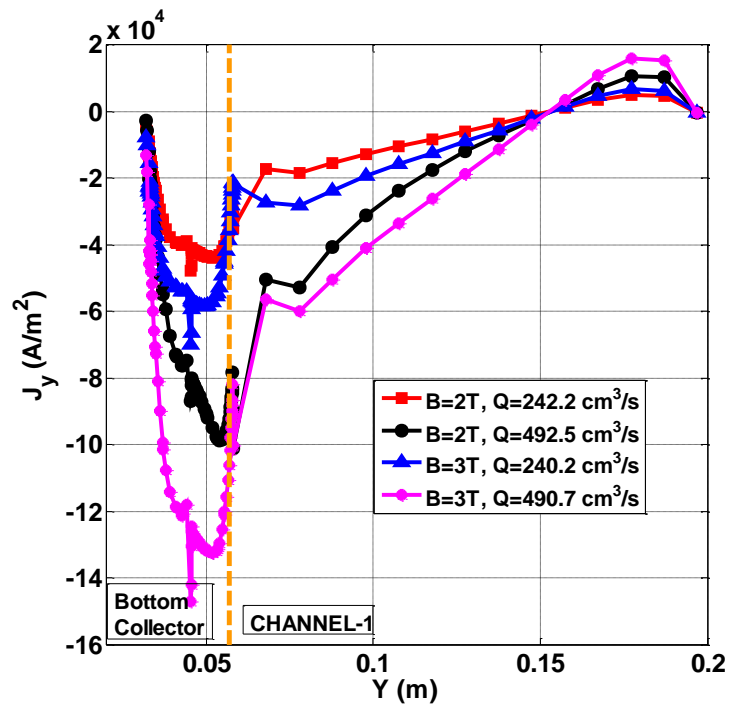


Figure 5.8: Axial current (J_y) profile along the centre of the channel-1 including the bottom inlet header region

5.8 Evaluation of actual flow rate in the test section based on measured side wall potential

Since all the numerical values of the potential differences displayed in earlier Figs. 5.5(a) and Fig. 5.5(b) are higher than the experimental values, it would be interesting to evaluate quantitatively the difference between the actual value of the flowrate Q_{real} in experiments and the value Q_{num} used in calculations. As an example, we use the data presented in Table-5.2 ($B_0 = 3 \text{ T}$, $Q = 240.2 \text{ cm}^3/\text{s}$) which is in better compliance with the numerical results obtained using laminar model. Let us assume that the differences of potentials induced on the walls of channel-3 at three locations (B, M & T) decrease in proportion to some coefficient 'A' with decreasing flow rate. The specific value of this coefficient can be estimated by minimizing the value of the r.m.s. deviation (σ_Q), as defined in Equation (5.13)

$$\sigma_Q = \sqrt{\frac{\sum_{\ell=1}^3 \sum_{j=1}^5 \left(A \Delta\phi_{3,j}^{\ell,\text{num}} - \Delta\phi_{3,j}^{\ell,\text{expt}} \right)^2}{15}} \quad \text{Eqn(5.13)}$$

From the condition of minimum of the function σ_Q with respect to A ($d\sigma_Q/dA = 0$), follows that

$$A = \frac{\sum_{\ell=1}^3 \sum_{j=1}^5 \Delta\phi_{3,j}^{\ell,\text{num}} \Delta\phi_{3,j}^{\ell,\text{expt}}}{\sum_{\ell=1}^3 \sum_{j=1}^5 \left(\Delta\phi_{3,j}^{\ell,\text{num}} \right)^2} = 0.9451 \quad \text{Eqn (5.14)}$$

The coefficient A defined in this way characterizes the difference between the actual flow rate in the experimental model and the flow rate measured by the flow meter.

Hence the real flow rate in the experiment can be evaluated using equation (5.14)

$$Q_{\text{real}} = 0.9451 \bullet Q_{\text{num}} \quad \text{Eqn(5.15)}$$

Using Eqn (5.15) the actual flow rate in the test section for various case studies is estimated. Table 5-6 presents the comparison with the estimated values from the measured side wall electric potential data and numerical profile. The actual flow rate obtained from equation (5.15)

matches well with the estimated values from side wall potential data with maximum deviation of less than 1% at higher magnetic field ($B_0 \geq 2.0$ T). Thus we believe that the average velocity in individual channel and hence flow rate as estimated from equation (5.10) is realistic and is close to the actual flow rate in respective channels.

Table 5-6: Actual flow rate for various case studies and its comparison with estimated flow rate based on measured side wall potential data and numerical profile

B_0 (T)	Flowrate by Flow Meter Q (cm ³ /s)	Actual Flowrate Q_{real} (cm ³ /s)	Estimated Flowrate Q_E (cm ³ /s)	Deviation (%)
2.0	242.2	228.9	223.1	2.5
2.0	492.5	465.5	462.4	0.7
3.0	240.2	227.0	227.3	0.1
3.0	490.7	463.8	467.2	0.7

5.9 Pressure in multichannel test section

The total pressure drop in the test section including the extended section of inlet/outlet pipeline is measured with the pressure transmitter located at A1 and A5 for various flow rates and applied magnetic fields. Even though electromagnetic effects are stronger due to electrically conducting walls and high applied magnetic field intensity, as the flow path of Pb-Li is consisting of multiple L/U bends and sudden expansion/contraction at the inlet/outlet sections, existence of local turbulence in the flow can't be ruled out. Especially at relatively lower applied magnetic field and higher flow rates and hence lower Ha/Re values inertial effects may dominate the flow characteristics and the assumption of laminar model in the present analyses will be inadequate as confirmed in previous section of similarity coefficient analysis.

In an attempt to identify the existence of different flow regimes, the normalized measured pressure drop ($\Delta P^* = \Delta P / (0.5 * \rho * U_0^2 * Ha)$) is plotted with corresponding Ha/Re values as shown in Fig. 5.9 (a). Here, U_0 is the average velocity in Channel-3. It is observed that at higher magnetic fields the normalized pressure drop is increasing linearly with Ha/Re

and hence the dimensional pressure drop is linear with flow rate ($\nabla p \approx \sigma a U_0 B_0^2$) as expected in an electromagnetic force dominated MHD flow. But at lower magnetic field ($B = 1\text{T}$), the pressure drop falls from a peak value at $Ha/Re = 0.013$. By comparing all the pressure drop data at lower Ha/Re values (see Fig. 5.9 (b)) it is seen that there is jump at $Ha/Re = 0.013$ and thus indicates a likely transition of flow regime. So the analysis of measured values of total pressure drop again confirms the validity of laminar approximation in the present numerical model. In the laminar flow regime, the MHD normalized pressure drop ($\Delta P / \sigma a U_0 B_0^2$) decreases as $\sim N^{-0.72}$ as shown in Fig. 5.10. Similar observations of the normalized pressure drop with N were also made in the insulating rectangular duct [18]. This indicates 3-D pressure drop due to axial currents at various bends and electrical coupling of different structural walls decreases with increasing N .

Fig. 5.9(a)

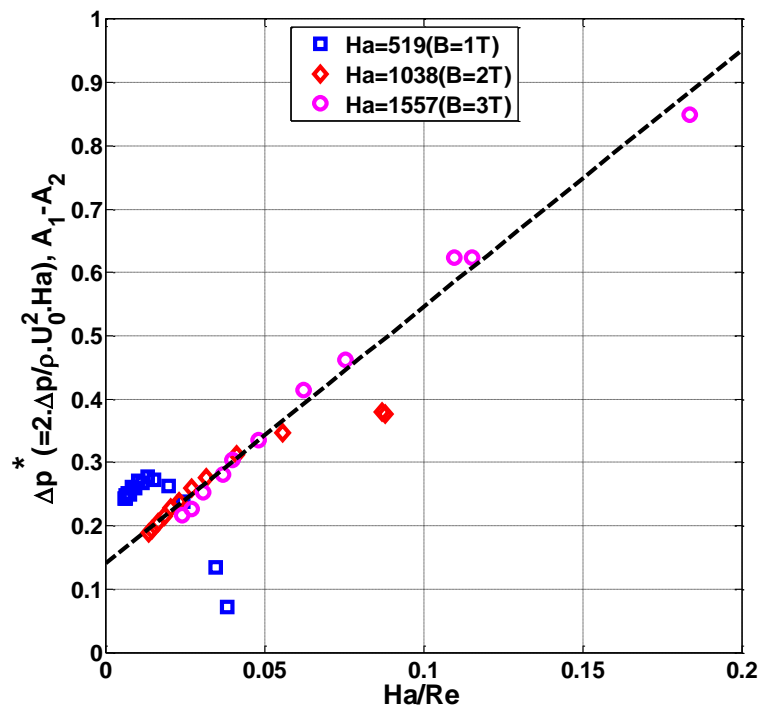


Fig. 5.9(b)

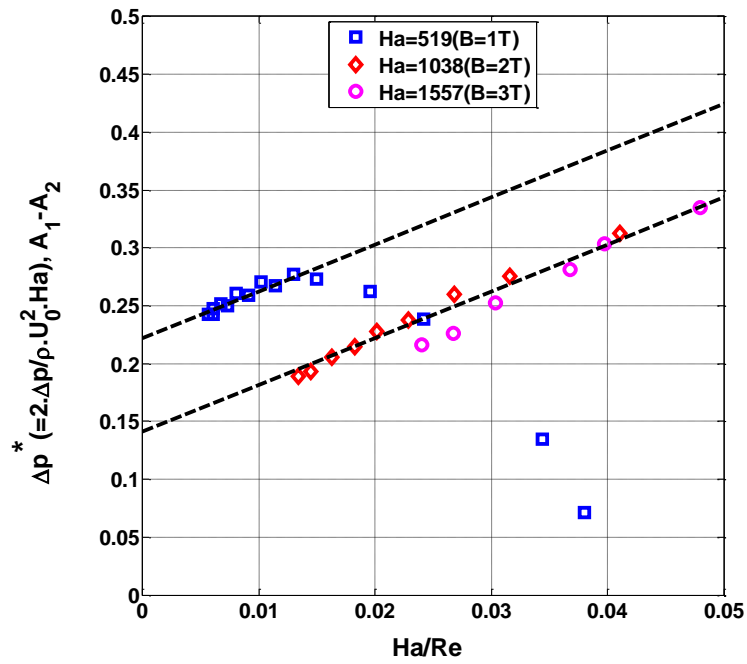


Figure 5.9: Variation of normalized measured pressure drop (ΔP^*) with Ha/Re in multi-channel test section including inlet/outlet pipe (up to A_1 & A_2); for all experiment range in Fig. 5.9(a) and for lower range in Fig. 5.9(b)

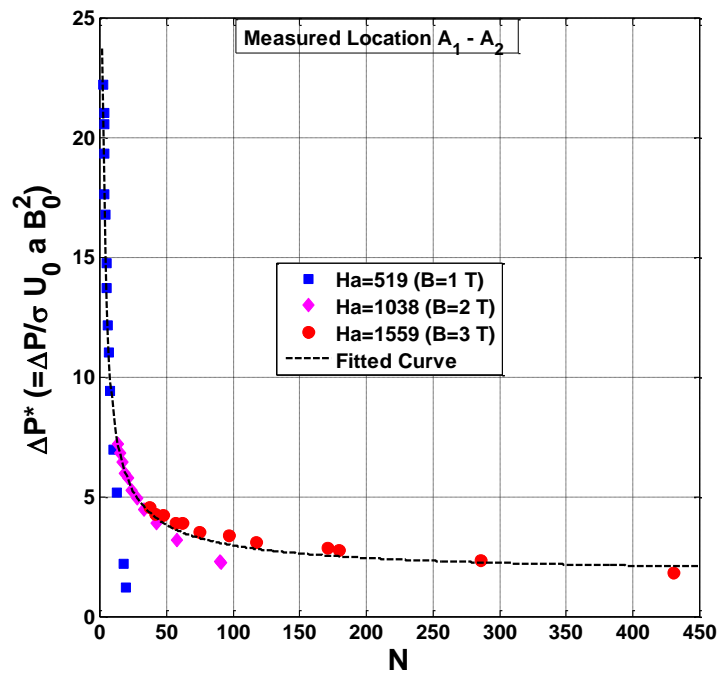


Figure 5.10: Variation of normalized pressure drop with Interaction parameter (N) in multichannel test section

The inlet/outlet pipeline extension up to A1 & A2 pressure transmitter locations consists of 3 different sections: Test section inlet is connected with a smaller pipe of inner diameter 15.8 mm (length 98.5 mm) followed by pipeline of larger inner dia. 16.5 mm (length 464.5 mm) which is then integrated with the main loop pipe of 27.3 mm inner diameter (length 790 mm up to location A1) through a 90-degree bend (see Fig. 5.11.). Outlet pipe extension up to location A2 is similar to the inlet section, but the larger pipe (inner dia. 27.3 mm) of length 980 mm is attached without any bending. The total pressure drop in the test section including inlet/outlet pipe estimated from the numerical simulation is compared with measured pressure drop by A1 & A2 pressure transmitter and is presented in Table-5.7. Since the axial magnetic field is very low and parallel to the flow direction in the inlet/outlet pipeline section except at the bending, the flow is assumed turbulent for estimation of pressure drop beyond the computation domain (ΔP_{pipe}). As can be seen in Table 5-7, reasonably good agreement is observed for the numerical and measured values for case of $B_0 = 2\text{T}$. However, more deviation is observed as the applied magnetic field strength is increased to $B_0 = 3\text{T}$. The higher deviation is anticipated from the fact that non account of additional MHD pressure loss in the bending region of the inlet section where flow path is transverse to the axial magnetic field. The pressure loss due to higher velocity, although very weak field strength at this bending location is expected to contribute significant drop in pressure for the case of 3T as compare to the case of 2T and hence more deviation.

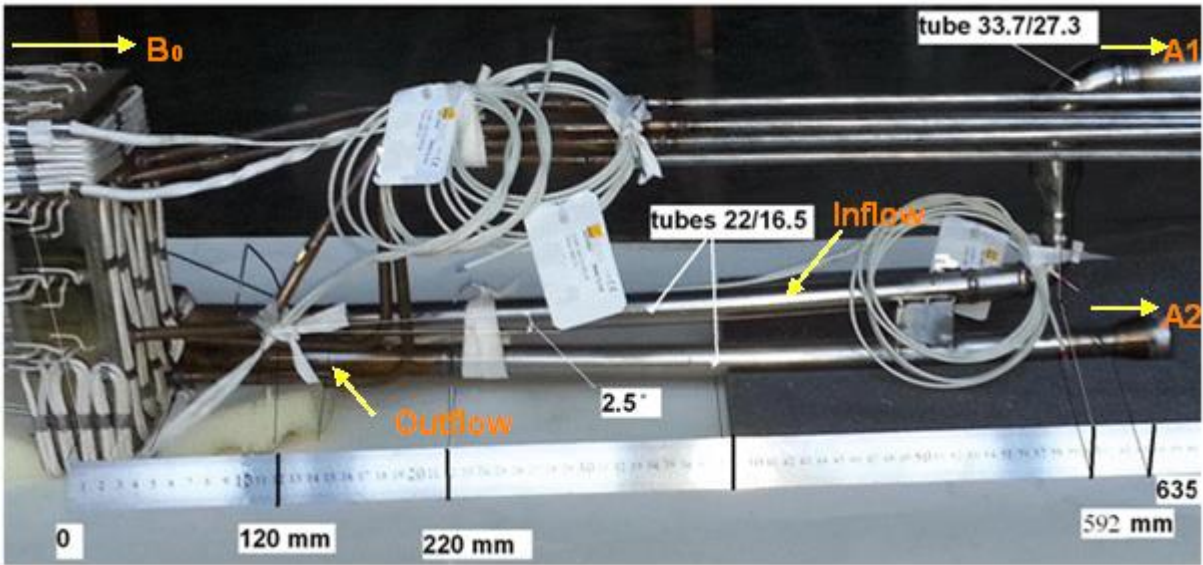


Figure 5.11: Photograph of inlet/outlet pipe and their extension towards pressure transmitters A1 and A2

Table 5-7: Comparison of total pressure drop obtained by numerical solution and corresponding values of the experiments for various case studies in multi-channel test section

Case	$\Delta P_{\text{Num.}}$ (bar)			$\Delta P_{\text{Expt.}}$ (bar)	Deviation with experiment %
	ΔP_{TS} (bar)	ΔP_{pipe} (bar)	ΔP_{Total} (bar)		
$B_0=2\text{T}$, $Q=242.2\text{ cm}^3/\text{s}$	0.446	0.139	0.585	0.584	0.2
$B_0=2\text{T}$, $Q=492.5\text{ cm}^3/\text{s}$	1.187	0.561	1.748	1.763	0.9
$B_0=3\text{T}$, $Q=240.2\text{ cm}^3/\text{s}$	0.84	0.137	0.98	1.126	13
$B_0=3\text{T}$, $Q=490.7\text{ cm}^3/\text{s}$	1.99	0.557	2.55	2.876	11.3

5.10 Summary of MHD studies in multichannel test section

Experiments and numerical analyses for Pb-Li MHD flow in a test section having coupled parallel and counter-parallel flow configuration, L and U-type bends, have been carried out at high characteristics parameters relevant to fusion blanket conditions. Although the test section model is not exactly the scaled down replica of LLCB TBM, the Pb-Li flow paths in the model simulate some of the features of LLCB variants. Numerical flow simulation

in the experiment test section has been carried out using FLUENT code and compared with the experimental data. A similarity coefficient (K) is proposed to compare the numerical wall potential profile with the corresponding experiment. It is observed that the degree of similarity is close to 97% at higher magnetic fields ($B_0 \geq 2T$) and hence proves the validity of laminar model in these flow regimes. The total flow rate and its distribution in parallel channels are estimated from the measured side wall potential and non-dimensional numerical profile of respective channel. The flow rate distribution in the parallel channels as predicted by the numerical computation is in agreement with the distribution measured from side wall potential data of respective channels. It is observed that the flow rate measured by the flow meter is consistently higher by the estimated values in all the case studies. So the actual flow rate is evaluated from the return channel (channel-3) side wall potential data and a constant coefficient is derived for correction in flow rate. The actual flow rate estimated with this new coefficient is confirmed with the corresponding estimation from measured side wall potential data. It is observed that a higher fraction of flow is drawn by the channel adjacent to the return channel of opposite flow path. The unequal flow distribution is attributed to the interaction of circulating 3-D currents with the applied magnetic fields in the bottom manifold region generated from the top and bottom walls along with geometrical factors of inlet flow conditions. The magnitude of 3-D currents is higher at lower N and saturates at higher values. Measured pressure drop in the test-section indicates a linear proportionality to scaling parameter of $\sigma a U_0 B_0^2$ at higher Ha/Re values and a transition of flow regime at Ha/Re = 0.013 for the present experimental test-section. The analysis indicates that FLUENT code based on laminar model can be used to simulate liquid metal MHD flow in electrically conducting multiple parallel channels under high characteristic flow parameters. Moreover, the results of such numerical studies can be used for further comparison with the results of a future flow model which accounts the effects of flow turbulence.

5.11 Numerical analysis of MHD flow in RF-test section for mock-up of LLCB variant with liquid metal NaK

In the India proposed LLCB TBM for ITER, Liquid metal flow is distributed among multiple parallel poloidal channels from a common inlet header. Liquid metal flow to the common header is supplied through an inlet manifold which is subject to varying toroidal magnetic fields. The toroidal magnetic field present for the confinement of D-T fusion plasma, is more or less uniform in the TBM but significant variation is there in the inlet/outlet manifold. Since the magnetic field is transverse to the flow path in LLCB flow configuration including inlet/outlet manifolds, MHD effects are intense in contrast to the corresponding hydrodynamic case especially in the absence of electrical insulation layer isolating structural walls and liquid metal. Schematic view of the proposed Indian Lead Lithium Ceramic Breeder (LLCB) TBM is shown in Fig. 5.12. Further, in some of the variants of LLCB, each parallel poloidal channel may be subdivided into a number of sub-ducts by inserting partition plates to increase the mechanical strength as well as to control the flow rate in the channel [1, 2, 19]. The varying magnetic field condition in the inlet manifold and partition plates in the poloidal channel alters the flow rate and velocity distribution in the TBM. Prediction of accurate flow and velocity distribution in individual channels and their sub-ducts is essential for MHD and heat transfer calculations. Generally, the flow distribution in the parallel channels/ sub-ducts depends on the characteristic Hartmann Number $Ha = B_0 a \sqrt{\sigma/\mu}$, and Interaction Parameter $N = \sigma a B_0^2 / \rho U$, applied magnetic field profile, inlet conditions, relative wall conductance ratio $C = \sigma_w t_w / \sigma a$ and electrical coupling in the channels etc. Here B_0 -magnetic field induction, U -mean flow velocity, a -characteristic length; σ , ρ , μ – liquid metal electrical conductivity, density and dynamic viscosity respectively; σ_w , t_w -wall electrical conductivity and thickness. It is very essential to test the performance of the MHD code that will be used for designing the TBM. Some experiments and analysis of scaled helium cooled lead-lithium Mock-up have been carried out by K. Starke, et al. [5] Similar 3D simulations of Pb-Li MHD flow has been carried

out by N.B. Morley et al. in a scaled down geometry to simulate the manifold regions of US Dual Coolant Lead Lithium TBM. [7]

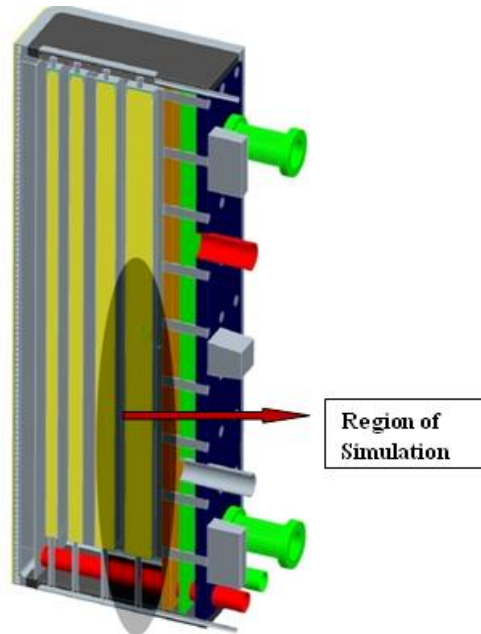


Figure 5.12: Region of MHD flow simulation (shaded ellipse) for Indian LLCB variant

It is also necessary to carry out Mock-up experiments which have all essential geometric complexities and characteristic parameters close to that of typical TBM and compare the results with the MHD code. In view of this experiments have been carried out at Efremov institute with liquid metal NaK in a test section that simulate some of the flow channels of the LLCB (the region of simulation is shown in Fig. 5.12) TBM with features of partition plate and varying magnetic field in the inlet manifold. The range of characteristic Hartmann number (Ha) and Interaction parameter (N) of these experiments are 860 to 1474 and 12 to 2000 respectively. The flow rate distribution in each channel and its associated sub-ducts has been measured for various flow rates as well as potential, pressure and velocity distribution. Numerical simulation has been carried out with scale 1:1 of the experiment test-section using the MHD module of FLUENT. In the present study result of numerical simulation for various flow properties like side wall electric potential distribution, pressure and velocity distribution is compared with

measured values. The varying magnetic field in the numerical simulation is implemented through user defined code for modelling of external magnetic fields.

5.12 RF-test section and experiment set up

Liquid metal loop at Efremov Institute of Russian Federation include vertically oriented RF-test section, electromagnet, electromagnetic pump (EMP), liquid metal/water cooler, electric heaters, electromagnetic flow meter (EFM) calibrated over normal nozzle, pressure and temperature sensors. NaK eutectic alloy (22% Na) was used in this simulation experiments and was kept at 62 ± 1 °C. Experiments have been carried out for various flow rates with NaK ranging from 0.31 m³/h to 8.0 m³/h corresponding to mass flow rate of 0.074 to 1.91 kg/s.

Test section made of SS included inlet pipe, inlet collector of rectangular cross section, two rows of parallel poloidal (vertical) ducts and outer collector with outlet pipe. The photograph of the test section in the experimental loop is shown in Fig. 5.13. The detailed dimension of various channels in the test section is shown in Fig. 5.14. The same dimensions are used for computation model of numerical simulation. Test section outer dimension along the magnetic field lines is 105 mm with 3 mm wall thickness (t_w). Region of uniform magnetic field in poloidal direction is 470 mm including 48 mm of inlet collector (with 3 mm bottom plate). The first poloidal channel (close to the inlet pipe) has two sub-ducts of rectangular cross section 12×48 mm (characteristic length $a=24$ mm), the second one – three sub-ducts 12×31 mm (characteristic length $a=15.5$ mm), inner partitions of all sub-ducts are 3 mm thick. Inlet pipe inner diameter was 28 mm (wall thickness 3 mm). There is no electrical insulation (insulation barriers) on fluid-wall interface to simulate the first possible stage of ITER tests.



Figure 5.13: Photograph of the RF-test section in Experimental NaK loop at Efremov Institute, Russian Federation

In the inlet/outlet region, liquid metal experience exponentially varying applied magnetic field and uniform field of 1T in the main test section. Magnetic field was measured prior to experiments with specially calibrated Hall probe and traversing mechanism in the whole region of magnetic field presence. Error of its measurement was less than 0.4%. Pressure distribution along the inlet pipe and sub-ducts was measured with pressure and differential pressure transducers, and NaK filled the measuring pipes up to transducer's sensitive elements. Error in measurement of pressure was less than 4% for flow rate around $0.3 \text{ m}^3/\text{h}$ and less than 2% for all the rest flow rates. Side wall electric potential difference was measured along all the sub-ducts. Measured signals were in the range 0.6-13 mV depending on the flow rate with the measured error less than 3.5%. Error in the mean over sub-duct height velocity estimation based on the measured potentials was less than 5%. LEVI probes to measure velocity distribution through potential measurements between two tips 1 mm apart were placed in one cross section (125 mm from Test-section bottom). Errors in the velocity measurements are

estimated to be less than 18 % at flow rate $0.3\text{m}^3/\text{h}$, 13% at $2.3\text{ m}^3/\text{h}$, 9% at $4.3\text{ m}^3/\text{h}$ and 7% at $6.3\text{m}^3/\text{h}$. Error in LEVI probes placement is $\pm 0.5\text{ mm}$.

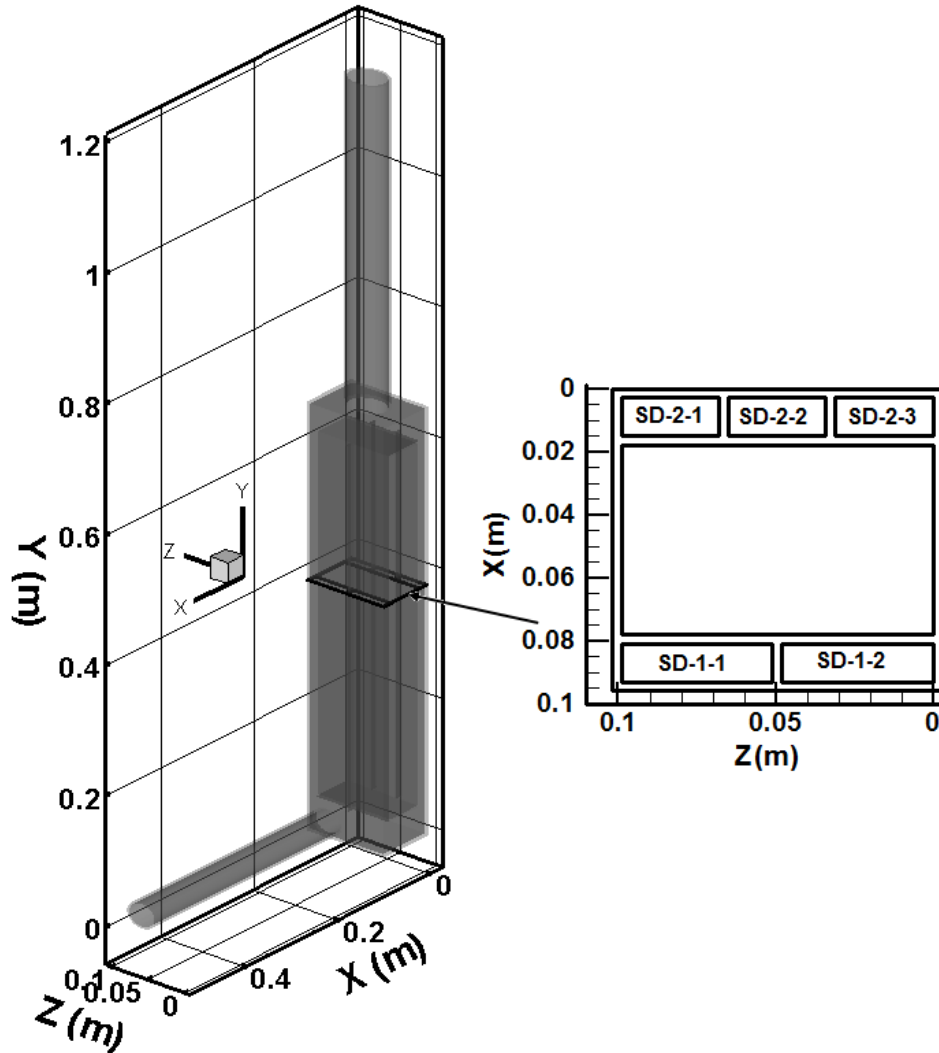


Figure 5.14: Detail dimension of the RF-test section and computation model. The cross section view of various sub-ducts is shown in embedded picture (SD: Sub-Duct)

Flow rate in the experiments was varied from ~ 0.3 to $\sim 8.0\text{ m}^3/\text{h}$ with EMP (error in the flow rate measurements was less than 3.6-2.9% at flow rates $0.3\text{-}1\text{ m}^3/\text{h}$ and less than 2.6% for flow rates $2.3\text{-}8\text{ m}^3/\text{h}$). Corresponding values of Ha number and interaction parameter are shown in Table-5.8 for the magnetic field of 1 T.

Table 5-8: Hartman number (Ha) and MHD interaction parameter (N) for various sub-ducts and inlet pipe in RF-test section

Total flow rate (m ³ /h)	Sub-duct 1-1 (Ha=1474)	Sub-duct 1-2 (Ha=1474)	Sub-duct 2-1 (Ha=952)	Sub-duct 2-2 (Ha=952)	Sub-duct 2-3 (Ha=952)	Inlet pipe (Ha=860)
8.0	57.9	68.7	63.3	56.5	64.0	12.1
2.3	203.3	237.9	226.2	198.7	227.8	42.2
0.31	1704.2	1987.6	1547.1	1407.6	1526.2	309.6

5.13 Numerical simulation

Numerical simulation of the experiment test section including inlet and outlet pipe flow with variable magnetic field has been carried out in the CFD facility of VJTI, Mumbai, India using FLUENT code. The steady state numerical solution has been obtained for the corresponding experimental flow rates as presented in Table-5.8. The characteristic Hartmann number (Ha) is 1474, 952 and 860 for sub-ducts of Channel-1, sub ducts of Channel-2 and for inlet pipe respectively.

The Governing equations and boundary conditions are described in section 5.13 of multi-channel simulation. The code was also benchmarked with Hunt's analytical solution [20] in a straight square geometry (25×25 mm²) and applied magnetic field of 4T (Ha=1038). The code has been successfully tested in a test section consisting of multiple 90° bends (flow turning from parallel to perpendicular and perpendicular to perpendicular leg of the bend) with a characteristic Ha number up to 2060 [13].

The domain of computation is confined to $0 \leq X \leq 0.966$ m, $0 \leq Y \leq 1.256$ m and -0.003 m $\leq Z \leq 0.102$ m (Fig. 5.14). The two poloidal channels (CHA-1 & CHA-2) start at Y=0.048 m from a single inlet collector header ($0 \leq Y \leq 0.048$ m) and subsequently enters into a similar outlet header at Y= 0.608 m. However, the partition plates in the poloidal channels (one in CHA-1 and two in CHA-2) extends only up to Y= 0.393 m. For present computation, the length

of the inlet and outlet circular pipe is taken as 900 mm ($0.066 \leq X \leq 0.966$ m) and 600 mm ($0.656 \leq Y \leq 1.256$) respectively (to reduce computation as the applied magnetic field is negligible beyond this length).

5.13.1 Grid details and Physical properties

A variable structured mesh with total number of volume elements ~2 million is used for computation. Side wall boundary layer is resolved by 5 number of grid points in both circular pipe as well as Test-section. There are no grid points in the Hartmann boundary layer but taken ~5 grids in the Hartmann and side walls. This is primarily to reduce total number of grid points. Since the returning currents through Hartman layer is negligibly small as compared to the current flowing through the Hartmann walls (in case of conducting walls), it was found that non-resolution of Hartmann layer will lead to very small error [21]. The properties of the NaK are taken as 857.6 kg/m^3 , $2.691 \times 10^6 \text{ S/m}$, $7.131 \times 10^{-4} \text{ Pa.s}$, for density (ρ), electrical Conductivity (σ) and dynamic viscosity (μ) respectively. The electrical conductivity (σ_w) of Hartmann wall and Side walls are taken as $1.28 \times 10^6 \text{ S/m}$.

5.14 Applied magnetic field profile

The applied magnetic field B ($0, 0, B_z$) profile is approximated from the measurements and is presented in the following relations for different regions of the test geometry. Contours and profiles of B_z field in a perpendicular plane to the applied field direction are shown in Fig. 5. 15.

- i) $B_z = 1.0$ [$-0.003 \leq Y \leq 0.47$ m, $0 \leq X \leq 0.066$ m]
- ii) $B_z = e^{-0.9901(y-470)/126}$ [$0.47 \leq Y \leq 0.535$ m, $0 \leq X \leq 0.066$ m]
- iii) $B_z = 0.6 e^{(535-y)/126}$ [$Y \geq 0.535$ m, $0 \leq X \leq 0.066$ m]
- iv) $B_z = 0.83 e^{(90-x)/126}$ [$X \geq 0.066$ m (inlet duct)]

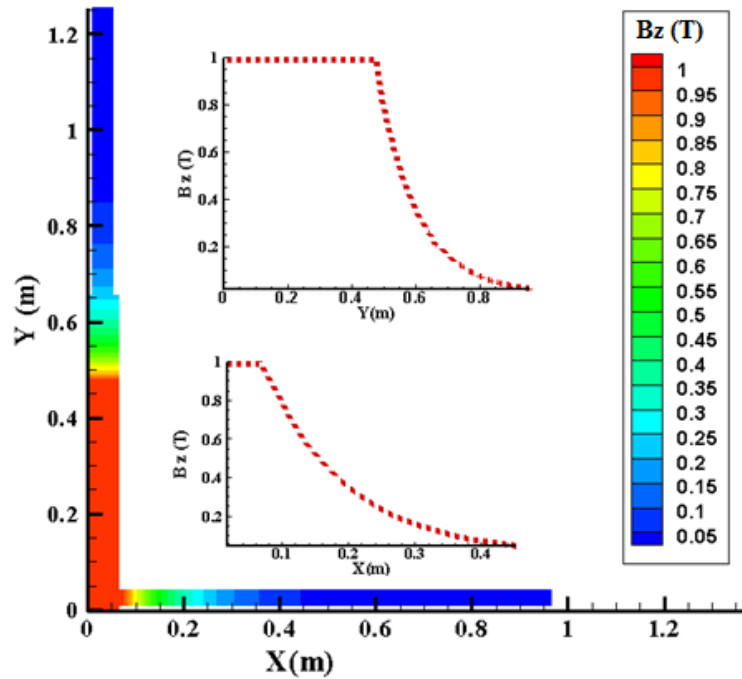


Figure 5.15: Contours and profile of B_z field in a plane perpendicular to the applied field

5.15 Numerical electric potential distribution and comparison with experiment in RF-test section

In Fig. 5.16 (a) and Fig. 5.16(b) numerically obtained side wall electric potential difference distributions in various sub-ducts are compared with measured values. The continuous line represents numerical profile and the symbols represent corresponding measured values in Fig. 5.16(a) and Fig. 5.16(b). The experimental and numerical simulation results indicate an asymmetric distribution in sub-ducts of Channel-1 and symmetric distribution in sub-ducts 2-1 and 2-3 of Channel-2. The reason is obviously the asymmetric position of the inlet pipe (see Fig. 3) that provides the asymmetry in flow rates for Channel-1 closest to the inlet pipe. For Channel-2, due to MHD interaction along the flow path in the collector flow distribution becomes symmetrical. It is observed further that the magnitude of side wall potential difference is relatively higher in the mid sub-duct of Channel-2 for all the cases indicating relatively larger flow rate in the mid sub-duct as compared to the other sub-

ducts of Channel-2. This is due to the difference in Hartmann walls equivalent thickness for the mid and outside sub-ducts [9]. The numerical results are fairly matching experimental data with maximum deviation being less than 5% in Channel-1 and less than 8% in Channel-2 respectively.

Fig. 5.16(a)

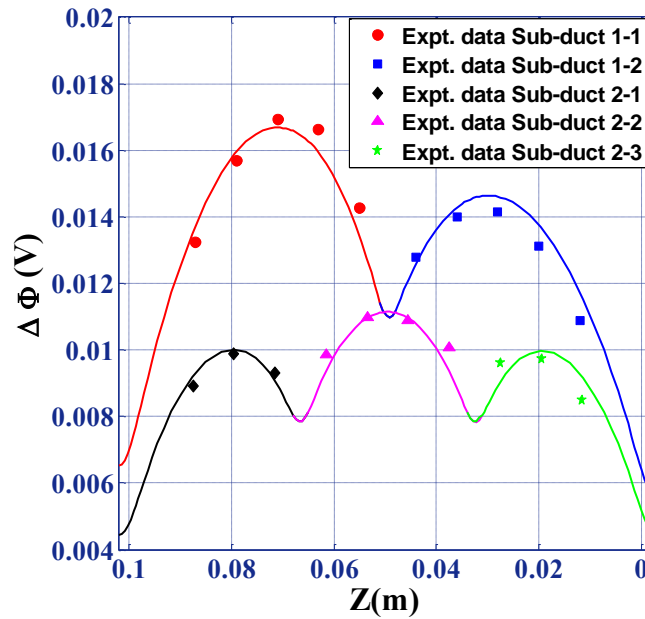


Fig. 5.16(b)

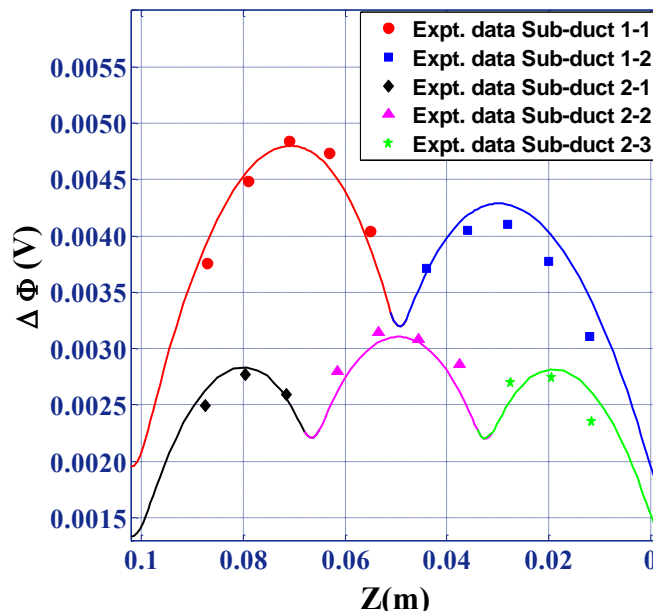


Figure 5.16: Side wall electric potential difference distribution along the applied magnetic field in ducts of CHA-1 and CHA-2 of RF-test section; for mass flow rate of 1.91kg/s (8.0m³/h) in Fig. 5.16(a) and for mass flow rate of 0.55kg/s (2.3 m³/h) in Fig. 5.16(b)

To determine the distance at which the flow becomes fully developed in the sub-ducts, numerically obtained side wall electric potential difference profiles of Channel-1 and Channel-2 have been plotted at various flow cross sections ($Y=0.052$ m, $Y=0.073$ m, $Y=0.092$ m, $Y=0.164$ m, $Y=0.383$ m) for flow rate of 0.55 kg/s as shown in Fig. 5.17(a) and Fig. 5.17(b). We see that at Y between 0.073 and 0.092 m the potential difference pattern indicates flow to be fully developed. This distance (25 – 44 mm from beginning of sub-ducts partitions) corresponds to one/two characteristic lengths ‘ a ’ ($a=0.024$ m for sub-ducts of Channel-1 and $a=0.0155$ m for sub-ducts of Channel-2). Further we see that as we proceed towards the top ($Y=0.383$ m) the peak is shifting towards centre. This is because beyond $Y=0.393$ m, there is no partition plate which shifts velocity peak towards centre of the channel in the downstream.

Fig. 5.17 (a):

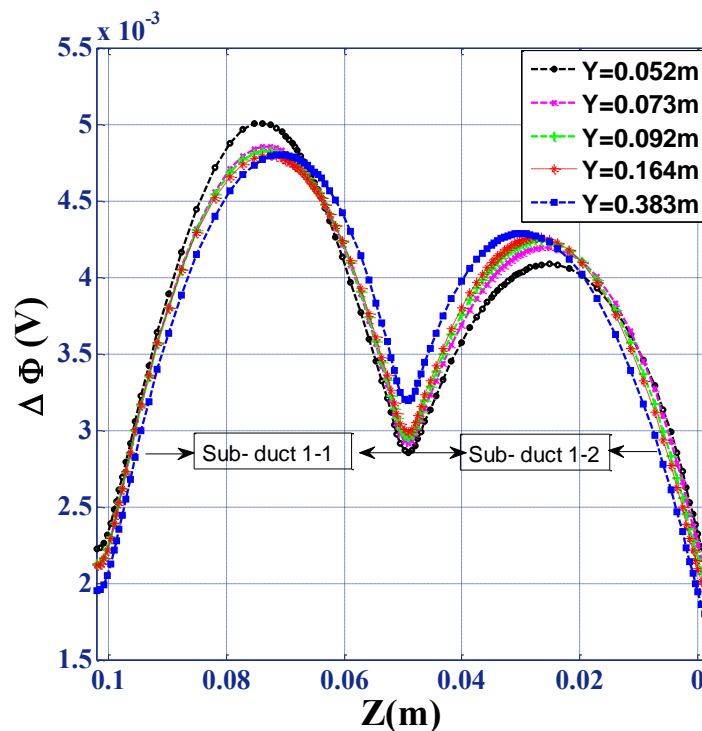


Fig. 5.17 (b):

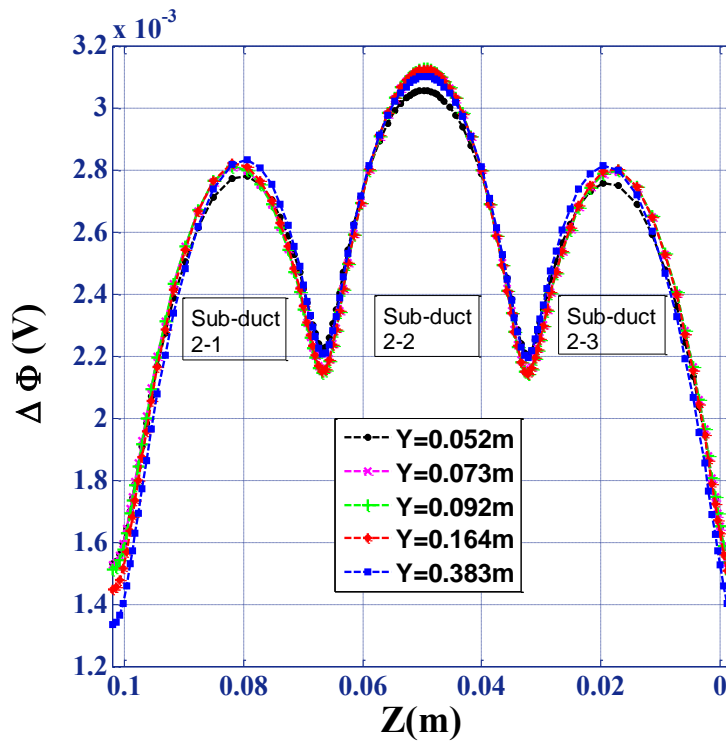


Figure 5.17: Side wall electric potential difference distribution at different cross sections for total mass flow rate of 0.55 kg/s (2.3 m³/h); for CHA-1 in Fig. 5.17(a) and for CHA-2 in Fig. 5.17(b)

5.16 Flow Rate distribution in RF-test section

The comparison of numerical flow rate distribution in each sub-duct with corresponding measured values and their relative contribution to total mass flow rate is summarised in Table 5-9 for total flow rates of 8.0 m³/h and 2.3 m³/h. The measured mean velocity and flow rate in individual sub-ducts are estimated from the respective side wall potential measurements at Y=0.383 m according to the following procedure.

Table 5-9: Flow rate distribution in various sub-ducts of RF-test section from numerical solution and comparison with experiment

CHANNEL /Sub-duct	CHANNEL-1		CHANNEL-2		
	Sub-duct 1-1	Sub-duct 1-2	Sub-duct 2-1	Sub-duct 2-2	Sub-duct 2-3
Total flow rate in mock-up, m ³ /h	2.3 (Experiment ¹)/2.3(Numerical ²)				
Flow rate in Channels, m ³ /h	1.43/1.388		0.91/0.916		
Flow rate in sub-ducts, m ³ /h	0.77/0.733	0.66/0.655	0.29/0.294	0.33/0.330	0.29/0.292
% of flow rate in channels	61.24/60.24		38.75/39.76		
% of flow rate in sub-ducts	33.19/31.81	28.45/28.43	12.5/12.77	14.22/14.31	12.5/12.68
Total flow rate in mock-up, m ³ /h	8.2 ¹ /8.0 ²				
Flow rate in Channels, m ³ /h	4.97/4.774		3.20/3.244		
Flow rate in sub-ducts, m ³ /h	2.70/2.543	2.27/2.231	1.03/1.033	1.15/1.181	1.02/1.03
% of flow rate in channels	60.84/59.54		39.16/40.46		
% of flow rate in sub-ducts	33.01/31.72	27.83/27.82	12.6/12.88	14.10/14.73	12.46/12.84

Notes: ¹ – flow rate based on electric potential measurement, ² – flow rate according to EMF

Averaged over duct height liquid metal velocity is obtained from circuit theory with known potential distribution from calculated electrical resistances of liquid metal and outer walls. Integration of this velocity distribution over sub-ducts cross section gives flow rate in sub-ducts. Sum of these flow rates differs from total flow rate measured with electromagnetic flow meter less than 3% [16]. The numerical results are matching well with experimental data for all the flow rates. The maximum deviation is less than 5 % for sub-duct 1-1 and less than

3% for all other sub-ducts. The Channel-1 contributes to nearly 60% of the total flow rate with unequal distribution in its sub-ducts. Whereas the flow distribution in outer sub-ducts of Channel-2 is nearly the same and the flow in mid sub-duct 2-2 is around 14% larger for all the flow rates. It has been observed that fraction of flow in Channels 1 and 2 is practically constant at flow rate larger than $1 \text{ m}^3/\text{h}$, $N \leq 470$ (see Fig. 5.18).

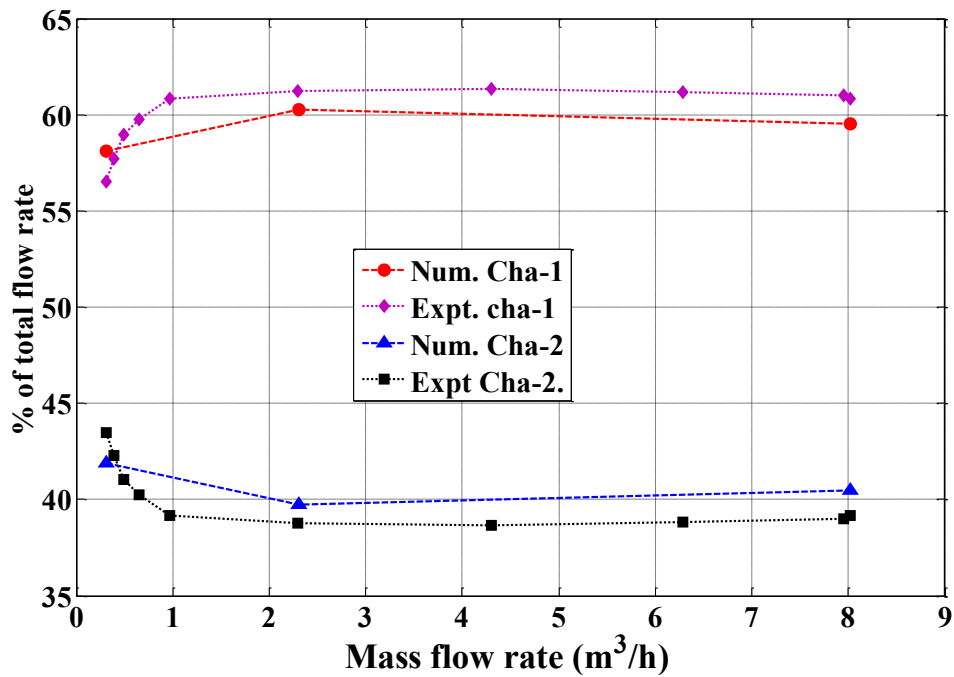


Figure 5.18: Fraction of flow in CHA-1 and CHA-2 for different flow rates and comparison with experiment

5.17 Velocity distribution in RF-test section

The contour of local velocity and profiles at the exit of the inlet pipe ($X=0.07 \text{ m}$, near the entrance of the inlet header to test-section) are shown in Fig. 5.19. As it can be seen the velocity profile parallel to the magnetic field is different compared to profile perpendicular to magnetic field. As expected the profile is flat parallel to the magnetic field. In Fig. 5.20(a), axial velocity component (Y-velocity) across the side walls of sub-duct 1-1 is plotted for different flow rates and at two cross-sections ($Y=0.092 \text{ m}$, nearer to the bottom duct and $Y=0.383 \text{ m}$ nearer to the

top). The asymmetric velocity distribution in sub-duct 1-1 is primarily due to asymmetric position of inlet pipe. The asymmetry is higher at higher flow rates and gradually tends to a symmetric profile as the flow advances in the sub-ducts. On the other hand, the flow distribution is more symmetric in sub-ducts of Channel-2 as it is relatively away from the inlet of the Test-section. In Fig. 20(b), axial velocity component (Y-velocity) across the side walls at the centre of sub-duct 2-3 is plotted at cross section $Y=0.092$ and $Y=0.383$ m for different flow rates.

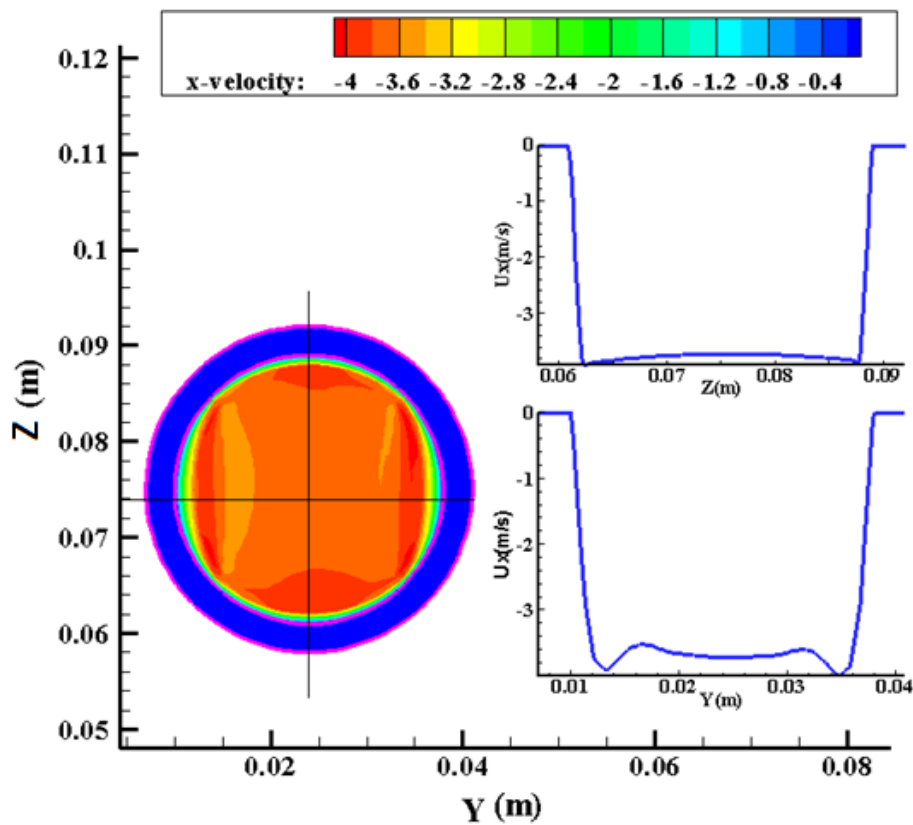


Figure 5.19: U_x (X-velocity) contour and profile at the centre of inlet pipe exit ($X=0.07$ m, near to the entry of mock up Test section) for flow rate of $8.0\text{m}^3/\text{h}$

Fig. 5.20(a):

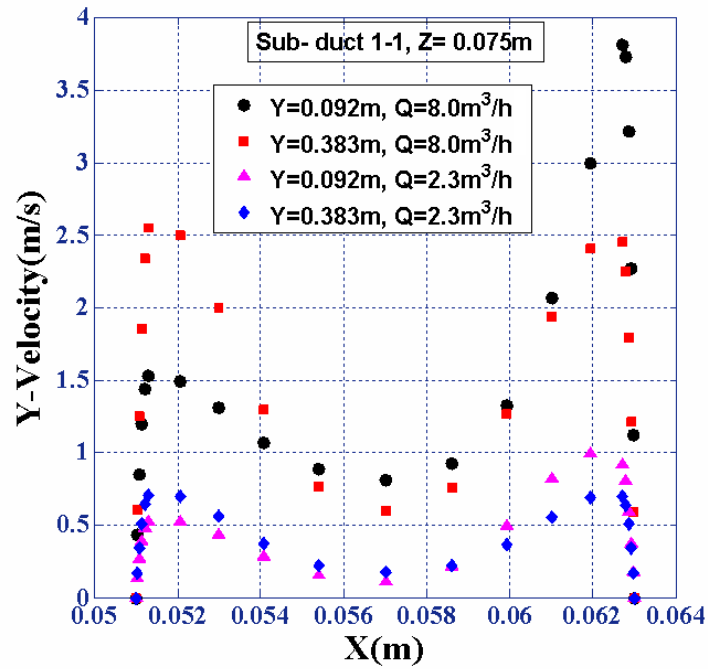


Fig. 5.20(b):

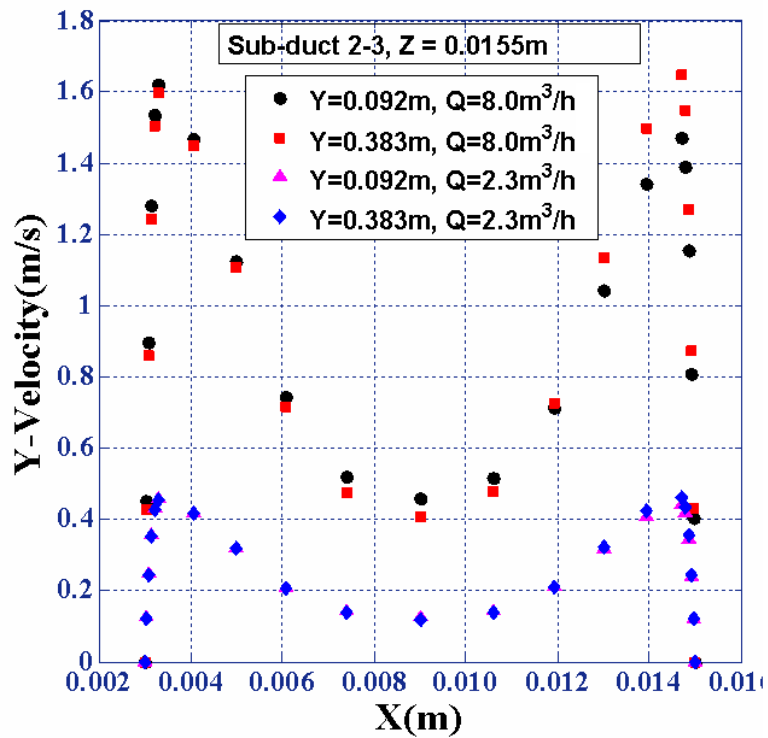


Figure 5.20: Numerical velocity profile across the side walls at cross section Y=0.092 and Y=0.383 m for various flow rates; at the centre of the sub-duct 1-1 in Fig. 5.20 (a) and at the centre of the sub-duct 2-3 in Fig. 5.20(b)

The velocity profile in XZ plane at Y=0.128 m was measured with LEVI (Liquid metal Electromagnetic Velocity Instrument) probe in sub-duct 1-1. Two point-like electrodes (tips) were placed 1 mm apart and 12 mm from probe body in upstream direction to measure potential difference in perpendicular magnetic field. In fact, the LEVI probe is the same that was used for experiments with Argonne National Laboratory, USA [22]. Estimations of electric current flowing between the tips show that it is negligible at experiment conditions. Total error of velocity measurement with LEVI probes is less than 7%. Mean flow rate obtained with integration of measured velocity profiles differs from that obtained from side walls electric potential measurements for flow rates from 2.3 to 6.3 m³/h is less than 4%. This accounts also for the error in the probe location (± 0.5 mm) and possible flow distortion by the probe. The measured values of velocity across the side walls at the centre of the sub-duct 1-1 are presented in Fig. 5.21 for flow rates 6.3m³/h and 2.3 m³/h and compared with corresponding numerical results. The velocities are normalised with sub-duct average velocity. Even though the profiles are clearly indicating asymmetric M-profile as predicted by the numerical simulation at laminar conditions, the deviation in the core is significant. This deviation may be attributed to possible residual turbulence which spreads the side layers in to the core increasing their thickness and decreasing side wall velocity jets. With the Reynolds number ($Re = \rho U a / \mu$) decreasing, the numerical results based on the laminar flow are closer to the experimental data. Similar conclusions based on experiments and numerical analysis are made in [3, 23].

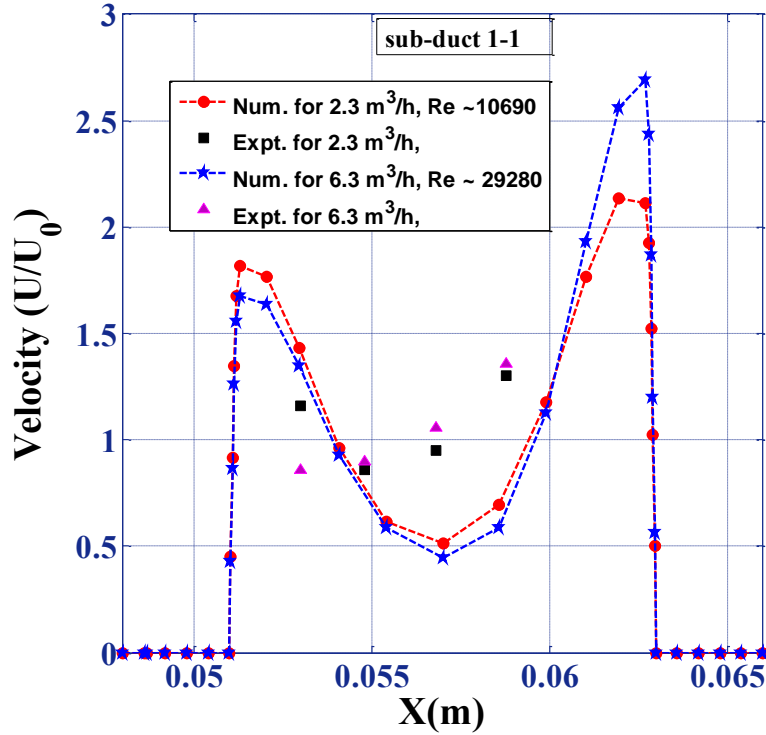


Figure 5.21: Non dimensional measured and numerical velocity profiles across the side walls of sub-duct 1-1 at $Y=0.128$ m and $Z=0.075$ m for total flow rate of 2.3 m³/h and for 6.3 m³/h

5.18 Velocity Vector and current stream lines

The velocity vector and flow path in plane $Y=0.024$ m (passing through inlet pipe and inlet collector/header), $Y=0.046$ m (near the entrance to sub-ducts) and $Y=0.092$ m (cross section with partition plate) are shown in Fig. 5.22 for flow rate of 2.3 m³/h. This figure indicates that maximum percentage of flow enters into sub-duct 1-1 (near to the inlet pipe) through the side layer and having an asymmetric distribution. Since the flow has traversed a distance of 0.048 m both in horizontal and vertical distance in plane perpendicular to the uniform applied field of 1 T before entering into the sub-ducts of Channel-2, the flow is rather symmetric due to suppression of inertial effects. In Fig. 5.23 current stream lines are plotted in plane $Y=0.383$ m which shows clearly the electrical coupling between the Channels. Current lines from the centre of sub-duct 2-1 and sub-duct 2-3 (Channel-2) are entering into the centre of sub-duct 1-1 and sub-duct 1-2 respectively through Hartmann walls. Since the Hartmann wall currents of sub-duct 2-1 and sub-duct 2-2 are shared by common partition plate, the

effective Hartmann wall thickness of the sub-duct 2-2 is reduced leading to reduced effective wall conductance (C). As the resistance to the current path increases, the result is a lower core current density and hence more flow in sub-duct 2-2.

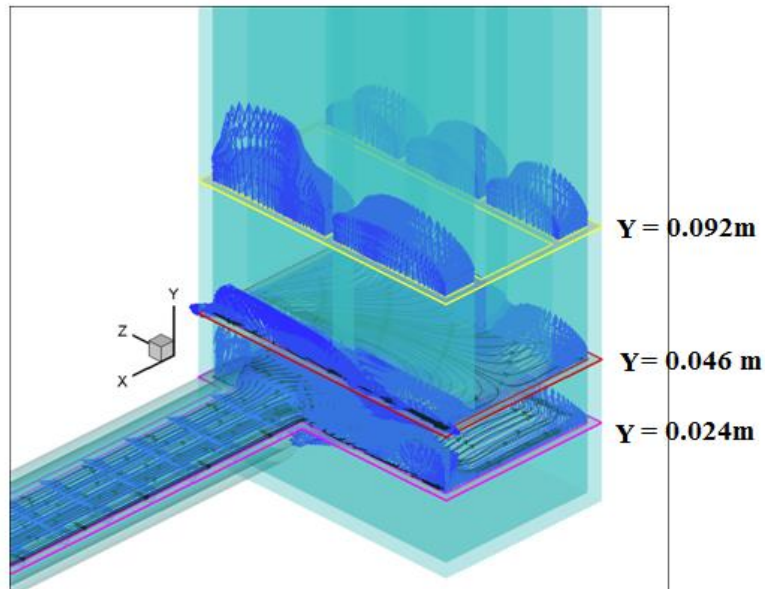


Figure 5.22: Velocity vectors and stream lines at different cross sections (Y=0.024 m (plane passing through the centre of the inlet pipe), Y=0.046 m (near exit of the inlet collector), Y=0.092 m) for flow rate of 8.0 m³/h

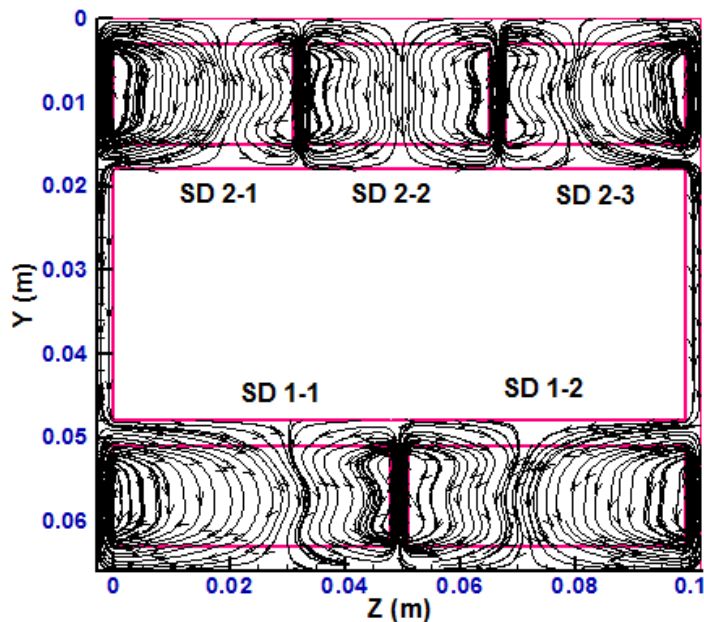


Figure 5.23: Current streamlines in the plane Y=0.383 m for flow rate 8.0 m³/h

5.19 Pressure distribution in RF-test section

Pressure profiles along the flow path at the centre of various sub-ducts for different flow rates ($Q=8.0 \text{ m}^3/\text{h}$ and $Q=2.3 \text{ m}^3/\text{h}$) are shown in the Fig. 5.24. The maximum pressure drop occurs near the exit region of the inlet pipe where the flow experiences maximum transverse applied magnetic field. This is due to high velocity in the pipe as compared to flow in any of the sub-ducts. The pressure drop is linear in all the sub-ducts due to dominance of MHD forces as it is proportional to the mean velocity. The total pressure drop in Test-section obtained from numerical simulation for different flow rates have been compared with measured values and shown in Table 5-10. The agreement is reasonably well with maximum deviation less than 7%.

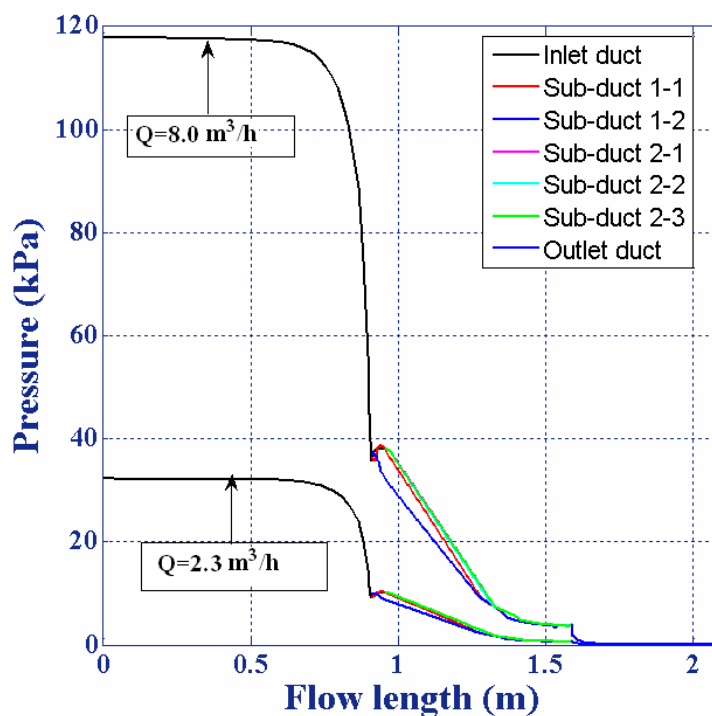


Figure 5.24: Pressure profile along the flow path at the centre of various sub-ducts for different flow rates ($Q=8.0 \text{ m}^3/\text{h}$ and $Q=2.3 \text{ m}^3/\text{h}$)

Table 5-10: Total pressure drop in the RF-test section for different flow conditions

Total flow rate, m ³ /h	Measured pressure drop/error, kPa/%	Numerical estimation, kPa
2.3	34.7/6	30.8
8.0	99.5/7	112.5

5.20 Summary of the numerical simulation in RF-test section

FLUENT code numerical results are matching well with experimental data. For flow rate distribution, total pressure drop and side wall potential, the deviation is less than or close to the experimental errors. Experimental velocity profiles between the side walls are the functions not only of Hartmann number (Ha) and relative wall electrical conductance (C) parameters but Reynolds number (Re) as well, and they lay close to numerical results for laminar flow at small Re numbers only. The reason is believed to be residual turbulence which spreads the side layers to the core increasing their thickness and decreasing side wall velocity jets. Flow distribution in parallel channels and sub-ducts is influenced by inlet pipe asymmetry and Hartmann walls equivalent thickness. Flow in sub-ducts becomes close to fully developed at a distance of one/two characteristic lengths (sub-duct half width in magnetic field direction) from sub-ducts beginning.

5.21 References

1. C. Paritosh, E. Rajendra Kumar, et al., Status and progress of Indian LLCB test blanket systems for ITER, Fusion Eng. and Des. 87 (2012)
2. I.R. Kirillov, D.A. Pertsev, Investigation of alternative configurations of the LLCB TBM to increase neutronic and thermo-hydraulics performances, Fusion Eng. and Des. 85 (2010)
3. S. Smolentsev, R. Moreau, et al., Characterization of key magnetohydrodynamic phenomena in PbLi flows for the US DCLL blanket, Fusion Eng. and Des. 83 (2008)

4. C. Mistrangelo, L. Bühler, Liquid metal magnetohydrodynamic flows in manifolds of dual coolant lead lithium blankets, *Fusion Eng. and Des.* 89 (2014)
5. K. Starke, L. Bühler, et al., Experimental MHD flow analyses in a mock-up of a test blanket module for ITER, *Fusion Eng. and Des.* 84 (2009)
6. C. Mistrangelo, L. Bühler, Electric flow coupling in the HCLL blanket concept, *Fusion Eng. and Des.* 83 (2008)
7. N. B. Morley, M. J. Ni, et al., MHD simulations of liquid metal flow through a toroidally oriented manifold, *Fusion Eng. and Des.* 83 (2008)
8. T. Rhodes, S. Smolentsev, et al., Magnetohydrodynamic pressure drop and flow balancing of liquid metal flow in a prototypic fusion blanket manifold, *Physics of Fluids* 30 (2018)
9. P. Satyamurthy, P.K. Swain, et al., Experiments and numerical MHD analysis of LLCB TBM Test-section with NaK at 1 T magnetic field, *Fusion Engineering and Design* 91 (2015)
10. FLUENT 12.0 produced by FLUENT Inc.
11. U. Muller, L. Buehler, Book: *Magnetofluiddynamic in Channels and container*, Springer, ISBN 3-540-41253-0 (2001)
12. S. Smolentsev, R. Moreau, et al., MHD thermofluid issues of liquid-metal blankets: Phenomena and advances, *Fusion Eng. and Des.* 85 (2010)
13. P. K. Swain, P. Satyamurthy, et al., 3D MHD Lead-Lithium liquid metal flow analysis and experiments in a test-section of multiple rectangular bends at moderate to high Hartmann Numbers, *Fusion Eng. and Des.*, 88 (2013)
14. B. Schulz, Thermophysical properties of the Li(17)Pb(83) alloy, *Fusion Eng. and Des.*, 14 (1991)
15. S.I. Sidorenko, A. Ya. Shishko, Variational method of calculation of MHD flows in channels with large aspect ratios and conducting walls, *Magnetohydrodynamics* 27 (1991)
16. D. M. Obukhov, I.R. Kirillov, et al., MHD characteristics of Test Blanket Module elements, PAMIR conference on fundamental and applied MHD, 9th Int. conference at Riga, (2014)
17. S. Ivanov, A. Shishko, et al., Calibration of MHD flow meter in PbLi loop from the measurement of electric potentials on walls of the rectangular channel in a strong magnetic field, PAMIR conference on Fundamental and Applied MHD, 8th Int. conference at Riga, (2011)
18. I. R. Kirrilov, C. B. Reed, et al., Present understanding of MHD and heat transfer phenomena for liquid metal blankets, *Fusion Eng. and Des.*, 27 (1995)
19. J. Reimann, L. Barleon, et al., Magnetohydrodynamic investigations of a self-cooled Pb-17Li blanket with poloidal-radial-toroidal ducts, *Fusion Eng. and Des.* 27 (1995)

20. J. C.R. Hunt, Magneto-hydrodynamics flow in rectangular duct, *J. Fluid Mech.* 21 (1965)
21. S. Subramanian, P.K. Swain, et al., Effect of Hartmann layer resolution for MHD flow in a straight conducting duct at high Hartmann numbers, *Sadhana*, 40 (2015)
22. I. A. Evtushenko, T. Q. Hua, et al., The effect of magnetic field on heat transfer in a slotted channel. *Fusion Engineering Design*, 27 (1995)
23. L. Buehler, S. Horanyi, Experimental investigation on the stability of MHD flows in a conducting flat rectangular duct for large Hartmann numbers, PAMIR conference on Fundamental and Applied MHD, 7th Int. conference at France, (2008)

6 CHAPTER

Thermofluid MHD Studies in a Model of Indian LLCB TBM at High Magnetic Field Relevant to ITER

6.1 Introduction

The Indian LLCB-TBM for ITER has both the features of solid breeder as well as liquid breeder concept in a single variant with the prospect of enhanced tritium production rate and high grade heat extraction. [1] Liquid metal Lead-Lithium(PbLi) serves the dual functionality of tritium breeder as well as coolant for ceramic solid breeders. The 'U' shaped first wall (FW), cooled by high-pressure helium gas flowing within embedded helium slots, encloses the breeding unit consisting of encapsulated Li_2TiO_3 pebbles ceramic breeder compartments and internal liquid metal flow channels. Liquid metal PbLi flows around the ceramic pebble bed compartments in slotted poloidal parallel channels to extract the volumetric nuclear heat that is produced in the ceramic pebbles and in Pb-Li itself and heat deposited by neutrons generated in the D-T reaction. [2, 3] The structural material of the blanket module including plasma facing First wall (FW) is primarily envisaged as low activation India specific ferritic martensitic steel (IN-RAFMS). [4] Unlike the cases of blanket modules with radiation resistant electrical/thermal insulation of liquid metal flow channels from the structural material [5], initial design of LLCB is proposed with bare electrically conducting structural walls.

Since the flow of Pb- Li experiences strong transverse toroidal magnetic field ($\sim 4\text{T}$) present for confining the fusion plasma, gives rise to intense MHD effects and hence significant modification in flow characteristics (suppression of turbulence, presence of M profiles and very thin Hartmann boundary layers etc.) with large additional pressure drop. [6, 7] For the liquid metal flow rate of $\sim 12\text{ kg/s}$ in the LLCB blanket the characteristic non-dimensional parameters,

Hartmann number ($Ha = B_0 a \sqrt{\sigma/\mu}$) which square is a measure of the electromagnetic force over viscous force, and interaction parameter ($N = \sigma a B_0^2 / \rho u$) that is the ratio of electromagnetic force to inertial force, have high values $\sim 1.8 \times 10^4$ and $\sim 5.0 \times 10^3$ respectively. Symbols B_0 , a , σ , μ in the definition of Hartmann number are strength of the applied magnetic field, characteristic length scale, electrical conductivity and dynamic viscosity of PbLi respectively. The Grashof number ($Gr = \rho g \beta \Delta T L^3 / \nu^2$) which measures the strength of buoyancy force over the viscous force is an important characteristic parameter for systems that account for buoyancy contribution in flow dynamics. For the LLCB variant, the numerical value of Gr is varying in different channels in the range of 10^8 to 10^{10} . Here, ' β ' is the volumetric coefficient of thermal expansion, ' ΔT ' is characteristic temperature difference estimated from the maximum wall temperature and linear average fluid temperature and ' L ' is the classical hydraulic diameter of the corresponding channel.

The MHD effects are further enhanced by complex liquid metal flow paths that consists of electrically coupled parallel channels, multiple L/U bends with sudden expansion or contraction, radial variation of deposited nuclear heat density, etc. The design and optimization of various components of blanket modules relies on accurate prediction of the flow rate distribution, pressure drop, regions of recirculation, velocity and temperature distribution through numerical simulation in full scale geometry. Numerical modeling of MHD flow in a full scale version with integrated helium cooled FW is also necessary for the estimation of structural wall temperature which will be further used for thermomechanical stress calculation. Although steady state thermal analysis has been carried out for structural analysis in some of the variants [1, 2], the effects of MHD was not considered and necessitated for exclusive modeling for assessment of various MHD flow features at high magnetic fields.

In the present study, 3-D numerical simulation is accomplished in one of the LLCB variants at typical fusion relevant magnetic fields ($B_0=4T$). The model geometry has all the flow features of a typical LLCB TBM and computation is performed in a full scale version with integrated helium cooled First wall using CFD code FLUENT [8]. An exploded view of the components of LLCB TBM is shown in Fig. 6.1. Benchmarking of the code with analytical solutions as well as with experiment data at high magnetic fields is already reported [9, 10]. As the characteristic Hartmann number and interaction parameter is high ($Ha=17845$, $N=4697$), the flow is expected to be laminar or quasi 2D (Q2D) turbulent due to the action of the dominating electromagnetic body force through joule dissipation along with viscous dissipation [11, 12]. At this stage knowledge of Q2D turbulent model and its implementation into 3D solver of any commercial CFD code is limited in literature and need extensive benchmarking studies for practical engineering applications. So the present study considers the flow is laminar for preliminary design calculation. The applicability of the laminar model at high magnetic fields and similar MHD flow features in elements of LLCB is also reported in various laboratory scale experiments with working fluid PbLI or NaK[13, 14].

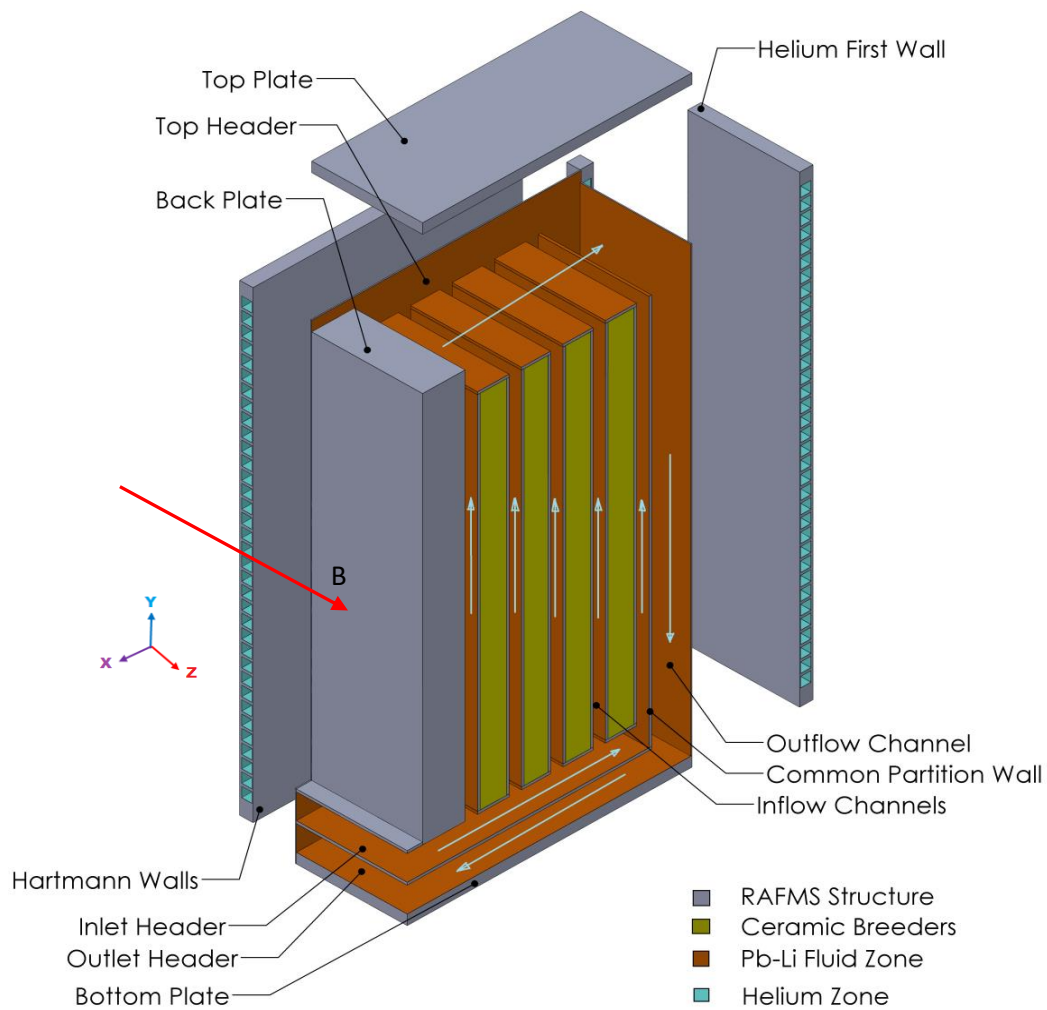


Figure 6.1: Exploded view of PbLi flow configuration in LLCB TBM variant

The main outcomes of the present study include analysis of velocity and current distribution, identification of recirculation/vortex regions which are potential for tritium trapping zones or local hot spots and pressure drop in the blanket module. The flow rate distribution in coupled parallel channels that are feed from a common inlet header is obtained for a total mass flow rate of 12kg/s. Themofluid MHD study is carried out to obtain the structural wall temperature distribution in various zones. Net heat extraction rate by First wall helium cooling circuit and PbLi is also estimated for a given neutronic heat load.

6.2 Description of model geometry

Numerical simulation is performed in actual dimensions which are of 1660 mm in poloidal (y), 484mm in toroidal (z) and 546 mm in radial (x) direction. There are 5 poloidal flow channels around the 4 ceramic breeders blocks in which PbLi is flowing to extract the heat. The dimensions of Pbi flow channels around the breeder blocks are shown in Fig. 2. Liquid metal PbLi enters into these parallel poloidal channels from the common bottom inlet header attached with the inlet. Flow is vertically upward in the poloidal channels before it turns radial at the common top collector header. Then liquid metal returns through a parallel poloidal channel at the plasma facing First wall and exit through a common bottom outlet header. The incoming and outgoing flow channels are separated by a 5mm thick common partition wall. Each incoming PbLi flow channel width is of 24 mm and the return channel width is 76 mm. The applied magnetic field in toroidal direction (z) is transverse throughout the PbLi flow path in LLCB TBM. Breeder blocks of variable widths are enclosed in 5mm thick rectangular boxes. As shown in Fig. 6.2, the U-shaped First wall that encapsulate the internal channels and breeder blocks is composed of two 4 mm thick U-type parallel IN-RAFMS plates with provisions for helium flow routed through internal channels. Total number of 64 square helium channels (20 mm x 20 mm) which are stacked parallel in the poloidal direction (y) and each channel is separated from the other by 5 mm thick mid rib. The other external walls like top/bottom wall and channel-5 associated back/cover plate is of thickness 0.02m and 0.082 m respectively.

6.3.1 Governing Equations

For obtaining magneto-hydraulic solution, the following system of equations governing the steady state MHD flow of incompressible, electrical conducting fluid under the influence of external magnetic field has been solved in FLUENT [8] code. The effects of induced magnetic field are neglected due to small magnetic Reynolds number ($Re_m < 1$) [15] and the electromagnetic body force, as source term in the momentum equation is coupled with other equations based on electric potential formulation. In view of electrical conducting channels and moderate characteristic parameters ($Ha = 17845$, $N = 4697$) the flow is expected to be laminar as Ha/Re value is above the critical number of transition ($Ha/Re > 0.02$) from turbulent to laminar regime [16].

$$(\vec{U} \cdot \vec{\nabla})\vec{U} = \frac{-\vec{\nabla}p}{\rho} + \nu \nabla^2 \vec{U} + \frac{\vec{J} \times \vec{B}_0}{\rho} \quad \text{Eqn(6.1)}$$

$$\vec{\nabla} \cdot \vec{U} = 0 \quad \text{Eqn(6.2)}$$

$$\vec{J} = \sigma (-\vec{\nabla}\phi + \vec{U} \times \vec{B}_0) \quad \text{Eqn(6.3)}$$

$$\vec{\nabla} \cdot \vec{J} = 0 \quad \text{Eqn(6.4)}$$

Here, ρ , \vec{U} , ν , σ are density, velocity, kinematic viscosity, electrical conductivity of the fluid whereas p , \vec{J} , \vec{B}_0 , ϕ are pressure, electric current density, magnetic field induction, and electric potential respectively.

Eqns (3) and (4) are combined in potential method formulation to solve electric potential ϕ from the following equation,

$$\nabla^2 \phi = \vec{\nabla} \cdot (\vec{U} \times \vec{B}_0) \quad \text{Eqn(6.5)}$$

Here, B_0 is the strength of applied magnetic field.

In the solid domain the following equation is solved for the electric potential

$$\nabla^2 \phi_w = 0 \quad \text{Eqn(6.6)}$$

Here, ϕ_w is the potential distribution in the walls. At the fluid-wall interface, in addition to no-slip condition for the velocity, continuity of the normal component (to the walls) of current density ($J_n = J_{nw}$) have been ensured through coupled boundary condition. Here J_n refers to the normal component of current density on the fluid side and J_{nw} corresponds to the wall side.

The system of governing equations is solved in a finite volume and pressure based solver of CFD code FLUENT. Electric potential variable of equation (5) and equation (6) is solved through user defined scalar transport equation. For spatial discretization in momentum and electric potential equation, second order upwind scheme and SIMPLE algorithm is used for pressure velocity coupling. At First, the converged solution is obtained without activating the energy equation and subsequently used as base solution for solving the energy equation.

The steady state energy equation has been solved to obtain the temperature distribution in structural materials, PbLi and ceramic breeder zones. Heat transfer rate to the embedded First wall helium cooling channels is also estimated. Governing equations for temperature and modified velocity field due to buoyancy as presented in equation (7) and (8) is solved along with the mass continuity, charge conservation and electric potential equations as described in eqn (2) to eqn (6). In the energy equation (7) the source term due to work done by viscous and fluid expansion is neglected because of their insignificant contributions. Gravitational acceleration of 9.8 m/s^2 is specified in the vertical downward direction (negative Y-direction). The variation of temperature dependent physical properties like density($\rho(T)$), dynamic viscosity($\mu(T)$) and electrical conductivity of PbLi($\sigma(T)$) with temperature has been taken into account as per equations (9), (10) and (11) respectively [17]. However, in the solid domain, fixed material properties are used at temperature of 623 K. The physical properties of the PbLi

and RAFMS structure [18] for initial magneto-hydraulic solution is taken as constant at 623 K and respective numerical values are shown in Table 6-1.

$$C_p [\vec{\nabla} \cdot (\rho \vec{U} T)] = \vec{\nabla} \cdot (\kappa \vec{\nabla} T) + \frac{\vec{J} \cdot \vec{J}}{\sigma} + S_T \quad \text{Eqn(6.7)}$$

$$\rho(\vec{U} \cdot \vec{\nabla}) \vec{U} = -\vec{\nabla} P + \mu \nabla^2 \vec{U} + \vec{J} \times \vec{B}_0 + (\rho - \rho_0) \vec{g} \quad \text{Eqn(6.8)}$$

$$\rho(T) = 9499 - (0.85 * (T - 508)) \quad \text{Eqn(6.9)}$$

$$\mu(T) = 1.87E - 4 * \exp[11640 / (8.31 * T)] \quad \text{Eqn(6.10)}$$

$$\sigma(T) = [102.3E - 8 + 0.0426E - 8 * T]^{-1} \quad \text{Eqn(6.11)}$$

Here, C_p is the specific heat ($J. Kg^{-1}.K^{-1}$), κ is the thermal conductivity ($W.m^{-1}.K^{-1}$), ρ_0 is the reference density ($kg.m^{-3}$) of PbLi and S_T is the volumetric source term (W/m^3).

The third term in right hand side of equation (7) is the joule heating term and fourth source term (S_T) is the volumetric heat deposited by neutrons in PbLi as well as structural materials.

Table 6-1: Physical properties of materials used in numerical simulation (non-thermal)

Physical property	Lead-Lithium(PbLi) [17]	IN-RAFMS [18]	Lithium-Titanate(Li ₂ TiO ₃)
Density (ρ), (kg/m ³)	9401.25	7770	3430
Specific heat (C_p), (J/kg-K)	189.32	565	1341.42
Thermal conductivity (λ), (W/m-K)	14.16	33.20	1.0
Electric conductivity (σ), (1/ Ω -m)	0.7692E6	1.31E6	1.0E-6
Dynamic viscosity (μ), (Pa-s)	0.00177	–	–

6.3.2 Boundary conditions

For velocity field, no-slip condition has been used at the solid surface. At the inlet uniform velocity corresponding to mass flow rate of 12kg/s and at the outlet, a homogenous Dirichlet pressure condition ($p=0$) is applied. For the electric potential, insulation is assumed beyond the outer walls and a homogeneous Neumann condition $\partial\phi/\partial n = 0$ is applied. In case of simulation without any heat load, the outer walls of all the breeders are electrically insulated. But for the case of thermofluid simulation, the solid-solid interface of breeder structural wall and ceramic breeder is treated as coupled wall similar to the fluid-solid interface. The heat transfer coefficient ($h=3691$ W/m²) is specified at the helium contact walls which is evaluated using correlations [19, 20] for helium flow rate of 1.63 kg/s (corresponding He velocity 50 m/s) and average bulk helium temperature of 599 K. To simulate the incoming heat flux from plasma side, surface heat flux of 0.3 MW/m² is specified at the plasma facing side of U-shaped FW.

6.3.3 Mesh

The accuracy and computation time of numerical simulation is strongly dependent on quality of the mesh used in modeling of the geometry. In view of this, a multi blocked structured mesh having hexahedral elements is generated for the entire geometry with adequately resolved characteristic Hartmann layers and side wall boundary layers for accurate prediction of flow field variables. The total volume element of the computation geometry is 3.51 million. For a given edge, variable spacing is adopted wherever changes in the flow variables are expected to be large like Hartmann and side boundary layers, flow turning at the L/U bends etc. A view of the mesh structure in a poloidal (vertical) cross section is shown in Fig. 6.3. Unlike the PbLi flow channels, the First wall (FW) with embedded helium flow slots is meshed with a rather uniformly spaced coarse mesh due to absent of any boundary layer associated with helium flow. So the common interface at the First wall and rest of the blanket module is non conformal (see zoomed region labeled-1 as shown in in Fig. 6.3). Whereas, all other interfaces including internal breeder walls are conformal. The Hartmann boundary layer along the applied magnetic field direction ($\delta_H = a / Ha$) which is of the order of 12 μm and side wall boundary layer of thickness 0.0016m along the channel width ($\delta_s = a / \sqrt{Ha}$) is resolved with at least 2 elements and 6 to 9 elements respectively. As the node spacing is gradually increasing from boundary wall, element size in center region (core) of flow cross section is relatively large. A view of the mesh in a flow cross section of bottom inlet outlet header along with number of elements in Hartmann boundary layer is shown in Fig. 6.4. The number of nodes in a typical radial-toroidal flow cross section is 31 along radial(X-direction) and 71 along toroidal (Y-direction). Similarly, the number of nodes in other elements of LLCB is presented in Table 6-2. This optimum grid structure is adopted after performing grid independent analysis with higher mesh and based on our previous experience of numerical studies carried out in test section experiment at high magnetic fields.

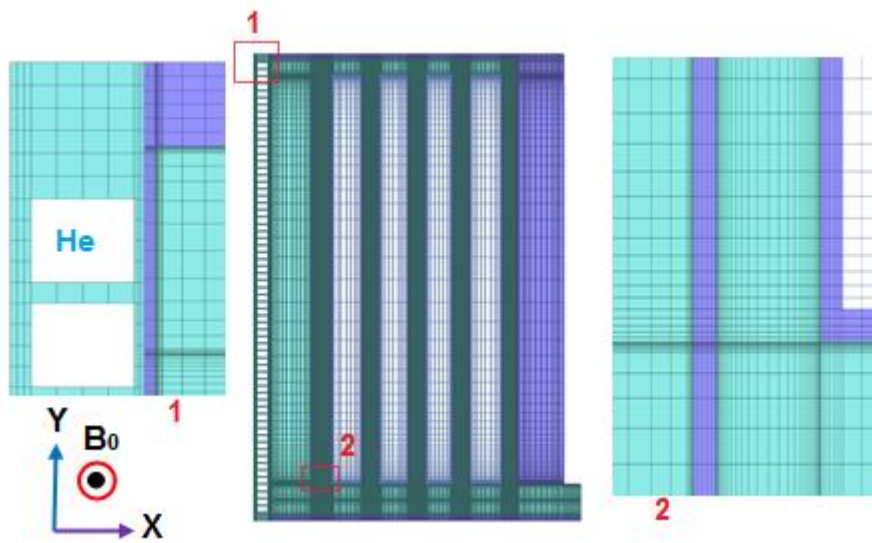


Figure 6.3: Mesh structure in a vertical cross section of LLCB. Close view of FW interface at top corner (zoomed label-1) and entrance region of channel-1(zoomed label-2)

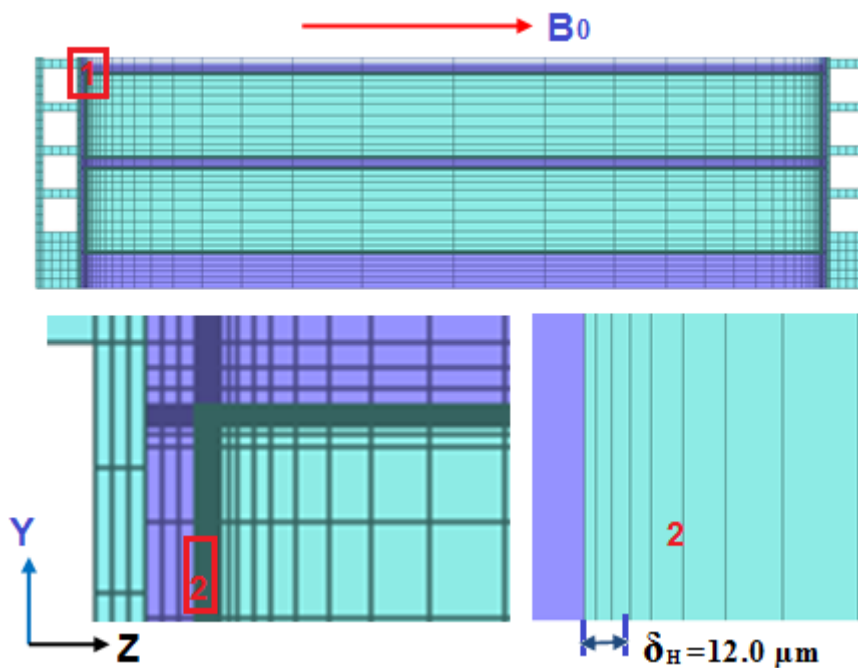


Figure 6.4: View of mesh in a flow cross section of bottom inlet outlet header. Close view at Hartmann wall (zoomed label-1) and elements in Hartmann layer (zoomed label-2)

Table 6-2: Number of nodes along radial (X), toroidal(Y) and poloidal direction(Z) for various element of LLCB TBM

Element of LLCB TBM	radial (X)	toroidal(Y)	poloidal (Z)	Hartmann Boundary layer	Side wall Boundary layer
channel-1,2,3, 4, 5	31	71	125	02	09
Inlet, outlet header	290	71	25	02	07
Back plate	16	71	125	--	--
FW, Breeder and common partition walls	06	71	125	--	--
Top and bottom wall	290	71	08	--	--

6.4 Results of MHD flow analysis

Although numerical experiments have been carried with different magnetic field (1-4 T), results of steady state solution for highest magnetic fields (4T) is presented in the following sections. The approximate converged solution is assumed by verifying the insignificant change in flow variables in successive iterations as well as monitoring the residuals for sufficient long computation time.

6.4.1 Velocity profile

Liquid metal PbLi enters into the 5 vertical channels (poloidal direction) unevenly from the common bottom inlet header. Then the flow is redistributed in each channel to form characteristic M-shaped profile across the side walls as expected in a typical MHD flow. The axial velocity profile (Y-velocity) across the side walls at different heights of channel-1 along with return flow channel is shown in Fig. 5 (a) and for channel-2, channel-3, channel-4 and channel-5 is shown in Fig. 5(b).

Fig. 6.5(a):

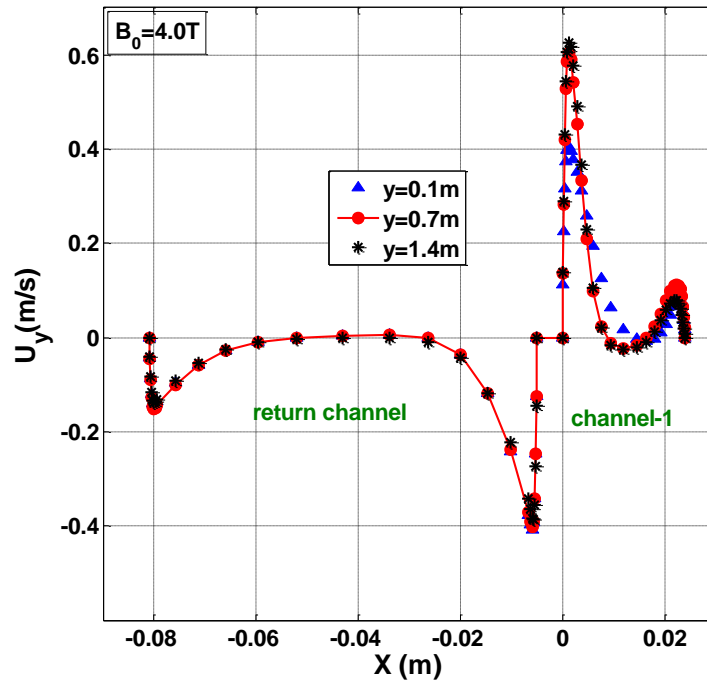


Fig. 6.5(b):

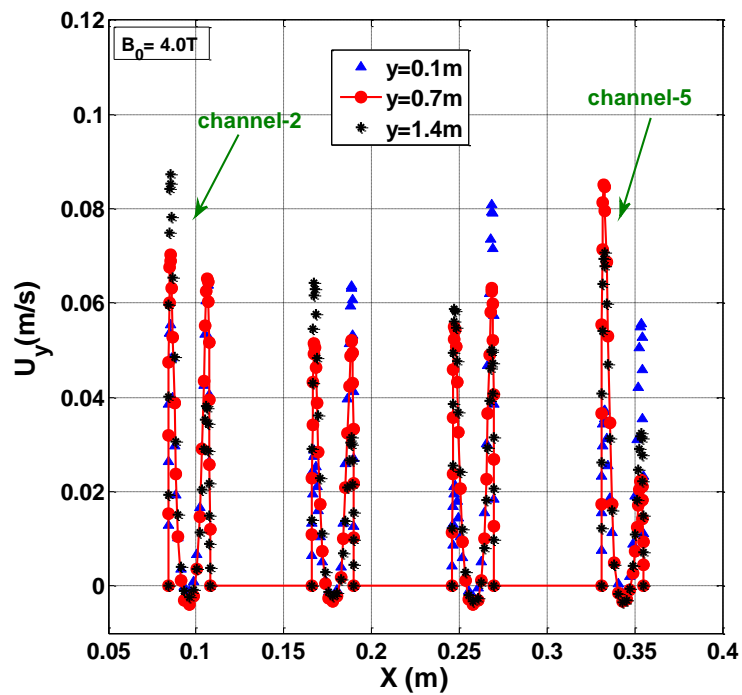


Figure 6.5: Axial velocity profile across the center of side walls at different poloidal heights; for return channel and channel-1 in Fig. 6.5(a) and for channel-2 to channel-5 in Fig. 6.5(b)

It is observed that the peak velocity in the side layer jet adjacent to the common partition wall of channel-1 and return channel is highest among all the flow channels. For a better view, the axial velocity profile at either side of the common wall of channel-1 and return channel is shown in Fig. 6.6(a) at a radial-toroidal flow cross section ($Y=0.75\text{m}$). The M-shape profile is asymmetric across the side walls of channel-2, channel-3, and channel-4 (see Fig. 6.5(b)) even the wall thickness is symmetric. The flow asymmetry is caused by asymmetric wall electric potential distribution due to electrical coupling with adjacent channels. The peak velocity of the side layer jet of channel-5 adjacent to the back plate is lowest among all the channels which is attributed to the higher electrical conductance of thicker back plate (0.082 m). However, the velocity profile is symmetric across the Hartmann walls and reverse flow of low axial velocity is observed in the central core region of all the flow channels (see Fig. 6.6(b)). The increase of side layer peak velocity is also observed adjacent to the common partition wall of bottom inlet-outlet header having counter current flow configuration and shown in Fig. 6.7.

Fig. 6.6(a):

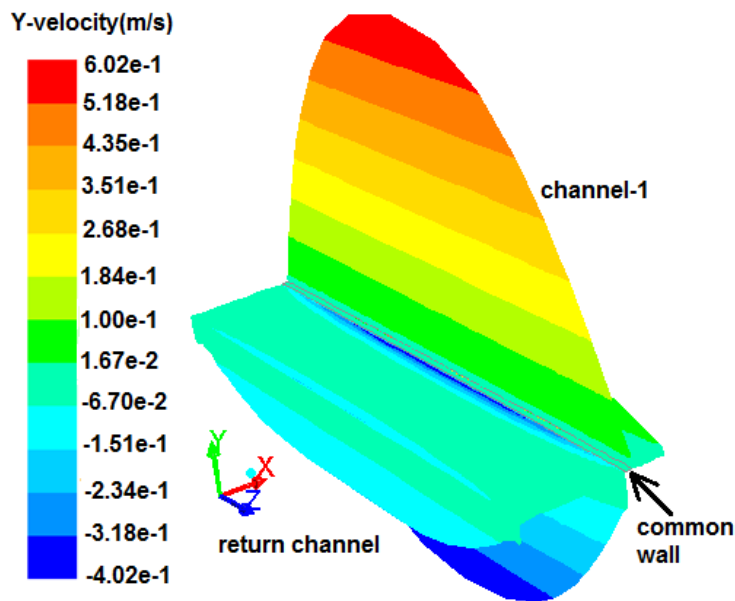


Fig. 6.6(b):

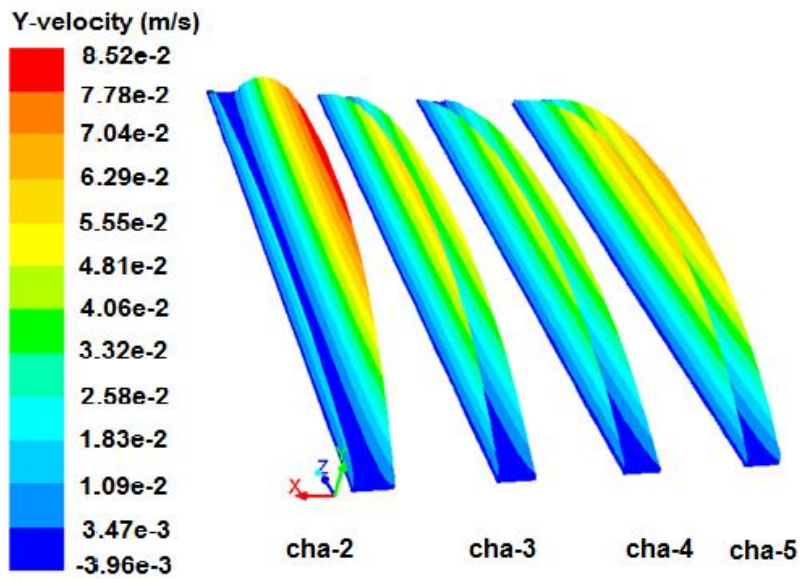


Figure 6.6: 3D axial velocity profile in a flow cross section at $Y=0.75\text{m}$ and $B_0=4\text{T}$; for channel-1 and return path in Fig. 6.6(a) and for channel-2 to channel-5 in Fig. 6.6(b)

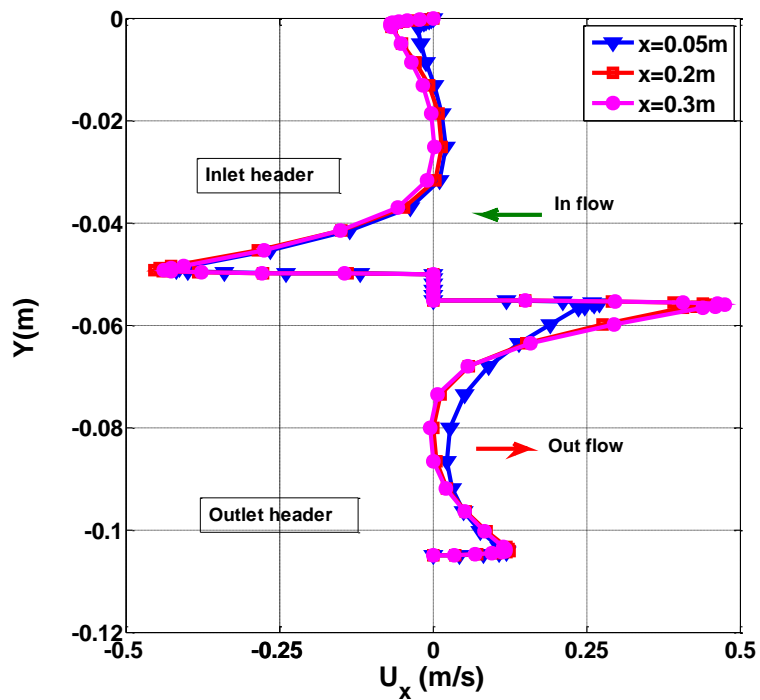


Figure 6.7: Axial velocity profile across the side walls of bottom inlet/outlet header at the center of header cross section and $B_0=4\text{T}$

The presence of helium slots in the FW makes the wall conductance non homogenous. Absences of material in the region of perforations offer higher resistance to the flow of electric current. As a result, the wall electric potential distribution is affected along liquid solid interface and leads to varying peak velocity in the side layer. Numerical investigation for effects of helium cooling channel in a central flow cross section of HCLL blanket is already reported assuming the flow is fully developed [21]. Expecting similar effects on the local velocity profile of the return channel adjacent to the FW, variation of peak velocity in the side layer jet is investigated. The placements of helium channels in the FW are equidistant along the poloidal flow path. A schematic for the cut view of FW radial-poloidal cross section is shown in Fig. 6.8. So spatial variation of local velocity is expected to follow the periodic pattern similar to the locations of helium channels at least in the region of constant pressure gradient where the effects of U-bend and L-bend from the respective top and bottom region is minimum. The variation of side layer peak velocity which is located at a distance of $9.2E-4$ m ($\delta x/a=0.0043$) from the wall and at the symmetric vertical plane ($Z=0.214$ m) of return channel is shown in Fig. 6.9. As can be seen in the Fig. 6.9, significant variation of peak velocity is observed with varying strength along the poloidal flow path. But spatial variation of local peak velocity is observed to be weakly correlated with the locations of the helium slots. Instead, the velocity variation is found to be highly correlated with the trend of transverse electric field (E_x), which is a function of the local electric potential at the solid-liquid interface. In this case of 3-D current distribution, axial currents (J_y) generated in the upstream and downstream of flow path are also closed through the FW in addition to the transverse currents (J_x) induced in the return channel. In fact, the distribution of electric potential is a result of complex 3-D electrical current flow in the FW. So it is difficult to isolate the contribution of inhomogeneous wall electrical conductivity alone on the local velocity like the case analysed in a fully develop (2-D) flow [21]. The magnitude of velocity variation is not symmetric which is attributed to the unequal

flow of axial currents from the top and bottom regions. The details of electrical current paths are described in the subsequent section.

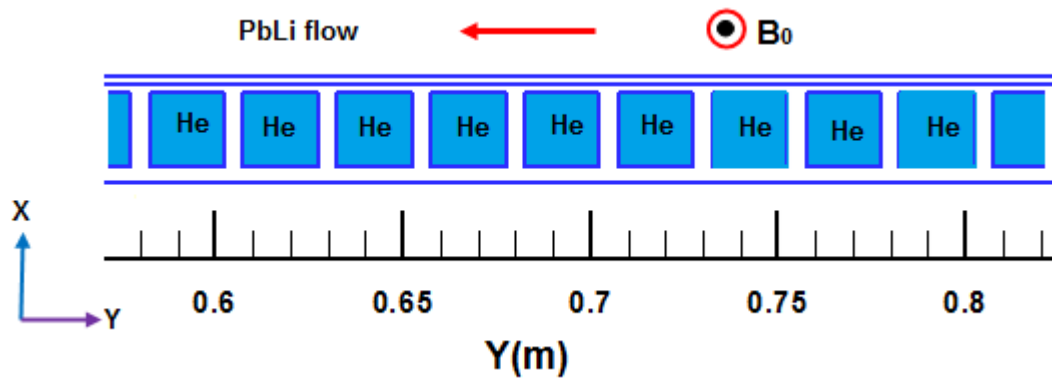


Figure 6.8: Schematic for cut view of FW radial poloidal cross section

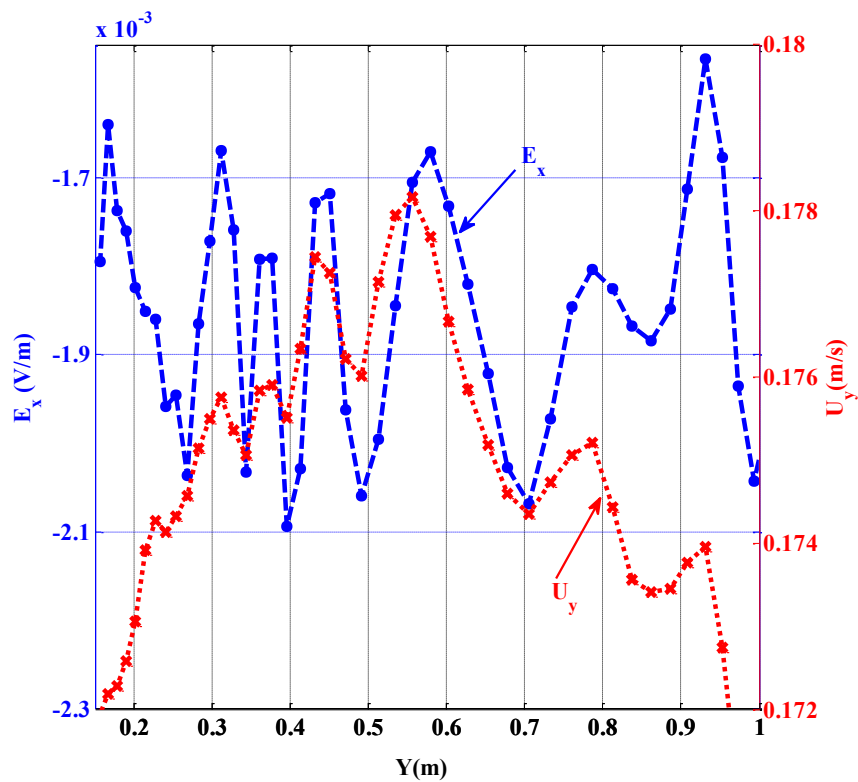


Figure 6.9: Poloidal variation of jet velocity and transverse electric field(E_x) in the side layer of return channel adjacent to helium cooled FW

6.4.2 *Current and Velocity Streamlines*

The physical explanation for increase in the side layer peak velocity in counter current flow channels sharing a common wall can be drawn by analyzing the electrical current path across the wall. For the case of channel-1 and return flow channel, the transverse current (J_x) is opposite across the common partition wall because of the counter current flow configuration (see Fig. 6.10). As the flow rate is higher in the return channel, the higher induced voltage across the side walls increases the absolute electric potential at the electrically conducting common partition wall. The electric potential and transverse electric field profile across the side walls of channel-1 and return channel including common partition wall (5mm thick) is shown in Fig. 6.11 at a poloidal height of $y=0.7\text{m}$ and at the center of the duct cross section. As can be seen, higher electric potential at the common partition wall leads to increase of the local transverse electric field (E_x) component. In accordance with the Ohm's law, the magnitude of local transverse current (J_x) which is mainly responsible for the electromagnetic drag is reduced and hence increases the local velocity component in the axial direction. Numerical analysis of fully develop MHD flow in coupled rectangular channel has earlier been reported in which one of the case study is for coupled channels that are arranged perpendicular to the magnetic field [22].

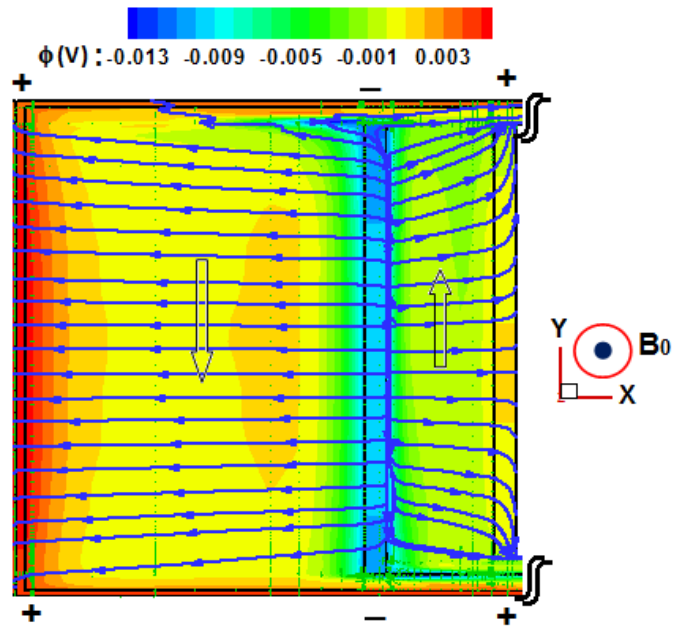


Figure 6.10: Electric potential distribution and current path in a vertical plane near the common partition wall of channel-1 and return path

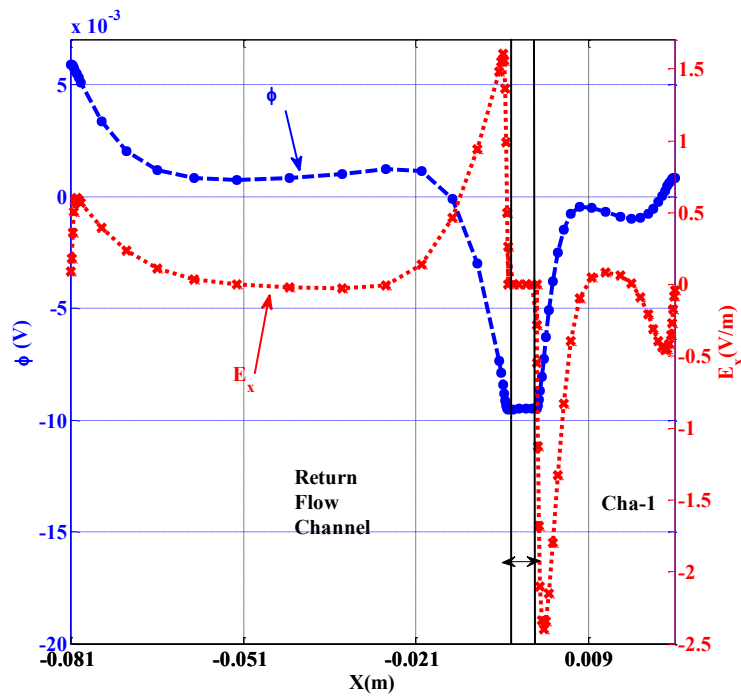


Figure 6.11: The electric potential (left) and transverse electric field (right) profile across the side walls of channel-1 and return channel separated by common partition wall

The formation of higher velocity jets was attributed to current distribution parallel to the magnetic field direction near the common wall of counter flow configuration. With the similar analogy, current path in a flow cross section ($Y=0.7\text{m}$) as shown in Fig. 6.12 is analyzed. Since the opposite oriented transverse current (J_x) induced in channel-1 and return path are flowing parallel in the common wall, the effective wall thickness is lower which in turn, increases the relative wall potential due to higher resistance to the global flow of electric current. As discussed earlier the higher electric potential and hence transverse electric field (E_x) forcing a significant fraction of transverse current (J_x) to turn in the side layers before entering into the side wall and hence results in a higher jet velocity. Similar phenomenon occurs at the common partition wall of bottom inlet-outlet header which leads to increase of the peak velocity in the side layer.

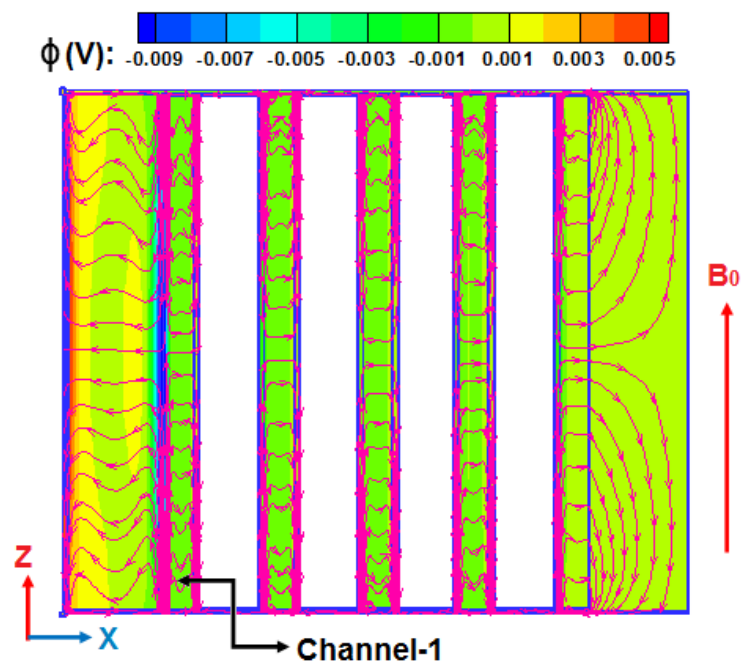


Figure 6.12: Current streamline and potential distribution in a cross section of all the flow channels at $Y=0.7\text{m}$

PbLi flow paths in the LLCB TBM consist of several 90-degree L and U bends when it turns from the radial to poloidal and vice versa at the entrance and exit of the poloidal channels. Change of flow direction and differential flow rate in electrically coupled radial poloidal channels leads to induced potential of varying strength and even opposite polarity in some of the side walls of connected channels. As an example, the top wall and the back plate are at positive potential whereas, common partition wall at the bottom inlet-outlet header is at negative potential (see Fig. 6.13). So these differential distributions of electric potential in the connected walls drive 3D currents not only in the structural walls but in the associated liquid metal flow channels also. In addition to these current driven by potential differences, 3D axial currents in the long poloidal channels are also generated at the connecting region to top and bottom headers as well as in the return channel due to sudden expansion or contraction of the flow cross section. These axial currents have significant effects on the velocity distribution across the side walls of poloidal flow channels. The current stream lines in a vertical central plane ($Z=0.214$ m) and contour of electric potential is shown in Fig. 6.13. As can be seen, axial currents in the top and bottom region of poloidal channels make the orientation of the current path different from the centre region. Interestingly, the axial current in the return channel, channel-1 and channel-5 is of opposite polarity at the top and bottom region, whereas, it is unidirectional in other channels. When the axial currents are converging or diverging in one of the side walls of the poloidal channel, it has significant effects on the velocity and wall electric potential profile. For the case of channel-1 and channel-5, the converging or diverging current in the right side wall leads to formation of potential valley or potential hill respectively (see Fig. 6.14).

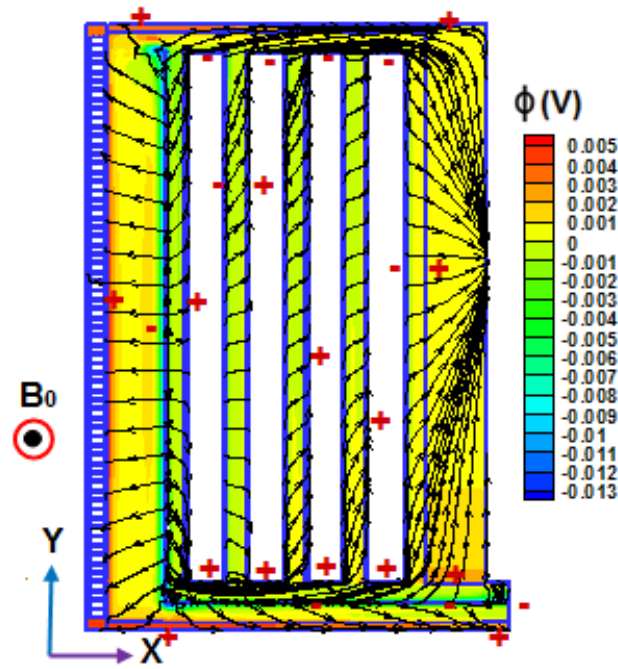


Figure 6.13: Contour of electric potential and current streamlines in the central plane at $z=0.214\text{m}$

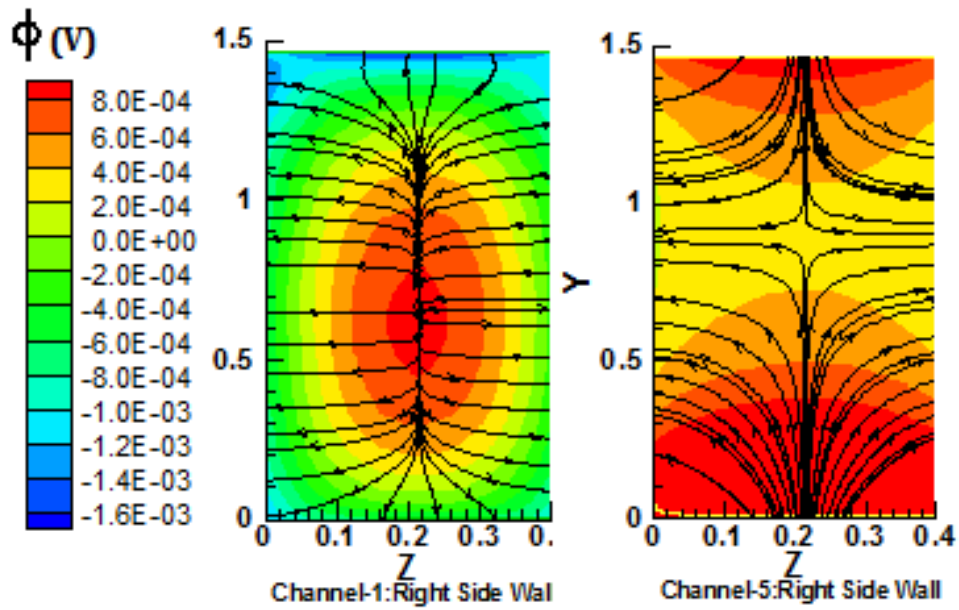


Figure 6.14: Electric potential contour with converging/diverging current lines in right side wall of channel-1 and channel-5

When axial currents are converging or diverging in a poloidal flow channel, fluid is swept from central core region to one of the sidewalls by the action of sidewise electromagnetic force which is generated due to the interaction of the axial currents with the applied magnetic field. For the case of channel-1, the upward flow of axial current (J_y) in the bottom region generates body force in the positive x direction which sweeps the fluid towards the right side wall and increases the peak velocity thereof inside the boundary layer. With the formation of a local potential valley in the right side wall, the local transverse current density (J_x) is increased and fluid is forced to move from the right side boundary layer to the core region due to higher electromagnetic drag. In contrast, the lower electromagnetic drag because of higher electric potential increases the jet velocity near the opposite side wall. As the fluid proceeds past these potential valley locations, the wall potential in the right side wall increases gradually towards the top header region and hence draws more flow in the upstream side layer jet. Also, the downward flow of axial currents in the upstream region move the fluid from the core region to the left side boundary layers. Thus, a larger portion of the fluid flow is carried by two side layers and the core is left with less inertia and very slow moving fluid. In addition to that, the higher aspect ratio of the channel cross section ($0.024 \times 0.428 \text{ m}^2$) further reduces the core flow and the core turns out to be a potential region of flow reversal in case of any local imbalance between pressure and electromagnetic forces. In the bulk of the core region the pressure force is balanced by the electromagnetic force. However, due to strong axial currents, electromagnetic force exceeds the pressure force in certain sections and sets a reverse flow in the less inertial core region (see Fig. 15). The reverse flow in the central core region and high shear near one of the side walls due to higher jet velocity leads to formation of large vortex in the poloidal channel. Large vortex structures in the symmetry plane ($Z=0.214\text{m}$) of return channel (labelled with 1&2), channel-1(labelled with 3) and channel-5(labelled with 4) are shown in Fig. 16. It is observed that rotation of the vortex is clockwise in the channel-5 where

the wall axial current is converging (potential valley) and anticlockwise in the channel-1 where current is diverging (potential source) in one of the side walls of respective channels. Large vortexes are also created in the return channel due to similar phenomena.

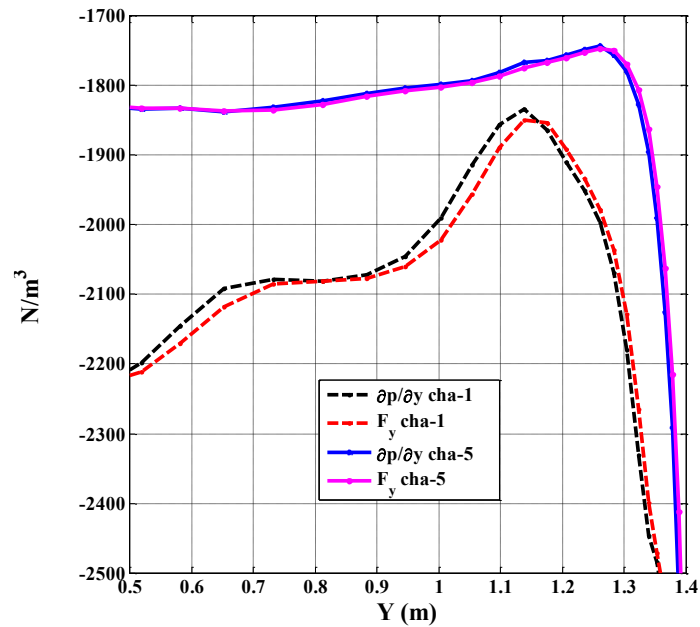


Figure 6.15: Comparison of pressure and electromagnetic force at the centerline of channel-1 and channel-5 for $B_0=4T$

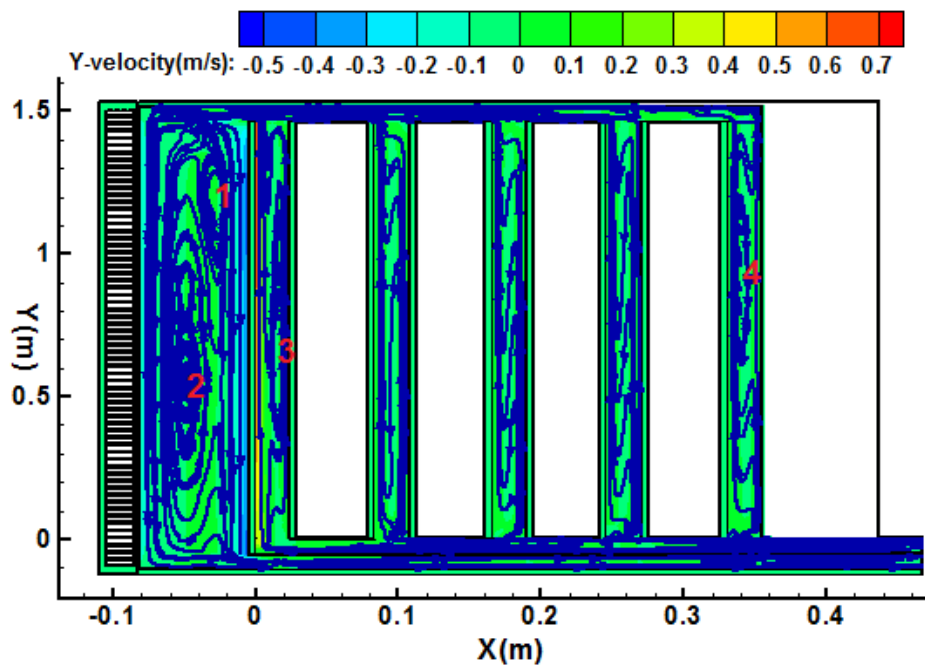


Figure 6.16: Y-velocity contour and velocity streamlines in the central plane at $z=0.214m$

6.5 Flow rate distribution in LLCB TBM model

Flow rate distribution in the parallel channels is influenced by several parameters including geometry, inlet conditions, orientation and strength of the applied magnetic field, relative wall conductance ratio of confining channel walls etc. In the absence of mock up experiment data at ITER relevant parameters, numerical prediction of flow rate distribution is useful for the design calculation. Table 6-3 presents the simulation result of flow rate distribution for the case of highest applied magnetic field $B_0=4\text{T}$ ($Ha=17845$) and its comparison with the case that is without any presence of applied magnetic field. The comparison is made to quantify the contribution of MHD effects over the inertia with regard to flow rate distribution. Based on the flow rate, Reynolds number for hydraulic case (Re) and MHD case (Re^*) for each flow channel is also presented in Table-6.3. The characteristic length scale is assumed 0.214 m for calculation of the Reynolds number. The flow is assumed turbulent for the case without any applied magnetic field and $k-\varepsilon$ turbulent model is used for simulation. It is observed that for MHD flow, a larger proportion of the fluid (60.5%) is drawn by channel-1 which is adjacent to the return path. In contrast, for the case of turbulent flow a relatively lower fraction of the fluid (33.4%) is drawn by channel-1. The higher flow rate in channel-1 in any case is primarily due to inertia and further enhancement of flow rate is caused by the MHD effects at the common partition wall having counterflow configuration across its sides. Distribution in channel-2 to channel-5 is more or less uniform with variation within 2.4% whereas, for case without magnetic field, the flow rate is monotonically reduced with minimum flow in the channel-5 close to the inlet. The hydrodynamic velocity profile of all the channels across the radial width in the symmetry plane ($Z=0.214\text{m}$) at a vertical height $Y=0.75\text{m}$ is shown in Fig. 6.17

Table 6-3: flow rate distribution in parallel channels for case of Ha= 17845 and its comparison with the case without any magnetic field.

Channel No.	Flow rate (kg/s) for case of Turbulent flow at $B_0 = 0$ T	Reynolds number (Re)	Flow rate (kg/s) for case of Laminar flow at $B_0 = 4$ T	Reynolds Number (Re^*)
channel-1	4.0068(33.4%)	47162	7.26 (60.5%)	85454
channel-2	3.0568(25.5%)	35980	1.43 (11.9%)	16832
channel-3	2.279(19.0%)	26825	1.01 (8.4%)	11888
channel-4	1.61 (13.4%)	18951	1.15 (9.6%)	13536
channel-5	1.04 (8.7%)	12241	1.15 (9.6%)	13536
Return channel	12.0 (100%)	141247	12.0(100%)	141247

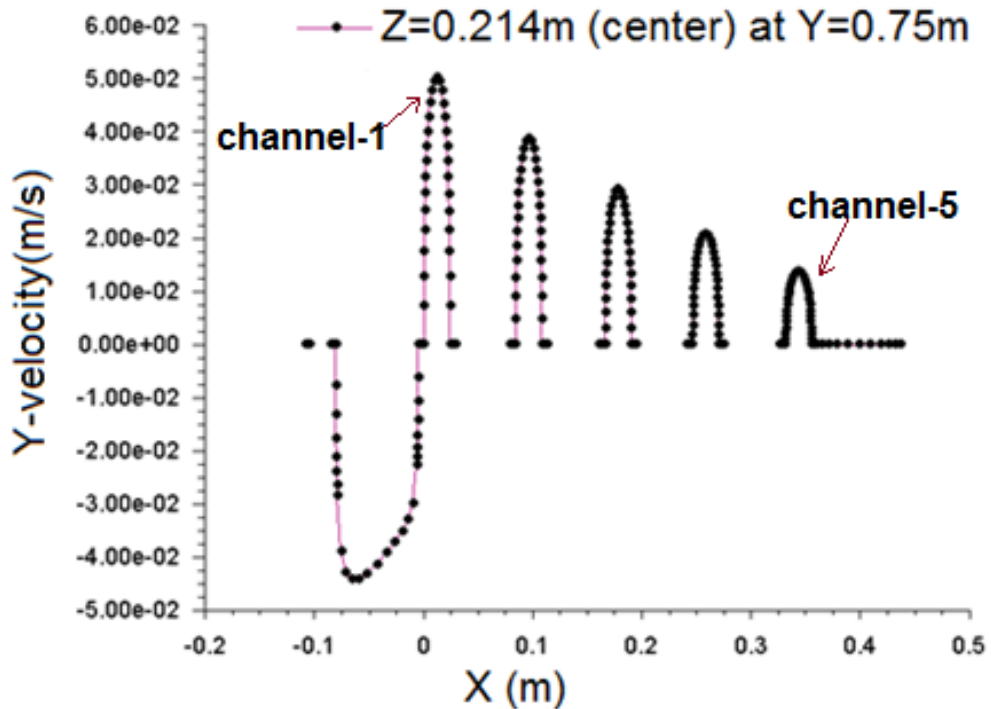


Figure 6.17: Hydrodynamic velocity profile across the radial width of all channels

6.6 Pressure distribution

The total pressure drop in the present numerical model is 35.4 kPa without considering the buoyancy effects. Axial pressure variation along the flow path ABCDEF at the central plane ($Z=0.214\text{m}$) is shown in Fig. 6.18. As shown in figure, the flow path consists of bottom inlet header(AB), channel-1(BC), portion of top connecting header(CD), return channel (DE) followed by bottom collecting header (EF). No constant pressure gradient regime is established in the bottom inlet header as the flow is continuously redistributed to the five vertical parallel channels. Similarly, continuously changing pressure gradient is observed in the bottom collector header as it is electrically coupled with the inlet header through the bottom common partition wall. However, there exists a constant pressure gradient regime in all the poloidal channels as observed in channel-1(path BC) and return channel (path DE).

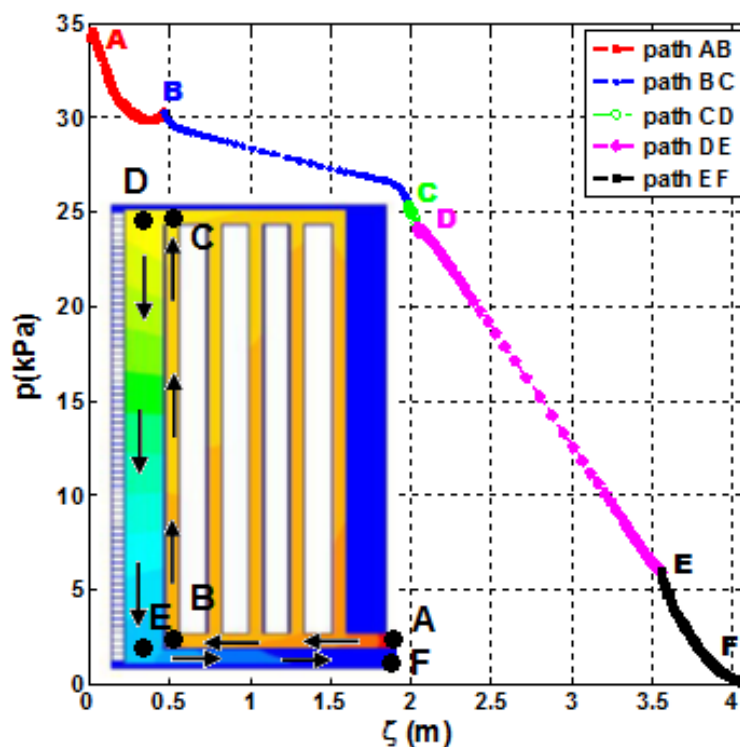


Figure 6.18: Axial pressure variation along the flow path ABCDEF as illustrated in the embedded picture at the central plane ($Z=0.214\text{m}$)

To get an idea of the average flow resistance offered by the individual flow channels, the normalized pressure ($p/\sigma_a U_m B_0^2$) is plotted against the normalized poloidal flow length $Y^*(Y/a)$ and shown in Fig. 6.19. The numerical dimensionless pressure gradient ∇p^* ($= \nabla p / (\sigma U_m B_0^2)$) is estimated from the slope of the curve and presented in Table-6.4. Here, U_m is the mean velocity in respective channel and 'a' is the half width along the applied magnetic field direction. In Table 6-4, numerical values of the non-dimensional pressure gradient for various flow channels is also compared with the corresponding theoretical estimations. It is to be noted that theoretical estimation of pressure gradient is derived from the fully develop theory models [23, 24] for isolated rectangular ducts.

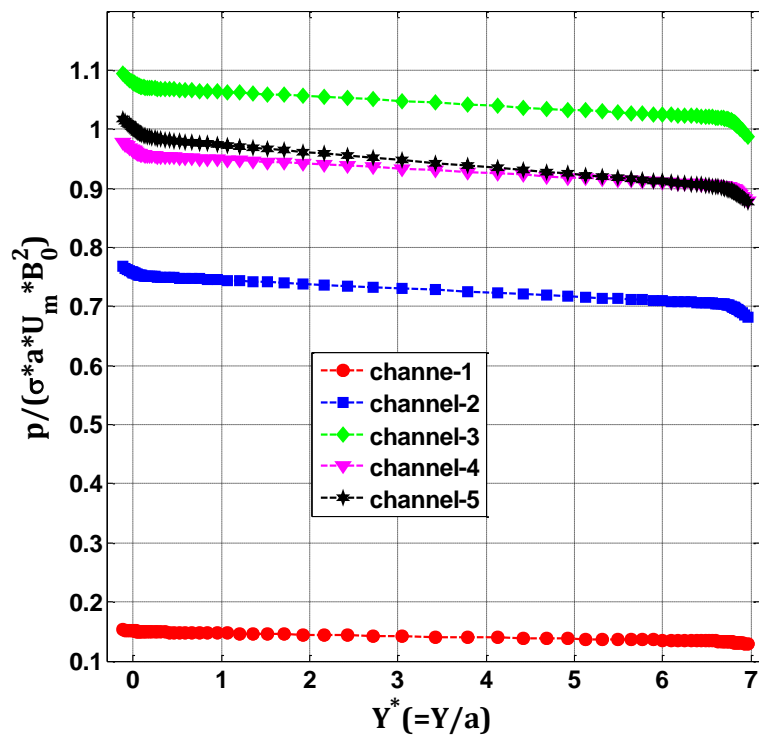


Figure 6.19: Variation of normalized pressure ($p/\sigma_a U_m B_0^2$) against the normalized poloidal flow length of channel-1 to channel-5

Table 6-4: Comparison of theoretical and numerical values of pressure gradient in LLCB flow channels

Flow channel	Relative conductance of side wall (C_s)		pressure gradient (kPa/m)		Non dimensional pressure gradient ($\nabla p / (\sigma U_m B_0^2)$)	
	Left side wall (C_{sl})	Right side wall (C_{sr})	Numerical	Theoretical	Numerical	Theoretical
channel-1	0.0398	0.0398	2.126	6.748	0.0023	0.0073
channel-2	0.0398	0.0398	1.284	1.329	0.00705	0.0073
channel-3	0.0398	0.0398	0.985	0.938	0.00766	0.0073
channel-4	0.0398	0.0398	1.12	1.069	0.00765	0.0073
channel-5	0.0398	0.653	1.82	1.889	0.01243	0.0129
Return channel	0.095	0.0398	12.54	12.1	0.026	0.025

As the confining walls of PbLi flow channels are of different thickness, relative wall conductance of side wall ($C_s = \sigma_{sw} * t_{sw} / \sigma_f * a$) and Hartmann wall ($C_h = \sigma_{hw} * t_{hw} / \sigma_f * a$) of respective channel is summarized in Table-6.4. These relative wall conductance ratios are important characteristic non dimensional parameters that are required for estimation of fully develop MHD pressure drop. Here variables σ_{sw} , t_{sw} and σ_{hw} , t_{hw} are the electrical conductivity and wall thickness of side and Hartmann wall respectively. Since the Hartmann wall of all the flow channel include embedded slots for helium flow, the effective thickness is considered taking into account the helium volume fraction which numerical value is 0.012 m. It is observed that numerical non-dimensional pressure gradient for channel-2, channel-3 and channel-4 is maximum 4.9% higher than the respective theoretical values. For channel-5, since one of the side wall is thicker ($t_{sw}=0.082m$), the corresponding side wall conductance ratio is higher ($C_{sr}=0.653$) and hence a higher pressure gradient is observed. But in channel-1 which is adjacent to the counter flow return channel, the numerical pressure gradient is significantly

lower than the theoretical values. This indicates local electrical coupling effects of countercurrent flow configuration offer lower flow resistance as far as pressure drop is concerned and hence draw more flow than other electrically coupled poloidal channels with co-flow configuration. The increased flow rate in channel-1 leads to higher absolute MHD pressure drop(~4kPa) in comparison with other incoming channels(2-2.5kPa).

6.7 Thermofluid MHD analysis of LLCB TBM

Heat deposition in elements of LLCB TBM and surface heat flux to plasma facing FW used in the present numerical simulation is based on the neutronic performance analysis of a conceptual design LLCB model [25] and presented in Table 6-5. A suitable functional form of the heat density variation along the radial direction (X) is provided as user defined heat source input to the numerical model. In the breeder zones the heat density is assumed to be uniform while exponential and polynomial functions are fitted into the PbLi and RAFMS zones respectively. The radial heat density profile across the TBM along with the coefficients of respective function in various zones are summarized in Eqns(12) & (13) The total integral heat deposition rate in all the zones of LLCB is 0.46MW which is consistent with the estimation by neutronic analysis.

i) Heat density profile in PbLi zone

$$q_{\text{PbLi}} = 4.5436 \times 10^6 \exp[-6.918 * X] \quad \text{Eqn(6.12)}$$

ii) Heat density profile in RAFMS walls

$$q_{\text{RAFMS}} = \sum_{n=1}^4 P_n X^n \quad \text{Eqn(6.13)}$$

P1=1.58E6, P2=-1.67E7, P3=-1.64E8, P4=-6.14E8, P5=9.11E8

Table 6-5: Heat density in various zones of LLCB TBM based on neutronic estimation

First Wall		PbLi channel		Breeders	
component thickness(mm)	q(MW/m ³)	channel thickness(mm)	q(MW/m ³)	breeder thickness (mm).	q(W/m ³)
plasma facing F-1(4 mm)	5.12	return channel (76)	3.31	breeder-1(50)	1.61
Mid Ribs(5 mm)	4.81	channel-1 (24)	2.01	breeder-2 (48)	0.95
F-2PbLi contact F-2(4 mm)	4.31	channel-2 (24)	1.32	breeder-3 (46)	0.57
--	--	channel-3 (24)	0.73	breeder-4 (51)	0.33
--	--	channel-4 (24)	0.41	--	--
--	--	channel-5 (24)	0.25	--	--

As described in section 6.2, the U shaped First wall of the present LLCB model is consisting of two 4mm thick parallel plates which accommodate 64 equally spaced square slots for helium flow. The parallel helium channels each having a flow cross section of 20 mm × 20 mm are separated by 5mm thick mid ribs throughout the U-shape First wall. The average volumetric heat load in the plasma facing side, mid ribs and PbLi side of the wall is 5.12 MW/m³, 4.81 MW/m³, 4.31 MW/m³, respectively. Schematic of cross sectional cut view of FW with surface and volumetric heat data is shown in Fig. 6. 20.

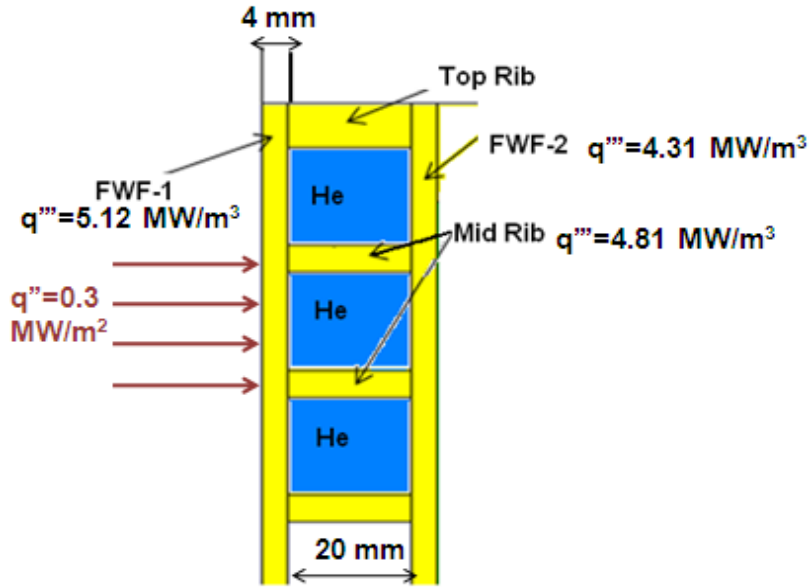


Figure 6.20: Schematic of cross sectional cut view of FW with surface and volumetric heat data

6.7.1 Results of thermofluid analysis

Since part of the neutron heat load of LLCB TBM is carried by First wall helium cooling circuit, it is required to quantify the net heat transfer rate to helium for proper heat balance in steady state condition. The results indicate that total heat transfer rate to helium is 0.444MW and heat transfer rate to PbLi is 0.257 MW. Excluding the surface heat load of 0.241 MW to helium at plasma facing First wall side, the net heat transfer rate by both helium and PbLi is 0.46MW which is consistent with the neutronic heat deposition data. So using equation (14), the net rise in helium and PbLi temperature is estimated to be 52.4 K and 115 K respectively. The specific heat of helium and PbLi is considered as $5195 \text{ J.kg}^{-1}.\text{K}^{-1}$ and $186 \text{ J.kg}^{-1}.\text{K}^{-1}$

$$\dot{Q} = \dot{m}C_p\Delta T \quad \text{Eqn(6.14)}$$

Here C_p and \dot{m} is the specific heat and mass flow rate of the fluid and \dot{Q} is the heat transfer rate into the fluid.

The temperature contour in the central plane perpendicular to the applied magnetic field as shown in Fig. 6.21(a) indicate a higher temperature in the breeder zones and the maximum temperature of 1240 K is at the breeder-1 where the heat deposition density is highest. The

maximum temperature of structural walls which are in contact with PbLi is analysed in view of design limitation for RAFMS structural material. Local maximum temperature of 782 K is observed at the top edges of the breeder-1 wall which are connected with the U-shape First wall where applied magnetic field is normal to the wall (see Fig. 6.21(b)). Even though the First wall is cooled by helium, higher temperature near the top edge of breeder-1 attached with First wall is observed due to following reasons. One is the vertically upward flow of PbLi around the breeder that led to higher fluid temperature than the bottom region and other is the very low velocity beyond the Hartmann boundary layer associated with the First wall. Thus a higher temperature zone is formed at the connected region of breeder-1 and First wall (Hartmann wall) especially towards the top region. Temperature distribution in the common partition wall (see Fig. 6.21(c)) is similar to the breeder structural wall but the local maximum temperature is lower (755 K) as it is cooled by PbLi at both the sides. The central portion of the breeder wall as well as common partition wall is adequately cooled due to higher side layer velocity. Major portion of the plasma facing First wall temperature is less than 693 K due to significant helium cooling at the inner side (see Fig. 6.21(d)). But a higher temperature observed in the top and bottom edge of the First wall associated with the top and bottom walls which is attributed to the absence of helium cooling in the current simulation model and is expected to be cooled by auxiliary systems in the realistic scenario. However, no hot spot is observed in the recirculation zones of poloidal channel which can be attributed to the better heat transfer due to higher thermal conductivity of PbLi. It is evident from the analysis of thermofluid studies that First wall helium cooling has significant effects in limiting the structural wall temperature within permissible limits.

Fig. 6.21(a)

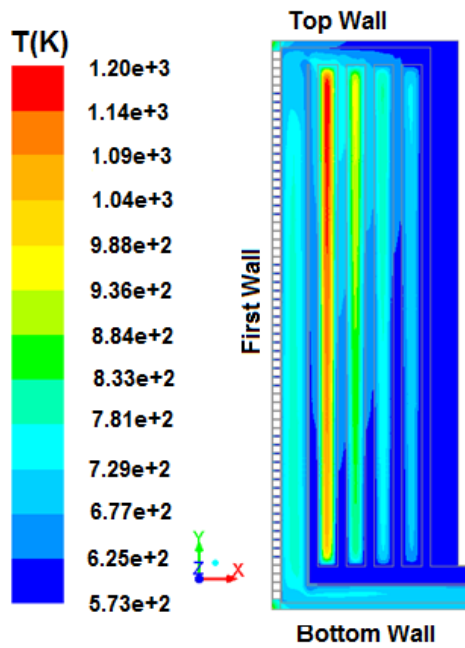


Fig. 6.21(b)

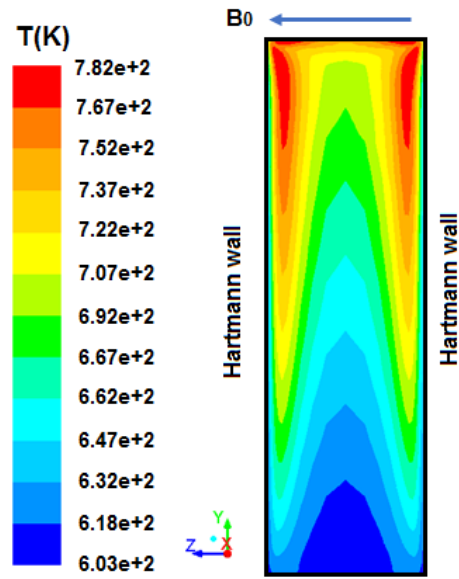


Fig. 6.21(C)

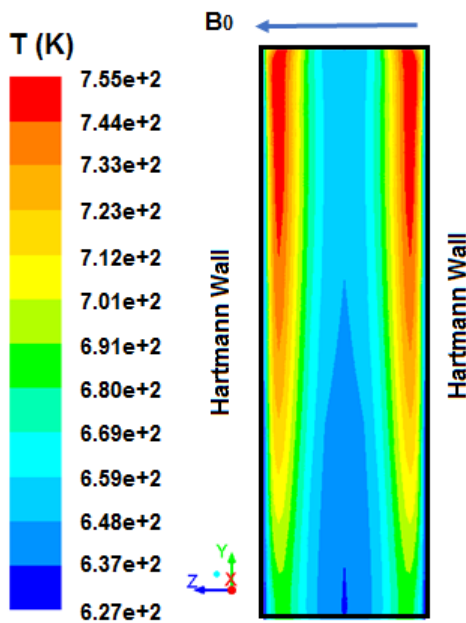


Fig. 6.21(d)

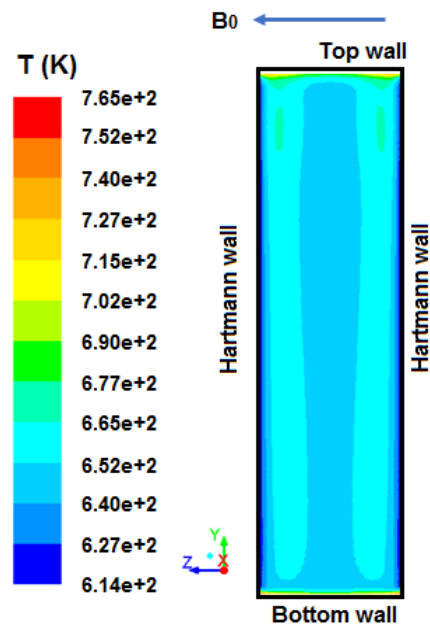


Figure 6.21: Contour of temperature in the central plane in Fig. 6.21(a), breeder-1 wall in contact with PbLi in Fig. 6.21(b), common partition wall plasma facing side in Fig. 6.21(C), Inner side of the first wall in contact with PbLi in Fig. 6.21(d)

6.7.2 *Modification in flow properties due to buoyancy effects*

The velocity profile of isothermal MHD case is significantly modified due to the effects of buoyancy force especially in the return flow and upcoming poloidal channels associated with breeder-1 and breeder-2 where temperature gradient is significant. As can be seen from Fig. B, the peak velocity of the side layer jet in channel-1, channel-2 and channel-3 is increased due to the action of buoyancy force in the stream wise direction. The effects of buoyancy force are more near the heated breeder walls. Whereas, the core temperature of the return flow channel is rather high than the helium cooled side wall and common partition wall. Since the radial width of the return channel is more(76mm) and the buoyancy force is opposing the flow in bulk of the flow region, the peak velocity of the side layer jet is further enhanced even if the buoyancy force is opposite in the side layers of the return flow channel. From the velocity distribution it is evident that the reverse flow region exists in different poloidal flow channels of LLCB. To identify those regions, the velocity streamlines are plotted in a central plane($z=0.214\text{m}$) and shown in Fig. C. As can be seen the observed vortex and reverse flow regions for thermal MHD case are similar to those observed in magneto-hydraulic case. But, the size of the vortex is different due to the influence of strong buoyancy force at least in the return flow and first two upcoming channels of the LLCB model. It is necessary to quantify the sizing and characterise in more detail relating to the phenomena associated with boundary layer separation. The present study can be assumed as a reference for future investigation pertaining to those important characteristics.

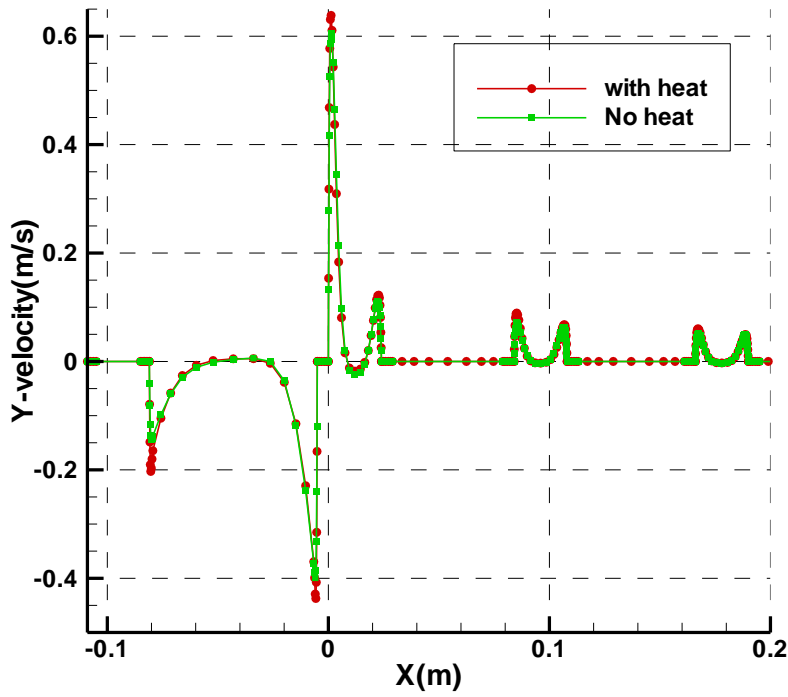


Figure 6.22: Comparison of radial velocity profile for case of isothermal MHD and thermal-MHD flow in the central plane ($Z=0.214\text{m}$) and poloidal height of $Y=0.85\text{ m}$ at $B_0=4\text{T}$.

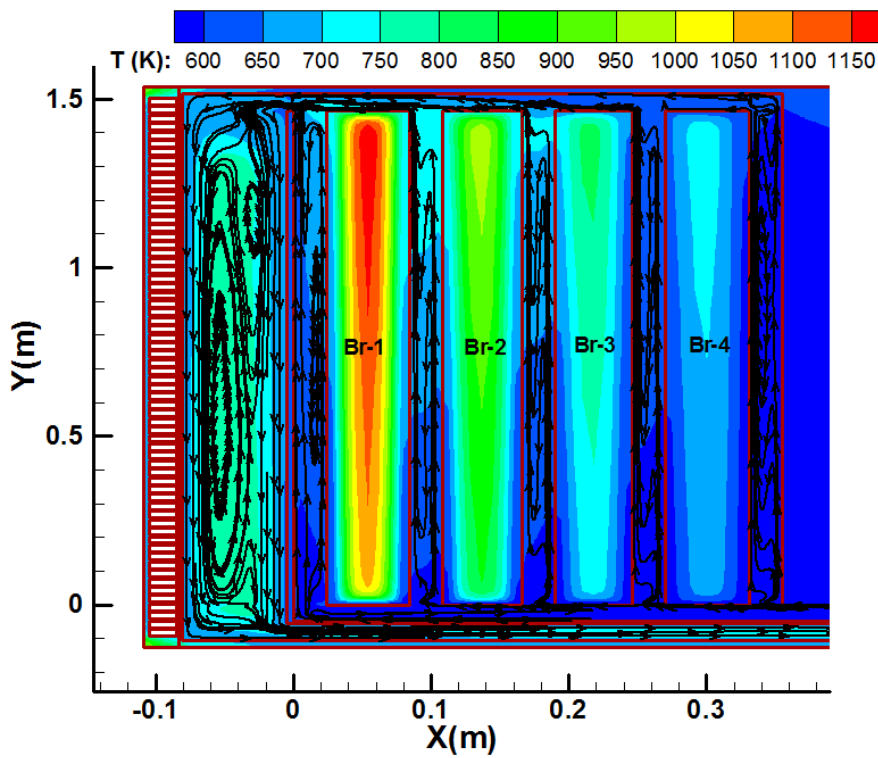


Figure 6.23: Temperature contour and velocity streamlines in the central plane ($Z=0.214\text{ m}$) for thermal MHD flow at $B_0=4\text{T}$

6.7.3 *Comparison with classical Boussinesq model*

In earlier simulations of LLCB variants, a different functional form of the temperature dependent density property was used in the energy as well as momentum conservation equation. In that case, the obtained temperature profile was significantly different at least in the return path and 1st poloidal channel where the buoyancy effects were prominent. In the return channel where the buoyancy force is opposite to the flow direction, stagnant flow zones were observed near the First wall adjacent side layer instead of a jet like structure. So it was thought the temperature dependent density in the energy equation possibly affects the temperature profile due to variation of local Peclet number(Pe). It is of interest to compare the present result with the classical Boussinesq approximation in which constant density property is used along with additional buoyancy source term in momentum balance equation. As the density variation in the return flow path and adjacent channel-1 is relatively more due to high temperature gradient, the radial temperature profile is compared at the central plane($Z=0.214\text{m}$) and $Y=0.85\text{m}$ for these two channels as shown in Fig. 6.24. It is observed that the temperature difference is quite small. So it is concluded that the energy equation can be solved with a constant density based on the classical Boussinesq model.

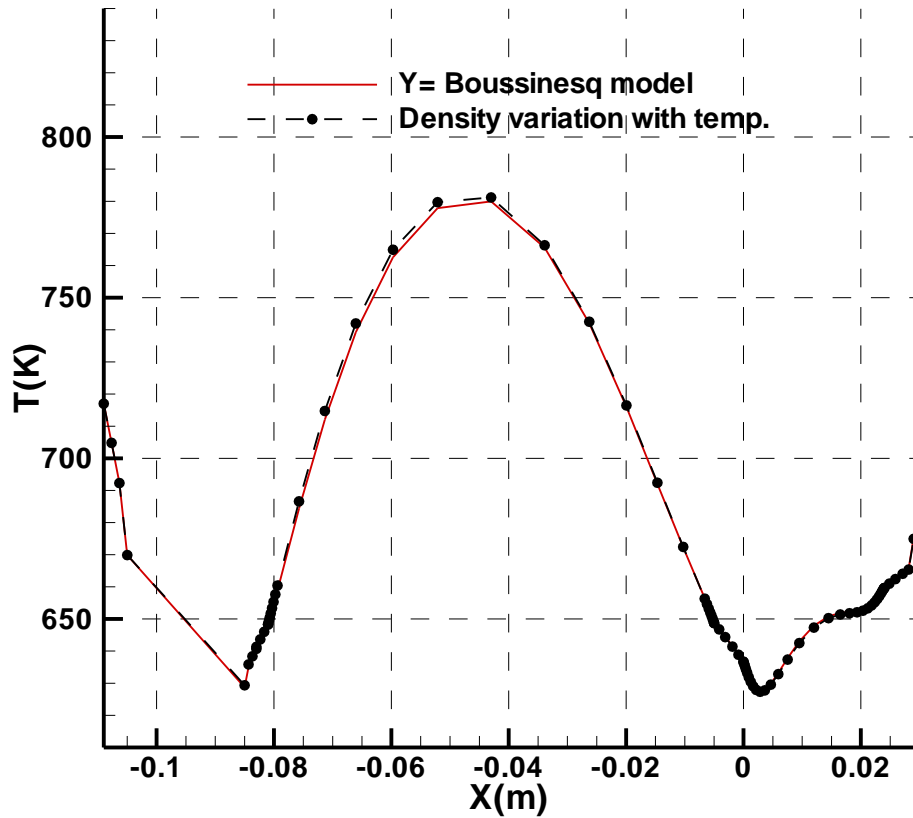


Figure 6.24: Comparison of radial temperature profile for case of density variation with temperature with that of classical Boussinesq approximation at $Y=0.85\text{m}$

6.8 Summary of thermofluid analysis in LLCB TBM

Thermofluid MHD analysis has been carried out in a full scale variant of Indian LLCB TBM at high Hartmann number ($Ha=17845$). Helium cooled plasma facing First wall is included in the integral geometric model for realistic simulation of dual coolant flow configuration. The laminar steady state velocity profile and flow rate distribution in electrically coupled poloidal parallel channels is estimated. It has been observed that a large velocity shoots up in the side boundary layer of counter current flow configuration channels sharing a common partition wall. The higher velocity is attributed to the stronger electrical coupling at the common partition wall due to MHD effects and results in higher proportion of flow rate relative to other channels. Numerical value of non-dimensional pressure gradient in the electrical

coupled parallel channels with co-flow configuration is marginally higher than theoretical estimations based on fully developed models. In high aspect ratio poloidal channels where axial currents are converging or diverging, a large vortex structure is formed with a reverse flow at the center. Temperature distribution in various structural walls is obtained for a given user defined radially varying heat source which is computed from the functional fit of the neutronic heat density data of a similar variant. Local hot spots are observed in the Hartmann walls of certain high heat deposition regions such as breeder-1 and common partition walls. The higher temperature is attributed to the lower axial velocity and hotter fluid in the corresponding boundary layers. Formation of large vortex structures in the central region of some of the poloidal flow channels is not leading to potential hot spots due to better heat transfer by higher thermal conductivity of the liquid metal. However, the side walls of most of the channel are relatively cooled due to higher jet velocity in associated boundary layers. It is also observed that First wall helium cooling has significant effects in limiting the temperature of external as well as internal breeder walls. Thermal load sharing by both First wall helium cooling circuits coupled with PbLi MHD flow is estimated for further optimization of the flow rate in future variants.

6.9 References

1. I.R. Kirillov, D.A. Pertsev, Investigation of alternative configurations of the LLCBTBM to increase neutronic and thermo-hydraulics performances, Fusion Eng. Des. 85 (2010)
2. P. Chaudhuri, S. Ranjithkumar, et al., Progress in engineering design of Indian LLCB TBM set for testing in ITER, Fusion Eng. Des. 89 (2014)
3. S. Ranjithkumar, D. Sharma, et al., Engineering design and analysis of Indian LLCB TBM set, Fusion Eng. Des. 109–111 (2016)
4. T. Jayakumar, M.D. Mathew, et al., Reduced activation ferritic martensitic steel and fabrication technologies for the Indian test blanket module in ITER, Fusion Sci. Technol. 65 (2019)

5. S. Smolentsev, N.B. Morley, et al., Dual-coolant lead–lithium (DCLL) blanket status and R&D needs, *Fusion Eng. Des.* 100 (2015)
6. M. Abdou, N.B. Morley, et al., Blanket/First wall challenges and required R&D on the pathway to DEMO, *Fusion Eng. Des.* 100 (2015)
7. C. Mistrangelo, L. Bühler, Electric flow coupling in the HCLL blanket concept, *Fusion Eng. Des.* 83 (2008)
8. FLUENT 12.0 produced by FLUENT Inc.
9. P.K. Swain, P. Satyamurthy, et al., 3D MHD lead–lithium liquid metal flow analysis and experiments in a test section of multiple rectangular bends at moderate to high Hartmann Numbers, *Fusion Eng. Des.* 88 (2013)
10. J.C.R. Hunt, Magneto-hydrodynamics flow in rectangular duct, *J. Fluid Mech.* 21 (1965)
11. R.J. Lingwood, T. Alboussiere, On the stability of the Hartmann layer, *Phys. Fluids* 11 (1999).
12. P. Moresco, T. Alboussiere, Experimental study of the instability of the Hartmann layer, *Fluid Mech.* 504 (2004)
13. P.K. Swain, A. Shishko, et al., Numerical and experimental MHD studies of LeadLithium liquid metal flows in multichannel test-section at high magnetic fields, *Fusion Eng. Des.* 132 (2018)
14. P. Satyamurthy, P.K. Swain, et al., Experiments and numerical MHD analysis of LLCB TBM test-section with NaK at 1T magnetic field, *Fusion Eng. Des.* 91 (2015)
15. U. Muller, L. Buhler, Book: *Magnetofluiddynamic in Channels and Container*, Springer: ISBN 3-540-41253-0 (2001)
16. S. Smolentsev, R. Moreau, et al., MHD thermofluid issues of liquid metal blankets: phenomena and advances, *Fusion Eng. Des.* 85 (2010)
17. B. Schulz, Thermophysical properties of the Li(17)Pb(83) alloy, *Fusion Eng. Des.* 14 (1991)
18. A.F. Tavassoli, A. Alamo, et al., Material design data for reduced activation ferritic martensitic steel type EUROFER, *J. Nucl. Mater.* 329 (2004)
19. Z. Xu, R. Meyder, et al., Design and validation of breeder unit of heliumcooled pebble bed blanket for demo fusion reactor, *Fusion Eng. Des.* 81 (2006)
20. G. Aiello, F. Gabriel, L. Giancarli, G. Rampal, J.-F. Salavy, Thermal–hydraulic analysis of the HCLL DEMO blanket, *Fusion Eng. Des.* 82 (2007)

21. C. Mistrangelo, L. Bühler, Influence of helium cooling channels on magnetohydrodynamic flows in the HCLL blanket, *Fusion Eng. Des.* 84 (2009)
22. X. Zhang, C. Pan, X. Zengyu, Investigation of coupling MHD rectangular ducts flows based on a fully developed modeling, *IEEE Trans. Plasma Sci.* 42 (2014)
23. A. Y. Ying, M. S. Tillack, MHD heat transfer in elongated rectangular ducts for liquid metal blankets, *Fusion Technol.* 19 (1991)
24. S.I. Sidorenko, A.Ya. Shishko, Variational method of calculation of MHD flows in channels with large aspect ratios and conducting walls, *Magnetohydrodynamics* 27 (1991)
25. H.L. Swami, A.K. Shaw, et al., Neutronic performance of Indian LLCB TBM set conceptual design in ITER, *Fusion Eng. Des.* 113 (2016)

7 CHAPTER

Thermofluid MHD Effects of Partition Plates in the Indian Variant LLCB TBM for ITER

7.1 Introduction

Liquid metal flow paths in the India proposed LLCB Test Blanket Module for ITER are primarily consisting of multiple electrically coupled parallel channels with a number of L/U-type rectangular bends. The vertically oriented parallel poloidal flow channels are confined by interspaced ceramic breeder blocks and are mounted on a common radial-toroidal header for flow distribution. Alloy of Lead-Lithium (PbLi) is circulated around these columnar ceramic blocks to remove the volumetric radiation heat deposited by neutrons in both liquid PbLi and solid ceramic breeder zones [1, 2]. Schematic view of the flow configuration and key elements of the LLCB variant is shown in Fig. 7.1. In the proposed LLCB flow configuration, liquid metal flow rate is relatively higher compared to other TBM concepts like Helium Cooled Lead Lithium (HCLL) and Dual Coolant Lead Lithium (DCLL) as proposed by the EU and US respectively. The electrical conducting structure with higher flow velocity in presence of strong transverse toroidal magnetic lead to large induced electrical current which further interact with the magnetic field to generate large electromagnetic drag. The opposing nature of electromagnetic force in the bulk of the flow domain results in large overall pressure drop. There is a significant modification in flow properties due to varying degrees of electrical coupling among parallel channels and change in heat transfer characteristics facilitated by intense magnetohydrodynamic effects. The characteristic parameters governing the themofluid mhd flow are basically the Hartman number (Ha), hydrodynamic Reynolds number(Re) and Grashof number (Gr). The square of Ha is a measure of the relative strength of electromagnetic force, Re is a measure of the inertial force and Gr is a measure of the buoyancy force over

viscous force respectively. Numerical estimation of these parameters involves a geometric length scale which is associated with the cross section aspect ratio of a typical flow channel of the blanket module. Particularly for LLCB variants, the radial and poloidal flow channels are long and slotted rectangular ducts having high aspect ratio flow cross section. Here, the aspect ratio (ϵ) is defined as the ratio of toroidal width (a) to the radial width (b) of the flow cross section. In a typical flow cross section, the toroidal width is approximately ~ 17 times larger than the corresponding radial width [3]. So the numerical value of Ha, Re, and Gr turns out to be higher numbers, typically in the range of 1×10^4 to 2×10^4 , 10^3 to 10^5 and 10^8 to 10^{10} for Ha, Re and Gr respectively at an applied magnetic field of $B_0=4T$. The higher Hartmann number (Ha) and the geometric channel aspect ratio (ϵ) lead to large variation of side layer jet velocity adjacent to the side wall along the applied magnetic field direction [4]. However, it has been observed that the flow profiles in a given cross section have large variations due to higher channel aspect ratio (ϵ). The velocity jet associated with the side walls is having a large variation along the magnetic field direction (toroidal). This has resulted in large variation of side wall temperature which may lead to significant thermo-mechanical stress and geometric deformations [5].

In view of addressing these issues and to enhance the overall mechanical strength of the blanket module, thin radial-poloidal vertical plates are envisaged to be placed in the poloidal flow channels. These intra vertical plates are named as partition walls. The partition plates are oriented normal to the toroidal magnetic field and thus resemble internal Hartmann walls (see Fig. 7.1). A single partition plate at the central plane divides/splits a poloidal flow channel into two symmetrical ducts with a reduced channel aspect ratio in each sub-duct. However, these plates provide additional paths for the closure of induced electric current generated in respective sub-ducts. The electrical currents are not only closed through the common wall but with the associated Hartmann boundary layer also. As a result, the induced transverse current

density in each sub-duct is increased and the pressure drop is likely to be more than the case without partition walls. The velocity profile along the magnetic field is expected to be modified due to uneven wall thickness and flow rate redistribution among parallel channels due to change in local MHD drag coefficients. From the thermal hydraulic prospective, temperature distribution in partition walls is a critical concern. Unlike the helium cooled outer structures, the volumetric heat of these internal structures have to be extracted by PbLi only. The present study is aimed at analyzing thermofluid MHD effects arising due to internal partition plates in a model of LLCB variant.

Similar to the internal partition wall of Indian LLCB variant, numerical analysis based on fully developed models were reported in a model of HCLL TBM where the applied toroidal magnetic field is parallel to internal cooling plates/grid plates confining radial flow channels [6]. Experiment and numerical analysis in a test section consisting of parallel channels with multiple sub-channels formed by internal partition plates had been reported at low magnetic field ($B_0=1\text{T}$) [7]. In this present study, results of 3-D numerical simulation that have been carried out in a full scale model at ITER relevant magnetic field (4T) is presented. The model takes into account a single partition plate in each of the poloidal flow channels. Thermal performance has been assessed for realistic heat deposition data based on neutronic calculation in similar variants. Effects of the partition wall on velocity, electric potential, current path, flow rate distribution and temperature distribution of various key elements are presented. The effect of buoyancy on magneto-hydraulic velocity profile is also presented in channels of large temperature gradient.

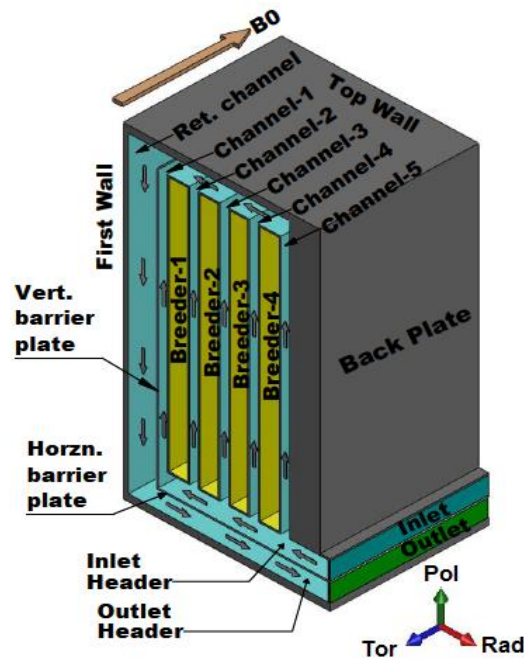


Figure 7.1: Schematic of PbLi flow configuration in variants of Indian LLCB TBM

The present study is aimed at analyzing 3D MHD effects of internal partition plates in a plane perpendicular to the high magnetic field of a full scale variant of LLCB model consisting of multiple electrically coupled channels. The partition plates subdivide each poloidal flow channel into two symmetrical sub-ducts. However, these plates resemble as internal Hartmann wall of the main channel and provide path to the induced electric current not only through the walls but also through the associated Hartmann boundary layer. As a result of the additional path to electric current, the pressure drop is likely to increase due to increase in transverse current density. The degree of varying electrical coupling and local resistance will affect the flow rate distribution among the parallel poloidal channels. The velocity profile across the Hartmann walls is also expected to be modified due to uneven wall thickness. In addition, temperature distribution of these internal structural walls is a critical concern from thermal point of view as heat of these internal walls have to be extracted by PbLi only, unlike the helium cooled outer structures. Some of the objective of the present study is to estimate the temperature

distribution of various key elements for a given volumetric heat deposition. 3D MHD numerical simulation has been carried out at ITER relevant magnetic field (4T) to assess the performance of a full scale LLCB variant with single partition plate in each of the poloidal flow channel. Effects of the partition wall on velocity, electric potential, current path and flow rate distribution in parallel channels are presented. It is observed that axial velocity near the boundary layer of thin partition wall and side walls is modified significantly. Pressure drop and redistribution of flow rate due to partition plates is assessed by comparing the results with a case without any partition wall. Thermal analyses in the present model have been carried out for a realistic heat deposition data based on neutronic calculation in similar variant. The effect of buoyancy on magneto-hydraulic velocity profile is also presented in channels of large temperature gradient.

7.2 Problem definition and governing equations

The present numerical study is performed in the actual dimensions of a typical LLCB variant but with a simplified version of the plasma facing First wall (FW). The heat load of the FW component of the actual LLCB blanket is supposed to be cooled by helium flowing in a number of embedded cooling ducts placed in between the double wall type U-shaped structure. The proposed FW configuration of a baseline design, as shown in Fig. 7.2, the square helium duct of 20mm side is enclosed by two 4 mm plates and each helium duct is separated by a 4 mm thick intermediate rib plate. Numerical modeling of the integrated model with exact FW configuration is not only cumbersome but also large time consuming, particularly the present geometry which is modeled with multi-zone structured mesh due to the requirement of different spatial resolution in fluid and solid regions. The limitation of available computational resources and to reduce the computation efforts the complex FW structure is modeled with a simplified one of single wall type without any internal helium cooling ducts. Following this simplification, the entire structure is possible to be meshed with structured type and conformal mapping at

each fluid-solid interface. Arrangements for computation nodes with conformal mappings have an advantage of faster convergence and less computation error than over non-conformal interfaces.

The model FW has given due consideration to the relevant parameter, the relative wall electrical conductance ratio, which is the ratio of electrical conductance of the wall to that of the fluid [8]. As the induced electric currents in MHD duct flow are shorted through conducting walls, the simplified single wall type FW as shown in Fig. 2(b) of the model geometry takes into account equivalent wall conductance ratio of ~ 0.09 as in the original configuration. The effective thickness of 0.01167m is estimated from the consideration of actual material volume including mid rib plates, which separate consecutive helium ducts embedded throughout the poloidal height, and material contribution from the top and bottom portion of the FW where thick top and bottom walls are connected. Provision for helium cooling is ensured through convective boundary conditions at the outer surface of the model FW with a suitable heat transfer coefficient and ambient temperature. It should be noted that such a simplified version of the FW will lead to higher wall temperature even though helium cooling is taken care of due to a rather thick wall approximation. However, the present study undermines the accurate FW temperature as it has already been established in our earlier modeling work carried out in an exact baseline configuration of LLCB variant.

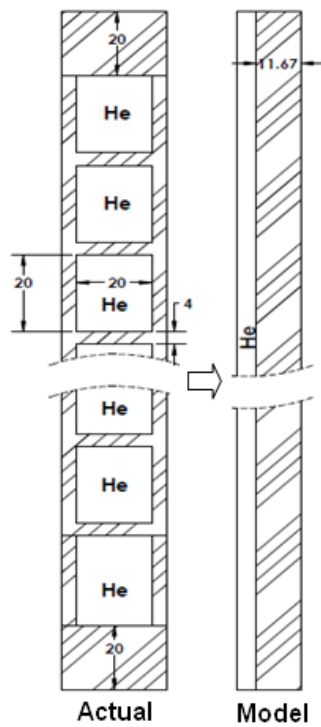


Figure 7.2: Schematic of helium flow in actual FW and model configuration

7.2.1 Model geometry

In this model geometry liquid metal PbLi enters into a rectangular bottom inlet header which distributes the flow in five poloidal flow channels. The poloidal channels are basically formed by the four interspaced breeder blocks of varying thickness. Incoming flow in these parallel channels is upward and takes out heat of the ceramic breeders contained in steel boxes. Each poloidal flow channel is further subdivided into two symmetric sub-channels by a thin radial-poloidal partition plate of thickness 5mm. An isometric cut view of the simulation model with partition plates and PbLi flow configuration in respective sub-channels is shown in Fig.7.3. Upward flow in the poloidal channels then recombines at the top header similar to the bottom inlet header and returns through a wider parallel channel adjacent to the FW. PbLi downward flow in the return channel and upward flow in the 1st poloidal channel is separated by a 5 mm thick common poloidal-toroidal plate named as common vertical barrier. The return channel is further connected to a rectangular bottom outlet header parallel to the inlet header

section. Radial incoming and outgoing flow in these bottom headers are separated by a 5mm thick common radial-toroidal plate named as common horizontal barrier. In this present model, radial width of each incoming poloidal flow channel is assumed uniform (24 mm) while width of the return poloidal channel is 0.076m. Breeder blocks of variable widths are enclosed in 5mm thick rectangular boxes. Numerical simulation is performed in actual dimensions: 1.66m poloidal (y), 0.484m in toroidal (z) and 0.6 m in radial (x) direction. Detail dimension of various structural elements, breeder zones and flow channels of the model is shown in Fig. 7.4 The applied magnetic field is in the toroidal direction (z) and transverse throughout the PbLi flow path.

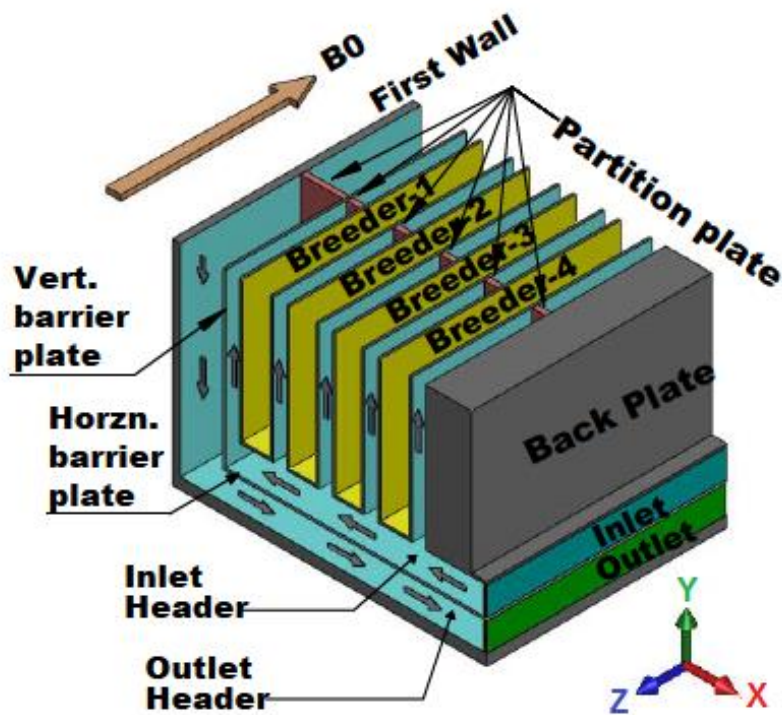


Figure 7.3: Isometric cut-view of the model with partition plate in poloidal flow channels

Fig. 7.4 (a)

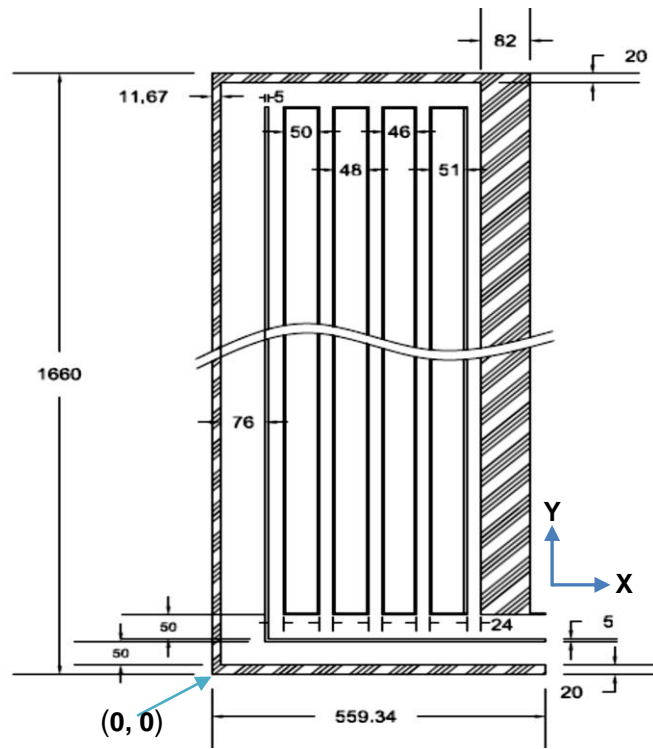


Fig. 7.4(b)

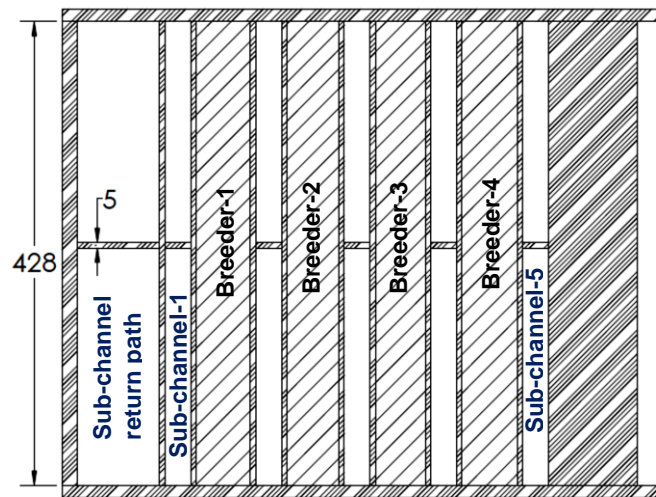


Figure 7.4: Detail dimension (mm) of various elements of the numerical model; Front view in Fig. 4(a) and Top view in Fig. 4(b)

7.2.2 Governing equations

For steady state magneto-hydraulic solution of an incompressible electrical conducting fluid, the following system of governing MHD equations are solved numerically using MHD solver of FLUENT [10] code. Since the magnetic Reynolds number (R_{em}) of the problem is small ($R_{em} < 1$), the effects of induced magnetic field are neglected [11] and the source term of electromagnetic body force in the momentum balance equation is determined from the coupled MHD equations based on electric potential formulation. A prior analysis of the flow distribution in similar variants has yielded characteristic Reynolds number (Re) in the range 6730-25750 for different flow channels of LLCB blanket. So the preliminary estimation for critical Reynolds number based on the thickness of the Hartmann layer (Re/Ha), which is a key parameter to anticipate different flow regimes, is well above the limit ($Re/Ha > 3.3E-3$) for laminarization/transition to turbulent regime. In view of the electrical conducting channel walls and high magnetic field strength of $B_0=4T$ ($Ha = 8095$), the flow is considered to be laminar for the present model [12, 13].

$$(\vec{U} \cdot \vec{\nabla})\vec{U} = \frac{-\vec{\nabla}p}{\rho} + \nu \nabla^2 \vec{U} + \frac{\vec{J} \times \vec{B}_0}{\rho} \quad (1) \quad [\text{Modified Navier-Stokes equation}]$$

$$\vec{\nabla} \cdot \vec{U} = 0 \quad (2) \quad [\text{Conservation of mass}]$$

$$\vec{J} = \sigma (-\vec{\nabla}\phi + \vec{U} \times \vec{B}_0) \quad (3) \quad [\text{Generalised Ohm's law}]$$

$$\vec{\nabla} \cdot \vec{J} = 0 \quad (4) \quad [\text{Conservation of charge}]$$

Here, ρ , \vec{U} , ν , σ are density, velocity, kinematic viscosity, electrical conductivity of the fluid whereas p , \vec{J} , \vec{B}_0 , ϕ are pressure, electric current density, magnetic field induction, and electric potential respectively.

Equations (3) and (4) are combined in potential method formulation to solve electric potential ϕ from the following equation,

$$\nabla^2 \phi = \vec{\nabla} \cdot (\vec{U} \times \vec{B}_0) \quad (5)$$

Here, B_0 is the strength of applied magnetic field.

In the solid domain the following equation is solved for the electric potential

$$\nabla^2 \phi_w = 0 \quad (6)$$

Here, ϕ_w is the potential distribution in the walls. At the fluid-wall interface, in addition to no-slip condition for the velocity, continuity of the normal component (to the walls) of current density ($J_n = J_{nw}$) have been ensured through coupled boundary condition. Here J_n refers to the normal component of current density on the fluid side and J_{nw} corresponds to the wall side.

The system of governing equations is solved in a finite volume and pressure based solver of CFD code FLUENT. All the flow variables are computed with double precision in a multiple processor computer. Electric potential variable of equation (5) and equation (6) are solved through user defined scalar transport equation. For spatial discretization in momentum and electric potential equation, a second order upwind scheme and SIMPLE algorithm is used for pressure velocity coupling. At First, the converged solution for magneto-hydraulic problem is obtained without activating the energy equation and subsequently utilised as base solution to proceed for solving the energy equation.

Temperature distribution in structural materials, ceramic breeder zones and heat transfer to the external wall helium cooling circuit are obtained from a steady state solution of the energy equation as presented in eqn (7). The source term due to work done by viscous and fluid expansion is neglected in eqn(7) because of their insignificant contributions. The third term in the right hand side of eqn (7) is the joule heating term and fourth source term (S_T) is the volumetric heat deposited by neutrons in PbLi as well as structural materials. To account for the effect of buoyancy, the density variation with temperature is modelled as per Boussinesq approximation and the velocity field is computed from the momentum balance equation that

includes buoyancy source term as presented in eqn(8). Governing equations for buoyancy accounted velocity and temperature equations are solved along with the mass continuity, charge conservation and electric potential equations as described earlier in eqn (2) to eqn (6). Gravitational acceleration of 9.8 m/s^2 is specified in the vertical downward direction (negative Y-direction).

$$C_p [\vec{\nabla} \cdot (\rho \vec{U} T)] = \vec{\nabla} \cdot (\kappa \vec{\nabla} T) + \frac{\vec{J} \cdot \vec{J}}{\sigma} + S_T \quad (7)$$

$$\rho (\vec{U} \cdot \vec{\nabla}) \vec{U} = -\vec{\nabla} P + \mu \nabla^2 \vec{U} + \vec{J} \times \vec{B}_0 + (\rho - \rho_0) \vec{g} \quad (8)$$

Here, C_p is the specific heat ($\text{J. Kg}^{-1}.\text{K}^{-1}$), κ is the thermal conductivity ($\text{W.m}^{-1}.\text{K}^{-1}$), ρ_0 is the reference density (kg.m^{-3}) of PbLi and S_T is the volumetric source term (W/m^3).

7.2.3 Boundary conditions

For the velocity field, no-slip condition has been used at the solid surface. At the inlet uniform velocity corresponding to mass flow rate of 12 kg/s and at the outlet, a homogeneous Dirichlet pressure condition ($p=0$) is applied. For the electric potential, insulation is assumed beyond the outer walls and a homogeneous Neumann condition $\partial\phi/\partial n = 0$ is applied. In case of simulation without any heat input, the interface of electrically conducting structural walls and solid breeders are treated as insulated walls. This assumption is made owing to very low electrical conductivity of breeders. But for the case of thermofluid simulation, the solid-solid interface of breeder structural wall and ceramic breeder is treated as a coupled wall similar to the fluid-solid interface. The external wall of U-shaped FW is specified as a convective boundary wall with heat transfer coefficient of $h=3691 \text{ W/m}^2$. Numerical value of the heat transfer coefficient is evaluated using correlations [16, 17] for helium flow rate of 1.63 kg/s (corresponding He velocity 50 m/s) and bulk helium temperature of 599 K . The average helium temperature is estimated from the integral heat due to surface heat flux of 0.3 MW/m^2 from plasma side.

7.3 Numerical simulation

The problem of thermo-fluid MHD simulation is attempted in two stages for a fixed flow rate and applied magnetic field strength of 4T. First, the computation is carried out without any heat load to the structure or breeder units. The physical properties of the PbLi and RAFMS structure [15] for initial magneto-hydraulic solution is taken as constant at 623 K and respective numerical values are shown in Table 7-1.

The converged magneto-hydraulic solution is then used as an initial solution for thermal calculation in the second stage. To account for change in the velocity field due to effects of buoyancy, the steady state energy equation is solved along with the continuity and modified momentum balance equations in a coupled way as in the first stage. So the initial magneto-hydraulic solution helps in faster convergence of the thermal solution. The modified momentum balance equation (8) includes additional source term of buoyancy force based on Boussinesq approximation. The density variation with temperature is also accounted for in contrast to the classical Boussinesq approximation while solving the energy equation.

The variation of temperature dependent physical properties like density($\rho(T)$), dynamic viscosity($\mu(T)$) and electrical conductivity of PbLi($\sigma(T)$) with temperature has been taken into account as per equations (9), (10) and (11) respectively [14]. However, in the solid domain, fixed material properties are used at a temperature of 623 K.

$$\rho(T) = 10450 * (1 - 161E - 6 * T) \quad (9)$$

$$\mu(T) = 1.87E - 4 * \exp[11640 / (8.31 * T)] \quad (10)$$

$$\sigma(T) = [102.3E - 8 + 0.0426E - 8 * T]^{-1} \quad (11)$$

Table 7-1: Physical properties of materials used in numerical simulation

Physical property	Lead-Lithium(PbLi) [14]	RAFMS structure [15]	Lithium-Titanate(Li ₂ TiO ₃)
Density (ρ), (kg/m ³)	9486	8000	3430
Specific heat (C_p), (J/kg-K)	189	565	1341.42
Thermal conductivity (λ), (W/m-K)	14.16	33.20	1.0
Electric conductivity (σ), (1/ Ω -m)	7.892E5	1.31E6	1.0E-6
Dynamic viscosity (μ), (Pa-s)	2.155E-3	–	–

7.3.1 Details of Grid

Multi blocked structured mesh having hexahedral elements is generated for the entire geometry with adequately resolved characteristic Hartmann layers and side wall boundary layers for accurate and reliable prediction of flow field variables. With the presence of internal partition wall the Hartmann number ($Ha = B_0 a \sqrt{\sigma/\mu}$) is 8095 for highest magnetic field strength $B_0=4T$ and characteristic length $a = 0.2115m$ which is half the width of sub-channel along the field direction. The thickness of the Hartmann boundary layer ($\delta_h = a/Ha$) of the order of 13 μm . The zone is resolved with uniformly spaced 2 elements at both external and internal Hartmann walls. The side wall boundary layer of thickness ($\delta_s = a/\sqrt{Ha}$) of the order 1.175 mm is resolved by at least 5-6 grid points of variable spacing for all the PbLi flow channel. Node spacing is gradually increased from boundary wall to center region (core) where velocity gradient is relatively low. A view of the mesh in a flow cross section of channel-1 and return flow channel is shown in Fig. 7.5. The number of nodes in a typical radial-toroidal flow cross section of a sub-channel is 26 along radial(X-direction) and 29 along toroidal (Z-direction). Thickness of the FW (0.01167m) and breeder structural walls including partition walls (0.005 m) is meshed with uniformly spaced 11 grid points and 6 grid points respectively. The total volume element of the computation geometry is 4.2 million. This optimum grid

structure is based on our grid independent analysis in similar geometries and previous experience of numerical studies carried out in test section experiment at high magnetic fields [9, 1]

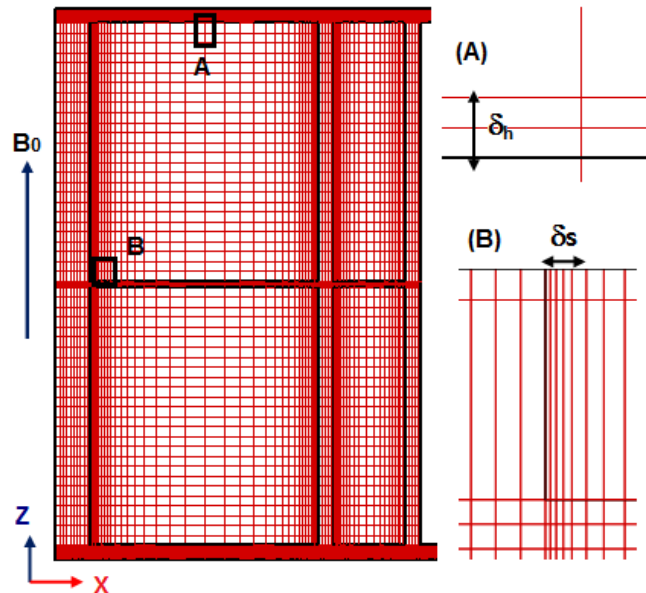


Figure 7.5: Mesh structure and zoomed view of Hartmann and side layer resolution in a flow cross section of channel-1 and return channel

7.4 Results and discussions

In this section numerical results of magneto-hydraulic solution (without any heat load) are presented and organised as follows: First, the effects of partition plate on velocity field is discussed. The obtained velocity field is further compared with a case without any partition plates. Afterwards, electric current streamlines and the wall potential distribution in coupled electric ducts and their effects on flow field is discussed. Subsequently, flow rate distribution in various sub-channels due to MHD and in the absence of magnetic field (hydraulic case) is presented for quantitative comparison.

7.4.1 Effects of partition plate on velocity profile

The information of velocity profile in different poloidal flow channels is essential prior to the thermal analysis. With the insertion of partition plate, each poloidal flow channel is divided into two sub-channels in which the internal Hartmann wall is thinner (0.005m) than

the thicker (0.01167m) helium cooled outer Hartmann wall. Because of this uneven thickness of Hartmann walls of a sub-channel the velocity profile is expected to be altered significantly along the magnetic field direction. The axial velocity profile across the Hartmann walls of each channel at the centre of the flow cross section is shown in Fig.7.6. It is interesting to notice that axial velocity near the thinner internal Hartmann wall is significantly larger than the thicker outer Hartmann walls. But because of symmetry the profile is symmetric in the sub-channels of a poloidal flow channel. In a sub-channel, the Hartmann profile is parabolic with a minimum at the center of the duct cross section. For sub-channels of channel-1, a reverse flow in the core region is observed along with high axial velocity near the internal partition wall. As the radial width (0.024m) of the flow channels are much smaller than the toroidal width (0.2115m), distinct core region of uniform velocity is not observed. So the Hartmann profile in such type of high aspect ratio duct cross section is quite different from the conventional MHD flow with typical flat core at high Hartmann number.

On the other hand, axial velocity profile across the side walls of all the sub-channels, as shown in Fig. 7.7 (a) and Fig. 7.7(b), exhibit velocity jet in the side wall boundary layers as observed in typical MHD flow. The jet velocity is order of magnitude higher than the maximum velocity observed at their corresponding Hartmann walls. The complex electrical coupling among the sub-ducts with co-flow and counter flow configuration result in asymmetric jet across the side walls of all the sub-channels. The pronounced effects are observed in the side layers of channel-1 and return flow path adjacent to the vertical barrier wall (see Fig. 7.7(a)). For channel-1 that draw major fraction of the flow rate, the jet velocity is maximum near the vertical barrier plate with a slow moving reverse flow in the core region.

The increased velocity jet velocity is primarily attributed to the MHD effects of strong electromagnetic coupling through the conducting vertical barrier plate which is common to the both upcoming channel-1 and down ward flow through return channel. The counter current

flow in these channels lead to opposite polarity induced current which then form closed loop in their respective channel sharing the common side wall, thereby reducing the effective thickness and increasing the resistance to the current flow. This lead to an increase of common wall electric potential and subsequently the main cause for increased jet velocity in the adjacent side layers. The distribution of electric potential and current stream lines in this region are discussed in the following section. Also axial currents generated from the top and bottom walls induce side wall electromagnetic forces which sweep the fluid from the core region to one of the side layer and increases the corresponding jet velocity. In addition to these coupling effects, a large fraction of the fluid is rather carried by the side layers due to large aspect ratio of the channel dimension. The combined effects of strong electromagnetic coupling, flow of axial currents and large aspect ratio lead to form strong jets in the side layers associated with common vertical barrier plate. Thus, the flow inertia in the core region of the sub channels of channel-1 is very less due to lower flow rate and velocity.

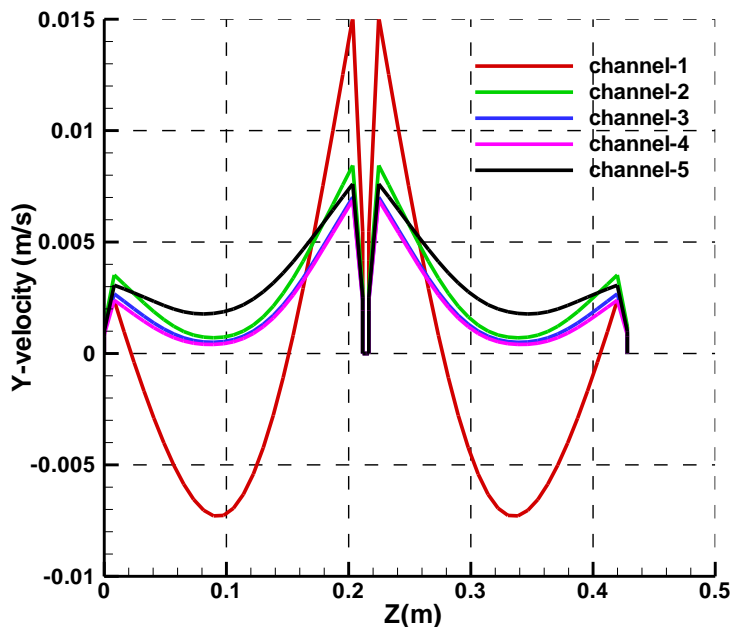


Figure 7.6: Velocity profile across the Hartmann walls including partition plate for different channels

Fig. 7.7 (a)

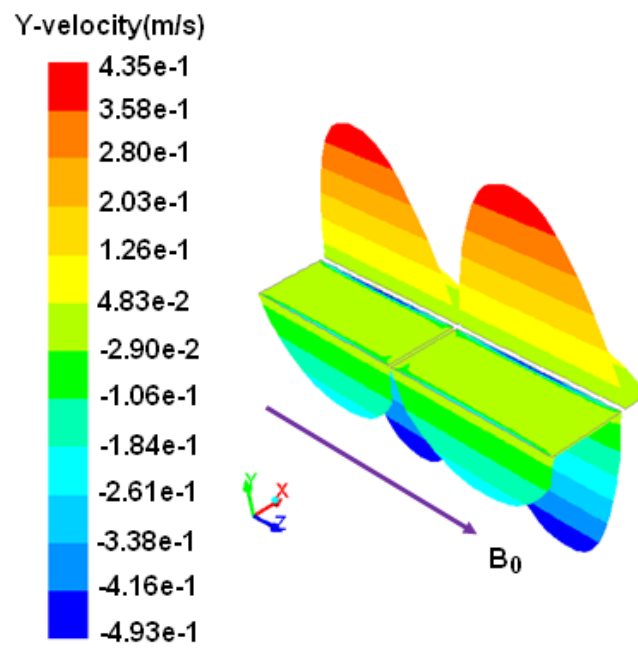


Fig. 7.7 (b)

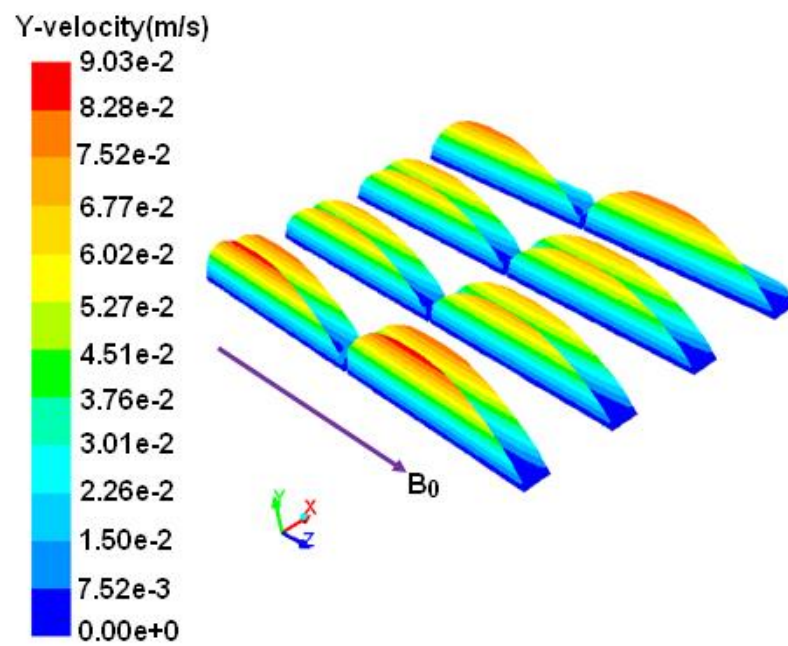


Figure 7.7: 3-D velocity profile in a flow cross section of LLCB; for channel-1 and return path in Fig. 7.7 (a) and for channel-1 to channel-5 in Fig. 7.7 (b)

To obtain the fully developed profile and get an idea of the developed flow length in a poloidal column of 1.55 m height, axial velocity profile across the centre of the side walls of all the sub-channels for different poloidal height was analysed and shown in Fig. 7.8. Since the relative magnitude of velocity in sub-channel-1 and return path is much more than other sub-channels, velocity profile for channel-1 and return channel is shown in Fig. 7.8(a) and across the side walls of channel-2 to channel-5 are shown in Fig. 7.8(b) for clear presentation. It can be seen that the velocity profile is continuously changing throughout the poloidal height. Although the poloidal height of a sub-channel is 15 times the characteristic length, the flow could not achieve fully developed configuration due to flow of 3-D axial currents. The flow cross sections at which axial currents favorably turn towards one of the side wall and become additive to the induced transverse current, the net transverse current in the core region is marginally augmented. It happens that in sub-channels of channel-1, the retarding Lorentz force exceed the pressure force particularly in the core region where viscous and inertia contribution to the momentum balance is negligible, a flow reversal occurs in that(core)region. But for sub-channels of other channel no reverse flow has been observed. Further, the flow profile is compared with the numerical simulation carried out in a similar LLCB variant where there is no partition wall in the poloidal flow channel.

Fig. 7.8(a)

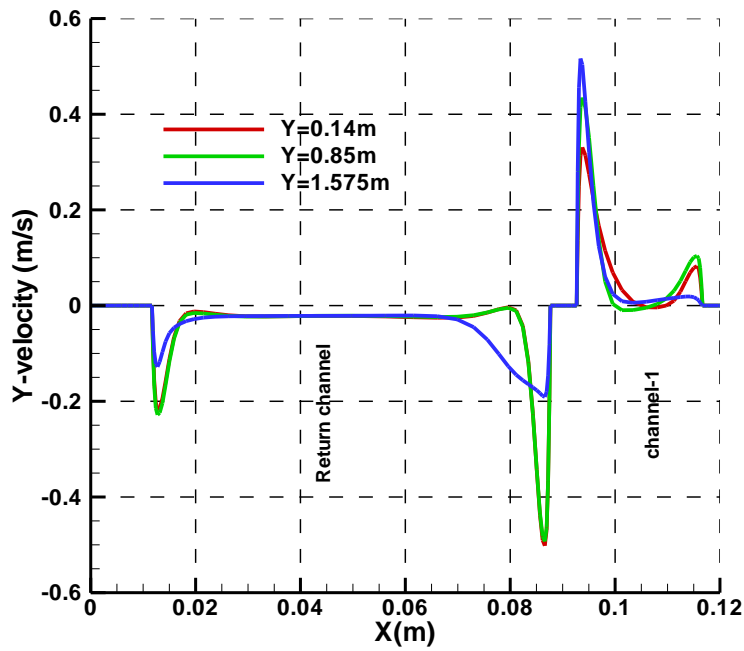


Fig. 7.8 (b)

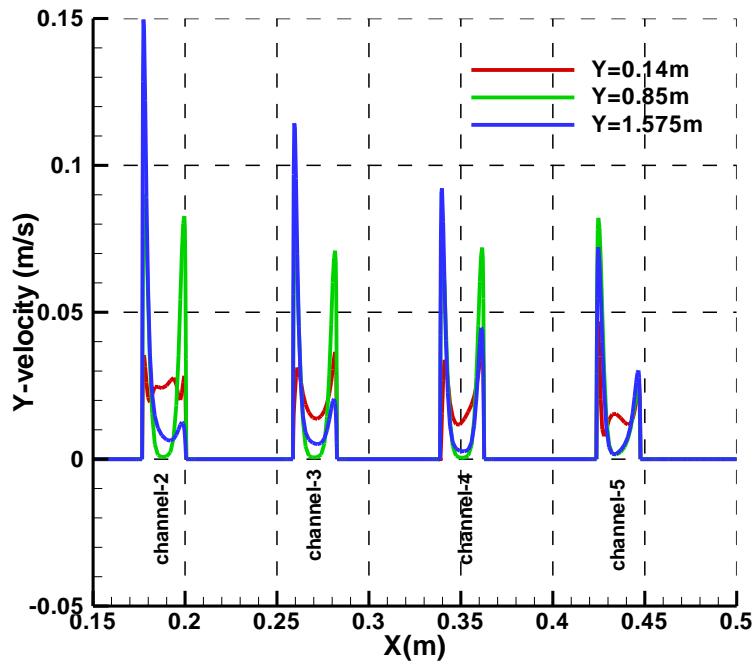


Figure 7.8: Velocity profile across the center of side walls at different poloidal heights and $B_0=4T$; for sub-channel-1 and return flow sub-channel in Fig. 7.8(a) and for sub-channel-2 to sub channel-5 in Fig. 7.8(b)

For assessment of the effects on side wall jet structure, velocity profile in a particular flow cross section ($y=0.85\text{m}$) is compared for both the case studies. As can be seen in Fig. 7.9(a) for the case without any partition wall, the peak velocity in the side layer jet of channel-1 adjacent to the vertical barrier plate is even more than the case with partition wall. In the return path, the core velocity is relatively reduced with a thicker side wall boundary layer if there is no partition plate in the poloidal channel. At the same time, it is interesting to observe the velocity profile as shown in Fig. 7.9(b) for all the channels starting from channel-2 to channel-5 that the side layer jet velocity and core velocity is enhanced when partition walls are present in those channels. This increase of velocity near breeder walls of those channels have positive effects on the heat transfer. Although the nature of the profile is same for both the cases, no reverse flow in the core region other than channel-1 observed when partition plate was present. Whereas, reverse flow was observed in all the poloidal flow channels for the case without any partition wall.

Fig. 7.9(a):

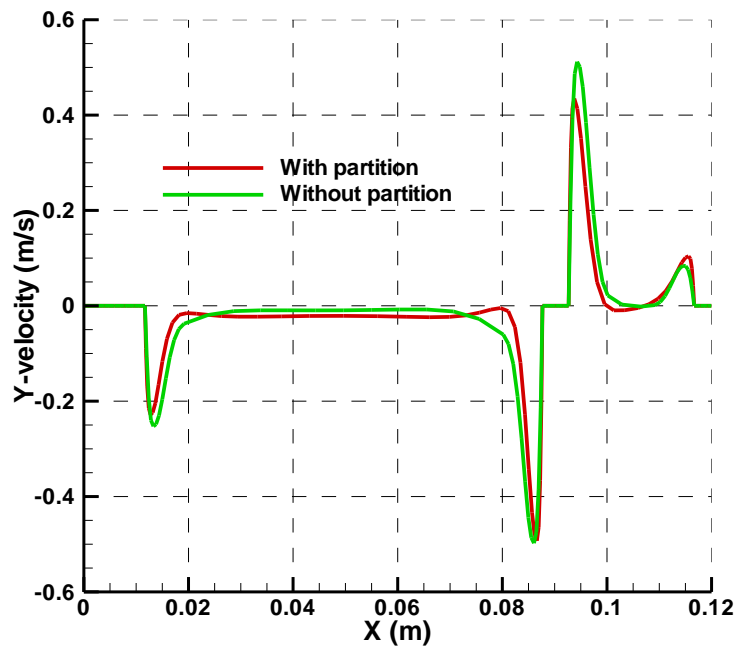


Fig. 7.9(b):

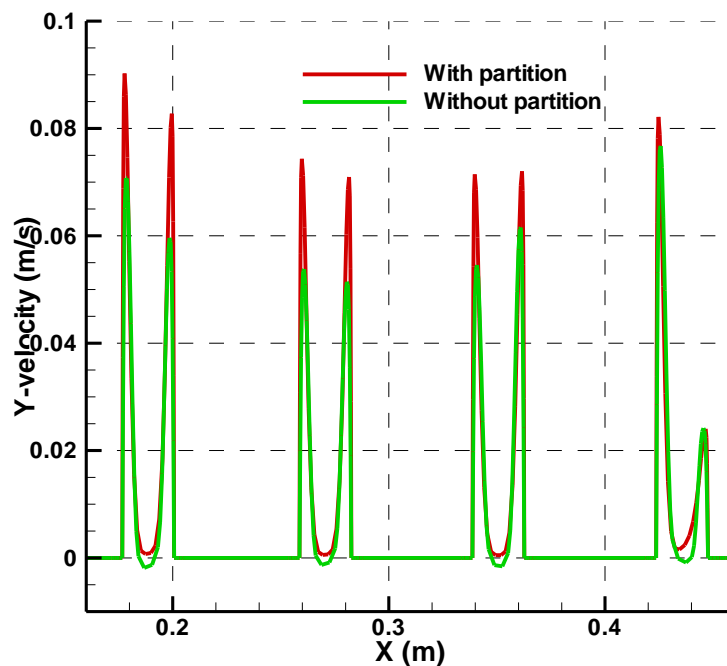


Figure 7.9: Comparison of axial velocity profile across the center of side walls at $Y=0.85\text{m}$; for channel-1 and return path in Fig. 7.9(a) and for channel-2 to channel-5 in Fig. 7.9(b)

7.4.2 Electric potential distribution and current streamlines

The induced electrical current in each of the poloidal sub channels forming closed loops inside the sub-channels with the partition wall as an internal Hartmann wall. Also the current paths are linked with the adjacent poloidal channels through the connecting walls and make the whole system as electrically coupled with each other. To view the electrical coupling of sub channels, the current streamlines along with contour of induced electric potential are shown in Fig. 7.10 for a flow cross section at $Y=0.85\text{ m}$. It is interesting to see the bending of current path lines near the common partition wall of channel-1 and the return channel where the flow configuration is counter current wise at either side of the wall. The direction of transverse current density (J_x) in sub-channel-1 and adjacent return sub-channel is opposite and is flowing parallel to the applied magnetic field direction inside the common wall. Thereby the wall electric potential is increased due to higher local resistance offered to the flow of electric current caused by lower effective wall thickness. The higher electric potential leads to higher transverse electric field (E_x) which in turn forcing the significant local transverse current to

flow in the parallel layers. As can be seen in Fig.10 the maximum bending of the current lines is near the boundary layer of common partition wall and that results in increase of the local axial velocity due to local lower electromagnetic drag.

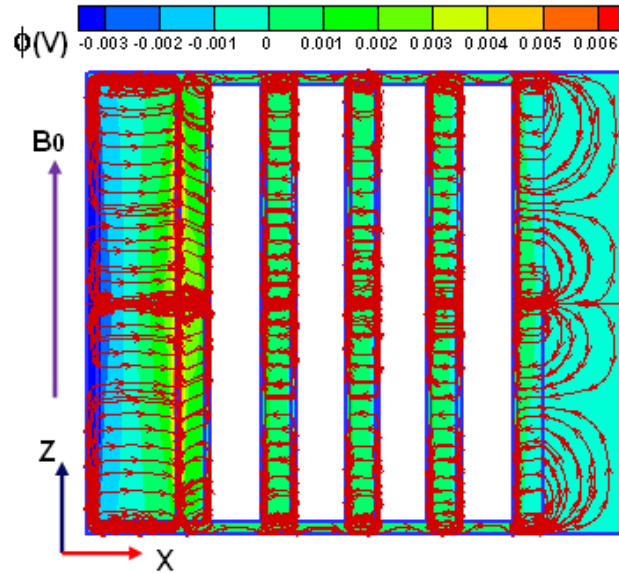


Figure 7.10: Contour of electric potential and current stream line in a flow cross section at Y-0.875m

Another interesting feature of the current distribution is observed near the partition wall of poloidal flow channels. Streamlines of current density in a flow cross section indicates formation of additional internal current loops that are closed through the Hartmann layer of the partition walls. A closure view of current paths for sub channels of return channel and channel-1 as shown in Fig. 7.11(a) illustrate closed current loop formation at the corner fluid region adjacent to the Hartmann boundary layer of partition wall. Similar internal current loops are observed at each of the corner region formed by partition wall and respective side walls of other sub channels and is shown in Fig. 7.11(b). For sub channels of channel-1 and channel-5, where effective electrical conductance of one of the side wall is much lower than the other side wall, current loop is formed at the corners associated with lower effective side wall electrical conductance only. As a consequent of these internal loops, the transverse current is opposite to that of core region near the partition wall. So the Lorentz force is acting along the

pressure force as opposed to the core region and thus axial velocity is increased near the partition wall. Asymmetry of side wall electrical conductance in channel-1 due to the presence of thin common wall (0.005m) and channel-5 due to thicker back plate (0.082m) is also reason for the high asymmetric flow profile in those channels.

Fig. 7.11 (a)

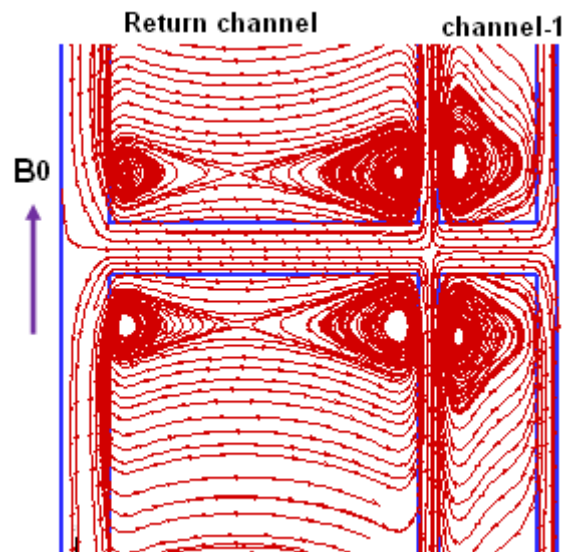


Fig. 7.11 (b)

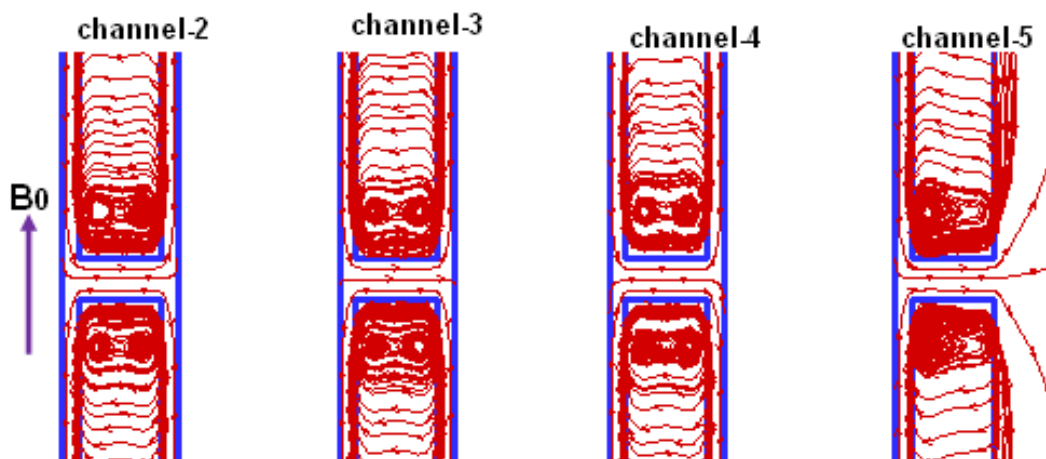


Figure 7.11: Zoomed view of current stream lines; near the partition wall of return channel and channel-1 in Fig. 7.11(a), for channel-2, 3, 4 and channel-5 in Fig. 7.11(b)

7.4.3 Flow rate distribution

PbLi enters into the poloidal flow channels from the bottom inlet header with differential flow rate depending on the electromagnetic resistance offered by respective channels. The distribution is a function of the Ha as well as function of the Reynolds number(Re). With the presence of central partition plate in the poloidal channels, the pressure drop will increase because of increased induced current density facilitated by additional current paths. Different strength of electrical coupling among the parallel channels may lead to non-uniform rise in pressure drop which may alter the flow rate distribution. So estimation of flow rate in individual channel and change in distribution due to presence of partition plates is an important design parameter. Table 7-2 presents the comparison of the flow rate distribution obtained from the numerical prediction for the case with and without partition plate with total flow rate of 12 kg/s and applied magnetic field 4.0 T. As can be seen, the integral flow rate in the respective poloidal channel is significantly affected by the insertions of partition plate. The maximum deviation is observed for the channel-1 which is adjacent to the return channel of counter flow configuration. The flow rate is reduced to 44.4% as compared to 55.5% for the case without any partition. But the increase of flow rate in other co-flow channels is non uniform with least effect in channel-5 adjacent to the thicker back plate (0.082 m). Numerical results also predicted that the flow rate in the sub-channels of each channel is identical as the central partition plate split each channel into two symmetric sub ducts. As mentioned earlier, the higher integral flow rate in the channel-1 is attributed to strong MHD effects linked with common partition wall and lowest flow rate in channel-5 is because of higher electromagnetic braking due to thicker back plate. When the applied magnetic field is absent the flow rate distribution is estimated using standard k- ϵ model. A major fraction of the flow is still drawn by channel-1 because of the flow inertia and gradually decreases towards the channel-5 located near the inlet section. So the higher flow rate to channel is attributed to effects of inertia and further increased by the MHD effects associated with common partition wall.

Table 7-2: Comparison of flow rate distribution for the case of with and without partition plate

channel number	Flow rate (kg/s)			
	Hydrodynamic case with partition at $B_0=0T$	Magneto-hydraulic case without partition at $B_0=4T$	Magneto-hydraulic case with partition at $B_0=4T$	Thermo-fluid MHD case with partition at $B_0=4T$
channel-1	4.25(35.4%)	6.66(55.5%)	5.33 (44.4%)	5.45(45.4%)
channel-2	2.95(24.6%)	1.5(12.5%)	2.0 (16.7%)	2.1(17.5%)
channel-3	2.16(18.0%)	1.23 (10.2%)	1.66 (13.8%)	1.67(13.9%)
channel-4	1.59(13.3%)	1.35 (11.3%)	1.62 (13.5%)	1.53 (12.8%)
channel-5	1.04(8.7%)	1.26 (10.5%)	1.39 (11.6%)	1.25 (10.4%)

7.5 Thermofluid analysis

Thermofluid analysis is performed considering the heat deposition data in various elements based on neutronic calculation in a similar conceptual LLCB variant [18]. The radial variation of deposited heat is considered without any variation along the toroidal and poloidal direction. Suitable functional form is fitted into the heat density data of different group of zones and provided as user defined volumetric heat source input for thermal calculation. For heat density in PbLi (q_{PbLi}), an exponential function as displayed in Eqn(12) and polynomial function (q_{RAFMS}) as displayed in Eqn(13) are considered as user defined functions for internal structural breeder walls including partition wall. The heat density input profiles (q_{Hart}) for external Hartmann walls are simulated with similar polynomial function with suitable coefficients as presented in Eqn(14) The heat distribution in each breeder region is assumed uniform. Variation of heat density profile along the radial direction and across all the zones of present numerical model is shown in Fig. 7.12. The integrated heat load over the entire model is estimated to be 460 kW which is consistent with the neutronic calculation.

$$q_{PbLi} = 4.5436 \times 10^6 e^{-6.918 * X} \quad \text{Eqn (12)}$$

$$q_{\text{RAFMS}} = \sum_{n=0}^4 P_n X^n \quad \text{Eqn (13)}$$

$$P_0=9.8384E5, P_1=1.5665E7, P_2=-1.5235E8, P_3=4.2646E8, P_4=-3.9038E8$$

$$q_{\text{Hart}} = \sum_{n=1}^4 A_n X^n \quad \text{Eqn (14)}$$

$$A_0=5.8591E6, A_1=-8.0776E7, A_2=4.8631E8, A_3=-1.2965E9, A_4=1.2375E9$$

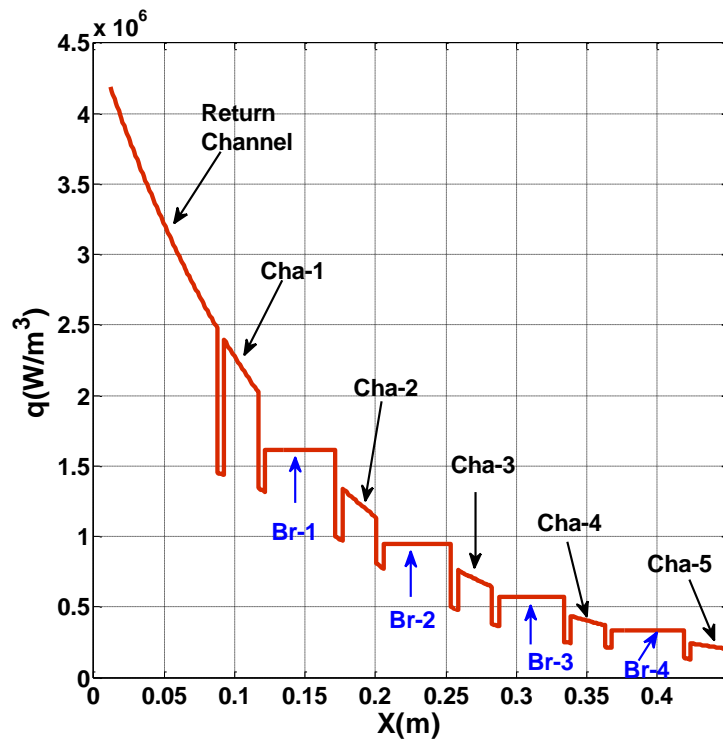


Figure 7.12: Radial variation of heat density profile in various zones of LLCB model

7.5.1 Steady state heat distribution

The total heat load in TBM is ~460 kW that includes volumetric heat of U shaped First wall (47kW), ceramic breeders (105.3kW), RAFMS breeder walls (14.76kW) partition plates (2.26kW) and PbLi heat (290.6 kW). Numerical solution for steady state heat transfer rate by liquid metal PbLi is 297 kW and helium cooling circuit through first wall and Hartmann wall is 164kW. Thus integral rate of heat transfer is 461kW which is agreement with the input heat load. So considering an additional heat flux from the FW plasma side surface (241kW), the net heat load to helium circuit is estimated to be 442 kW. Based on these numerical values of

steady state heat distribution, the net rise in PbLi and helium temperature is estimated using Eqn (15). Assuming helium flow rate of 1.63 kg/s and specific heat of 5195 J/kg-K the net temperature rise turns out to be 48 K whereas the net rise of PbLi temperature is 131 K for a flow rate of 12 kg/s. Based on the estimated heat load to helium, the average bulk helium temperature at the First wall outer surface is fixed with 597 K (assuming inlet He temperature 573 K) for convective heat transfer boundary condition.

$$\dot{Q} = \dot{m}C_p \Delta T \quad \text{Eqn(15)}$$

Here C_p and \dot{m} is the specific heat and mass flow rate of the fluid and \dot{Q} is the heat transfer rate into the fluid

7.5.2 Temperature distribution

Unlike the helium cooled first wall, internal structural walls like common wall, poloidal channel internal partition walls and breeder walls are cooled by PbLi only. So the local temperature in these structural walls which are in contact with PbLi could exceed the allowable limit. These hot spots may lead to higher corrosion rate and pose serious design constraint. The present simulation is concerned with the hot spots of internal structures rather than helium cooled FW which is implicitly modelled. The temperature distribution in internal partition walls are shown in Fig. 7.13. Although the flow rate is highest in channel-1, higher temperature of 806 K (533 °C) is observed in the top portion mainly due to higher PbLi heat density and hotter fluid in top regions. But the rest of the partition walls are adequately cooled even though helium cooling is absent due to the higher axial velocity as discussed in *section-7.4.1* for velocity distribution. Temperature distribution in the vertical/horizontal barrier wall that separates the incoming flow channel-1 and return channel is shown in Fig. 7.14. The temperature in the central region gradually increases from the bottom and reaches a maximum of 788 K (515 °C) at the top central region. As the sides (parallel to applied magnetic field) are

attached to the helium cooled first wall no hot spots are observed in these regions. Similar observations are made for the temperature distribution of breeder-1 and breeder-2 structural walls where neutronic heat load is highest among all the breeders and shown in Fig. 7.15(a) and Fig. 7.15(b) respectively. The maximum temperature of 806 K (533 °C) is observed for the plasma facing side of the breeder-1 wall at the top region adjacent to the internal partition. To get an idea about the maximum temperature of successive breeders, a temperature profile along the radial direction passing through the centre of each partition plate is shown in Fig. 7.16 at different heights. As can be seen the maximum temperature of 1260 K (987 °C) is observed in the center of breeder-1 at vertical height of Y=1.5m. So the numerical analysis indicates most of the structural material temperature is below the desired limit (500 °C) except some locations where temperatures exceed marginally for the present PbLi flow rate.

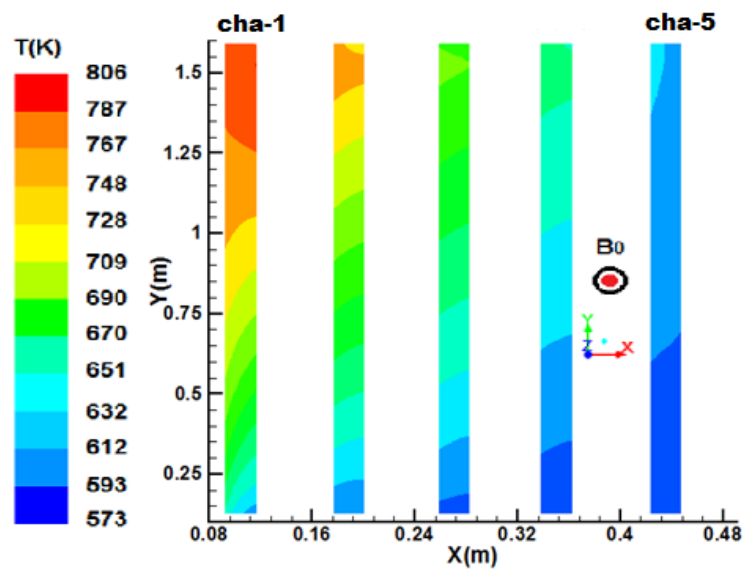


Figure 7.13: Temperature contour in the internal partition walls

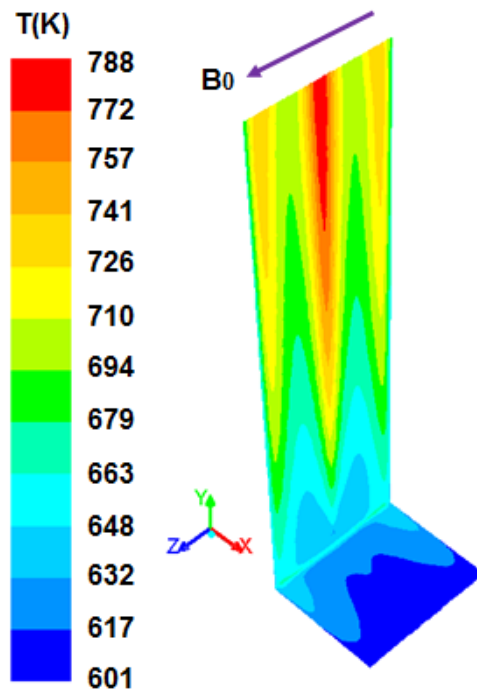


Figure 7.14: Temperature contour in the vertical/horizontal barrier wall

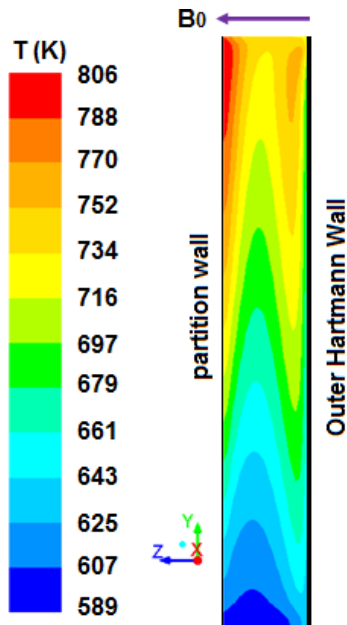


Fig. 7.15(a)

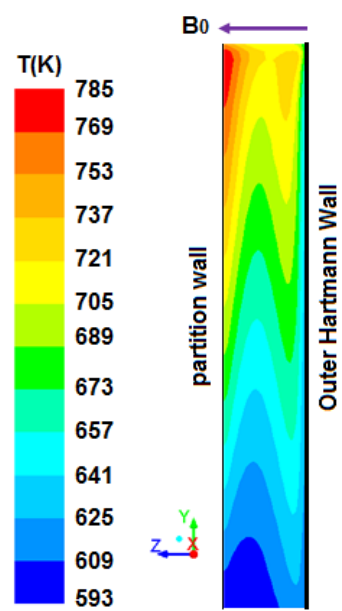


Fig. 7.15(b)

Figure 7.15: Temperature contour for the walls of breeder-1 in Fig. 7.15 (a) and for breeder-2 in Fig. 7.15 (b)

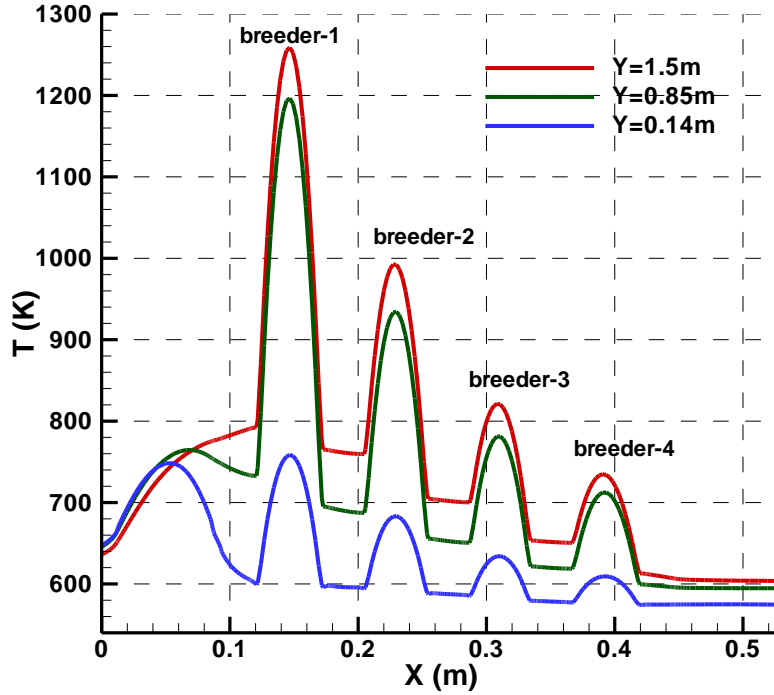


Figure 7.16: Temperature profile along radial direction at different heights

Thermofluid computation in the present LLCB variant enables to estimate the maximum attainable Nusselt number(Nu) in a laminar MHD flow. Particularly the walls which are cooled by PbLi exclusively are of practical interest for theoretical estimation of the wall temperature. Since the Peclet number ($Pe = Re \cdot Pr$) of the problem varies in the range 10^2 - 10^3 and thermal boundary layer thickness follows $1/\sqrt{Pe}$, the poloidal length of 1.6 m is just insufficient to achieve a fully developed thermal boundary layer. So the local Nusselt number value estimated using eqn. (16) varies along the flow direction at various walls depending on the local wall temperature(T_w) and adjacent fluid temperature (T_f) as:

$$Nu = \frac{(T_w - T_f) / \delta_f}{(\bar{T}_w - T_{ref}) / a} \quad (16)$$

Here, \bar{T}_w and T_{ref} are respectively the average wall and the bulk fluid temperature, ' δ_f ' is the normal distance of the fluid element from the wall and 'a' is the characteristic Hartmann length.

The reference bulk temperature (linear average) for different sub-channels and average wall temperature (area weighted) are summarised in Table 7-3. For the side walls the fluid temperature is considered at distance $\delta_f=1.0736 \times 10^{-3}$ m, where the jet velocity in the side layer is maximum. For partition walls the same is considered at distance $\delta_f=2.441 \times 10^{-2}$ m, which is located beyond the Hartmann layer.

Table 7-3: The average temperature of structural wall and PbLi temperature rise in different channels of LLCB

Average structural wall temperature		PbLi temperature(K)			
Wall Name	Average (Area weighted)	Channel Name	Entrance	Exit	Average(linear)
Vertical barrier plate (return channel side)	709	Return channel	704	786	745
Vertical barrier plate (channel-1 side)	694	channel-1	598	732	665
Breeder-1(channel-2)	678	channel-2	595	723	659
Breeder-2(channel-2)	668	channel-3	586	677	631
Partition wall (return cha)	758	channel-4	577	636	606
Partition wall (channel - 1, channel-2)	724, 698	channel-5	573	609	591

In view of different Nu at a given flow cross section (due to variable wall temperature), the local Nu is presented at the central line of the corresponding wall for comparison and qualitative analysis. The most relevant walls are the vertical barrier plate(VBP) and breeder-1 & breeder-2 walls which are cooled by high velocity jet with large side layer volume flux. The variation of Nu along the poloidal direction at these walls is shown in Fig. 7. 17(a). Similarly,

the variation of Nu at the internal partition wall of the return channel, channel-1 and channel-2 are shown in Fig. 7.17(b).

Fig. 7.17(a)

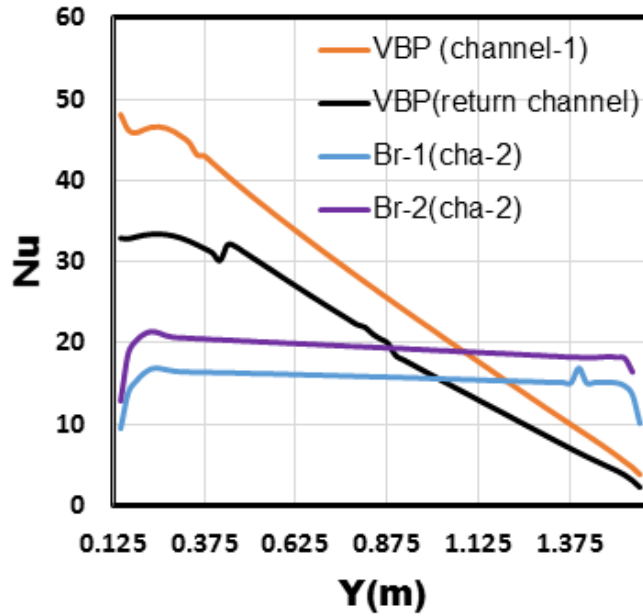


Fig. 7.17(b)

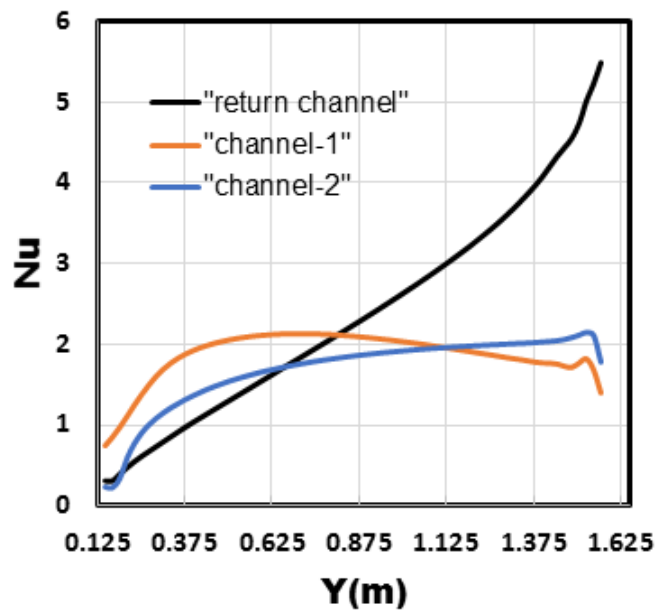


Figure 7.17: Nusselt number variation along the poloidal direction for side walls cooled by high axial velocity jet in Fig. 17(a) and for internal partition wall cooled by low axial velocity in Fig. 17(b)

For other walls the results are intermediate and not reported. As can be seen the magnitude of Nu at VBP is significantly higher than the value in hydrodynamic laminar flow regime ($Nu \leq 10$) in most of the flow length. The higher Nu is attributed to the better convective heat transfer by high velocity side layer jets at these walls even though the flow is laminar. For internal partition walls, Nu is much less ($Nu \leq 3$) than their corresponding side walls except the partition wall of the return channel. The lower Nu at partition wall is attributed to the low axial velocity in the adjacent Hartmann layer. The result of numerical simulation indicates average increase of PbLi temperature for channel-1, channel-2 channel-3 channel-4 and channel-5 is 134 K, 128 K, 91 K, 59 K, and 36 K respectively (see Table 7-3). So there is a large variation in the heating of PbLi in different poloidal channels. From thermomechanical stress perspective more uniform PbLi heating is preferred in the parallel poloidal channels for effective use of radiation heat. It is also to be noted that the present model considers equal radial width (0.024m) for all the flow channels. In future design the geometrical parameters such as varying radial width of PbLi flow channel, increasing number of partition plates in the high flow rate channels etc. can be adopted for an optimum design.

7.5.3 Comparison of breeder wall temperature with a case without partition wall

As discussed earlier, the peak velocity in a side layer jet associated with breeder-2, 3 and 4 is relatively more when the partition wall is present in the poloidal flow channels compared to the case without any partition wall. The increased peak velocity in the side layers resulted in better heat transfer and consequently lowered the overall temperature of side wall. For comparison, temperature distributions in the wall surface of breeder-1 ((in contact with PbLi flow of channel-2) and breeder-2 (associated with channel-3) are shown in Fig. 7.18 (a) and Fig. 7.18 (b) respectively when the partition plates are absent in corresponding flow channels. It can be seen that the maximum temperature for breeder -1 and breeder-2 reach to

925K and 833 K respectively which are higher compared to respective cases with the internal partition wall (see Fig. 7.15).

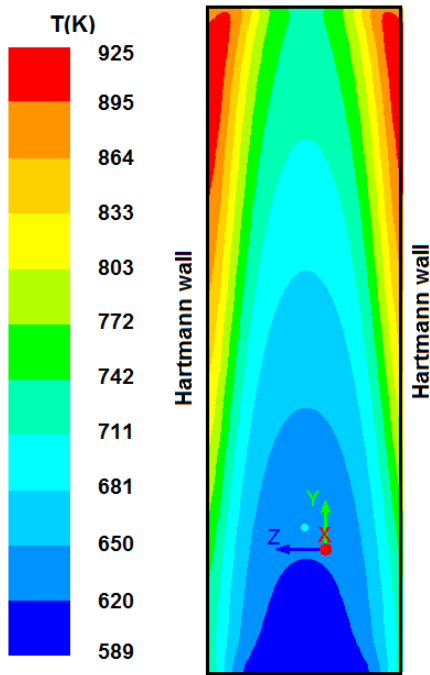


Fig. 7.18(a)

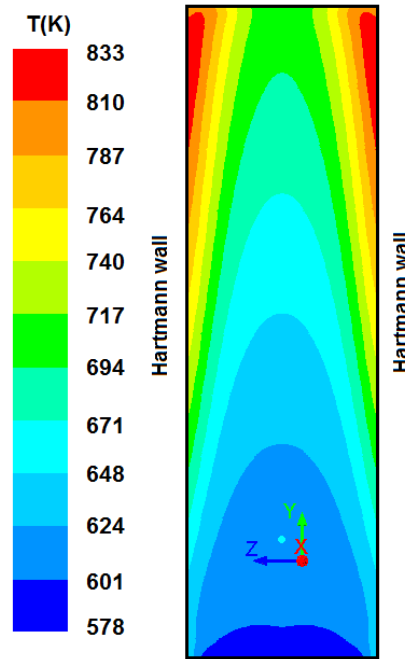


Fig.7.18(b)

Figure 7.18: Temperature distribution in breeder-1 surface contact with PbLi flow channel-2 in Fig. 7.18(a) and breeder-2 associated with channel-3 in Fig. 7.18(b) for the simulation case without any partition wall

The centerline temperatures of the surfaces of breeder-1 and breeder-2 in contact with PbLi are also compared for both the cases and shown in Fig. 7.19. Since the breeder-1 surface is associated with channel-1 flow at one side (where there is a reduced side layer peak velocity) and cooled by channel-2 flow (with increased jet velocity) at the other side, the difference in centerline temperature is non-monotonous. But for breeder-2, there is a significant lowering of centerline temperature due to higher jet velocity in the associated side layers. Thus it is evident that the heat transfer through side walls is better when partition plates are introduced.

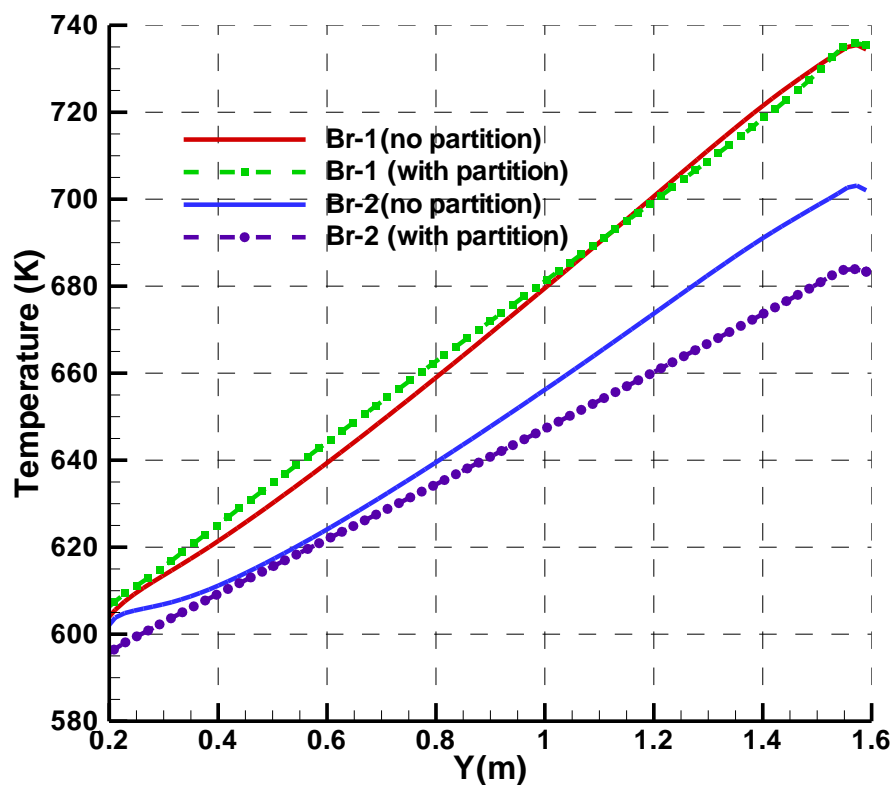


Figure 7.19: Comparison of centerline temperature of breeder walls for the case with and without partition wall in LLCB flow channel

7.5.4 *Effects of buoyancy with partition wall*

Because of exponential variation of volumetric heat and non-uniform cooling, high temperature gradient exists in the PbLi flow channels adjacent to the plasma facing first wall. The changes in the flow properties like PbLi density, viscosity, velocity etc. are significant in these channels. The variation of densities in a vertical central plane of return flow sub-channel and sub-channel-1 are shown in Fig. 7. 20. In the return channel the density is lower at the centre due to higher temperature and decreases gradually towards the bottom header as the temperature rises along the downward flow direction. Whereas for channel-1 the density gradient is more at the bottom with a lower value at the common vertical barrier plate and the gradient falls as the flow proceeds along vertical direction. For other sub-channels the density is lower in the side layers of corresponding heated breeder walls. Consequently, the flow profile is modified throughout the poloidal heights of the channels. The differential temperature profile and varying strength of buoyancy force in the upcoming poloidal flow channels also result in minor modification of the magneto-hydraulic flow rate distribution. A comparison is presented in Table 7-2. The flow rates in the high heat deposited channels (such as channel-1 and channel-2) are additionally increased by ~1% and the same fraction is compensated by the reduced flow rates in channel-4 and channel-5.

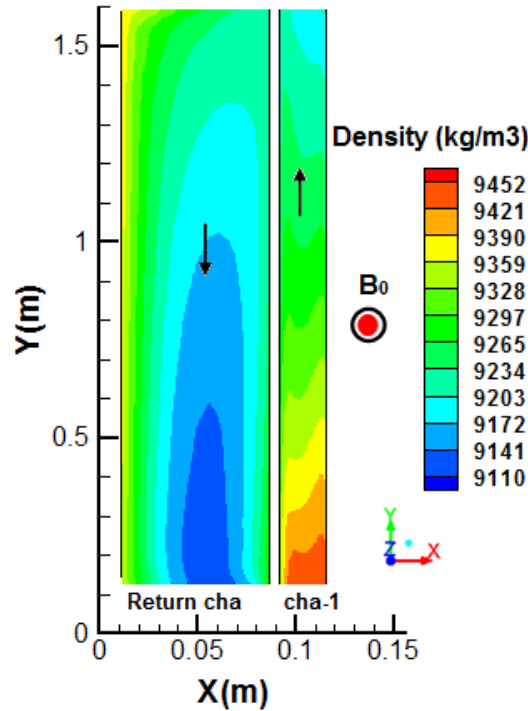


Figure 7.20: Contour of density in the vertical central plane of channel-1 and return flow path

The modification of axial velocity profiles across the side walls of sub-channels of return path and channel-1 and channel-2 to channel-5 due to buoyancy effects are shown separately in Fig. 7. 21(a) and Fig. 7. 21(b) respectively at the central plane($Z=0.106\text{mm}$) and at a poloidal height of $Y=0.85\text{m}$. The buoyancy effect is expected to be pronounced in the sub channels of return and channel-1 because of high heat deposition with exponential variation in radial direction. For the return channel where buoyancy force is opposing the flow along with the electromagnetic force, the two side walls (helium cooled FW and vertical barrier plate) are having lower temperature than the central core region. So flow reversal is expected in the slow moving downward flow in the core region. Considering the average FW temperature of 661 K and bulk fluid temperature of $\sim 744\text{ K}$, the Grashof number (Gr) which determines the relative magnitude of buoyancy force over the viscous force is estimated to be 3.6×10^9 . The estimated local Reynolds number around $Re=1.5 \times 10^5$, the ratio of Gr/Re^2 around 0.3 indicate the system in a mixed convection flow regime. Due to the opposing action of buoyancy force the jet

velocity adjacent to the FW is slightly reduced. However, no reverse flow regions are observed in the central plane ($Z=0.106\text{m}$) of the return sub-channel as can be seen from the velocity streamlines plot of Fig. 7.22. It appears that although the buoyancy force is significant, it is not insufficient to set a flow reversal in the return path. The opposing buoyancy force in the central region of larger width (0.076m) has resulted in a small increase of the side layer peak velocity adjacent to the vertical barrier plate. On other hand, the upward flow in channel-1 is aided by buoyancy force. As discussed in magneto-fluid case, the high velocity jet in the side layer of the vertical barrier plate resulted in a very low core velocity and subsequently lead to flow reversal due to stronger electromagnetic force. For thermofluid MHD case, the vortex regions in sub channels of channel-1 still persist but the size of those vortices are relatively stretched by the local buoyancy effects. Because of high velocity jets in the adjacent side layer, the vertical barrier plate is always at higher temperature than the nearby fluid temperature. The higher temperature led to lower density and lower viscosity near the wall region compared to the core. Owing to reduced viscous drag, the jet velocity is further enhanced by buoyancy and pressure force. In the sub-channels of channel-1 with Gr number value of 1.1×10^9 , the dominance of electromagnetic force still prevails in the flow dynamics as the Lykoudis number ($Ly=Ha^4/Gr$) (is a measure of relative strength of electromagnetic force over the buoyancy force) is of the order 10^3 . Here, Gr is estimated considering the average vertical barrier plate temperature of 694 K and mean fluid temp of 665 K and characteristic length scale same as the Hartmann length scale ($a=0.10575\text{m}$). As the deposited heat density falls towards the back plate the increase of jet velocity in the side layers of sub-channel-2 to sub-channel-4 gradually decreases.

Fig. 7. 21(a)

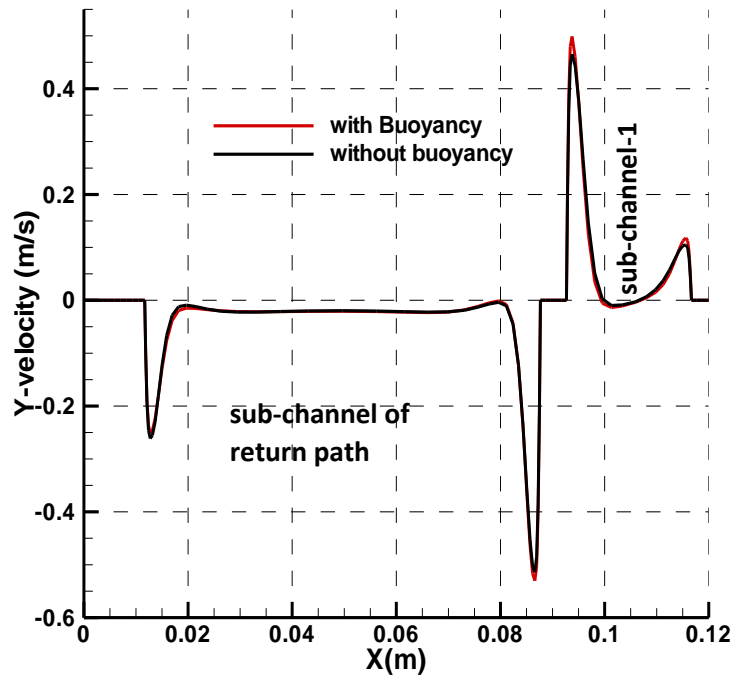


Fig. 7. 21(b)

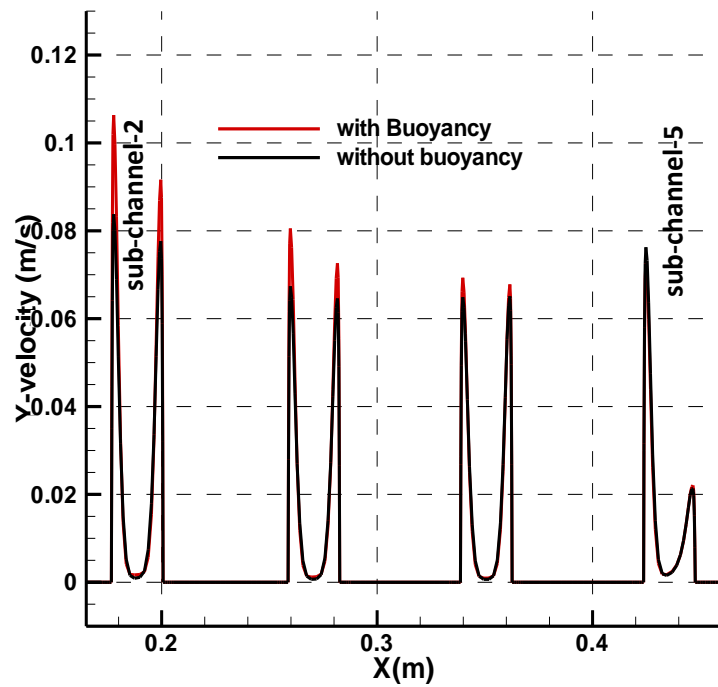


Figure 7.21: Comparison of axial velocity profile across the side walls for magneto-hydraulic (without buoyancy) and thermofluid MHD case studies at the central plane ($Z=0.106\text{mm}$) and poloidal height $Y=0.85\text{m}$, (a) for return path and sub-channel-1 and (b) for sub-channel-2 to channel-5

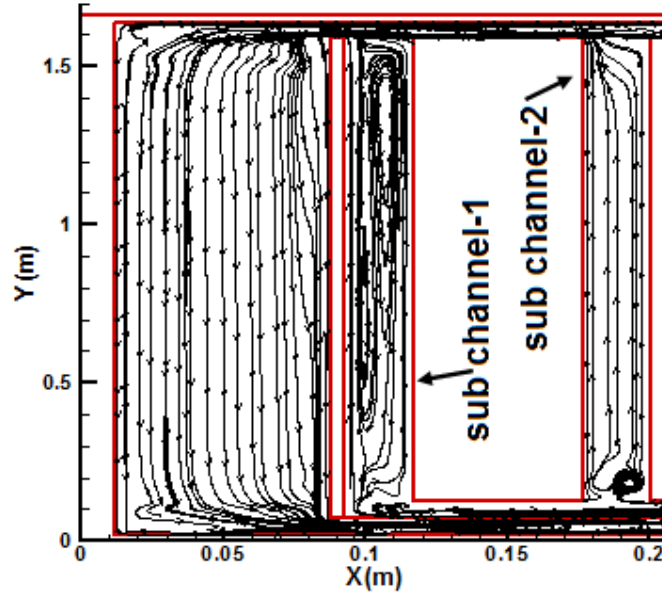


Figure 7.22: Velocity path lines in the central plane of sub-channel-1, sub-channel-2 and return flow sub-channel obtained from thermofluid MHD simulation

7.6 Pressure

In the presence of internal partition wall the characteristic length scale is reduced. So the pressure drop which is proportional to the relative wall electrical conductance of Hartmann wall ($Ch_1 = \sigma_w * t_{hw} / \sigma_f * a$) is expected to be more. Here t_{hw} is the thickness of the external Hartmann wall (0.01167m) and 'a' is the characteristic length scale which is 0.10575m for the case with internal partition wall and 0.214 m for the case without any partition. Due to different characteristic length, the relative Hartmann wall conductance for case with partition (Ch_2) is two times more than that of case without any partition wall ($Ch_1 = 0.09$). Physically the induced transverse current density is increased due to shorter electric current path and hence offers lower resistance than the case without partition wall. The increased induced current density lead to stronger electromagnetic drag force and hence higher pressure drop. The total magneto-hydraulic and thermofluid MHD pressure drop for the present case with internal partition wall is ~63 kPa and ~61 kPa respectively which is significantly higher than the case without partition wall where pressure drop is ~38 kPa. But the nature of the pressure profile is the same in both

cases. The contour of pressure profile in a central poloidal flow plane ($Z=0.106\text{m}$) is shown in Fig. 7.19. Large proportion of the pressure drop is observed in the return channel because of higher flow rate. Numerical value of pressure coefficients for i^{th} channel is estimated from the normalized pressure gradient ∇p_i^* ($= \nabla p_i / (\sigma U_{m,i} B_0^2)$) of respective channels and comparison is presented in Table 7-4. Here, $U_{m,i}$ is the numerical mean velocity in respective flow channels. In Table 7-4 Δp_1 and Δp_2 correspond to the pressure drop for case without and with presence of partition wall respectively

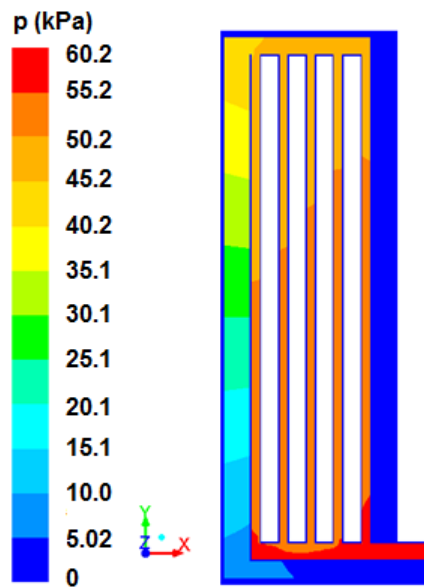


Figure 7.23: Contour of static pressure in the central poloidal plane ($Z=0.106\text{m}$)

Table 7-4: Comparison of normalized pressure drop for case with and without partition wall

Channel no.	$\Delta p_1(\text{kPa})$	∇p_1^*	$\Delta p_2(\text{kPa})$	∇p_2^*	$\Delta p_2^*/\Delta p_1^*$
channel-1	3.15	0.0137	10.44	0.0355	2.59
channel-2	2.26	0.0576	7.35	0.085	1.47
channel-3	1.75	0.0688	6.42	0.0996	1.45
channel-4	2.06	0.0647	6.33	0.1021	1.58
channel-5	3.20	0.0762	8.09	0.1285	1.68
Return channel	17.84	0.0199	34.0	0.0407	2.05

As can be seen in Table 7-4, the dimensionless pressure gradient (∇p_2^*) for the case with partition wall is increased for all the sub-channels. But the enhanced electromagnetic resistance

does not follow exactly linear variation with an increase in the ratio of relative Hartmann wall conductance. The increase of flow resistance is relatively more for sub-channel-1 and return path compared to other parallel sub-channels. So the analysis indicates strong electromagnetic coupling in the counter flow configuration than that in the co-flow. The result of non-uniform increase in the drag coefficient is primarily responsible for change in the flow rate distribution among the poloidal flow channels compared to the case without partition wall. In case of neutronic heat load the buoyancy force is against the pressure force in the return channel due to flow along gravitational force. Still the total pressure drop is less which can be attributed to the favourable buoyancy action along the pressure force in the upward flow channels. For the present thermofluid numerical model with internal partition wall the net reduction in pressure drop is only 2kPa which is ~3.3% of the total pressure drop. So the contribution of buoyancy to the overall MHD pressure drop is insignificant compared to its effect on the velocity distribution.

7.7 Summary of thermofluid MHD effects of partition plates in LLCB TBM

Numerical simulation in 3-D is performed to study the thermofluid effects of partition walls in a LLCB model TBM proposed by India at ITER relevant magnetic fields. It is observed that the partition plate has significant effects on distribution of velocity, electric current along with flow rate distribution in parallel channels and pressure drop. Axial velocity is significantly higher in the Hartmann boundary layer of thin internal partition wall than corresponding thicker Hartmann wall comprising U shaped first wall. The increased velocity is attributed to the formation of additional current loops adjacent to the partition wall. Effects on side wall jet structure and redistribution of flow rate among the parallel poloidal channels due to introduction of partition plates are analysed by comparing the results with a similar LLCB model with no such partition. Thermofluid analysis is carried out to obtain the temperature distribution of structural elements for a given heat load profile based on neutronic estimation.

It is observed that the peak velocities in the side layer jet of lower flow rate channels are further increased, which have resulted in lower wall temperature and hence indicates better heat transfer in those channels. In addition, the recirculation zones which were earlier formed in most the long slotted poloidal flow channels are absent if the partition plates are introduced. Even though the heat transfer in the lower flow rate channels has improved, there exist large variation in the PbLi heating of different poloidal flow channels. So the analysis indicates further scope in optimising the geometry of LLCB variant by varying the number of partition plates and radial width of flow channel for effective use of radiation heat. Thermal hot spots in internal structures that are cooled by PbLi only are identified. At these zones the temperature exceeds allowable limit of 773K. The estimated Nusselt number at the side walls, cooled by high velocity jet is found to be higher than the corresponding hydrodynamic counterpart in the laminar flow regime. The flow profile for thermofluid case is found to be significantly different from the corresponding magneto-fluid profile due to differential action of the buoyancy force in co-flow and counter-flow channels. Whereas, the contribution of buoyancy to the overall pressure drop is observed to be marginal. The total pressure drop is increased if the partition plates are introduced and the estimated numerical values of pressure coefficients for various channels are found to be higher than the corresponding cases without partition. The increase of drag coefficients in the counter-flow channels is higher than the co-flow channels which may be attributed to the different strength of electromagnetic coupling among the parallel channels.

7.8 References

1. P.K. Swain, Pratik Koli, S. Ghorui, P. Mukherjee, A.V. Deshpande, Thermofluid MHD studies in a model of Indian LLCB TBM at high magneticfield relevant to ITER, Fusion Eng. Des. 150 (2020)
2. S. Ranjithkumar, D. Sharma, et al., Engineering design and analysis of Indian LLCB TBM set, Fusion Eng. Des. 109 (2016)
3. P. Chaudhuri, S. Ranjithkumar, et al., Progress in engineering design of Indian LLCB TBM set for testing in ITER, Fusion Eng. Des. 89 (2014)

4. A. Patel, R. Bhattacharyay, et.al, 3D thermo-fluid MHD simulation of single straight channel flow in LLCB TBM, Fusion Eng. and Des. 87 (2012)
5. A. Y. Ying and M. S. Tillack, MHD heat transfer in elongated rectangular ducts for liquid metal blankets, Fusion technology 19 (1991)
6. C. Mistrangelo, L. Buehler, Electric flow coupling in the HCLL blanket concept, Fusion Eng. and Des. 83 (2008)
7. P. Satyamurthy, P.K. Swain, et al., Experiments and numerical MHD analysis of LLCB TBM Test-section with NaK at 1 T magnetic field, Fusion Eng. and Des. 91 (2015)
8. T.Q.Hua, B.F. Picologlou, et al., MHD thermal hydraulic analysis of three-dimensional liquid metal flows in fusion blanket ducts, Fusion Eng. and Des. 8 (1989)
9. P.K. Swain, P. Satyamurthy, et al., 3D MHD lead–lithium liquid metal flow analysis and experiments in a Test-Section of multiple rectangular bends at moderate to high Hartmann numbers, Fusion Eng. and Des.88 (2013)
10. U. Muller, L. Buehler, Book: Magnetofluiddynamic in channels and container, springer, 2001 ISBN 3-540-41253-0
11. Fluent code produced by ANSYS FLUENT Inc
12. P. Moresco, T. Alboussiere, Experimental study of the instability of the Hartmann layer, Fluid Mech 504 (2004)
13. S. Smolentsev, R. Moreau, et al., MHD thermofluid issues of liquid metal blankets: phenomena and advances, Fusion Eng. Des. 85 (2010)
14. B. Schulz, Thermophysical properties of the Li(17)Pb(83) alloy, Fusion Eng. Des. 14 (1991)
15. A.F. Tavassoli, A. Alamo, et al., Material design data for reduced activation ferritic martensitic steel type EUROFER, J. Nucl. Mater. 329–333 (2004)
16. Z. Xu, R. Meyder, et al., Design and validation of breeder unit of helium cooled pebble bed blanket for demo fusion reactor, Fusion Eng. Des. 81 (2006)
17. G. Aiello, F. Gabriel, et al., Thermal–hydraulic analysis of the HCLL DEMO blanket, Fusion Eng. Des. 82 (2007)
18. H.L. Swami, A.K. Shaw, et al., Neutronic performance of Indian LLCB TBM set conceptual design in ITER, Fusion Eng. Des. 113 (2016)

Thesis Highlight

Name of the Student: Pravat Kumar Swain

Name of the CI/OCC: BARC, Trombay

Enrolment No.: PHYS01201404021

Thesis Title: Liquid Metal MHD studies at High Magnetic Fields Relevant to Fusion Test Blankets

Sub-Area of Discipline: Physics

Discipline: Physical sciences

Date of viva voce: 10/11/2020

The Indian proposal of Lead Lithium cooled Ceramic Breeder(LLCB) TBM for ITER program is conceptualized with the philosophy of self-cooling and tritium breeding from both the solid ceramics (LiTiO_3) and liquid metal Lead-Lithium (PbLi) eutectic in a single variant. The flow of PbLi in channels of LLCB as shown in Fig. 1 is subject to high toroidal magnetic field ($B_0=4\text{T}$) which leads to coupled flow-field interaction through induced Lorentz force and increases the complexity of the problem.

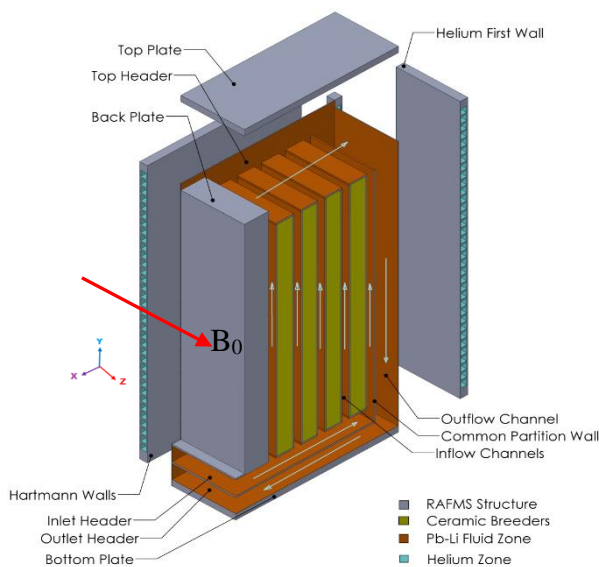


Fig.1: PbLi flow configuration in LLCB TBM

The dominating electromagnetic body force has substantial consequences in the thermal hydraulic performances determined by magnetohydrodynamics(MHD) at high characteristic Hartmann number(Ha) and Interaction parameter(N). Analytical, numerical and experimental studies have been performed at high magnetic fields ($B_0=1-4\text{ T}$) to understand and analyse various MHD

phenomena of a generic liquid metal blanket including thermo-fluid MHD issues in context to the design of LLCB TBM.

Validation cases such as Hunt's flow, MHD flows in ducts of finite electrical conductivity, flow subject to condition of varying magnetic field, etc. have been performed for code benchmarking and model validation. A number of interesting unique features have been observed for MHD flow at different characteristic parameters. To generate data for LLCB design, series of liquid metal R&D experiments at high magnetic fields(1-4T) have been performed jointly at Institute of Physics, University of Latvia (IPUL) in various complex geometries like test section with multiple 90-degree bends, electrically coupled multichannel TS, shielding effects of magnetic structural material, etc. to address different aspects of LLCB flow configuration. Numerical simulations in 3-D have been performed in those identical experiment test sections to assess the limitation of numerical model and its applicability to fusion relevant parameters. Based on these results, MHD simulation has been carried out in a full scale variant integrated with complex helium cooled first wall. The velocity and flow rate distribution in different channels, pressure drop, electrical coupling of parallel flow channels, wall temperatures, the buoyancy effects and heat load sharing among helium and PbLi coolant circuits have been estimated for a realistic heat deposition based on neutronic calculation. MHD analysis has been further extended to analyse the thermofluid effects of partition plates in a model of LLCB variant.

ABSTRACT

The understanding and characterisation of magnetohydrodynamic (MHD) duct flow is essential for the design and performance evaluation of liquid metal based tritium breeding blankets proposed for the ITER program. As the liquid metal flow in typical flow channels of a blanket module experiences a high transverse plasma confining toroidal magnetic field ($B_0=4\text{T}$), strong electromagnetic body forces are generated from the interaction of flow induced electric currents and the toroidal field itself. The high relative strength of electromagnetic force over viscous and inertial forces as determined by dimensionless parameter Hartmann number ($Ha = B_0 a \sqrt{\sigma/\mu}$) and interaction parameter ($N = \sigma a B_0^2 / \rho u$) leads to intense MHD effects with significant modifications in the hydrodynamic flow and heat transfer characteristics. The present studies aim at understanding and analyzing various MHD phenomena and conjugate heat transfer issues anticipated in a generic liquid metal fusion blanket including the INDIA proposed Lead Lithium cooled Ceramic Breeder (LLCB) Test Blanket Module (TBM). Analytical, numerical and experimental MHD studies have been performed in context to the design of LLCB variants and at ITER relevant characteristics parameters which appear in the range of 10^3 - 10^4 and 10^3 - 10^5 for Ha and N respectively.

Validation cases such as Hunt's flow, MHD flows in ducts of finite electrical conductivity, flow subject to condition of varying magnetic field, etc. have been performed for CFD code benchmarking and numerical model validation. A number of interesting unique features have been observed for MHD flow at different characteristic parameters. To generate data for LLCB design, series of liquid metal R&D experiments at high magnetic fields ($B_0=1-4\text{T}$) have been performed jointly at Institute of Physics, University of Latvia (IPUL) in various complex blanket elements such as test section consists of multiple 90-degree bends and electrically coupled multichannel test section, shielding effects of magnetic structural material, etc. to address different aspects of MHD flow in LLCB configuration. Numerical simulations in 3-D have been carried out in those identical experiment test sections to assess the limitation of numerical model and its applicability to fusion relevant parameters. Based on these studies, MHD simulation has been carried out in a full scale variant integrated with complex helium cooled first wall at $Ha \sim 18000$. The velocity and flow rate distribution in different channels, pressure drop, electrical coupling of parallel flow channels, key structural wall temperatures, the buoyancy effects and heat load sharing among helium and PbLi coolant circuits have been estimated for a realistic heat deposition based on neutronic calculation. MHD analysis has been further extended to analyse the thermofluid effects of partition plates in the poloidal flow channels of a model LLCB variant.